THE DESIGN OF A LOW-NOISE ROTOR-ONLY AXIAL FLOW FAN SERIES

Sybrand Johannes van der Spuy

Thesis presented in partial fulfillment of the requirements
for the degree of Master of Engineering (Mechanical) at
the University of Stellenbosch

Thesis Supervisor: Prof T. W. von Backström

Department of Mechanical Engineering
University of Stellenbosch
December 1997

DECLARATION

I, Sybrand Johannes van der Spuy, the undersigned, hereby declare that this thesis is my own original work. It is being submitted for the Degree of Master of Engineering (Mechanical) at the University of Stellenbosch. It has not been submitted, in its entirety or in part, for any degree or examination at any other University.

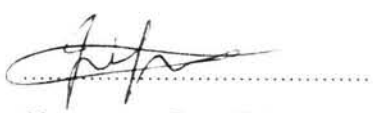

Signature of candidate

This 10th day of February 1998

ABSTRACT

A design routine was derived for designing a series of rotor-only axial flow fans. The routine was applied by designing two different series of axial flow fans. The first design was for a general application rotor-only axial flow fan. This fan series was designed, built and tested in co-operation with Howden Air Industries for both research and commercial purposes. The second design was for a low-noise fan series, which was designed, built and tested by the University of Stellenbosch for research purposes only.

The design theory used the principle of blade cropping, meaning that one blade was designed to fit all the different fan sizes. The fan series was designed for diameters ranging from 315 mm to 1000 mm. The fan rotors were designed to conform to a velocity profile of minimum exit kinetic flux. The general application fan design was concentrated around the popular fan diameter sizes of 500 mm, 560 mm and 630 mm and a rotor speed of 1440 rpm, using a commercially available fan series as reference. The low-noise fan design concentrated on one fan size only, namely 630 mm, while also making use of the principle of forward blade sweep. The remaining fan design principles stayed the same as for the general application fan design. The F-series airfoils were used as blade sections for both fan designs.

Both fan series were tested for fan noise and performance in accordance with the BS 848 Standards part 1 (1980) and 2 (1985). A selection of fan diameter sizes was tested for the general application fan to verify its performance over a range of fan sizes. This indicated a fan series with a wide range of efficient operation, including excellent noise characteristics. A 630 mm diameter fan was used to test the low-noise fan series. It showed both high efficiency and low noise characteristics. The reduction in fan noise achieved with the low-noise fan does not justify the amount of work and costs involved in the designing process, compared to the general application fan.

OPSOMMING

'n Ontwerpsroetine vir die ontwerp van 'n reeks enkelrotor aksiaalwaaiers is ontwikkel. Die roetine is toegepas deur twee verskillende reekse aksiaalwaaiers te ontwerp. Die eerste ontwerp was vir 'n algemene toepassings enkelrotor aksiaalwaaier. Die waaierreeks is ontwerp, gebou en getoets in samewerking met Howden Air Industries vir beide navorsings - en kommersiële doeleindes. Die tweede ontwerp was vir 'n lae geraas waaierreeks. Dié reeks is ontwerp, gebou en getoets deur die Universiteit van Stellenbosch vir navorsingsdoeleindes.

Die onwerpsteorie het gebruik gemaak van die beginsel van lemverkorting, waardeur een lem ontwerp is om op al die groottes waaierdeursneë te pas. Die waaierreekse is ontwerp vir waaierdeursneë tussen 315 mm en 1000 mm. Die rotors is ontwerp om 'n uitlaatsnelheidsprofiel te gee wat 'n minimum verlies in kinetiese energie toelaat. Die algemene toepassings waaierontwerp het gekonsentreer rondom die gewilde waaierdeursneë van 500 mm, 560 en 630 mm. Dit is ontwerp vir 'n rotorspoed van 1440 met 'n kommersiëel beskikbare waaierreeks wat as verwysing gebruik is. Die lae geraas waaierreeks het op slegs een waaiergrootte gekonsentreer, naamlik 630 mm. Die lae geraas waaierreeks is ook ontwerp met vorentoe gekurfde lemme. Die res van die ontwerpsbeginsels was dieselfde as vir die algemene toepassings waaierreeks. Die F-reeks vleuelprofiele is gebruik vir die lemseksies van beide waaierreekse.

Beide waaiereekse is getoets vir waaiergeraas en -effektiwiteit deur gebruik te maak van die BS 848 Standaarde deel 1 (1980) en 2 (1985). 'n Verskeidenheid van waaierdeursneë van die algemene toepassings waaierreeks is getoets om die waaier se vertoning oor 'n gebied van waaiergroottes te bepaal. Die resultaat was 'n waaierreeks met 'n wye gebied van effektiewe werking, asook uitstekende geraaseienskappe. 'n 630 mm Deursnee waaier is gebruik om die lae geraas waaier te toets. Die toetse het 'n waaier getoon wat beide hoë effektiwiteit en lae geraaseienskappe het. Die afname in waaiergeraas wat verkry is met die lae geraas waaier, in vergelyking met die algemene toepassings waaier, regverdig egter nie die werk en kostes verbonde aan die ontwerp van dié waaierreeks nie.

ACKNOWLEDGEMENTS

I would like to thank the following individuals and organisations for their assistance with the completion of this thesis:

Professor T. W. von Backström for his consistent guidance and expertise.

The members of the Department of Mechanical Engineering for their theoretical and practical contributions.

Howden Air Industries who contributed financially.

My wife, Elana, and parents for their support and patience towards the completion of the thesis.

My friends for their help and inspiration.

TABLE OF CONTENTS

LIST OF TABLES

LIST OF FIGURES

NOMENCLATURE

Symbol	Description	Units
a	outer/inner radius ratio	-
a	swirl coefficient	variable
a_0	air sonic velocity	m/s
A	dimensionless work rate	-
A	test ducting area	m^2
A	blade section area	m^2
A	blade segment area	m^2
A_{stl}	circumferential area between two streamlines	m^2
A_{root}	blade root area	m^2
b	outer wall radius	m
B	dimensionless flow rate	-
c	chord length	m
c	constant for axial velocity	-
$\bar{c}$	blade chord length in direction perpendicular to blade axis of swept blade	m
C	force coefficients	-
C	absolute velocity	m/s
C	sound measurement correction	dB
C	fan characteristic value	dBA
C_{pi}	ideal static pressure rise coefficient	-
d	ducting diameter	m
d	nose droop in % chord or fraction of chord	-
d	blade root diameter	m
$delP_T$	total pressure change	Pa
delta	angle between F and L on blade	(°)
d_f	wake width at blade trailing edge	m
d_i	diameter of conical inlet	m
d_t	blade thickness at blade trailing edge	m
$c'B_{cor}$	fan noise correction term	dBA

ΔdB	sound pressure level decay	dB
D	drag force on blade	N
Dw	downwash perturbation	m/s
D_f	fan diameter	m
E	Young's modulus	Pa
E	fan sound power	W
f	frequency	Hz
F	resultant blade force	N
F	dimensionless kinetic energy flux	-
F	value used to compare sound levels of different configurations	m^8/s^6
g	gravitational acceleration	m/s^2
G	constant for defining blade axis sweep	m^{-1}
h	pressure	m H_2O
h	perpendicular distance from fan hub	m
hd	hub diameter	m
i	incidence angle	(°)
I	second moment of area	m^4
J	second polar moment of area	m^4
k	constant for swirl velocity	-
k	profile adaption coefficient for camber	$(°)^{-1}$
K	constant for defining blade axis sweep	-
K_c	kinetic energy	J
K_1	constant for flow coefficient	-
l	profile adaption coeffcient for thickness	-
l_a	length of torque transducer calibration arm	m
l_{mom}	moment arm of aerodynamic forces	m
$\bar{l}$	blade length in direction of blade axis of swept blade	m
L	lift force on blade	N
L	kinetic energy flux	W
Lp	sound pressure level for fan	dB
LIF	lift interference factor	-
m	mass	kg
m	profile adaption coefficient for droop	-

m	deviation angle coefficient	-
m_a	mass of torque transducer calibration arm	kg
m_d	number of cycles of circumferential pressure variation	-
mV	milliVolt reading	mV
mV_{delta}	pressure transducer milliVolt offset	mV
mV_{ext}	extension cable correction	mV
mV_{pvf}	milliVolt pressure over conical inlet	mV
$\dot{m}$	mass flow	kg/s
M	moment	Nm
M_{cm}	critical circumferential Mach number of rotor tip	-
M_m	circumferential Mach number of rotor tip	-
M_R	radial blade Mach number	-
n	number of blade segments	-
n	swirl exponent	-
n_b	number of blades	-
p	fan pressure	Pa
p	pressure drop	Pa
p	pressure at a point	Pa
p_{ref}	reference sound pressure	Pa
p_{slm}	sound pressure	Pa
Δp	pressure drop across conical inlet	Pa
P_{atm}	atmospheric pressure	Pa
P	power	W
PWL	sound power level	dBW
q	dynamic pressure	Pa
q_m	mass flow rate	kg/s
Q	volume flow	m^3/s
Q_{max}	maximum volume flow for specific fan	m^3/s
r	radius	m
r_{stl}	radial location of streamline	m
rpm	rotational speed	rpm
R	gas constant	J/kg.K
Re	Reynolds number	-

s	blade pitch	m
sf	safety factor	-
SPL	sound pressure level	dB
SPL_f	turbulent fan noise	dB
t	radius as fraction of fan outer radius	-
t	blade thickness in % chord	-
T	temperature	K
T	shaft torsion	Nm
T_{atm}	atmospheric temperature	K
T_{root}	torsion in blade root	Nm
u	dimensionless swirl velocity	-
U	circumferential blade speed	m/s
v	dimensionless axial velocity	-
V	velocity	m/s
W	relative velocity	m/s
Wo	fan power consumption	W
x	axial distance from rotor	m
x	distance along blade chord as fraction of chord	-
Δx	distance offset between segment centroid and quarter-chord point	m
Δx_d	change in distance parallel to rotor	m
y_c	distance of blade camberline perpendicular on chord as fraction of chord	-
Y	profile coordinates perpendicular on chord in % chord	-
z	distance along axis of rotation	m

Greek Symbols

α	absolute flow angle	(°)
α	angle of attack	(°)
$\alpha\varepsilon$	flow coefficient	-
α_{0d}	angle of attack for zero nose droop	(°)
β	relative flow angle	(°)
Δ	axial velocity perturbation	-

Δ_0	axial velocity perturbation at actuator disk	-
Δ^0	downwash deviation angle	(°)
δ	deviation angle	(°)
ε	whirl coefficient	-
ϕ	flow coefficient	-
ϕ	angle between F and rotor plane of rotation	(°)
γ	pitch angle (relative to plane of rotation)	(°)
Γ	blade circulation	m^2/s
$\tan(\gamma)$	drag/lift ratio	-
η	geometric blade sweep angle	(°)
η	efficiency	-
λ	aerodynamic blade sweep angle	(°)
λ_0	eigenvalue for divergence condition	-
Λ	sweep angle	(°)
μ	viscosity	Ns/m^2
ν	hub-tip ratio	-
θ	camber angle	rad
θ_s	blade axis sweep angle	(°)
ρ	fan blade material density	kg/m^3
ρ	density	kg/m^3
σ	solidity ratio	-
σ	axial stress	Pa
τ	shear stress	Pa
Ω	rotational speed	rad/s
ω	rotational speed	rad/s
ψ	pressure coefficient	-
ξ	stagger angle (relative to axis of rotation)	rad
ξ	flow loss coefficient for fan test facility	-

Subscripts

a	axial
a	annulus
add	additional moment due to lift force offset
axial	axial force
atm	ambient
bend	bending moment
bo	usable air power
c	corrected sound pressure level
cent	moment due to centrifugal forces
c/4	quarter-chord moment
df	fan dynamic pressure
D	drag coefficient
e	effective power
f	sound pressure level at point
f	fan
inner	inner radius of blade root
i	inner radius of hub radius
I	milliVolt reading over conical inlet
k	kinetic power loss
L	lift coefficient
L	lower profile of blade
Li	lift coefficient taking blade interference into account
m	mean value
m	mechanical
mc/4	quarter-chord moment coefficient
o	outer radius or blade tip radius
outer	outer radius of blade root
p	pressure height at pressure measuring point
p	pressure transducer milliVolt reading
r	rotor
ro	read-out

root	blade root section
s	"swept" blade variables
s	static
s	shaft power
sf	fan static pressure
shear	shear force
sigma	axial stress
slm	sound level meter milliVolt reading
swept	moment due to forward blade sweep
t	total
tau	shear stress
tf	fan total pressure
torsion	torsion moment
total	total stress
T	torque transducer milliVolt reading
U	upper profile of blade
vf	pressure height at conical inlet
w	whirl
water	water
1	fan inlet side
2	fan outlet side
3	measuring point upstream of fan
4	measuring point downstream of fan
∞	axial distance far up- or downstream from rotor

1. INTRODUCTION

The trend in low cost fan manufacturing today is to design a series of fans consisting of different fan diameters using one rotor blade design and two or more hub sizes. The rotor blades are sized (cropped) to fit different combinations of fan and hub diameters inside the specified fan casing. Instead of designing one fan for a specific operating point, a series of fans must be designed to satisfy an operating range. The objectives of this thesis were as follows:

1. Formulate a simple, general fan design process for a fan series.
2. Apply this theory to general application fan design.
3. Apply this theory to low-noise fan design.
4. Manufacture and test the designed fans.

This thesis was written in conjunction with a project by the University of Stellenbosch Department of Mechanical Engineering to design a general application rotor-only axial flow fan series for Howden Air Industries (HAI), which could compete successfully in the South African market. This provided the unique opportunity of a practical thesis, because the final product would not only be a once-off test model, but a marketable product. HAI provided a set of design requirements that the fan series had to adhere to. Regular discussions were held with HAI to ensure that the specified design requirements were met. It was decided to use these requirements as basis for the thesis as well. The design requirements as given by HAI are in Table 1.1.

Table 1.1: Design requirements set forth by HAI

Fan diameters [mm]	315, 400, 560, 630, 710, 800, 900, 1000
Pressure duty [Pa]	100 to 1800
Flowrate [m^3/s]	0.2 to 30
Maximum tip speed [m/s]	115

The fans that were designed, are used in an air handling capacity to provide ventilation for rooms, factories and laboratories, to transport various gaseous fluids, to provide cooling through air movement and in air conditioning units. In South Africa, with its wide variety of primary industries, combined with a harsh climate, the need for air handling is very large. A wide variety of axial flow fans is available on the local market. This includes a number of imported fan designs as well as some local manufactured designs. Unfortunately the local fan designs are often copies made of imported designs under the pretext of reverse engineering.

The apparent simplicity of the rotor-only axial flow fan design has lead to numerous low-efficiency applications, where these fans or systems are not designed to meet the required pressure duty. This leads to the occurrence of fan stalling and consequently an increase in fan noise. Often the occurrence of fan noise is due to bad engineering principles used when designing fan installations (Wallis, 1983). These include obstructions in the airways in front of and behind the fan, mismatch between fan and system characteristics, fan stalling and unnecessary fan vibration due to incorrect mounting. The need for low-noise machinery was motivated by an increased awareness of hearing health. For instance, the maximum acceptable noise in a laboratory prescribed by the South African Bureau of Standards (SABS, 1983) is 40 dB. Axial fans must be installed correctly and designed with low-noise performance in mind. Reducing noise levels by means of sound insulation can be very costly. The technology for low-noise fans is available in South Africa in the form of imported products, for example air-conditioning units. Illustrations of a general application axial flow fan and a low noise axial flow fan are included in Figure 1.1 and Figure 1.2 on page 97.

This thesis is a continuation and extension of the work done by Bruneau (1994). It must be emphasised that where Bruneau's thesis was a pure research project, this thesis was in principal a manufacturing thesis with research being a secondary objective. Bruneau designed a general application single rotor axial flow fan using the main fan design principles as explained by Wallis (1983). The purpose of Bruneau's thesis was to improve the efficiency of large diameter axial flow fans. He did this by designing fans of 1.2 m diameter and testing them on a BS 848 type A, free inlet and free outlet, testing facility. He designed two prototypes, each one with a different wing profile, and compared them with the scale models of axial flow fans used in air-cooled condensers in power plants. He verified his design procedure by obtaining good results from his fan designs.

The fans designed in this thesis were noise and performance tested on a test facility which was designed using the BS 848 Standards (1980 and 1985) as a guide. This test facility, situated in one of the laboratories of the University of Stellenbosch, made provision for a type D fan, namely a fan with a ducted inlet and outlet. The test facility, as well as the instrumentation used, is described in a final year project by Van der Spuy (1994). This test facility was not suitable for large diameter fans because the length of the test facility increases as the fan diameter being tested increases, giving rise to a problem with laboratory space if the fan diameter is too large. The type D test facility is the facility type most often used by designers of fan series to test their fans. This type of test facility was used for most of the tests done during this project. The type A test facility previously mentioned is also owned by the University of Stellenbosch but is situated outdoors where the fan size is not of prime importance. Fan diameters up to 1.5 m can be tested in this facility.

The thesis was divided into three main parts, namely:

1. Designing a series of general application axial flow fans
2. Designing a series of low-noise axial flow fans
3. Testing the designed fans

The first part included the basic fan design procedure made applicable to a series of axial flow fans. The second part used the procedure described in the first part to design a series of low-noise axial flow fans, while the third part included the testing of both fan designs in such a way that a good estimate of the feasibility of the designs and design procedure could be obtained. It was attempted to keep all procedures as simple as possible.

2. LITERATURE SURVEY

According to Wallis (1983), axial flow fans can be placed in three main categories, namely:

1. Air circulator, or free fan - a fan that rotates in an open air space
2. Diaphragm-mounted fan - transfers air between two relatively large air spaces
3. Ducted fan - the fan is enclosed by a duct entering and leaving the fan.

As explained previously, the researcher concentrated on the third category because of the test facilities available.The basic fan design principles should not differ between the fans of the three different categories.

2.1. ADVANCES IN FAN DESIGN

According to Bass (1987) the basis of fan design stemmed from the aircraft propeller theory developed by Betz, Prandtl and Glauert. According to Van Niekerk (1964) this theory, along with the book by Keller (1937) on ducted axial flow fans formed the early guidelines for fan design. Other early contributions, specifically on wind tunnel applications, were made by Patterson (1944) and Thwaites (1951).

Van Niekerk provided a pioneering approach to fan design by minimising empirical methods and assumptions used in the design procedure. He also attempted to bring fan noise minimisation into the fan design procedure. The comprehensive book on axial flow fan design, analysis and testing by Wallis (1983), focused on optimised fan design techniques, while also referring to aspects such as fan noise and ducting. Bass (1987) distinguished between two different fan design routines, namely an isolated airfoil approach and a rotating cascade approach. He advocated the use of two-dimensional airfoil characteristics and referred to the generation of acoustic noise by improper fan installation. Smith (1987) promoted the use of a simple three dimensional approach to axial flow fan design, because it allowed for the estimation of deviation and losses.

The involvement of computers in fan design depends on the complexity of the design theory used. Bard et al. (1987) discussed the use of computers to calculate flow patterns in rotating machinery. This tool is also useful for estimating system effects on fan performance. Wright et al. (1987) provided a simple analysis of axial flow fan design theory to be used for computer aided design of

these fans. He managed to relate aerodynamic performance to the geometric features of a fan and provided a framework for estimating performance, efficiency and noise. This work was continued by Jackson et al. (1991) in developing an axial flow fan design system.

Bruneau (1994) drew up a design routine for ducted rotor-only axial flow fans using the guidelines provided by Wallis (1983) and implemented it in the form of three computer programmes. He also designed and built two experimental fans and tested them in accordance with the BS 848 standards. These fans performed very well.

2.2. GENERAL FAN DESIGN ASPECTS

Bruneau (1994) divided his design procedure into three categories:

1. Optimisation of the vortex distribution for the fan outlet velocity profile. This included the application of radial equilibrium to the optimised swirl velocity distribution to determine the accompanying axial velocity distribution.
2. Optimisation of the hub-tip ratio.
3. Designing the fan blades. This section included calculation of the blade parameters.

Since the work in this thesis is based on the work done by Bruneau (1994), the design assessment is done in a similar order but the contents of the theory are not the same.

2.2.1. OUTLET VELOCITY PROFILE SELECTION

The most popular fan whirl distribution used by fan designers is the free vortex velocity distribution. This constitutes a constant axial velocity distribution, zero radial velocity through the fan annulus, zero inlet circumferential velocity and an outlet circumferential velocity that is inversely proportional to the fan radius. Van Niekerk (1965) used the free vortex velocity distribution in his work, because of the simplifications due to the axial velocity that is constant with radius. As pointed out by Van Niekerk (1965) this velocity leads to an outlet whirl coefficient that is a linear function of the inverse of the fan radius, where the whirl coefficient was defined as:

$$\varepsilon = \frac{C_{w2}}{C_{a2}} \qquad (2.1)$$

where

$$C_{a2} = c$$

$$C_{w2} = \frac{k}{r}$$

and c and k are constant values.

Wallis (1983) also centred his design techniques on a free vortex velocity distribution. He pointed out that the constant total pressure rise and axial velocity along the fan blade span, associated with this design assumption, are never present in practice due to the annulus wall boundary layers and off-design conditions. Wallis (1983) also stated that a steady, swirl-free, axisymmetric, axial and unseparated fan entry flow is a requirement for this approach. Although these requirements can seldom be met in practice due to the nature of the duct system, he maintained that a free vortex design approach provides the most satisfactory results. According to Bass (1987) other advantages of the free vortex design are that no energy loss occurs due to a downstream redistribution of kinetic energy and that it occurs naturally in the absence of constraints. The disadvantage of the free vortex design is the high blade root loading it implies, which restricts it to low fan loading and high hub-tip ratios. Downie et al. (1993) pointed out that the pressure rise capabilities of an axial fan rotor is limited by the use of a free vortex flow design, while the local total pressure rise increases towards the blade tip when an arbitrary vortex flow design is used.

Bruneau (1994) assumed a power law distribution for the design of axial flow turbomachines:

$$C_{w2} = a \times r^{n} \qquad (2.2)$$

He distinguished between four different swirl distributions:

1. Free vortex (n = -1). As stated already, this distribution leads to considerable computational simplifications. Bruneau (1994) also claimed that it leads to a blade design with excessive blade twist and root swirl.
2. Constant flow angle design (n = 1). This results in broadly similar velocity triangles as the free vortex case, with the same resulting problem of high blade twist.
3. Super vortex (n = -2). This results in severe blade twist and large exit velocity variations.
4. Constant swirl (n = 0). This results in a large radial variation of axial velocity.

Bruneau (1994) stated that the design of a fan with a non-free vortex velocity distribution is far more complex than a free vortex design: the axial velocity distribution and the work rate are not constant but has to be computed by integrating between the fan hub and tip. He optimised the vortex distribution for the minimum loss of exit kinetic energy, using n and a in equation (2.2). This indicated that an outlet swirl distribution nearly identical to a free vortex was the optimum distribution for his axial fan application.

An article by Von Backström et al. (1996) described the minimisation of the exit kinetic energy loss of an axial fan by optimising the exit velocity distribution. This optimisation did not assume any form of vortex distribution as was the case with Bruneau (1994), but adhered to the constraints of constant volume flow and work input and simple radial equilibrium. Although the exit kinetic energy flux was reduced by a maximum of 1.8 percentage points, compared to the free vortex case for the constraints imposed, the exit velocity distribution can lead to a 50 % decrease in blade twist.

2.2.2. DETERMINING THE OPTIMUM HUB-TIP RATIO

Van Niekerk (1965) determined relationships between fan efficiency, volume flow through the fan, pressure rise across the fan and hub-tip ratio, working from basic fan design principles. His theory was restricted by the availability of the correct values for the annulus efficiency (η_a) and the average values for the drag/lift ratio (tan γ) for the fan blades. To summarise this theory, the method used by Bruneau (1994) is given. He specified the following input data:

1. The range of different hub-tip ratios to be used.
2. The desired fan static pressure.
3. The volume flow rate
4. The estimated value of average drag/lift ratio for the blade.
5. Tip radius.
6. Rotational speed.
7. An estimated value for annulus efficiency.

Bruneau then used the equations of Van Niekerk to calculate values of total and static efficiency. The equations for the efficiencies are as follows:

$$\left(1-\eta_t\right)_{ave.} = \frac{2}{3}\times\frac{\left(\tan\gamma\right)_{ave.}}{\phi}\times\frac{\left(1-\nu^3\right)}{\left(1-\nu^2\right)}+\frac{2\left(\tan\gamma\right)_{ave.}\times\left[\phi-\varepsilon_i\nu\right]}{\left(1+\nu\right)} + \left(1-\eta_a\right)\times\frac{\phi}{2\varepsilon_i\nu} \tag{2.3}$$

$$\left(1-\eta_s\right)_{ave.} = \frac{2}{3}\times\frac{\left(\tan\gamma\right)_{ave.}}{\phi}\times\frac{\left(1-\nu^3\right)}{\left(1-\nu^2\right)}+\frac{2\left(\tan\gamma\right)_{ave.}\times\left[\phi-\varepsilon_i\nu\right]}{\left(1+\nu\right)} + \left(1-\eta_a\right)\times\frac{\phi}{2\varepsilon_i\nu}+\frac{\phi}{2\varepsilon_i\nu}\times\left[1-2\times\left(\varepsilon_i\nu\right)^2\times\frac{\ln\nu}{\left(1-\nu^2\right)}\right] \tag{2.4}$$

The use of the equations resulted in a series of constant hub-tip ratio curves, where fan efficiencies were plotted against fan static pressure rise. The value for static pressure rise was given by:

$$p_{sf} = \eta_s \times \rho \times \Omega \times r_i \times C_{w2i}$$

Since the desired static pressure value was known, the optimum hub-tip ratio was determined as the value which gave the highest efficiency for the specified pressure rise. This indicated an optimum hub-tip ratio of 0.4 for his application. Although Wallis (1983) did not describe a procedure for optimising the hub-tip ratio, he mentioned the fact that to increase the dynamic pressure rise through the fan, the relative velocity has to be increased by increasing the hub-tip ratio. He determined the hub-tip ratio by restricting the hub swirl coefficient, ε_i, to be less than one, where:

$$\varepsilon_i = \frac{C_{w2i}}{C_{a2i}} \tag{2.5}$$

2.2.3. FAN BLADE DESIGN

According to Wallis (1983) each fan blade section can be considered as a two-dimensional airfoil that is independent of conditions at other radii. Bruneau (1994) followed a similar approach in his design procedures, although he discussed the effects of radial equilibrium through the fan annulus. Bass (1987) stated that a two-dimensional design approach would be satisfactory partly due to the complexity of the computational techniques needed for a three-dimensional analysis, although he mentioned the fact that three-dimensional effects tend to occur at the interaction between the fan blade and fan hub and shroud. These effects tend to delay the onset of stalling due to the radial displacement of the boundary layer.

Smith (1987) advocated the use of a simple three-dimensional approach to design an axial fan blade. He divided the fan annulus into five annular stream tubes, spaced in equal radial intervals, and then performed the calculations at the six boundaries, taking radial equilibrium between the stream tubes into account. A similar approach was advocated by Wright et al. (1987) who called it a "mild three-dimensional" model.

Keller (1937) advised loading factors and solidities to be below 1.0 and 1.1 respectively, while Van Niekerk (1965) restricted his design theory to the use of isolated airfoil data by constraining the blade loading factor to be smaller than 1.0. Wallis (1961) considered fan blades to be in cascade above solidities of 1.0. In his later work Wallis (1983) assumed a smooth transition from cascade to isolated airfoil data and derived a series of simple design curves. These curves represent the variation of C_L/C_{Li} versus solidity and stagger angle. Hay et al. (1978) stated that the most significant cascade effect is the change in lift coefficient. He also proposed the use of a plot of C_L/C_{Li} against pitch/chord ratio. This change of lift coefficient depends on the value of stagger angle. The advantage of this plot above the one used by Wallis (1983), was that it also allowed for cases where the lift coefficient was increased by cascade effects.

Wright (1987) advocated the use of NACA two-dimensional cascade rules for solidities higher than 0.6. He based the values for zero solidity on isolated airfoil data and then interpolated between 0.0 and 0.6 to obtain the required airfoil data. In an article by Meyers et al. (1993) a new inviscid design

technique, developed from low-solidity procedures, was used to obtain the airfoil data between 0.0 and 0.6.

In his book on fan design Wallis (1983) listed five different blade profiles suitable for fan blade design:

1. F-series profiles
2. NACA 65 series profiles
3. Flat undersurface (Clark Y, Göttingen and RAF 6) profiles
4. Elliptical airfoils
5. Cambered plate airfoils

The use of elliptical fan blade profiles is restricted to reversible fan assemblies, since the airfoil characteristics are the same in both directions.

In an article on the development of axial flow fan blade sections, Wallis (1972) compared the NACA 4-digit series, NACA 65 series, Clark Y, RAF 6, C4 and C7 blade profiles. He concluded that sections with a modified circular arc camber line, clothed with a C4 or C7 thickness profile, give the optimal design solution because of their high lift-drag ratios. In a further article Wallis (1978) investigated the F-series airfoils. These airfoil sections consist of circular arc camber lines, modified to incorporate leading edge droop. The camber lines are then clothed with C4 streamlined shapes. Wallis (1978) also documented the airfoil's shape and flow characteristics.

Hay et al. (1978) compared the NACA 65, Göttingen, circular arc cambered plates and C4 profiles. They concluded that of these examples the cambered plate profile was the least efficient, while the C4 profile had the best lift-drag ratio and was suitable for very high blade loading. For his thesis Bruneau (1994) selected two blade profiles, namely a Clark Y profile and a NASA LS series profile. He used the Clark Y profile blade as a control design with which he could compare the NASA LS profile. Although the NASA LS profile blades showed excellent lift-drag characteristics, they could not match the Clark Y profile blades in static pressure rise and static efficiency. This was mainly due to the Clark Y profile's larger hub chords, the fact that the NASA LS series blades could not be tailored for camber variation as well as the NASA LS series blades having a higher drag for the lift coefficient at which the blades were designed.

A fan blade design procedure was described by Wallis (1983) in his book on fan design. The purpose of any fan blade design procedure is to determine the geometry of the blade that is described by the radial variation of chord, camber angle and stagger angle. These variables are defined in Figure 4.6 as part of the design process.

Once the velocity profile through the fan annulus has been determined, the radial variation can be represented using velocity diagrams as illustrated in Figure 2.1. With the help of these diagrams the value for camber angle can be determined using:

$$\theta = (\beta_1 - \beta_2) + (\delta - i) \tag{2.6}$$

The value for blade solidity, which is given by:

$$\sigma = \frac{c}{s} \tag{2.7}$$

is determined from the equation for blade loading factor:

$$C_L \sigma = 2 \times \left(\frac{C_{w2}}{C_{am}} \right) \times \cos \beta_m \tag{2.8}$$

where

$$\tan \beta_m = \frac{1}{2} \times (\tan \beta_1 + \tan \beta_2) \tag{2.9}$$

$$C_{am} = \frac{1}{2} \times (C_{a1} + C_{a2}) \tag{2.10}$$

Wallis (1983) recommended a value for C_L of 1.0 at the hub and between 0.4 and 0.6 at the tip to be used in equation (2.8). A linear interpolation between the hub and tip lift coefficient gives the variation of C_L along the blade span. Inserting these values for C_L into equation (2.8) the variation of blade solidity along the blade span can be determined. From these values of σ the variation of chord along the blade span can be determined:

$$c = \frac{2 \times \pi \times r}{\sigma \times n_b} \tag{2.11}$$

Once the values for C_L along the blade span has been determined, the variation of the angle of attack can be determined from suitable blade profile data. The blade stagger angle is then given by:

$$\xi = \beta_1 - \alpha \tag{2.12}$$

McKenzie (1987) optimised the blade geometry by determining the optimum value for s/c at the different radii:

$$(s/c)_{opt} = 9 \times (0.567 - C_{pi}) \tag{2.13}$$

where

$$C_{pi} = 1 - \left(\frac{W_2}{W_1}\right)^2 \tag{2.14}$$

Hay et al. (1978) optimised the angle of attack for a specific camber angle to obtain the desired air exit angle. His choice of lift coefficients for the blade was governed by the stalling point of the blade profile. According to him the lift coefficient should be such that the corresponding angle of attack was at least 2° less than the stall angle of attack. A different design approach was followed by Downie et al. (1993) where the fan was designed without specifying the velocity profile in the annulus. Instead the designer specified local total pressure rise coefficients according to which a trial swirl distribution was chosen. A number of iterations was needed before a practical rotor design was obtained.

2.3. FAN NOISE

According to Gordon (1972) fan noise is aerodynamic in origin. When turbulent air flow interacts with a solid surface or when turbulence is generated by a solid surface, changes in the momentum field around the surface are generated. These momentum changes require fluctuating pressures which can be considered as the fan noise. Regarding fan noise, Gordon (1972) made a few important observations:

1. All fans create turbulent air flow, generating noise.
2. Since turbulence increases with flow speed, fan noise increases with air flow speed.
3. Flow separation or fan stall will increase fan noise.
4. Fixed surfaces close to the fan blades will increase the fan noise.

5. The vibration of the fan blades does not contribute to the fan noise.

Graham (1975) stated that the noise characteristic is an integral part of the fan design. He pointed out that even well designed fans will generate noise, since the features that enable them to meet performance requirements also create noise. Fan noise can be kept to a minimum, but never completely eliminated. Since the primary purpose of a fan is to move a quantity of air against a given pressure difference, the relative importance of fan noise in the overall fan design problem must always be kept in perspective. Eck (1973) found that in many cases the sound level had its lowest value in the range of maximum efficiency. This statement was supported by Wallis (1983) who pointed out that excessive fan noise can be interpreted as indicative of some aerodynamic design flaw.

2.3.1. SOURCES OF AXIAL FLOW FAN NOISE

The sources of axial flow fan noise have been described by many researchers of fan noise. This discussion concentrated on a few of the most extensive descriptions. Sharland (1964) stated that the nature of fan noise is indicated by its frequency spectrum. The general form of this frequency distribution is a broad spectrum extending over a wide range of frequencies with a number of discrete frequency peaks superimposed on it. These peaks occur at the fundamental blade passage frequency and its harmonics. The relative strength of the different noise components varies with the type of axial flow fan. Noise from low tip speed ventilating fans is almost entirely broad band, while the noise from high speed compressors is characterised by discrete frequency tones. The fact that fan noise levels are so dependent on blade speed suggests that the noise sources of a fan are dipole in nature. This means that the noise originates from fluctuating forces exerted by the fan blades on the air as it passes through the fan.

As stated by Japikse (1986), broadband noise is generated on fan blade - and vane surfaces by the interaction of flow fluctuations that have random time histories. Sharland (1964) described three mechanisms by which broadband noise is created:

1. The surface pressure field arising from turbulent boundary layers inside a fan.
2. The vorticity shed from the fan blades into the air flow.
3. The cases where the fan blade is moving in a flow which is initially turbulent.

All three of these mechanisms create fluctuating forces which result in fan noise. Wright (1976) recognised another source of boundary layer noise, namely laminar boundary layer noise, which occurs at low rotor speeds. He described the two boundary layer noises, laminar and turbulent, as rotor self-noise. Although the laminar boundary layer noise is the most dominant noise source of the two, it is easy to prevent by inducing a turbulent boundary layer artificially. This means that the noise generated by the turbulent boundary layers is the primary source of broadband noise.

Wright (1976) also discussed the discrete frequency peaks rising above the broadband noise. These peaks occur most frequently at multiples of the blade passing frequency. This means that a fan with many blades will have only one or two such peaks in its spectrum, while a fan with few blades will have a tightly packed spectrum. He identified three sources of these discrete frequencies:

1. The discrete frequencies produced by the steady thrust of the fan rotor are determined by the thrust, blade number and speed of the rotor.
2. On or near the axis of rotation, low order blade loading harmonics, produced by asymmetries in the flow, also contribute to the spectrum. This source of noise is negligible for low speed high blade number rotors where the blade loading is basically identical from blade to blade.
3. Excess rotor noise is generated by various degrees of impulsive blade loading. An example of this is the rotor-stator interaction in a fan.

Tyler et al. (1962) considered the discrete frequencies, concentrating on the steady blade forces. They determined that these fluctuations will propagate along a circular duct when M_m, the circumferential Mach number of the rotor tips, is greater than a critical Mach number, Mc_m.

When

$$M_m < Mc_m$$

the rate at which the fluctuations decay along the cylinder is given by:

$$\frac{\Delta db}{\Delta x_d \; b} = 8.69 \times m_d \times \sqrt{Mc_m^{\,2} - M_m^{\,2}} \qquad (2.15)$$

Wright (1976) concluded that the basic sources of rotor noise are the steady blade thrust noise and turbulent boundary layer noise.

2.3.2. FAN NOISE PREVENTION

Wright (1976) defined excess rotor noise as the noise that is created by an axial flow fan and can be removed without redesigning the fan. This means that a certain amount of fan noise can be removed by proper installation and operation of the fan. Wright (1976) recognised rotor-stator interaction, flow separation, cross-winds, upstream flow obstructions and blade-tip vortex interaction as causes of this noise.

Wallis (1983) stated that in order to achieve the minimum noise level for a normal axial flow fan, the fan must be designed, installed and operated in accordance with good aerodynamic principles. He listed these as follows:

1. The upstream duct system must be free of disturbed and swirling flow.
2. The flow into the fan annulus must be smooth.
3. The upstream vanes or support struts must be free of flow separation and have low drag. Their trailing edges must be at least one half vane or strut chord upstream from the rotor leading edge.
4. The rotor blades must be properly matched in twist, chord and camber and have small tip clearances.
5. The straightener vanes or support struts must also be free of flow separation and have low drag. They must be located at least half a rotor blade chord downstream of the blade trailing edge
6. The number of rotor blades and stator vanes must be unequal and should not possess a common factor. The product of the number of stator vanes or support struts and the rotor rotational speed must also not equal the rotor blade natural frequency.
7. The flow downstream of the fan must be unseparated.

Hay et al. (1987) proposed a different approach to fan noise prevention. Due to the large amount of fan noise caused by installation effects, they identified a requirement for a fan that is insensitive to flow maldistributions. This suggested that a fan must be designed well away from the stall line to allow a wide margin of flow variation before the fan reaches stall and its associated high noise levels. They followed the same design procedure as prescribed in a previous article by Hay et al. (1978) while taking the expected flow variations into account. The lower sensitivity of the fan to inflow distortion should lead to a lower installed noise level. This design philosophy is particularly suited for fans in industrial applications subject to various installation effects.

2.3.3. LOW-NOISE FAN DESIGN

Graham (1975) stated that it is impossible to design a high pressure axial flow fan that generates only low sound power levels, since fan noise is an integral part of fan performance. He also pointed out that there is no quick way of lowering the noise of a good fan design. This means that there is no abrupt change in noise characteristics if the fan design is altered slightly. Wright (1976) concluded that the quietest rotor for a given thrust, from a broad band noise point of view, has a low tip speed, high solidity and maximum blade incidence angle of 4°. The rotor diameter must also be as large as possible to enable a small throughflow velocity.

Longhouse (1976) considered fan noise with design aspects such as tip clearance and pitch angles in mind. He concluded that no significant decrease in fan noise is achieved for reduced blade tip clearances, except for a zero blade tip clearance. Increasing the blade pitch angle will either increase or decrease the fan noise depending on the dominating noise source at a specific volume flow. Increasing the blade pitch angle requires a reduced fan speed to achieve the same pressure rise as before, but increases the blade loading. This means that while the loading noise increases, the noise due to the air speed decreases. Depending on which of these noise sources dominate at a certain volume flow, the fan noise will either decrease or increase.

In an article on axial flow fan noise Fukano, Kodama and Senoo (1977) modelled an equation to describe the turbulent noise generation by a fan:

$$SPL = 10 \times \log\left(3 \times \rho_{atm} \times a_0 \times E/8 \times \pi \times z^2 \times p_{ref}^2\right) \qquad (2.16)$$

where

$$E = \left(\pi \times \rho_{atm} \times n_b \times D_f \times U_o^6/16800 \times a_0^3\right) \times d_f \qquad (2.17)$$

This was used as the basis of an article by Fukano, Kodama and Takamatsu (1977) who investigated the effect of number of blades, chord length and camber on the fan turbulent noise. The experimental values for noise level were compared with those obtained using the formula described in the first paper. The experiments agreed with the theory in predicting the trailing edge boundary layer thickness on the rotor blade, or wake width, as one of the important factors determining the sound

pressure level of a fan, where the sum of the trailing edge thickness and the boundary layer is given by:

$$d_r = d_t + (0.37 \times c/4) \times Re_c^{-0.2} \qquad (2.18)$$

This means that the noise level increases with an increasing number of blades when the blade chord remains constant. If the number of blades is kept small, each blade can be seen as an independent noise source. The effect of a number of blades can therefore be seen as the product of the blade number and the sound power originating from one blade. Since the wake width increases with chord length, Fukano, Kodama and Takamatsu (1977) also concluded that the fan sound pressure level increases with chord length when comparing two sets of fan blades having the same number of blades and running at the same speed. They also found that the fan sound pressure level is independent of a change in camber angle for camber angles less than 20°. For camber angles larger than 20°, the wake width increases rapidly due to flow separation, leading to a subsequent increase in fan noise. Combining the effect of blade number and chord length for the same solidity, the sound pressure level is lower for the larger chord length and smaller blade number. This is due to the fact that the sound pressure level is directly proportional to the blade number and also proportional to the 0.8 power of the chord length.

In a further article by Fukano et al. (1978) a similar approach to that used in their previous articles was followed to determine the effect of rotational frequency, blade thickness and outer blade profile. As expected, they found that the fan noise increases with fan rotational speed and follows approximately a $U_o^{5.8}$ law , where U_o is the fan tip speed. They also found that the fan sound pressure level is reduced by reducing the blade trailing edge thickness on the suction side of the blade. The fan sound pressure level is reduced further by sweeping the blade profile, either linearly or circularly, in the rotational direction to obtain a forward swept blade. This series of fan research was continued by Fukano et al. (1986) when they investigated the effect of blade tip clearance on fan noise and performance. They concluded that a smaller tip clearance reduce the sound pressure level significantly, although a too small tip clearance is impractical because of high manufacturing costs. A tip clearance of 0.6 mm is considered the optimum. Related to the tip clearance effect is the discrete frequency noise due to eccentricity between the duct axis and rotor shaft. These discrete frequency terms include a plane wave mode which travels down the duct without decaying. Although these

discrete terms will not contribute much to the overall sound pressure level they can be very annoying.

According to Van der Spek (1994) the correct way to achieve fan noise reduction is by either decreasing the characteristic fan shape noise value (C) or the blade tip speed in the following equation for sound power level:

$$PWL = C_f + 30 \times \log U_o + 10 \times \log \frac{p_f \times Q}{1000} - 5 \times \log D_f + dB_{cor} \qquad (2.19)$$

without reducing the fan pressure rise, flow rate or fan efficiency. Obtaining the same pressure duty while reducing the fan blade tip speed is achieved by increasing the fan solidity using a larger number of blades. Reduction of the fan shape value (C) is achieved by enlarging the chord length, combined with a reduction of the number of blades and forward sweeping fan blades. The noise reduction due to the forward swept blades can be explained as follows:

1. The forward sweep causes a phase shifting cancellation of fan noise generated at different radii.
2. Forward sweep limits the growth of boundary swirls at the blade edges by truncating the natural path of the trailing edge.
3. The velocity perpendicular to the trailing edge line, which generates noisy swirls, is smaller.
4. The big tip angle on the leading edge side reduces tip vortex shedding.

Wright et al. (1989) investigated the effect of fan blade sweep and developed a design theory for designing swept blades. They compared previously designed swept blade axial flow fans and derived a graphical relation between a local sweep angle for a 10 dB noise reduction and the blade relative Mach number. Although Wright et al. (1989) listed other effects of blade sweep, no analytical data describing these effects is given. After designing and testing a forward-swept blade fan, they concluded that swept-blade fans show a significant reduction in fan noise levels.

Kawaguchi et al (1993) examined the effect of the fineness of the fan blade nose on the fan noise and found that using a fan blade with a large radius leading edge brings about a decrease in fan turbulent noise without deterioration of fan performance. Akaike et el. (1994) did a rotational noise analysis on an axial flow fan and investigated the effect of unequal blade pitches on the blade passing

frequency noise. By using unequally spaced blades these discrete noise components are dispersed into band frequency components. They found that the resulting band frequency components gave a decrease in fan rotational noise.

3. FAN LAY-OUT DESIGN

A fan series normally consists of a single blade design that is adapted to the different fan diameters by blade cropping. The blades are used in conjunction with two or three different hub sizes with various blade numbers, to provide a variation of fan characteristics with one fan diameter size. When designing a fan series one has to optimise the whole range of fan configurations (combinations of fan diameter and hub diameter size) over the specified duty range to determine the best combination of fan diameter and hub size, the optimum hub diameters as well as the best whirl distribution from which to design the fan blade. The first step in designing the axial fan range was to determine a basic lay-out, combination of fan diameter and hub size, of all the fan sizes according to the specifications (see Table 1.1). This involved determining an optimum hub-tip ratio to be used in calculating the hub diameters. Since the popular tendency when designing an axial flow fan series is to constrict the design to the use of only two different hub diameters for the entire range, the design was simplified by following this trend. This meant that the distribution of the hub diameters along the range of fans had to be determined. This included determining the size of the two hub diameters.

3.1. EXIT VELOCITY PROFILE

Von Backström et al. (1996) determined the optimum exit velocity profile by minimising the kinetic flux losses in varying the flow and pressure coefficient. These losses are considered to be the greatest source of losses in a rotor-only axial flow fan. The article by Von Backström et al. is described in more detail in Appendix A. The model incorporated the following assumptions:

1. A uniform total pressure distribution across the fan inlet.
2. The Euler turbo-machinery equation is applicable.
3. Simple radial equilibrium applies in front of and behind the fan.
4. The flow is assumed to be incompressible and inviscid.

The velocity profiles were obtained by minimising the integral for kinetic energy flux at the fan outlet. This is given by:

$$L = \pi \times \rho \times \int_{ri}^{ro} r.C_a.\left(C_a^{\,2} + C_w^{\,2}\right).dr \qquad (3.1)$$

By non-dimensionalising as follows:

$$t = r / r_i \tag{3.2}$$

$$a = r_o / r_i \tag{3.3}$$

$$u(t) = C_w(r_i \times t)/(r_i \times \Omega) \tag{3.4}$$

$$v(t) = C_a(r_i \times t)/(r_i \times \Omega) \tag{3.5}$$

equation (3.1) was simplified to:

$$F = L/(\pi \times \rho \times r^5 \times \Omega^3)$$

$$= \int_{ri}^{ro} v.(v^2 + u^2).t.dt \tag{3.6}$$

This functional (equation (3.6)) was minimised according to the following constraints:

1) Radial Equilibrium:

$$\Omega \times \left[\frac{d(C_w . r)}{dr}\right] = \frac{C_w}{r} \times \left[\frac{d(C_w . r)}{dr}\right] + C_a \times \frac{dC_a}{dr}$$

$$\Rightarrow t \times \frac{du}{dt} + u = \frac{u^2}{t} + u \times \frac{du}{dt} + v \times \frac{dv}{dt} \tag{3.7}$$

2) Dimensionless Work Rate:

$$A = \frac{1}{\Omega^2 \times r_i^5} \int_{ri}^{ro} r^2 . C_a . C_w . dr$$

$$= \int_1^a t^2 . u . v . dt$$

$$= W_o/(2 \times \pi \times \rho \times r_i^5 \times \Omega^3) \tag{3.8}$$

where

$$W_o = 2 \times \pi \times \rho \times \Omega \times \int_{ri}^{ro} r^2 . C_a . C_w . dr$$

3) Dimensionless Flow Rate:

$$B = \frac{1}{\Omega \times r_i^3} \int_{ri}^{ro} r.C_a.dr$$

$$= \int_1^a t.v.dt$$

$$= \dot{m} / \left(2 \times \pi \times \rho \times r_i^3 \times \Omega\right) \qquad (3.9)$$

where

$$\dot{m} = 2 \times \pi \times \rho \times \int_{ri}^{ro} r.C_a.dr$$

The minimisation problem was discretised into a numerical problem and solved for given values of a, A and B. Von Backström et al. found that discretising the blade radius into twenty equal intervals (n = 20) proved sufficient for this analysis. They also showed that if one keeps within the prescribed design limitations (see Appendix A), only a small percentage point decrease in exit kinetic energy is achieved when using the optimised velocity distribution instead of the free vortex velocity distribution for the same values of a, A and B. As illustrated in Figure 3.1 there is a distinct difference between the two velocity distributions. Since the variation in swirl velocity for the optimised velocity profile is less than for the free vortex velocity profile, the twist along the fan blade length will be less than when a free vortex exit velocity distribution is used. This motivates the use of the optimised velocity in the blade design process by lowering the manufacturing costs of such a fan blade. Von Backström at al. also found that when the design limitations are exceeded, larger improvements on the efficiency of a fan making use of the optimised profile are possible.

3.2. FAN HUB DESIGN FOR FAN SERIES

The fan hub design procedure included determining the optimum hub-tip ratio when using the minimum kinetic energy exit velocity profile, determining the hub diameter that would give the optimum performance when taking the whole fan diameter range into account and deciding how many different hub diameters to use.

3.2.1. DETERMINING THE OPTIMUM HUB-TIP RATIO

The detailed derivation of the method used for this section is also given in Appendix A The hub-tip ratio was optimised for maximum static efficiency. This meant that the static efficiency of the fan had to be estimated without any knowledge of the form of the exit velocity profile or the blade design. The problem was solved by summarising the various power terms involved in a fan to give an account of the energy entering and leaving the fan. These included the effective power transferred to the air, the kinetic power loss, the power leaving the fan rotor and the shaft power transferred to the fan rotor. The following assumptions were made:

1. As mentioned previously in section 3.1 the improvement obtained by using the optimised velocity profile instead of the free vortex velocity profile gave a decrease in exit kinetic energy flux of only 0 to 2 percentage points. This justified the use of the simplifications associated with the free vortex velocity profile at this stage where the form of the optimised velocity profile was not yet known.
2. No mechanical losses were assumed to occur in the fan. This meant that the shaft power entering the fan is equal to the Euler power.
3. For the final calculations a rotor efficiency of 85 % was assumed. This enabled the calculation of the energy transfer from the power entering the fan rotor to that leaving the fan rotor.

Taking these assumptions into account the power terms were given by:

1. Kinetic power loss

$$P_k = \left(\int_{ri}^{ro} \frac{1}{2} C_a^2 . \rho C_a \, 2\pi r \, dr\right) + \left(\int_{ri}^{ro} \frac{1}{2} C_w^2 . \rho C_a \, 2\pi r \, dr\right) \qquad (3.10)$$

2. Shaft power

$$P_s = \int_{ri}^{ro} r\,\Omega\,C_w \cdot \rho\,C_a\,2\,\pi\,r\,dr \qquad (3.11)$$

3. The usable air power

$$P_{bo} = \eta_r \times P_s \qquad (3.12)$$

4. The effective fan power

$$P_e = P_{bo} - P_k \qquad (3.13)$$

The fan static efficiency is then:

$$\eta_s = \frac{P_e}{P_s}$$

$$= \left(\frac{P_{bo} - P_k}{P_s}\right)$$

$$= \left(\eta_r - \frac{P_k}{P_s}\right) \qquad (3.14)$$

The fan static efficiency calculated in equation (3.14) takes into account the swirl velocity behind the fan when calculating the kinetic power loss. This differs from the equations prescribed by the BS 848 Standards, where the dynamic pressure rise over the fan is calculated as the dynamic pressure due to the axial velocity behind the fan. The method of calculation used for the static efficiency and pressure is clearly stated when necessary. If the values for shaft power and kinetic power loss are inserted into the equation, taking free vortex flow into account, it follows that:

$$\frac{P_k}{P_s} = \frac{1}{2} \times \frac{C_a}{U_o} \times \frac{C_a}{C_{wo}} + \frac{C_{wo}}{U_o} \times \frac{1}{\left(1 - \frac{r_i^2}{r_o^2}\right)} \times \ln\left(\frac{r_o}{r_i}\right) \qquad (3.15)$$

The terms of the equation were simplified by using the equations for hub-tip ratio, flow coefficient and total pressure rise coefficient. These equations are given in Appendix A, equations (A.1) to (A.3). Equation (3.15) was simplified as follows:

$$\frac{P_k}{P_s} = \frac{\phi^2}{\psi} + \frac{\psi}{2} \times \frac{1}{\left(1-\nu^2\right)} \times \ln\left(\frac{1}{\nu}\right) \tag{3.16}$$

Inserting this equation into equation (3.14) gave:

$$\eta_s = \left(\eta_r - \frac{\phi^2}{\psi} + \frac{\psi}{2} \times \frac{1}{\left(1-\nu^2\right)} \times \ln(\nu)\right) \tag{3.17}$$

Using the maximum allowable value for the pressure coefficient according to equation (A.5), equation (3.17) was simplified to:

$$\eta_s = \left(\eta_r - \frac{\phi}{2 \times \nu} + \frac{\nu \times \phi}{\left(1-\nu^2\right)} \times \ln(\nu)\right) \tag{3.18}$$

Since the hub-tip ratio can be used to calculate the flow area through the fan, there is a definite relation between the hub-tip ratio and the flow coefficient. This is given by:

$$\phi = \frac{Q}{U_o \times \pi \times r_o^2 \times \left(1-\nu^2\right)}$$

$$= \frac{K_1}{\left(1-\nu^2\right)} \tag{3.19}$$

Inserting equation (3.19) into equation (3.18) the following was obtained:

$$\eta_s = \left(\eta_r - \frac{K_1}{2 \times \nu \times \left(1-\nu^2\right)} + \frac{\nu \times K_1}{\left(1-\nu^2\right)^2} \times \ln(\nu)\right) \tag{3.20}$$

In order to obtain the hub-tip ratio for maximum static efficiency, the derivative of equation (3.43) with respect to ν was calculated:

$$\frac{d\eta_s}{d\nu} = \frac{-K_1 \times \left(1 - 3\nu^2\right)}{2 \times \left(\nu - \nu^3\right)^2} + K_1 \times \left(\frac{2 \times \left(1 - \nu^2\right) + 8 \times \nu^2}{4 \times \left(1 - \nu^2\right)^3}\right) \ln\left(\frac{1}{\nu}\right) - \frac{K_1}{\left(1 - \nu^2\right)^2} \qquad (3.21)$$

Setting equation (3.21) equal to zero and solving ν, a hub-tip ratio was obtained that gave a maximum value for η_s in equation (3.20). Looking at equation (3.21) one will note that the constant K_1 cancels out when setting equation (3.21) equal to zero. This means that the value for hub-tip ratio is independent of the volume flow. Although the optimum value for hub-tip ratio is not independent of the pressure coefficient, the variation of hub-tip ratio with variation in pressure coefficient was found to be very small. The optimum hub-tip ratio, corresponding to a maximum pressure coefficient, was calculated as:

$$\nu_{opt} = 0.485$$

As mentioned earlier, this value applies to free vortex flow. Due to the small difference between the efficiencies of the two types of velocity profiles this fact could be ignored.

3.2.2. DETERMINING THE DISTRIBUTION OF HUB DIAMETERS

A fan series usually consists of a range of different fan diameters, using the same blade and hub design. To increase the efficiency of the fan series as a whole, as well as to increase the number of possible configurations for the fan series, more than one hub size is used. A minimum of two hub diameters was used to optimise the different fan sizes. This means that a certain size hub diameter which suits the smallest diameter fan optimally will not necessarily suit the largest diameter fan to the same extent. To determine the different hub diameters, as well as for which diameter fan to use them, the fan series had to be optimised to a specific maximum, namely maximum efficiency as determined by equation (3.20) (assuming a maximum pressure coefficient).

The two smaller hub diameters were calculated as:

$$hd_1 = \nu_{opt} \times D_{f1} \tag{3.22}$$

$$hd_2 = \nu_{opt} \times D_{f2} \tag{3.23}$$

The hub diameter size and distribution were optimised by integrating each fan's efficiency over its approximate flow range numerically and adding all these integrals together. The optimised solution was taken as the one providing the maximum sum of the above integrals. The fan diameters, D_{f1} and D_{f2}, were iteratively chosen from the series of commercial size fan diameters between 315 mm and 1000 mm (see Table 1.1) to be used in the optimisation. It was decided to equate D_{f1} in equation (3.22) equal to the smallest fan diameter in the series, to ensure a sufficient blade length (larger than 80 mm) when the small hub diameter, hd_1, is used in conjunction with this fan diameter. The second hub diameter was calculated using any of the remaining fan diameters smaller than 1000 mm for D_{f2} in equation (3.23).

In the optimisation, the fan sizes using the small hub diameter and the fan sizes using the larger hub diameter, were varied. This determined the optimum distribution of the hub diameters between the different fan diameters. While varying the hub diameters' distribution, the larger hub diameter's size was also varied from being optimised for the 400 mm fan to being optimised for the 1000 mm fan, depending on the distribution chosen for the hub diameters. The optimisation was also monitored to ensure proper blade lengths. When further uncertainties existed, the optimisation was performed using only the 500 mm to 630 mm diameter fans, since these are currently the most popular fan sizes in the industry. A summary of the results of this optimisation is given in Table 3.1.

Table 3.1: Optimisation results

Diameter [mm]	Hub Diam. [mm]	Blade Length [mm]	Hub/tip	Tip Speed [m/s]
315	153	81	0.486	47.5
400	153	124	0.383	60.3
500	246	129	0.485	75.4
560	246	159	0.433	84.4
630	246	194	0.385	95.0
710	246	234	0.342	107.1
800	246	279	0.303	60.3
900	246	329	0.269	67.9
1000	246	379	0.243	75.4

The small hub diameter of 150 mm can also be used for the larger diameter fans, where the required pressure rise over the fan is low. Due to the blade length constraint, the second hub diameter can only be used for the 500 mm and larger diameter fans to ensure a higher pressure rise over the fan. The fan tip speeds are well within the constraint of 115 m/s, where it is assumed that the fans with a diameter smaller than 710 mm would have a maximum speed of 2880 rpm and the larger fans a maximum speed of 1440 rpm. The average hub-tip ratio is 0.37.

4. FAN BLADE DESIGN

This chapter describes the design of two fan blades to be used in a fan series: one for general application and one as a low-noise fan blade. It incorporated the data calculated in chapter 3 (see Table 4.1). Sample calculations of all the relevant calculations are given in Appendix B.

Table 4.1 Summary of data for lay-out design

Large hub diameter [mm]	246
Small hub diameter [mm]	153
Maximum blade length [mm]	377
Minimum blade length [mm]	81
Preferred fan speed [rpm]	1440

It was decided to round the hub diameters off to 250 mm and 150 mm for the large and small hub diameter respectively, to correspond to existing hub designs. The preferred fan speed of 1440 rpm is the speed most commonly used for these fans. Speeds of 2880 rpm and 720 rpm occur at the small and large fan diameters respectively. The blade design procedure was very similar to that used by Bruneau (1994) with the biggest difference being the minimum exit kinetic energy velocity profile. Although Bruneau designed blades for a larger diameter fan, he followed the basic steps as specified by Wallis (1983). He used an exit velocity profile similar to a free vortex profile which assumes a constant axial velocity before and after the fan and a whirl velocity inversely proportional to the radius. This resulted in a certain number of simplifications, especially where the actuator disk theory was concerned. The same data and design procedures were used in designing both types of fan blades, although provision was made for blade sweep in the low-noise fan design. The blade profile was selected from standard profiles.

4.1. CALCULATION OF FAN EXIT VELOCITY PROFILE

The velocity profile was selected with the help of the paper by Von Backström et al. (1996). The actual calculations were done with the help of a computer programme written by Dr. J. D. Buys of the Department of Mathematics. As explained in chapter 3 this method minimises the exit kinetic energy, which is the dominant source of energy loss in a rotor-only axial fan, while constraining the fan to do the same amount of work at the same volume flow as a fan with a free vortex velocity profile with the same hub-tip ratio.

4.1.1. CHOOSING THE VALUES FOR a, A AND B

To obtain the flow - and work rate values according to which the blade design was done, values for ν, ϕ and ψ had to be selected (see equations (A.1) to (A.3)). These values were selected with the help of the data sheets of a typical comparative fan series from HAI. Looking at a range of different fan sizes and taking the popular fan sizes (500 mm, 560 mm and 630 mm) into account, values of ν, ϕ and ψ were chosen for each possible fan configuration. These values made provision for the two hub diameters (150 mm and 250 mm) used on these fans, as well as half or full blade solidity for each hub diameter. The comparative fan series was designed in such a way that the 150 mm hub diameter can accommodate a maximum of ten blades and the 250 mm hub diameter a maximum of fourteen blades. This gives a 40% increase in solidity with each change in the blade number, from the minimum number of blades used, namely five, to the maximum number of blades used, namely fourteen. The values for ϕ were obtained by taking each of the fan configurations' maximum obtainable volume flow rate and dividing it by two. This ensured that the design point for which the fan was designed, was in the centre of the fan configuration's area of operation. This gave:

$$\phi = \frac{C_a}{U_o}$$

$$= \frac{Q\left(\pi \times \left(r_o^2 - r_i^2\right)\right)}{\Omega \times r_o} \qquad (4.1)$$

with

$$Q = \frac{Q_{max}}{2} \qquad (4.2)$$

$$\Omega = 2 \times \pi \times rpm/60 \qquad (4.3)$$

The rpm value used was 1440 rpm as mentioned in the introduction of this chapter. The values for ψ were calculated by reading the values for fan shaft power from the comparative fan data sheets. The readings were made at the average blade setting angle of 25°. A rotor efficiency of 85% and mechanical efficiency of 90% were assumed to give a total efficiency of 76.5%. This value corresponded well to the optimum total efficiency for a 19J Woods fan (Van der Spuy, 1994). The fan shaft power was calculated as follows:

$$P_s = Q \times p_{tf} / (\eta_m \times \eta_r)$$
$$= Q \times p_{tf} / \eta_t \qquad (4.4)$$

This gives:

$$p_{tf} = \frac{P_s \times \eta_t}{Q} \qquad (4.5)$$

If we assume:

$$\psi = \frac{2p_{tf}}{\rho \times U_o^2}$$

then

$$\psi = \frac{2P_s \times \eta_t}{\rho \times U_o^2 \times Q} \qquad (4.6)$$

The obtained values are shown in table 4.2. From these values it showed clearly that the values of ψ were exceeding the constraint mentioned in the optimised velocity profile calculations (equation (A.5)). Values of η_s calculated with the help of free vortex theory (see equation (3.17)) were approximately 40% for the selected flow - and work rate configurations for the different fans. The value for rotor efficiency in equation (3.17) was replaced by the value for total efficiency used in equation (4.4), taking mechanical efficiency into account. The value for total efficiency used in these calculations was 76.5%, as mentioned above.

Table 4.2: Different configurations for which velocity profiles were optimised

fan dia. [mm]	Hub dia. [mm]	Blades	Q design [m^3/s]	$P_s$design [W]	ν	ϕ	ψ	$2\phi\nu$	η_s free vor.
500	150	5	1.4	360	0.30	0.21	0.23	0.12	0.43
500	150	10	1.6	570	0.30	0.24	0.31	0.14	0.38
560	150	5	1.9	570	0.27	0.20	0.21	0.11	0.43
560	150	10	2.2	940	0.27	0.23	0.30	0.12	0.38
560	250	7	2	800	0.45	0.24	0.28	0.21	0.42
560	250	14	2.25	1150	0.45	0.27	0.36	0.24	0.38
630	150	5	2.7	850	0.24	0.19	0.17	0.09	0.42
630	150	10	3.1	1400	0.24	0.22	0.25	0.11	0.38
630	250	7	2.8	1200	0.40	0.22	0.24	0.18	0.42
630	250	14	3.1	1700	0.40	0.25	0.30	0.20	0.40
710	150	5	3.8	1350	0.21	0.19	0.15	0.08	0.41
710	250	7	4	1800	0.35	0.22	0.20	0.15	0.41
800	250	7	5.8	3000	0.31	0.21	0.18	0.13	0.40
900	250	7	7.8	4000	0.28	0.20	0.14	0.11	0.40
1000	250	7	10.4	5700	0.25	0.19	0.12	0.09	0.39

4.1.2. ANALYSIS OF THE VELOCITY PROFILES

The velocity profiles were graphed for u(t) and v(t) versus t, where t is the radius ratio (see equations (3.2) to (3.5)). From these profiles the relative inlet and exit velocity angles were calculated using standard fan velocity diagrams (see Figure 2.1). A uniform axial and zero whirl inlet velocity profile was assumed. This gave:

$$\alpha_1 = 0$$

$$C_{a1} = Q/\left(\pi \times \left(r_o^2 - r_i^2\right)\right)$$

$$C_{w1} = 0$$

$$\beta_1 = \tan^{-1}\left(\frac{U}{C_{a1}}\right)$$

where

$$U = \Omega \times r$$

On the exit side the calculated optimised velocity profiles were used to calculate:

$$\alpha_2 = \tan^{-1}\left(\frac{C_{w2}}{C_{a2}}\right)$$

$$\beta_2 = \tan^{-1}\left(\frac{U - C_{w2}}{C_{a2}}\right)$$

From the relative inlet and outlet flow angles the approximate camber and stagger angles were calculated as follows:

$$\theta = \beta_1 - \beta_2 \qquad (4.7)$$

$$\xi = \tan^{-1}\left[\frac{1}{2} \times \left(\tan\beta_1 + \tan\beta_2\right)\right] \qquad (4.8)$$

Using the above equations, no deviation or incidence angles were assumed. Calculations of the above values were used to compare the approximate amount of blade camber and blade twist for the different configurations (see Figures 4.1a and 4.1b).

With the camber corresponding to the camber angle and the twist corresponding to the change in stagger angle over the blade length, the amount of camber and twist both seem to decrease with increasing hub-tip ratio, decreasing flow coefficient and pressure coefficient. To accommodate the different fan sizes, a profile with an 'average' camber and twist distribution was needed. This led to the use of the {0.25 / 0.19 / 0.12} configuration as the design velocity profile. In the above notation 0.25 is the hub-tip ratio, 0.19 the flow coefficient and 0.12 the pressure coefficient. This fan configuration represents the 1000 mm diameter fan with a 250 mm hub and half-solidity (see Table 4.2). Leading to a further advantage of using this configuration was the fact that it covered the whole range of blade lengths. This meant that it would not be necessary to extrapolate the profile to cover the full extent of all the different fan diameters.

4.1.3. APPLYING ACTUATOR DISK THEORY TO THE VELOCITY PROFILES

The velocity profiles calculated in the previous section satisfy simple radial equilibrium, as given in equation (3.14) (Dixon, 1978), but this only applies far upstream and far downstream from the fan. Actuator disk theory was used to translate the velocity profiles to positions at the leading and trailing edge of the fan blade.

Simple actuator disk theory assumes that halfway through the fan, at the actuator disk, the axial velocity is given by (Dixon, 1978):

$$C_{a\,m} = \frac{1}{2} \times \left(C_{a\,x1} + C_{a\,x2} \right) \qquad (4.9)$$

At the positions up- and downstream of the fan, a difference in axial velocity at a certain point and the far up- and downstream positions is seen as a velocity perturbation. The axial velocity perturbation at the actuator disk is given by Δ_0 and that at a specific point by Δ. According to the actuator disk theory the perturbations decay exponentially away from the actuator disk. This gives:

$$\frac{\Delta}{\Delta_0} = 1 - \exp\left(\mp \frac{\pi \times x}{r_o - r_i} \right) \qquad (4.10)$$

The minus sign applies to the flow region in front of the fan and the plus sign to the flow region behind the fan. Since:

$$C_{a1} = C_{am} + \Delta \tag{4.11}$$

$$C_{a2} = C_{am} - \Delta \tag{4.12}$$

$$\Delta_0 = \frac{1}{2} \times \left(C_{a\infty 1} - C_{a\infty 2}\right) \tag{4.13}$$

This gives:

$$C_{a1} = C_{a\infty 1} - \frac{1}{2} \times \left(C_{a\infty 1} - C_{a\infty 2}\right) \times \exp\left(+\frac{\pi \times x}{r_o - r_i}\right) \tag{4.14}$$

$$C_{a2} = C_{a\infty 2} + \frac{1}{2} \times \left(C_{a\infty 1} - C_{a\infty 2}\right) \times \exp\left(-\frac{\pi \times x}{r_o - r_i}\right) \tag{4.15}$$

Equations (4.14) and (4.15) were used to determine the axial velocity distribution at the leading and trailing edges of the fan. The values for x were calculated as:

$$x = 0.43 \times c \times \cos(\xi) \tag{4.16}$$

$$x = 0.57 \times c \times \cos(\xi) \tag{4.17}$$

where equation (4.16) applied to equation (4.14) and equation (4.17) to equation (4.15). The values of 0.43 and 0.57 were obtained from the characteristics of the airfoil section used and corresponded to the position of the centroid. This meant that an approximate blade chord length had to be obtained at the start of the calculations. A value of 80 mm was used since it corresponded to the blade chord length of the comparative fan series fan blade. The value for (r_o - r_i) was taken to be equal to the blade length, namely 375 mm. Using the fact that the mass flow between two streamlines is constant, the streamline shape and position through the fan rotor could be determined. Since tangential momentum is conserved along a streamline, the value for ($r \times C_w$) is a constant along a streamline. The values for C_w at the far upstream and downstream positions were known, enabling the calculation of C_w at the leading and trailing edge of the fan blade. The resulting velocity distributions for the two different blade designs are given in Figures 4.2 and 4.3. These velocity distributions had to be adjusted slightly as the blade chord length became more apparent, leading to an iterative process.

4.2. GENERAL APPLICATION FAN BLADE DESIGN

This section describes the use of the velocity profiles obtained previously to design the general application fan blades. The design corresponded to the configuration of the fan for which the velocity profile was optimised. This meant that the design procedure was done for a seven bladed fan on the 250 mm hub diameter for the 1000 mm diameter fan. Since the hub diameters corresponded exactly to those of the comparative fan series it was decided to use the same number of fan blades, namely seven and fourteen blades, on the large hub diameter and ten and five blades on the small hub diameter. This meant that the hub and tip chord lengths of the designed fan blade had to be in the same region as those of the comparative fan series fan blades to keep the blade solidities in the same region.

4.2.1. BLADE SECTION PROFILE

Because of its high lift-drag ratios it was decided to base the fan blade design on the F-series airfoil (see Figure 4.4). The F-series airfoils is a modification of the C4 profile. According to Wallis (1972), airfoils based on a modified circular arc camber line constitutes a near-optimum aerodynamic design solution. Wallis (1977) considered the F-series airfoil a preferred design solution. The F-series profile consists of the C4 airfoil, modified to incorporate nose droop. This is achieved by adjusting the leading edge of the C4 camber line to a NACA 230 camber line. The thickness of these profiles is adjusted independent of the camber angle. The equations for the camber lines are given as:

1) for $x < 0.2025$

$$y_c = \left[\left(\frac{0.5}{\sin\theta\ 2}\right)^2 - (x-0.5)^2\right]^{1\,2} - \frac{0.5}{\tan\theta\ 2} + \left[120.5 \times d \times \left(x^3 - 0.607 \times x^2 + 0.1147 \times x\right)\right] \quad (4.18)$$

2) for $x > 0.2025$

$$y_c = \left[\left(\frac{0.5}{\sin\theta\ 2}\right)^2 - (x-0.5)^2\right]^{1\,2} - \frac{0.5}{\tan\theta\ 2} + \left[d \times (1-x)\right] \quad (4.19)$$

where y_c, x and d are all in fractions of the chord length.

The co-ordinates for a 10% thick, 10° camber angle and 1% nose droop airfoil were calculated by Wallis (1983). These consist of the upper and lower profile values for given X values. These equations are accurate for values of $\theta = 10°$ to 36°, t = 7% to 13% chord length and d = 0% to 3% chord length. The characteristics of the lift coefficient versus angle of attack curve stay the same, regardless of the value for thickness or nose droop, except in the vicinity of stall. The co-ordinates for the profile given in Wallis (1983) can be adjusted for any chosen profile by means of the following equations:

1) upper profile

$$Y_U = Y_U' + k_U \times (\theta - 10) + l_U \times (t - 10) + m_U \times (d - 1) \quad (4.20)$$

2) lower profile

$$Y_L = Y_L' + k_L \times (\theta - 10) + l_L \times (t - 10) + m_L \times (d - 1) \quad (4.21)$$

The values for Y, t and d are in percentage chord, where Y is measured perpendicular to the chord line. The values for Y', k, l and m differ along the length of the chord. A table containing these values along with their corresponding X values is given by Wallis (1983). This table was used in generating the blade co-ordinates after the parameters were calculated.

4.2.2. CALCULATING THE CHORD LENGTHS AND LIFT COEFFICIENTS

These calculations were based on the procedures described by Wallis (1983). According to Wallis (1983), the solidity ratio of the fan has to be taken into account during blade design. For a solidity higher than one, cascade effects had to be taken into account. For solidities less than one, the blades could be treated as isolated airfoils. Since the velocity profile used in the design was based on a seven bladed fan with a large hub diameter and chord lengths similar to that of the comparative series of fans, the solidity of the fan was never higher than 0.8. This simplified the calculations considerably, since no allowance had to be made for cascade effects.

The first step in the design was to calculate the flow angles for the velocity profiles that were adjusted by means of the actuator disk theory:

$$\alpha_1 = 0$$

$$\beta_1 = \tan^{-1}\left(\frac{U}{C_{a1}}\right)$$

$$\alpha_2 = \tan^{-1}\left(\frac{C_{w2}}{C_{a2}}\right)$$

$$\beta_2 = \tan^{-1}\left(\frac{U - C_{w2}}{C_{a2}}\right)$$

$$\beta_m = \tan^{-1}\frac{1}{2}\left(\tan\beta_1 + \tan\beta_2\right)$$

The average axial velocity over the blade chord was calculated as follows:

$$C_{am} = \frac{1}{2} \times \left(C_{a1} + C_{a2}\right)$$

These values were used to calculate the blade loading factor:

$$C_L\sigma = 2 \times \left(\frac{C_{w2}}{C_{am}}\right) \times \cos\beta_m \qquad (4.22)$$

with the solidity ratio:

$$\sigma = \frac{c}{s} \qquad (4.23)$$

We can also calculate s:

$$s = \frac{2 \times \pi \times r}{n_b} \qquad (4.24)$$

(The number of blades used in the design was seven, as explained earlier.)

The chord lengths at the hub and tip could now be calculated by choosing an appropriate value for C_L:

$$c = \frac{2 \times \pi \times r \times C_L \sigma}{n_b \times C_L} \qquad (4.25)$$

In order to obtain solidities similar to those of the comparative fan series, the values for the hub and tip chord lengths had to be in the same size range as the comparative fan series'. This was achieved by selecting a C_L value of 1.85 at the hub and a value of 0.8 at the blade tip. This gave a chord length of 86 mm at the hub and 71 mm at the tip. Although these values for C_L are very high, the use of nose droop and blade thickness distribution improved the blade stall characteristics. The chord length distribution along the blade length was calculated by linearly interpolating between the hub and tip blade chord lengths. These results were used to calculate the lift coefficient distribution:

$$C_L = 2 \times \frac{s}{c} \times \left(\frac{C_{w2}}{C_{am}} \right) \times \cos \beta_m \qquad (4.26)$$

Due to the effect of solidity the lift coefficient is altered by a lift interference factor. With the help of Wallis (1983) the lift interference factor was estimated (see Figure 4.5). This gave the final lift coefficient values as follows:

$$C_{Li} = C_L / LIF \qquad (4.27)$$

The lift coefficients and chord lengths along with the flow angles are given in Table 4.3.

Table 4.3: Calculated blade design variables for general application fan

blade length	chord	C_L	β_1	β_2
[m]	[m]		[°]	[°]
0	0.0867	1.85	56.29	30.46
0.0197	0.0859	1.872	59.48	37.86
0.0395	0.0850	1.763	61.66	46.23
0.0592	0.0842	1.662	63.86	52.12
0.0789	0.0834	1.559	65.73	56.59
0.0987	0.0826	1.452	67.51	60.50
0.1184	0.0817	1.368	68.97	63.31
0.1382	0.0809	1.286	70.34	65.79
0.1579	0.0801	1.218	71.5	67.72
0.1776	0.0794	1.156	72.57	69.42
0.1974	0.0784	1.102	73.51	70.83
0.2171	0.0776	1.053	74.37	72.08
0.2369	0.0767	1.01	75.14	73.15
0.2566	0.0759	0.97	75.85	74.11
0.2763	0.0751	0.935	76.49	74.95
0.2960	0.0743	0.903	77.08	75.71
0.3158	0.0734	0.874	77.62	76.37
0.3355	0.0726	0.846	78.12	77.02
0.3553	0.0718	0.824	78.57	77.56
0.375	0.0709	0.8	79.01	78.1

4.2.3. CALCULATING THE CAMBER AND STAGGER ANGLES

The stagger and camber angles are defined according to Figure 4.6. The variation in stagger angle reflects the amount of twist along the blade length, while the camber angle corresponds to the amount of curvature in the blade profile. The values for camber angle were obtained using:

$$\theta = \beta_1 - \beta_2 + \delta - i \qquad (4.28)$$

The values for incidence angle were taken from a graph in Wallis (1983) (see Figure 4.7). The values for δ were calculated using equation (4.29) (Carter, 1950):

$$\delta = \left(m \times (\beta_1 - \beta_2) \times \sqrt{\frac{s}{c}} \right) \Big/ \left(1 - m \times \sqrt{\frac{s}{c}} \right) \qquad (4.29)$$

This function gave deviation angle values that decreased with decreasing solidity, reaching a certain value from where it started increasing and eventually diverged. The values for deviation at these radii were kept constant with the lowest deviation angle value calculated. According to Bruneau (1994) the value for m could be approximated by equation (4.30):

$$m = 0.209253 + \frac{0.2322389}{10^2} \times \xi - \frac{0.3736909}{10^4} \times \xi^2 + \frac{0.8668135}{10^6} \times \xi^3 \qquad (4.30)$$

As can be seen equation (4.30) uses the value for stagger angle. In order to calculate the value for camber angle, the stagger angle had to be obtained first, using equation (4.31):

$$\xi = \beta_1 - \alpha \qquad (4.31)$$

where

α = angle of attack

The angles of attack for the blade profiles were obtained from the graph in Wallis (1983), reproduced in Figure 4.8. This angle had to be adjusted for the change in angle of attack because of the blade nose droop (Wallis, 1983):

$$\alpha = \alpha_{0d} - 0.57 \times d \qquad (4.32)$$

where d is in percentage chord.

The blade was designed for a maximum nose droop of 3% along the blade length to accommodate the high lift coefficients used in the design, while the blade thickness was varied linearly from 11% at the blade tip to 7% at the hub. According to Figure 4.8 the angle of attack is dependent on the camber angle of the blade profile. This meant that the angle of attack was obtained using the camber angle, which in turn affected the value for stagger angle, thereby changing the value for camber angle. In this way the value for both camber and stagger were obtained by iteration. To start the iteration the value for stagger angle was assumed to be equal to:

$$\xi = \beta_m$$

The resulting camber and stagger distributions are illustrated in Figure 4.9, along with the blade profile distribution at the different radii (see Figure 4.10).

4.2.4. BLADE ROOT DESIGN

The size of the new fan blade corresponded very well to that of the comparative fan series' fan blades. Therefore it was expected that the form and size of the blade root would not differ much from these blades' blade root. Since HAI already had a concept design for the blade root, it was decided to use this design and adapt it for the new blade design. The design has several improved features, such as a larger contact area as well as a well defined collar on the root shaft, which improves the ease of assembly by wedging into the cavity in the fan hub. Although the design was tested for static strength, it was expected to be able to withstand dynamic stresses also, because of the size similarities with the comparative fan series. A diagram of the blade root is illustrated in Figure 4.11.

4.3. LOW-NOISE FAN BLADE DESIGN

Although the design of the low-noise fan was not part of the HAI project, the low-noise blade design was done on the same principles as the general application fan. The low-noise fan was designed to deliver the same pressure duty as the fourteen bladed, 1000 mm diameter general application fan of the comparative fan series. Since it was designed for low-noise applications, the pressure duty of the fourteen bladed general application fan was achieved by using seven blades with a larger chord length. Calculating the values for ν, ϕ and ψ with the help of equations (A.1) to (A.3)

and (4.1) to (4.6), the {0.25/0.2/0.21}configuration values were obtained The velocity profile was calculated in the same way as for the general application fan and is illustrated in Figure 4.3. The F-series airfoil described in section 4.2.1 was also used for the low-noise fan, as well as the blade root design of section 4.2.4. This enabled the use of the same hub design for both blade designs.

4.3.1. DESIGN VARIABLES

Due to the similar design techniques the design variables were the same as the general application fan design, although provision had to be made for blade sweep. Wright et. al. (1989) provided a set of sweep-angle curves (see Figure 4.12) for various wave number modes which should result in a fan noise reduction of up to 10 dB for a specific mode number, when used to design a forward swept blade. According to him the curve for wave number mode equal to two will ensure a significant noise reduction in an axial flow fan. A mode number represents the frequency at which the noise occurs - a low mode number represents a low frequency noise. The curve was represented as follows:

$$\eta = 37.9261 + 79.1634 \times M_R - 0.3152/M_R - 23.0131 \times M_R^3 \qquad (4.33)$$

where η represents the blade sweep angle viewed from the front of the axial flow fan, in the plane perpendicular to the fan shaft (see Figure 4.13) and M_R is given by equation (4.34).

$$M_R = \frac{\Omega \times r}{\sqrt{RT}} \qquad (4.34)$$

where

$R = 287$ J/kgK

$T = 293.16$ K (20 °C)

Integrating equation (4.33) gave the equation for θ_s (see Figure 4.13). This equation was important in defining the form of the blade axis for design purposes:

$$\theta_s = 37.9261 \times \ln(r) + 79.1634 \times G \times r + \frac{0.3152}{G \times r} - \frac{23.0131 \times G^3 \times r^3}{3} + K \qquad (4.35)$$

where

$$G = \frac{M_R}{r}$$

Assuming a fan speed of 1440 rpm and using the fact that θ_s equals zero at the fan hub (r = 0.125 m), it was found that:

$$G = 0.4395$$

$$K = 68.778$$

Referring to Smith et. al. (1963) another angle was defined, namely the aerodynamic sweep angle, λ, which represented the amount of blade sweep along the blade surface itself, taking the blade stagger angle into account. Using Figure 4.14 to transform η into λ:

$$\tan \lambda = \tan \eta \times \cos \phi \qquad (4.36)$$

where

$$\phi = 90 - \xi$$

Following the reasoning of Smith et. al (1963) when calculating the blade variables, the flow was assumed to be on an axisymmetric stream surface, while the view parallel to the blade axis was used for the calculations. This meant that all the blade variables had to be transformed by the angle λ at the different radii (see Figure 4.15). These variables were identical to those used for the general application design.

According to Smith et. al. (1963) there is a tendency for the fluid crossing the pressure side of a swept cascade blade to move a greater distance in the spanwise distance than on the suction side. This means that the flow pattern in the vicinity of a "wall", for instance the fan hub, would be disturbed. To account for this, a variable called downwash was calculated and added to the camber angle value.

4.3.2. CALCULATING THE BLADE DESIGN VARIABLES

Using equation (4.33) the value for geometric sweep was calculated at the different radial stations. The flow angles were calculated with the help of the velocity triangles (see Figure 2.1). The velocities were obtained from the velocity profile mentioned in Section 4.1.3 (see Figure 4.3). The preliminary stagger angle was assumed to be equal to β_m:

$$\beta_m = \tan^{-1}\frac{1}{2}\left(\tan\beta_1 + \tan\beta_2\right)$$

This value was used in equation (4.36) to calculate the preliminary value for aerodynamic sweep, λ. Once the aerodynamic sweep was calculated, the "swept" values for the flow angles were calculated (see Figure 4.15):

$$\beta_{s1} = \tan^{-1}\left(\tan\beta_1 \times \cos\lambda\right)$$

$$\beta_{s2} = \tan^{-1}\left(\tan\beta_2 \times \cos\lambda\right)$$

$$\beta_{sm} = \tan^{-1}\frac{1}{2}\left(\tan\beta_{s1} + \tan\beta_{s2}\right)$$

These were used to calculate the blade loading factor:

$$C_L\sigma = 2 \times \left(\frac{C_{w2}}{C_{am}}\right) \times \cos\beta_{sm} \qquad (4.37)$$

where the velocities were calculated as in Section 4.2.2.

The values for solidity ratio, σ, at the fan hub and tip were calculated by selecting lift coefficient values at the hub and tip. A value for lift coefficient at the hub of 1.4 and at the tip of 0.7 was chosen, as proposed by Wallis (1983). Once the values for solidity ratio at the blade hub and tip were calculated, the values for "swept" blade spacing were calculated (Smith et. al. (1963)):

$$s_s = s/\sqrt{1 + \left(\tan\eta\right)^2} \qquad (4.38)$$

The value for s was determined using equation (4.24). The number of blades used in equation (4.24) was seven as explained in Section 4.3. Using the values for "swept" spacing, the "swept" chord at the blade hub and tip were determined using equation (4.39):

$$c_s = \sigma \times s_s \tag{4.39}$$

Interpolating linearly between the "swept" chord values at the hub and tip gave the "swept" chord distribution over the blade length. From these the solidity distribution over the blade were calculated using:

$$\sigma = c_s / s_s$$

The values for the solidity distribution were used to calculate the lift coefficient distribution along the blade length by using equation (4.37):

$$C_L = \frac{2}{\sigma} \times \left(\frac{C_{w2}}{C_{am}} \right) \times \cos \beta_{sm} \tag{4.40}$$

The "swept" camber angle distribution was calculated using equation (4.41):

$$\theta_s = \beta_{s1} - \beta_{s2} + \delta - i + \Delta^0 \tag{4.41}$$

where δ is obtained using equation (4.28) and i is obtained from the graph in Wallis (1983) (see Figure 4.7). The value of i is dependent on the value of θ and therefore the calculation of the camber angle is an iterative process. The value for downwash deviation angle, Δ^0, was calculated at the fan hub using the method proposed by Smith et. al. (1963).

The method starts off by calculating the value for downwash at the wall, Dw_w. This is followed by calculating the locations, a perpendicular distance h from the wall, for 50% and 10% of Dw_w, as a fraction of the chord length, c. A curve was fitted through these values to obtain the downwash distribution. The downwash deviation angles at the different radii were calculated as follows:

$$\Delta^0 = \frac{180}{\pi} \times \frac{\Gamma}{c \times W_m} \times Dw \tag{4.42}$$

where

Dw is the downwash at the appropriate radius

$c = c_s / \cos\lambda$

$W_m = C_{am} / \cos\beta_m$

with C_{am} and β_m calculated as in Section 4.2.2.

$$\Gamma = \frac{2\pi}{n_b} \times \left| r \times C_{w2} \right|$$

Due to the fact that the equations and graphs for deviation, incidence and downwash were more applicable to higher solidity blading, the camber angle would decrease with decreasing solidity until less than zero. This necessitated restricting the camber angle to be constant once it decreased to a value of 15°. This corresponded to the minimum value for camber angle used in the general application fan design which was equal to 16°. The minimum values for camber angle were chosen from the preliminary calculated camber angles as those values that were close to 15°.

The "swept" stagger angle distribution was calculated using equation (4.43):

$$\xi_s = \beta_{s1} - \alpha \qquad (4.43)$$

The values for angle of attack, α, were obtained from the graph in Wallis (1983) (see Figure 4.8). Since the stagger angles were approximated at the start of the calculations, the calculations were repeated with the new stagger angle values. After each set of calculations the stagger angles were checked until it converged satisfactorily. Finally, the "unswept" values for stagger and camber angle at the different radii were calculated:

$$\xi = \tan^{-1}\left(\tan\xi_s / \cos\lambda\right) \qquad (4.44)$$

$$\theta = \tan^{-1}\left(\tan\theta_s / \cos\lambda\right) \qquad (4.45)$$

The calculated properties of the low noise blade design are given in Table 4.4. The resulting camber and stagger angle distribution for the low-noise fan is given in Figure 4.16 and the blade profile distribution in Figure 4.17.

Table 4.4: Calculated blade properties for low-noise fan

blade length	chord	C_L	β_1	β_2	μ	λ
[m]	[m]		[°]	[°]	[°]	[°]
0	0.17	1.3	55.14	14.41	36.55	29.16
0.0197	0.172	1.513	57.92	17.59	37.99	31.16
0.0395	0.174	1.525	60.32	27.47	39.3	32.72
0.0592	0.175	1.45	62.32	37.15	40.45	34.03
0.0789	0.176	1.36	64.18	45.1	41.48	35.29
0.0987	0.178	1.272	65.86	51.22	42.46	36.55
0.1184	0.179	1.192	67.32	55.8	43.43	37.82
0.1382	0.181	1.123	68.65	59.41	44.35	39.02
0.1579	0.183	1.063	69.83	62.25	45.21	40.22
0.1776	0.184	1.011	70.9	64.6	46	41.42
0.1974	0.186	0.964	71.87	66.53	46.87	42.57
0.2171	0.188	0.922	72.76	68.19	47.67	43.66
0.2369	0.19	0.884	73.56	69.61	48.41	44.69
0.2566	0.192	0.85	74.3	70.85	49.22	45.72
0.2763	0.194	0.819	74.98	71.93	49.96	46.7
0.2960	0.196	0.792	75.6	72.89	50.71	47.67
0.3158	0.197	0.766	76.18	73.74	51.45	48.59
0.3355	0.199	0.742	76.73	74.54	52.2	49.45
0.3553	0.201	0.72	77.2	75.2	52.94	50.31
0.375	0.203	0.7	77.68	75.87	53.63	51.17

4.4. STRENGTH CALCULATIONS FOR FAN BLADES

The purpose of the strength calculations was to determine whether the manufactured fan blades could withstand the forces exerted on them during the tests performed. These calculations can also serve as guidelines for the production manufactured fan blades. With reference to Section 4.5, the

general application fan blades were to be manufactured entirely from aluminium, while the low-noise blades were to be manufactured from polyurethane resin with a steel blade root inserted into them. This blade root consisted of a 10 mm threaded steel shaft covered with an aluminium bush that fitted into the same hub as the general application fan blade.

A static strength analysis was performed on both the blades. The critical part of the blade static strength was expected to be the blade root section because of the fact that it had a comparatively small cross-sectional area in relation to the forces acting on it. This part was analysed by means of a few basic strength calculations. Referring to the comparative fan data sheets, two critical fan blade length and fan speed combinations were identified, namely 280 mm at 2880 rpm and 375 mm at 1440 rpm.

Due to the difference between the forces acting on the blades, different critical combinations apply to different calculations. For the general fan design the calculations for centrifugal forces acting on the blade assumed a speed of 2880 rpm at the design blade angle of 13.8° and blade length of 280 mm. The aerodynamic force calculations assumed a speed of 1440 rpm at 13.8° blade angle and 375 mm blade length. The calculations were done for nylon 6.6 as well as for sand cast aluminium (LM 24) to facilitate both types of production possibilities. For the low-noise fan design both the aerodynamic and centrifugal force calculations assumed a speed of 1440 rpm at the design blade angle of 15.4° and blade length of 375 mm. These calculations were done for a mild steel blade root. The material properties are given in Table 4.5. Since the swept blades were evaluated for the mild steel blade root and the blade root was identified as the critical part of the blade, only the density of the polyurethane material was needed to determine the centrifugal forces on the blade root.

Table 4.5: Fan blade material properties

	Nylon 6.6	Aluminium [LM 24]	Polyurethane	Steel
E [MPa]	2800	71000	not needed	207.10^3
Yield Strength [MPa]	75	180	not needed	370
Shear Strength [MPa]	37.5	90	not needed	185
Density [kg/m^3]	1140	2710	1577	7810

According to Wallis (1983) the calculations could be divided into the calculations for stresses due to centrifugal forces and the calculations for stresses due to aerodynamic forces. The forward-swept blades were also investigated for flutter and divergence with the help of Dowell et al. (1995). Sample calculations for the strength calculations are shown in Appendix C.

4.4.1. AERODYNAMIC LOADS

These loads can be listed as follows (see figure 4.18):

1) Twisting moment

This moment is introduced by the aerodynamic forces on the blade and deforms it into the high-pitch angle position.

2) Bending loads

Due to the lift and drag forces on the wing, a bending moment is created around the blade root. This moment determines the blade deflection.

3) Shear loads

The aerodynamic forces create a shearing load normal to the blade axis.

To estimate the aerodynamic forces, the same values for lift coefficient were used as in the blade design stage. The values for drag coefficient were obtained from Wallis (1983) (see Figure 4.19). Since no data on quarter-chord moments for the F-series profiles were available, the corresponding values for a NACA 65-410 wing profile with approximately the same shape were used (Abott et al., 1959). A list of these coefficients for both blade designs is included in Table 4.6 .

Table 4.6: Force coefficients used in design

	general application fan			low-noise fan		
Blade Length [m]	C_L	C_D	$C_{Mc\,4}$	C_L	C_D	$C_{Mc\,4}$
0	1.85	0.0142	-0.075	1.3	0.013	-0.075
0.0197	1.877	0.0128	-0.075	1.513	0.014	-0.075
0.0395	1.763	0.013	-0.075	1.525	0.014	-0.075
0.0592	1.662	0.014	-0.075	1.45	0.013	-0.075
0.079	1.559	0.0145	-0.075	1.36	0.015	-0.075
0.0987	1.452	0.014	-0.075	1.272	0.016	-0.075
0.1184	1.367	0.0132	-0.075	1.192	0.017	-0.075
0.1382	1.286	0.012	-0.075	1.123	0.015	-0.075
0.1579	1.218	0.011	-0.075	1.063	0.0125	-0.075
0.1776	1.156	0.0105	-0.075	1.011	0.012	-0.075
0.1974	1.102	0.0105	-0.075	0.964	0.0115	-0.075
0.2171	1.053	0.0105	-0.075	0.922	0.01	-0.075
0.2368	1.01	0.0105	-0.075	0.884	0.01	-0.075
0.2566	0.97	0.0105	-0.075	0.85	0.01	-0.075
0.2763	0.935	0.0105	-0.075	0.819	0.01	-0.075
0.2961	0.903	0.0106	-0.075	0.792	0.0105	-0.075
0.3158	0.874	0.0106	-0.075	0.766	0.0105	-0.075
0.3355	0.846	0.0107	-0.075	0.742	0.0105	-0.075
0.3553	0.824	0.0107	-0.075	0.72	0.0105	-0.075
0.375	0.8	0.0108	-0.075	0.7	0.0105	-0.075

Firstly, the lift and drag forces over each of the twenty segments were calculated. These segments were formed by the areas around each of the twenty radial divisions along which the blade was designed.

$$L = C_L \times \frac{1}{2} \times \rho \times C_{am}^{\ 2} \times A \qquad (4.46)$$

$$D = C_D \times \frac{1}{2} \times \rho \times C_{am}^{\ 2} \times A \qquad (4.47)$$

with

$\rho = 1.2\ kg/m^3$

$A = c \times \Delta r$

The value for resultant force was calculated:

$$F = \sqrt{L^2 + D^2}$$

and the angle between F and L:

$$delta = \tan^{-1} \frac{D}{L}$$

Since the value for stagger angle varies over the blade length, the resultant force acts in a changing direction as the stagger angle changes along the length. It was simplified by assuming that the blade parameters stay constant over each of the blade segments. In order to calculate the values for maximum bending stress and shear force, the direction in which the components of the resultant forces over the different segments gave the maximum bending moment was needed, as well as the direction which gave the maximum shear force. These reference directions were iteratively calculated by alternately choosing one of the directions of the resultant forces as the direction of maximum bending moment or shear force. The values for maximum bending moment and shear force were calculated as follows:

$$M_{bend} = \sum_{j=1}^{n} F_j \times \left(\cos\left(\phi_j - \phi_{ref}\right)\right) \times l_{mom} \qquad (4.48)$$

$$F_{shear} = \sum_{j=1}^{n} F_j \times \left(\cos\left(\phi_j - \phi_{ref}\right)\right) \qquad (4.49)$$

where

l_{mom} = the moment arm

$$\phi_j = \text{delta}_j + \left(90° - \xi_j\right)$$

$$n = 20$$

The aerodynamic twisting moment for each segment was calculated as follows:

$$M_{c\,4} = C_{Mc\,4} \times \frac{1}{2} \times \rho \times C_{a\,m}{}^2 \times A \times c \qquad (4.50)$$

Numerically, this gave:

$$M_{c\,4\,total} = \sum_{i=1}^{n} M_{c\,4\,i}$$

Since the quarter chord differed from the location of the segment centroid along which the blade segments were staggered, an additional moment is formed by this distance offset. According to Wallis (1983) the distance the centroid is located from the leading edge, parallel to the blade chord line, is almost constant at 43.45% of the chord length. This gave:

$$\Delta x = \left(0.4345 - 0.25\right) \times c$$

$$= 0.1845 \times c$$

Taking the stagger angle into account this gave:

$$M_{add} = 0.1845 \times c \times \cos\left(\xi\right) \times L \qquad (4.51)$$

Adding these values for the different blade sections gave:

$$M_{add\ total} = \sum_{i=1}^{n} M_{add\ i}$$

The forward swept blade also experienced a moment due to the distance that the blade axis is offset from the blade root axis. This changed equation (4.51) as follows:

$$M_{add} = \left[0.1845 \times c \times \cos\left(\xi\right) + r \times \sin\theta_s\right] \times L \qquad (4.52)$$

The results from this section were as follows:

Table 4.7: Resultant aerodynamic forces

	general appl. fan	low-noise fan
F_{shear} [N]	4.19585	10.0468
M_{bend} [Nm]	0.68723	1.83897
$M_{c/4\ total}$ [Nm]	0.00592	0.14216
M_{add} [Nm]	0.06257	2.09524

4.4.2. CENTRIFUGAL LOADS

The centrifugal loads can be divided into:

1) Twisting moment

This is a moment introduced by the fact that the blade is rotated around an axis other than the main axis of inertia and tends to deform the blade into the low-pitch position.

2) Centrifugal load

Due to the weight of the blade a radial force is created in the direction of the blades' main axis.

These forces are due to the revolution of the fan blades around a fixed axis. The biggest factor influencing these forces is the rotational speed of the fan blades.

The axial force due to the centrifugal loads is given by:

$$F_{axial} = \rho \times \Omega^2 \times \int_{ri}^{ro} (A \times r).\, dr \qquad (4.53)$$

Where

ρ = material density [kg/m^3]

Ω = fan revolution speed

= 303.687 rad/s

A = cross-section area [m^2]

The value for the cross-sectional area was obtained from a graph given by Wallis (1983) (see Figure 4.20). The centrifugal twisting moment is given by (Wallis, 1983):

$$M_{cent} = \rho \times \frac{\Omega^2}{2} \times \int_{ri}^{ro} \left(\sin(2 \times \gamma) \times (J_2 - J_1)\right). dr \qquad (4.54)$$

where

$$\gamma = 90° - \xi$$

J_2 and J_1 were also obtained from graphs in Wallis (1983) (see Figures 4.21 and 4.22). The results from this section were:

Table 4.8: Resultant centrifugal forces (densities given in Table 4.5)

	general appl. fan	low-noise fan
F_{axial} [N]	$\rho \times 1.5033$	$\rho \times 6.1402$
M_{cent} [Nm]	$\rho \times 0.00146$	$\rho \times 0.01436$

4.4.3. BLADE STRESSES

The critical part of the blade was identified as the blade root. For the general application fan these dimensions were as follows:

$r_{outer} = 0.0105$ m

$r_{inner} = 0.004$ m

The inner radius was included because of the fact that the blade root was hollow to minimise the material used during manufacture. For the low-noise fan the corresponding dimensions were:

$r_{outer} = 0.008$ m

$r_{inner} = 0$ m

The characteristic values for the cross-section were calculated as follows:

$$A_{root} = \pi \times \left(r_{outer}^{\ 2} - r_{inner}^{\ 2}\right) \qquad (4.55)$$

$$I_{root} = \frac{\pi \times \left(d_{outer}^{\ 4} - d_{inner}^{\ 4}\right)}{64} \qquad (4.56)$$

$$J_{root} = \frac{\pi \times \left(d_{outer}^{\ 4} - d_{inner}^{\ 4}\right)}{32} \tag{4.57}$$

These values, along with the forces calculated earlier, were used to calculate the stresses:

1) The shear stress perpendicular to the blade axis:

$$\tau_{shear} = \frac{F_{shear}}{A_{root}} \tag{4.58}$$

2) The axial stress due to the centrifugal forces

$$\sigma_{axial} = \frac{F_{axial}}{A_{root}} \tag{4.59}$$

3) The bending stress due to the aerodynamic forces

$$\sigma_{bend} = \frac{M_{bend} \times y_{max}}{I_{root}} \tag{4.60}$$

where

$$y_{max} = r_{outer} \quad [m]$$

4) The shear stress due to the torsion in the blade root

$$T_{root} = -\left(M_{c\ 4\ total} + M_{add\ total}\right) + M_{cent} + M_{swept}$$

where M_{swept} equals zero for the general application fan blade.

$$\tau_{torsion} = \frac{T_{root} \times r_{outer}}{J_{root}} \tag{4.61}$$

This gave the total stresses:

$$\tau_{total} = \tau_{shear} + \tau_{torsion}$$

$$\sigma_{total} = \sigma_{bend} + \sigma_{axial}$$

The safety factors were based on the yield strength and maximum shear strength:

$$sf_{sigma} = \frac{\sigma_{yield}}{\sigma_{total}}$$

$$sf_{tau} = \frac{\tau_{max}}{\tau_{total}}$$

The values for the safety factors indicated that the fan blade root was strong enough to support the fan blade. Since Wallis (1983) advises a safety factor of 3 or higher to facilitate fatigue strength, the blade design was satisfactory. A summary of the results, taking the material from which the blade root was manufactured into account, is given in Table 4.9.

Table 4.9: Calculated stresses and safety factors

	general application fan		low-noise fan
Value	Nylon	Aluminium	Steel
σ_{axial} [MPa]	5.78788	13.75891	48.15504
σ_{bend} [kPa]	772.08	772.08	4573.15
τ_{shear} [kPa]	14.17	14.17	49.97
$\tau_{torsion}$ [MPa]	0.89701	2.17995	25.37869
σ_{total} [MPa]	6.55996	14.53099	52.72819
τ_{total} [MPa]	0.91118	2.19412	25.42866
sf_{sigma}	11.4	12.4	7.0
sf_{tau}	41.2	41.02	7.3

4.4.4. AEROELASTIC CALCULATIONS FOR FORWARD-SWEPT FAN BLADES

According to Bisplinghoff et al. (1955) three types of wing critical speeds exist, namely divergence, bending-torsion flutter and aileron reversal speed. Figure 4.23 shows a qualitative relation between the critical speeds with varying amounts of backward and forward sweep. Bisplinghoff et al. (1955) concludes that the divergence speed is lower than both the bending-torsion flutter and aileron reversal speeds for forward swept wings. This means that a forward swept wing is "divergence critical".

In applying the divergence calculations to the forward swept fan blade design, the Eigenvalue equation of Dowell et al. (1995) were used. Dowel et al. (1995) derived a set of equations constituting an Eigenvalue problem for a beam of constant spanwise properties:

$$\lambda_D = \frac{\partial \bar{C}_L}{\partial \alpha} \frac{\sin \Lambda \times \cos \Lambda \times \bar{c} \times \bar{I}^3 \times q}{E \times I} \qquad (4.62)$$

$$= -6.33$$

The variables for equation (4.62) are illustrated in Figure 4.24. According to Dowell et al. (1955) a value of -6.33 or less for λ_D will provide the divergence condition. To determine whether the low-noise fan blade design will succumb to divergence, a straight beam with constant spanwise properties was used to conform to equation (4.62). To determine the critical blade properties, the beam properties were assumed equal to the blade hub properties in the one instance and equal to the blade tip properties in the other.

Table 4.10: Blade properties at hub and tip

	hub	tip
$\bar{c}$ [m]	0.124	0.148
t [% c]	11	7
I [m^4]	3.13×10^{-8}	1.32×10^{-8}

The sweep angle, Λ, was calculated from $\theta_{s\,ave}$ (see Figure 4.13), along the fan radius as follows:

$$\Lambda = \theta_{s\,ave} + \sin^{-1}\left(r_i \times \frac{\sin(\theta_{s\,ave})}{\bar{l}} \right)$$

The value for sweep angle is negative for a forward swept blade in equation (4.62). This gave the value for sweep as:

$$\Lambda = -43.366\,^\circ$$

The air velocity was taken as the average blade velocity along the blade radius at 1440 rpm. This gave the value for velocity as:

$$U = 47.124 \text{ m/s}$$

The values for I and $\frac{\partial \bar{C}_L}{\partial \alpha}$ were obtained from graphs in Wallis (see Figure 4.8 and 4.21). The values for λ_D obtained using equation (4.62) were as follows:

Table 4.11: Values for λ_D obtained using equation (4.62)

	λ_D
hub	-0.012
tip	-0.034

Since the values for λ_D were above the minimum value of -6.33, the forward swept blades were able to withstand the aerodynamic forces for the above conditions. The small values for λ_D are due to the steel insert used in the swept fan blade shaft.

4.5. FAN BLADE MANUFACTURE

The general application fan blade formed part of an external project and was manufactured by contractors. The low-noise fan was an internal project and all the manufacturing procedures were done by the University of Stellenbosch. A computer programme, originally written by Mr. L. Furstenburg, was adapted and used to calculate the co-ordinates of the blade surfaces. This programme used the calculated blade design variables of Section 4.2 and 4.3, along with the blade section profile information, to calculate the blade co-ordinates. The datafiles containing these co-ordinates were imported into Autocad and stored as drawing-files. (see Figures 4.25 and 4.26).

The general application fan drawing file was used by the contractors to manufacture the blade. For the low-noise fan design the conversion programme was adapted to calculate the top and bottom surface of the blade separately, along with a common cutting plane with each side. The co-ordinates were imported into Autocad as two separate drawing files. The two files were imported into a

Cimatron_90 package. This package is used to calculate the cutter paths for numerically controlled machining of an object.

Once the cutter paths were calculated and converted into NC-code, the two surfaces were cut from jeluton wood blocks (see Figure D1). These wood blocks were used as plugs to manufacture a split mould. The mould halves were manufactured from fibreglass. Steel inserts, of 5 mm thickness, were manufactured for each blade. These inserts had a 16 mm threaded root onto which an aluminium bush was fitted. This bush fitted into the same hub as the general application fan blade. The inserts were seated into the split mould and the blade was cast around it (see Figure D2). The fans were tested at 630 mm diameter and therefore the full length of the mould was not utilised.

The blades were seated in a hub that corresponded to the blade root profile. The general application fan blades could either be fitted into a 150 mm or 250 mm hub. The low-noise fan only utilised the 250 mm hub (see Figure D3 to D5). The setting angles of the general application fan were determined with respect to the full length of the blade. This means that a setting angle of 25° corresponded to an angle of 25° between the blade chord line at the tip and the surface perpendicular to the motor axis (see Figure 4.27). The degree indicators were shown on the blade root collar at 5° intervals, from 5° to 65°. This made provision for the relative large variation in stagger angle over the length of the blade which would affect the angle at which the blade can be set for different blade lengths. For example, a 375 mm blade would have a negative incidence at the hub if it was set at 5°. The low-noise fan was tested at its design blade angle only (see Chapter 5). The blade design angle was 31° with respect to the blade tip chord of a 240 mm blade.

5. EXPERIMENTAL ANALYSIS OF FAN DESIGNS

A selection of fan sizes was tested. The selection was determined by the available sizes of fan ducting and fan motors as well as the number of tests needed to cover the extent of the fan series that it was designed for. The fan designs were tested on a BS 848, type D, fan test facility (see Figure D6). The type D test facility simulates a fan used with a ducted in- and outlet. The BS 848, part 1 (1980) and 2 (1985), Standards were adjusted to provide a test facility on which noise and performance tests could be executed simultaneously (Van der Spuy (1994)). This combined test facility was used for the 483 mm and 630 mm fan diameters. The noise values obtained for the 630 mm diameter fan were used to compare the general application fan - and low-noise fan designs. The 800 mm diameter fan was tested in a similar test facility as the 480 mm and 630 mm fans, without a front anechoic chamber, because no noise measurements were measured for the 800 mm diameter fan. The results obtained were not comparable to other fan characteristics but tests run on the same facility could be compared with one another. The following noise and performance tests were done:

Table 5.1: Summary of fan tests done in the type D test facility

	Fan dia.	Hub	Speeds	Blade no.	Blade angles	noise tests?
	[mm]	[mm]	[rpm]		[°]	Yes/No
general appl. fan	483	150	960, 2880	5, 10	5, 15, 25, 35, 45	Yes
		250	960, 2880	7, 14	5, 15, 25, 35, 45	Yes
	630	150	960, 1440	5, 10	5, 15, 25, 35, 45	Yes
		250	960, 1440	7, 14	5, 15, 25, 35, 45	Yes
	800	150	1440	5, 10	5, 15, 25, 35, 45	No
		250	1440	7, 14	5, 15, 25, 35, 45	No
low-noise fan	630	250	720, 960, 1200	7	design angle	Yes

The number of tests performed for a specific fan size was influenced by the time and motor sizes available because the project was part of a contract with HAI. The general application fan was tested at blade angles of 10° intervals from 5° to 45° to reduce the number of tests needed to define the

fan's characteristics,. The restriction of the pad-mounted motor sizes, a 15 kW motor has a 250 mm diameter, prevented testing of the 630 mm and 800 mm general application fan at 2880 rpm because it required a too-high power duty from the motor. A pad-mounted motor is mounted in the centre of the shroud by four sets of bolts which keep it in position. The absence of a suitable fan motor size also prevented testing of the 483 mm fan at large blade angles at 2880 rpm. A belt-driven fan would not have been influenced by the heavy power requirements but was not applicable to this project.

The low-noise fan was tested at a maximum speed of 1200 rpm. The low-noise fan started vibrating excessively at approximately 1400 rpm. It was suspected that the vibration was due to the occurrence of resonance in the form of fan shaft whirling. The whirling occurred due to the relative larger weight of the low-noise fan, as well as the large distance between the fan rotor and motor supports. The large distance from the motor supports to the fan rotor was due to the torque transducer which was installed between the motor and the fan rotor. The distance was made even larger by the fact that a special coupling had to be installed to connect the torque transducer to the motor shaft. The fan performance characteristics of the low-noise fan and general application fan could be compared using the fan scaling laws for the different speeds but this was not possible with the noise data.. The 630 mm diameter general application fan was set at a blade angle which gave the same pressure characteristic as the low-noise fan to enable a comparison between the two fans, using the fan scaling laws. Noise data was collected for both fans at the same speed. Due to the fact that the blade sweep gave a large change in blade tip clearance when changing blade setting angle, the low-noise fan was tested with a constant blade setting angle.

Further tests were also performed for the 1000 mm diameter general application fan on a BS 848, type A, test facility (see Figure 5.1). These results could not be compared directly with the rest of the test results but it provided valuable insight into the behaviour of the general application fan series at its maximum fan diameter.

5.1. TEST FACILITY

A diagram of the type D test facility for the 630 mm diameter fan is included in Figure 5.2. The 483 mm test facility had the same inlet ducting as the 630 mm test facility, with a length of 483 mm ducting after the fan. The ducting connected to a conical section which fitted onto the outlet

anechoic chamber used for all the test facilities. The 800 mm test facility used the same conical inlet as the other test facilities, fitted to a conical section leading to the 800 mm diameter inlet ducting for the fan. The 800 mm outlet ducting fitted on a conical section which fitted on the outlet anechoic chamber (see Figure 5.3).

As mentioned previously, the general concept of the test facility was a combination of both BS 848 part 1 (1980) and part 2 (1985), enabling the simultaneous measurement of both fan performance and noise. Due to the fact that such a test facility met the requirements set forth by the BS 848 part 2 (1985) Standards for fan noise measurement, it deviated from the requirements for fan performance measurement set forth by BS 848 part 1 (1980). These deviations could be summarised as follows:

1. The omission of the Etoile flow straightener behind the fan (see Figure D7): The effect this had on the results was investigated by doing comparative tests for fan performance, with and without the flow straightener for a specific fan configuration, at the larger blade angles where the effect was expected to be the most significant. The results are illustrated in Figure 5.4 and 5.5. Installing the flow straightener prevented the taking of noise readings behind the fan, because the straightener and the noise measuring tube interfered with each other. The performance and noise measurements were measured simultaneously on the same test facility, without the flow straightener (see Section 6.1), to save time.
2. The addition of the two anechoic chambers at the in- and outlet of the facility used to measure fan performance: Although these extra lengths of ducting had the overall effect of increasing the system's resistance, the measured fan pressure rise was not affected, because the distance between the pressure tappings and the fan remained the same. For the 800 mm fan the front anechoic chamber was omitted.

5.1.1. GENERAL LAY-OUT OF THE TEST FACILITY

The flow rate into the tunnel was measured using a conical inlet (see Figure D8). This inlet was manufactured using the dimensions as supplied by the BS 848 part 1 (1980). The Standards prescribe the conical inlet, without calibrating it, for a pressure drop over the inlet that is less than 4000 Pa, i.e. ± 400 mm of water. This translates into a volume flow rate of not more than 29 m^3/s, which falls outside the volume flow range of the fans that were tested.

The volume flow rate in the tunnel was controlled by a standard throttle as described by the BS 848 part 2 (1985) (see Figure D9). The throttle ran on a threaded steel rod, enlarging or reducing the outlet area. The motor speed was controlled by a frequency inverter which corresponded to the fan motor size. The frequency inverter was set at a predetermined speed at which the tests were run, for example 12, 16 or 24 Hz. The actual motor speed was measured with a proximity switch and a frequency read-out. The measured data was corrected for deviation from the standard values for density and motor speed by means of the fan scaling laws.

5.1.2. LAY-OUT OF TEST APPARATUS

A general lay-out of the measuring equipment is given in Figure 5.6. The equipment used to measure the performance of the fan was as follows (see Figure D10 and D11):

1. HBM PDI 0.01 bar pressure transducer
2. HBM KWS 3073 bridge amplifier
3. HBM T4A 100 Nm torque transducer
4. FC 091 selection box
5. Frequency read-out
6. Proximity switch

The torque transducer was installed in line with the motor shaft, between the fan motor and the fan rotor (see Figure D11). This was one of the factors that inhibited the changing of fan motors according to the size motor needed because the torque transducer had to be fitted accurately to the front of the motor.

The equipment used to measure the fan noise was as follows (see Figure D12):

1. Bruël and Kjaer 2230 sound level meter
2. Rion NL-05 sound level meter
3. Sound measuring tube and extension cable for each sound level meter
4. PL 202 real-time Fast Fourier Transform analyzer

The calibration of all the instrumentation is described in Appendix E. The sound measuring tubes were manufactured according to the proportions required by the BS 848 part 2 (1985), with

allowance for the pre-amplifier at the end of the Rion sound level meters' extension cable. The extension cable for the Bruël and Kjaer sound level meter was manufactured from co-axial cable. As a result of the high impedance of this cable at certain frequencies, it was calibrated to take this effect into account (see Appendix E). The Rion extension cable was bought as a complete unit, including a pre-amplifier that prevented these high-impedance effects.

5.2. GENERAL TEST PROCEDURE FOR FAN TESTS

A number of fan tests had to be done to qualify the general application fan design for a range of fan configurations. The tests were performed in such a way that the essential characteristics, for example the point of stall or maximum pressure, of the specific configuration was portrayed. Five to eight readings were measured for a specific configuration at different flow settings, which made it possible to portray the behaviour of the fan series over as wide a range as possible.

The test facilities and test procedures were different for the various diameter fans tested and therefore a general description of the fan test procedure is given. Before a test was started the ambient pressure and temperature were measured. The pressure was measured in a passage just below the laboratory, while the temperature was measured in the laboratory using a thermostat. All the tests required speed control, speed measurement, volume flow rate control and volume flow rate measurement.

1. The motor speed was controlled by a frequency inverter. The required speed was set on the inverter in Hertz. The speed of the motor was not the actual speed because of losses occurring in the motor and therefore the measured data had to be corrected by using the fan scaling laws.
2. The actual motor speed was measured using a proximity switch which was activated by a switch activator. The activator was fitted on the motor shaft between the motor and the fan rotor. The motor speed was read on a frequency read-out which gave the shaft revolution speed in Hertz times six because the switch activator had six protrusions.
3. The volume flow rate was controlled by a throttle at the back of the test tunnel. The throttle was set by turning it on a threaded steel rod. The first throttle set point was the fully open position, giving a point as close as possible to the zero pressure line on the fan characteristics. Obtaining a point close to the zero pressure line proved to be difficult with

the larger fans because the system's resistance became high with the higher volume flow rates. In these cases the throttle was removed to measure at a lower pressure rise. After the set point was determined, the throttle was set at large intervals, becoming smaller as the outlet area decreased. The throttle was closed until audible fan stalling occurred, after which it was turned backwards a fixed number of turns and closed at small intervals (360° at a time) to determine the exact location of the stalling point. If no audible fan stalling occurred, the outlet area was decreased further at regular intervals until it was as close to zero as possible. The throttle was never completely closed (zero volume flow) as this would have damaged the fan motor. The lack of air flow over the fan motor, when the fan stalls or the throttle is completely closed down, will cause the fan motor to overheat.

4. The volume flow rate was measured at the conical inlet. It was measured using four static pressure taps equally spaced around the inlet. The pressure was measured using the pressure transducer. The specific pressure taps were selected through channel one on the selection box and the milliVolt reading was read on the bridge amplifier. The reading was converted to millimeter water using the calibration values, which was finally converted to Pascal. This value was then used in the equation specified by the BS 848 Standards to calculate the volume flow through the tunnel.

5. The accuracy of the measurements was determined with the help of the project by Van der Spuy (1994). During this project the test facility was calibrated by comparing the test results with the values from a known fan characteristic. On average the noise readings were accurate within 3.98 dB, the total efficiencies within 4.5% and the fan static pressures within 18.04 Pa.

5.2.1. TEST PROCEDURE FOR MEASURING FAN PERFORMANCE

These measurements included the static pressure measurements on both sides of the fan and the shaft torque measurement between the fan motor and the fan rotor.

1. The torque reading was measured using the torque transducer. The torque transducer gave the torque readings in milliVolts which was read on the second channel of the bridge amplifier. The readings were converted to Newton-meter values using the calibration values.
2. The pressure readings were measured in the same way as the volume flow readings. The pressure reading in front of the fan was read using channel two on the selection box and the reading behind the fan was read using channel three on the selection box. The pressure readings were converted to Pascal using the same procedure as before. After each set of pressure readings, including the volume flow readings, a reading was taken with the one end of the pressure transducer open to the atmosphere to determine whether any variation in the pressure transducer readings has occurred. If a variation occurred, it was subtracted from the pressure readings as a constant offset value.

5.2.2. TEST PROCEDURE FOR MEASURING FAN NOISE

The BS 848 part 2 (1985) Standards prescribe noise measurements to be taken in one third octave bands. These values are then used to calculate the octave band noise levels. It was decided to measure the fan noise in octave bands to save time, which reduced the number of readings for one noise level from twenty four to eight. The octave band display on the FFT-analyzer was used to distribute the noise signal into its frequency bands. Only one channel on the FFT-analyzer was used and the readings were read from 64 Hz to 8000 Hz.

The two sound measuring tubes with their extension cables were installed in the ducting at specified distances on both sides of the fan. The Standards prescribe that three measurements must be taken at 120° intervals around the ducting at the specified distances. It was decided to take only one measurement at the same location each time, using the tests of Van der Spuy (1994) as a guideline. There were two sound level meters available. The one meter was used for measurements in front of the fan and the other for measurements behind the fan. The Bruël and Kjaër meter was used in front of the fan and the Rion meter behind the fan. The sound level meters were switched on alternately

and the signal relayed to the FFT-analyzer via an electrical cable. After the signal was read, the cable was transferred to the other sound level meter to take the other reading.

5.3. PROCESSING OF FAN TEST DATA

The processing of the test data was done according to the equations prescribed by the BS 848 Standards part 1 (1980) and 2 (1985). Sample calculations for the data processing is given in Appendix F. A spreadsheet was set up for the data of one fan configuration. The spreadsheet made provision for the data from the tests done for the different fan blade angles. The data was then plotted into a graph from which the fan characteristics were obtained.

The speed of revolution of the fan was obtained from the frequency read-out as follows:

$$\text{rpm} = f_{ro} \times 10 \qquad (5.1)$$

In order to determine the volume flow rate, the pressure drop across the conical inlet had to be calculated:

$$\Delta p = \rho_{water} \times g \times |h_{vf}| \qquad (5.2)$$

where

h_{vf} = static pressure in millimeters water, obtained using the calibration values

This gave the volume flow rate:

$$Q = \left(\frac{1}{\rho_{atm}}\right) \times \alpha\varepsilon \times \left(\frac{\pi \times d_i^{\,2}}{4}\right) \times \sqrt{2 \times \rho_{atm} \times \Delta p} \qquad (5.3)$$

The value for air density in equation (5.3) was obtained from the values measured for ambient pressure and temperature. The value for $\alpha\varepsilon$ in equation (5.3) was determined by the Standards as:

$$\alpha\varepsilon = 1 - 0.5 \times Re_d^{-0.2} \qquad \text{for } 20000 < Re_d < 300000$$

$$= 0.96 \qquad \text{for } Re_d \geq 300000$$

5.3.1. PROCESSING OF FAN PERFORMANCE DATA

The static pressures that were measured at specified distances on either sides of the fan were used to obtain the total pressures just in front of and behind the fan. The pressure values were calculated using the equations prescribed by the Standards that assumed certain values for the pressure loss between the pressure measuring points and the points just in front of and behind the fan. If we assume point 3 to be the measuring point in front of the fan and point 4 to be the measuring point behind the fan, while point 1 is the point just in front of the fan and point 2 the point just behind the fan, we can use the equations as they are prescribed:

$$p_{t1} = \left(\rho_3 \times g \times h_{p3}\right) + \left[1 - \left(A_3/A_1\right)^2 \times \xi_{31}\right] \times \left(\frac{1}{2} \times \rho_3 \times V_3^{\,2}\right) \tag{5.4}$$

$$p_{t2} = \left(\rho_4 \times g \times h_{p4}\right) + \left[1 + \xi_{24}\right] \times \left(\frac{1}{2} \times \rho_4 \times V_4^{\,2}\right) \tag{5.5}$$

The values for ξ_{31}, ξ_{24}, ρ_3 and ρ_4 were calculated using the equations prescribed by the Standards. Using equations (5.4) and (5.5) the pressure characteristics of the fan were obtained:

$$p_{tf} = p_{t1} - p_{t2} \tag{5.6}$$

$$p_{df} = \frac{1}{2} \times \rho_4 \times V_4^{\,2} \tag{5.7}$$

$$p_{sf} = p_{tf} - p_{df} \tag{5.8}$$

The values for fan shaft torque and speed of revolution were used to calculate the power that was transferred from the fan motor to the fan rotor. The fan shaft torque was calculated by multiplying the measured voltage with the calibration value. The fan speed of revolution was calculated as explained in Section 5.3 and transformed from revolutions per minute to radians per second. The shaft power was calculated as follows:

$$P_s = T \times \Omega \tag{5.9}$$

In order for the different fans to be compared, the results had to be represented at the same density and revolution speed. A density of 1.2 kg/m^3 was used as the reference density, while the frequency inverter input speed used for each test was used as reference speed. The pressure, volume flow and

power values that were calculated were adjusted for the speed and density variation between the readings, using the fan scaling laws, as follows:

$$Q_2 = Q_1 \times \left(\frac{rpm_2}{rpm_1}\right) \times \left(\frac{D_{f2}}{D_{f1}}\right)^3 \tag{5.10}$$

$$p_2 = p_1 \times \left(\frac{rpm_2}{rpm_1}\right)^2 \times \left(\frac{\rho_{atm\,2}}{\rho_{atm\,1}}\right) \times \left(\frac{D_{f2}}{D_{f1}}\right)^2 \tag{5.11}$$

$$P_2 = P_1 \times \left(\frac{rpm_2}{rpm_1}\right)^3 \times \left(\frac{\rho_{atm\,2}}{\rho_{atm\,1}}\right) \times \left(\frac{D_{f2}}{D_{f1}}\right)^5 \tag{5.12}$$

We can calculate the values for fan efficiency by using the value for shaft power and calculating the power leaving the fan rotor as volume flow times pressure. The equations are prescribed by the Standards.

$$\eta_s = \frac{Q \times p_{sf}}{P_s} \tag{5.13}$$

$$\eta_t = \frac{Q \times p_{tf}}{P_s} \tag{5.14}$$

5.3.2. PROCESSING OF FAN NOISE DATA

As described in Section 5.2.2, the fan noise was measured at two different locations using two different sound level meters. Two different sets of calibration values had to be used. The calibration of the sound level meters and the calculation of the sound pressure levels for the various measurements are described in Appendix E and F respectively. Once the sound pressure levels in the various frequency bands have been obtained, they had to be corrected using the correction values as prescribed by the Standards. The set of corrections used in the calculations is described in Appendix F.

$$Lp_c = Lp_f + C_1 + C_2 + C_3 + C_4 + C_5 \tag{5.15}$$

The correction values vary for the different frequency bands as well as for the air velocity through the tunnel.

Using the values for corrected sound pressure level in front of and behind the fan, a single sound pressure level for a specific octave band was calculated:

$$Lp = 10 \times \log\left[\frac{1}{2} \times \left(10^{Lp_{c3}\ 10} + 10^{Lp_{c4}\ 10}\right)\right] \qquad (5.16)$$

This equation uses the octave band values instead of one-third octave band values as prescribed by the Standards because only the octave band values were measured.

6. DISCUSSION

Only the main results will be discussed due to the large number of fan tests that were peformed. Some of the test results will be mentioned and illustrated in this chapter. These include the results for a fan speed of 1440 rpm for the 483 mm, 630mm and 800 mm diameter fans, results for the low-noise fan as well as other results needed for comparison. A brief discussion will also be given on the test procedures followed.

6.1. TEST PROCEDURE

The method of testing was effective and time efficient, although a lot of writing by hand was required due to the large number of tests that had to be done. The volume flow readings were insensitive to a small change in the throttle position when the throttle was close to its maximum open position. At the high pressure configurations, for example 630/250/14/1440 and 800/250/14/1440, the system resistance of the test facility, with the throttle at maximum open, was too high for the fan to reach its maximum volume flow (zero static pressure over fan). It was impossible to close the throttle to such an extent that zero volume flow was obtained through the system for the smaller blade angles because the throttle did not close down the duct completely. For the larger blade angles the throttle was only closed untill stall occurred, as explained in Section 5.2.

The pressure reading in front of the fan, p_{s3}, was the most stable of all the pressure readings at the different locations. The pressure reading behind the fan, p_{s4}, fluctuated the most of all the pressure readings. The effect worsened as the blade angles increased, which indicates the existence of vortex or circumferential flow in the ducting. With the fan blades set at large blade angles, it tended to stall easier, leading to bigger velocity fluctuations in the ducting. The pressure readings behind the fan were stabilised by inserting a damper in the pressure tube line. The damper is similar to a settling chamber, with the pressure tube connected on either side of it.

The effect of the pressure fluctuations became less with a flow straightener installed in the test ducting (see Section 5.1). The flow straightener removed a considerable amount of the velocity fluctuations that were caused by an uneven velocity distribution in the ducting. It also caused a lower pressure reading behind the fan, while the remainder of the readings were the same as those

without the flow straightener. The lower pressure reading behind the fan gave a lower fan static pressure rise with the flow straightener for the same volume flow as the set-up without the flow straightener (see Figure 5.4). The efficiency values were also lower with the flow straightener than without the flow straightener (see Figure 5.5). Following consultation with Howden Air Industries regarding the general application fan tests, it was decided to use the test set-up without the flow straightener because the fans were intended for use with downstream ducting. It was also stipulated in the catalogue that the fans were tested without the flow straightener. The decision was also influenced by the reasons mentioned in Section 5.1.

The torque readings fluctuated for a while after the motor was switched on. The fluctuations was due to the warming of the bearings on which the rotor shaft was running. The bearings caused some torque in the shaft which decreased as the bearings warmed up. The residual torque was very low and therefore it was ignored during the fan tests. The fan speed readings were taken without fluctuations occurring on the frequency read-out.

The noise data on the FFT-analyzer gave very good readings, although it was very sensitive for saturation. The saturation occurred during very low or high readings. The FFT-analyzer tended to saturate below 0.1 % of its maximum value and above 60 % of its maximum value. The upper level of saturation only became apparent after a series of calibration tests with the sound level meters were performed. The FFT-analyzer worked on an averaging basis and therefore the more time allowed for the readings to stabilise, the better the readings. The noise readings were also sensitive to the condition of the surroundings, for example two readings for the same fan characteristics taken two weeks apart can differ. Keeping this in mind, an overall repeatability of less than 2 dB difference between readings can be considered as good.

Following the recommendations of Van der Spuy (1994) a lot of progress was made towards the implementation of a standard test apparatus set-up for fan testing, with the acquisition of a second sound level meter by the University of Stellenbosch. This enabled the simultaneous measurement of fan noise on both sides of the fan. The noise readings in front of the fan must also be brought up to standard by using a standard Bruël and Kjaer extension cable to connect the microphone to the sound level meter. The impedance in the self-made cable was so high that it complicated matters by necessitating the calibration of the cable itself. Once all the necessary test apparatus has been

acquired, the next step in updating the system will be to write a data collection computer program for the different data items. The program, used in conjunction with a data card, must also act as an averaging function to enable the collection of data over a fixed period. This will prevent the uncertainties associated with fluctuating readings, as experienced with the pressure readings behind the fan. The computer program must also make provision for a noise data input from the FFT-analyser.

6.2. GENERAL FAN DESIGN

With the help of the fan tests the following influences on fan behaviour were investigated, namely fan diameter, hub diameter, fan speed, fan solidity and fan blade setting angle. These effects were compared using static pressure, volume flow, total efficiency and fan noise. The total efficiencies were plotted because it included the effects of the fan shaft power and the fan dynamic pressure.

6.2.1. FAN DIAMETER

To investigate the effect of fan diameter on fan behaviour the 483/150/10/1440, 630/150/10/1440 and 800/150/10/1440 fan configurations were used (see Figures 6.3, 6.4, 6.11, 6.12, 6.21 and 6.22). The fans are compared using the graphs at a specific blade setting angle of 25°. The comparison is shown in Table 6.1.

Table 6.1: Summary of fan performance for different fan diameters at 25° blade angle

Configuration	p_{sf} max. [Pa]	Q max. [m^3/s]	η_t max. [%]
483/150/10/1440	160	2.5	72
630/150/10/1440	250	4.5	80
800/150/10/1440	410	8.25	78

The effect of the fan noise is evaluated when looking at the noise data of the 483/150/10/1440 and 630/150/10/1440 fans at a 25 ° blade setting angle (see Figures 6.27 and 6.29 and Tables 6.13 and 6.15) as summarised in Table 6.2.

Table 6.2: Summary of fan noise for different fan diameters at 25° blade angle

Configuration	SPL max. [dB]	SPL min. [dB]
483/150/10/1440	86	77
630/150/10/1440	87	79

Evaluating the general appearance of the data for the different fan diameters with respect to the configurations mentioned (Figures 6.3, 6.4, 6.11, 6.12, 6.21, 6.22, 6.27 and 6.29), it is clear that the form of the performance graphs is the same. The performance of the small blade angles (5° and 15°) decreased as the fan diameter increased. The decrease in performance of the smaller blade angles can be attributed to the large twist in the blade. The large fan diameters' angle of incidence at the blade tip for the small blade setting angles become very small and might even become negative if the blade setting is not done accurately. A small angle of incidence at the blade tip leads to a decrease in performance because that part of the blade does virtually no work and most of the work are done by the hub section of the blade.

There was a marked increase in the relative stalling capacity of the medium blade angle (25°), while it decreased relative to that of the medium blade angle for the larger blade angles (35° and 45°). The increase in stalling capacity of the medium blade angles is as expected, due to the increase in the working area of the blade. The increase in stalling capacity can also be attributed to the same effect found at the smaller blade angles. Although the angle of attack at the hub section of the blade is large and stalling occurs here, the tip of the blade is still doing work on the air, due to the blade twist creating a favourable angle of attack . The effect is more significant for the larger diameter fans because the fan blades are longer and more twist occurs, hence the increase in stalling capacity. The relative decrease in stalling capacity of the larger blade angles can be explained by the larger tip solidity of the smaller diameter fan due to its smaller diameter. The cascade effect, where interference occurs between the blades that can delay the onset of stall, is more prominent for a

larger part of the blade. Due to the high blade setting angle, the effect of the blade twist creating a favourable angle of attack at the blade tip is less than the cascade effect.

The form of the efficiency graphs also change as the fan diameter increases. The efficiency curves of the different blade angles become flatter as the fan diameter increases. Looking at the total efficiency values, it seems that a specific fan diameter utilises the blade design better than the other fan diameters, as illustrated by the total efficiencies being a maximum for the 630 mm diameter fan. The occurrence is due to the variation in the blade properties along the blade length. The average value of a blade property for a blade length (assuming the blade setting angle is the same for different diameters) varies according to the blade length, which varies according to the fan diameter. The values for total efficiency for the different blade angles tend to vary more with decreasing fan diameter. The increase in variation is due to the smaller diameter fan (483 mm) utilising the part of the fan blade that is close to the fan hub where, according to the blade design, there is a lot of variation in the blade properties along the blade length. The variation in blade properties makes the rotor very sensitive to a change in the blade setting angle - leading to a definite optimum blade setting angle for the smaller diameter fan. The larger diameter fans have a larger blade length where the properties vary less over the length of the blade, making the rotor less sensitive to a change in blade setting angle. The stabilising of the efficiency values with an increase in fan diameter is true for all the blade angles, excluding the 5° blade angle where the efficiency suddenly decreases for the diameter increase from 630 mm to 800 mm. This decrease in efficiency has already been discussed in the previous paragraph and is attributed to the angle of attack at the blade tip becoming very small or even negative.

The effect of fan diameter on fan performance can also be evaluated using the fan laws (see equations (5.10) to (5.12)). The fan laws were used to scale the static pressure and efficiency data of the 483/150/10/1440 fan to 630 mm and compare it with the 630/150/10/1440 fan. The comparisons are shown in Figure 6.38 and 6.39. The major trends on the graphs are discussed in this paragraph because a more detailed discussion on the effect of fan diameter on fan performance was already given in the previous two paragraphs. The fan laws are not valid for different diameter fans of the same blade design. The fan hub diameter and blade dimensions could not be scaled because both fan configurations used the same hub diameter, while the blades were cropped to fit the different fan diameter sizes. The graphs illustrate that the different lengths of fan blades will have a different

average angle of attack which leads to the different fan diameters not corresponding to one another for the volume flow values when scaled. The fan static pressure values indicate that the different blades have a higher or lower average angle of attack, leading to a higher or lower stall point. The efficiency values indicate that certain blade property distributions, determined by blade length and blade setting angle, will be more efficient than others.

In order to analyse the fan noise, the findings of Wright (1976) concerning the sources of fan noise must be recaptured. He considered three basic noise sources:

1. Rotor self-noise - the turbulent and laminar vortex shedding at the blade rear sections and at the blade tip.
2. Turbulence in the main air flow - caused by fan supports or any upstream obstruction, causing fluctuating loads on the fan blade.
3. Discrete peaks of sound pressure - associated with blade passing frequency which is a product of the fan rotation frequency and number of blades.

The discrete spectra decay in a ducted fan set-up and therefore this noise source can be ignored (Tyler et. al, 1962). The rotor self-noise, or broad band noise, consists of a laminar and a turbulent noise. Of these two the turbulent noise is the most common. If the fan tip Reynolds number is between 10^5 and 10^6, laminar noise can also occur at a frequency ten times higher than the centre frequency of the turbulent noise. To compare the fan noise data for the different configurations, equations (2.16), (2.17) and (2.18) were used:

$$SPL = 10 \times \log\left(3 \times \rho_{atm} \times a_0 \times E/8 \times \pi \times z^2 \times p_{ref}^2\right)$$

where

$$E = \left(\pi \times \rho_{atm} \times n_b \times D_f \times U_0^6/16800 \times a_0^3\right) \times d_f$$

and

$$d_f = d_t + \left(0.37 \times c/4\right) \times Re_c^{-0.2}$$

The test facility used by Fukano et al. (1977) to derive the equations, differed from the one used for this project and therefore the difference in sound values due to the different configurations and not the exact sound values were compared using the above equations. The following values were assumed to stay constant for the different test configurations, namely ρ_{atm}, a_0, z and p_{ref}.

The difference in sound pressure levels due to the different configurations could be investigated using:

$$\begin{aligned} SPL_1 - SPL_2 &= 10\log(K \times F_1) - 10\log(K \times F_2) \\ &= 10\log F_1 - 10\log F_2 \\ &= 10\log\left(\frac{F_1}{F_2}\right) \end{aligned} \tag{6.1}$$

where

$$F = n_b \times D_f \times U_o^6 \times d_f \tag{6.2}$$

For equation (2.18) the following values were assumed:

$c = 0.08$ m

$d_t = 0.001$ m

$\rho = 1.2$ kg/m^3

$\mu = 1.8 \times 10^{-5}$ Ns/m^2

Using the constants, equation (2.18) was simplified to:

$$d_f = 0.001 + (0.37 \times 0.08/4) \times \left(\frac{1.2 \times \left(\frac{Q \cos\beta_1}{\pi \times \frac{D_f^2}{4}} \right)}{1.8 \times 10^{-5}} \right)^{-0.2}$$

$$= 0.001 + 0.0074 \times \left(\frac{84882.6 \times Q \cos\beta_1}{D_f^2} \right)^{-0.2}$$

The Reynolds number used in the equation is based on the relative inlet velocity and therefore the volume flow is divided by the value for the relative flow angle at a blade setting angle of 25°. The relative flow angle was determined as the angle at the mean radius for that specific fan diameter. For the 483 mm diameter fan it was taken as 40° and for the 630 mm diameter fan it was taken as 43°. The values calculated using equation (6.1) were compared with the total sound pressure values

measured during the testing of the fans. The values were obtained using the methods prescribed by the BS 848 Standards part 2 (1985) as a guideline. The volume flow used in equation (6.1) was the average volume flow over the range across which the sound pressure levels were measured. The different comparisons between the equations of Fukano et al. (1977) and the test data are discussed in this chapter.

In contrast to the performance graphs where the form of the graphs stay more or less the same, the form of the noise graphs differ considerably between the 483/150/10/1440 and 630/150/10/1440 fan configurations. The higher noise values of the 630 mm diameter fan can be attributed to the fan's higher blade tip speeds. The variance in the noise data between the different blade angles is larger for the 483 mm diameter fan than for the 630 mm diameter fan. The large variance for the small diameter fan is due to the relative large change in average blade properties with a change in blade setting angle. The small diameter fans utilise that part of the fan blade where the blade properties vary extensively as the blade length increases.

The 483 mm diameter fan shows a general low noise level for the 63 Hz, 125 Hz and 250 Hz octave bands compared to the 630 mm diameter fan. The noise level of the 483 mm diameter fan decreases at 500 Hz with a sudden rise at 1000 Hz which gradually decreases to 8000 Hz. The 630 mm diameter fan's noise characteristics also indicate a drop in noise level at 500 Hz, which increases again at 1000 Hz and decreases again at 2000 Hz from where it rises steadily to 8000 Hz. The high peak at the 8000 Hz frequency was observed with all the 630 mm diameter fans, but not with the 483 mm diameter fans. The high peak might be a result of the high tip speed of the 630 mm diameter fan causing occurrence of laminar noise at the higher frequencies. The occurrence of laminar noise explains the difference in form between the 483 mm fan noise, which has only one distinct peak frequency due to turbulent noise and the 630 mm fan noise, where two peaks occur - the one due to turbulent noise and the other due to laminar noise.

Investigating the effect of fan diameter on sound pressure level using equation (6.1) with the 483/150/1440 and 630/150/1440 fans, the results were:

$$SPL_1 - SPL_2 = 10\log\left(\frac{F_1}{F_2}\right)$$

$$= 10\log\left(\frac{0.630 \times 0.630^6 \times \left(0.001 + 0.0074 \times \left(\frac{84882.6 \times \frac{3.597}{\cos 43}}{0.630^2}\right)^{-0.2}\right)}{0.483 \times 0.483^6 \times \left(0.001 + 0.0074 \times \left(\frac{84882.6 \times \frac{2.274}{\cos 40}}{0.483^2}\right)^{-0.2}\right)}\right)$$

$$= 8.085 \text{ dB}$$

The above value does not compare favourably to the effect measured as:

$$SPL_1 - SPL_2 = 93.738 - 92.900$$

$$= 0.834 \text{ dB}$$

The effect of the blade tip velocity is overestimated as illustrated by the large difference between the measured and theoretical values.

6.2.2. FAN SOLIDITY

When the effect of the change in hub diameter on a fan's performance is compared, it must also incorporate the change in blade number in this comparison because the different hub diameters use different numbers of fan blades. The fan solidity is an indication of the area of the fan diameter covered by the fan blade area. Observing the change in solidity, calculated according to equation (4.23), for the 630/150/5/1440, 630/150/10/1440, 630/250/7/1440 and 630/250/14/1440 fans at their outer radius and comparing the maximum static pressures, maximum volume flows, maximum total efficiency, minimum sound pressure levels and maximum sound pressure levels for a blade angle of 25°, the data is summarised in Tables 6.3 and 6.4 (see also Figures 6.9 to 6.16 and 6.28 to 6.31 and Tables 6.14 to 6.17).

Table 6.3: Summary of fan performance for different blade solidities at 25° blade angle

configuration	solidity	p_{sf} max. [Pa]	Q max. [m^3/s]	η_t max. [%]
630/150/5/1440	0.182	200	4	81
630/250/7/1440	0.255	220	4.3	80
630/150/10/1440	0.365	330	4.5	80
630/250/14/1440	0.510	350	4.75	74

Table 6.4: Summary of fan noise for different blade solidities at 25° blade angle

Configuration	SPL max. [dB]	SPL min. [dB]
630/150/5/1440	84	77
630/250/7/1440	90	80
630/150/10/1440	87	79
630/250/14/1440	86	78

Looking at the graphs as a whole, the stalling limits of all the larger blade angles improve with solidity. The improvement in stalling limits is due to the increased interaction (cascade effect) between the blades because the distance between consecutive blades decrease with solidity. The pressure limit of the smaller blade angles also increase with solidity. The maximum volume flow of the larger blade angles increase with solidity, while that of the 5° blade angle tend to stay almost constant (it decreases when going from the seven-bladed to ten-bladed fan). The increase in volume flow and pressure limit with solidity can be attributed to the larger total blade area creating a larger working surface. The decrease in volume flow at the 5° blade angle can be attributed to the closing of the air passage around the blade shaft area by the higher solidity fans. The effect is reduced with this specific blade design because of the small design stagger angles close to the blade root. At low solidities for example the five bladed fan, the blade interaction between the blades does not occur

and stall occurs more readily due to the small stagger angles. There is a definite trend in the appearance of the graphs as the solidity increases, although the difference between the 630/150/10/1440 and 630/250/7/1440 fans were very small. The larger hub diameter fan has a better stall limit for the 45° blade angle than the 150 mm hub diameter fan. The higher stall limit is due to the delay in back flow at the hub, caused by the higher hub to tip ratio (see Von Backström et al., 1996).

All the efficiency graphs show flat efficiency lines for the medium blade angles (25° and 35°). The gradient of the efficiency lines of the smaller blade angles tends to become larger as the solidity increases, while the maximum efficiency value decreases. The increase in gradient is due to the closing of the air passage by the fan blades at the small blade setting angles. The effect becomes more drastic as the solidity increases. The efficiency values for the large blade angle (45°) increase as the solidity increases. As mentioned earlier, the cascade effect which delays the onset of stall, increases with fan solidity which in turn increases the efficiency of the large blade angle by increasing its maximum static pressure rise.

The form of the noise data for the fans of different solidities tend to be very similar. The form of the noise data constitutes an almost constant sound pressure level at the low frequencies (63 Hz, 125 Hz and 250 Hz) with a sudden drop at 500 Hz, an increase at 1000 Hz and another drop at 2000 Hz, followed by a steady increase up untill 8000 Hz. The effect of a change in blade solidity on fan noise is an increase in the discrete rotor noise of the fan. The frequency of this rotor noise is determined by the product of the blade number and the rotor speed. The noise curves for the different fan solidities are almost identical due to the exponential decay of this type of noise before it reaches the microphone. The slight rise in fan noise that occurs can be attributed to the increase in noise sources due to the increase in fan blade area because of the higher solidity. The only exeption is the 45° blade angle noise data for the five-bladed fan. It shows a gradual decrease up untill 2000 Hz, followed by a steady rise in fan noise up untill 8000 Hz. The shape of the noise data can be explained by the five-bladed fans' low resistance to stall. These effects were present during testing of the five-bladed fan because of its susceptibility to stall, although the other fans' noise data does not include fan stall effects.

To investigate the effect of blade number on sound pressure level, the 630/150/5/1440 and 630/150/10/1440 fans were used. Using equation (6.1) the results were as follows:

$$SPL_1 - SPL_2 = 10\log\left(\frac{F_1}{F_2}\right)$$

$$= 10\log\left(\frac{10 \times \left(0.001 + 0.0074 \times \left(\frac{84882.6 \times \frac{3.597}{\cos 43}}{0.630^2}\right)^{-0.2}\right)}{5 \times \left(0.001 + 0.0074 \times \left(\frac{84882.6 \times \frac{3.458}{\cos 43}}{0.483^2}\right)^{-0.2}\right)}\right)$$

$$= 3.141\,\text{dB}$$

The measured effect was:

$$SPL_1 - SPL_2 = 93.738 - 91.033$$

$$= 2.705\,\text{dB}$$

The effect of the change in blade number from ten to five blades is closely reflected by the theoretical value. A difference of less than half a decibel would not be audible.

6.2.3. BLADE SETTING ANGLE

The effect of a change in blade angle on fan performance and noise can be investigated by looking at the 630/250/14/1440 fan (see Figure 6.15, 6.16, 6.31 and Table 6.17). A summary of the figures is given in Table 6.5 and 6.6. The equation by Fukano et al. (1977) does not provide for a variation in blade setting angle and therefore no comparison on the difference in sound pressure values was sought between the measured and theoretical values.

Table 6.5: Summary of fan performance for different blade angles

Blade Angle [°]	p_{sf} max. [Pa]	Q max. [m^3/s]	η_t max. [%]
5	300	1.8	62
15	400	3.4	74
25	350	4.75	74
35	320	5.6	74
45	320	6.2	71

Table 6.6: Summary of fan noise for different blade angles

Blade Angle [°]	SPL max. [dB]	SPL min. [dB]
5	87.5	79
15	86	80
25	86	79
35	88	78
45	91	80

The general form of the graphs is analysed by looking at the different pressure lines. The pressure limit increases from the 5° to the 15° blade angle. No stalling limit was detected with these blades. It is possible that the stalling limit for these blades was at such a small volume flow that it was not possible to detect. Another explanation is possible when looking at the 25° blade profile. The 25° blade shows a flat profile at the higher pressure values. The pressure does not drop after reaching the stall point, but continues to increase. At some configurations it even decreased before increasing again. The effect at the smaller blade angles might be similar but more drastic due to the smaller blade angle. The increase in static pressure following directly after the stalling point made it impossible to detect. The stalling limit decreases from the 25° to the 45° blade angle. The decrease

in stalling limit is due to the decrease in average stagger angle as the blade setting angle increased, leading to a higher average angle of attack. The volume flow range of each blade angle setting increases with blade angle, although the increase decreases as the blade angle gets larger. The increase in volume flow is due to the increasing axial force vector on the air column with increasing blade setting angle.

The efficiency profiles of the 25°, 35° and 45° blade angles all have the same form, while the 5° and 15° profiles tend to have a sharp decreasing gradient with increasing volume flow. The sharp gradient indicates that the small blade angles are sensitive to a change in volume flow. The sensitivity is due to the closing up of the air passage by the small blade angles, as explained in Section 6.2.2. The medium blade angle (25°) has the highest maximum total efficiency compared to the other blade angles. The 25° blade angle was also the design angle and although the fan blade was designed for a diameter of 1000 mm, the change of diameter to 630 mm might have moved the optimum blade angle to 23°. The 25° blade setting will still indicate an optimum because the fans were measured in 10° intervals.

The noise data shows a similar pattern for all the blade angles, except for the 45° blade angle where the noise decreases from 250 Hz up untill 2000 Hz. The other blade angles showed that the noise data decreases from 250 Hz to 500 Hz, rises untill 1000 Hz and drops again untill 2000 Hz. The deviation is caused by the cross-over frequency where the 45° blade setting changes from the noisiest setting at 500 Hz, to the least noisiest setting at 1000 Hz. The rest of the graph shows a pattern of increasing noise up untill 250 Hz as well as from 2000 Hz to 8000 Hz. From 63 Hz to 500 Hz the noise from the 45° blade angle is the highest and that from the 15° blade angle the lowest. The form of the noise graphs of the large blade angles at the low frequencies can be attributed to a larger volume flow, creating more turbulent noise in the air stream.

From 500 Hz untill 4000 Hz the noise from the 5° blade angle is the highest and that from the 25° angle the lowest. The high noise level caused by the small blade angles at the high frequencies can be attributed to the closing of the air passage by the small blade setting angle at the high solidity which causes high turbulent broad band noise. The effect is also observed with the other high solidity fan configuration, 630/150/10/1440. The laminar noise is much less at the high frequency (8000 Hz) due to the high turbulent noise for the 5° blade angle. At 8000 Hz the noise from the 45° blade angle is

the highest and the noise from the 5° blade angle the lowest. The fact that the 25° blade angle setting made the least amount of noise, also proves that it is the optimum blade angle.

6.2.4. FAN SPEED

The next effect investigated was varying fan speed. Looking at the 25° blade angle on Figures 6.11, 6.12, 6.17, 6.18, 6.29 and 6.32 and Tables 6.15 and 6.18, the following comparisons can be made:

Table 6.7: Summary of fan performance for different fan speeds

Configuration	p_{sf} max. [Pa]	Q max. [m^3/s]	η_t max. [%]
630/150/10/960	127	3	78
630/150/10/1440	325	4.5	80

Table 6.8: Summary of fan noise for different fan speeds

Configuration	SPL max. [dB]	SPL min. [dB]
630/150/10/960	84	74
630/150/10/1440	87	79

The effect of fan speed on fan performance can be evaluated using the fan laws (see equations (5.10) to (5.12)). The general appearance of the pressure graphs is best illustrated by looking at Figure 6.40, where the pressure graph for the 960 rpm configuration has been transformed using the fan laws and is illustrated on the same graph as the 1440 rpm configuration. The graph illustrates the fact that the pressure and volume flow values for the fan design adheres to the fan laws, which is an indication of the repeatability of the pressure and volume flow results. A similar effect is obtained for the efficiency graphs, as illustrated in Figure 6.41, although not as convincing. The graphs for corresponding blade angles have the same form, but the values for the lower speed fan tend to be less than those for the higher speed fan. The values indicate that at some of the lower fan speeds a higher relative power consumption is needed to obtain satisfactory pressure and volume flow values.

A comparison of the general form of the noise graphs shows some small differences between them. The lower speed fan shows a noise characteristic which decreases untill 500 Hz. It rises untill it reaches 1000 Hz, falls untill 2000 Hz and rises again untill 8000 Hz. The higher speed fan shows a characteristic which rises untill 250 Hz, falls at 500 Hz, rises at 1000 Hz, falls at 2000 Hz and rises again untill 8000 Hz. As expected the higher speed fan has overall higher fan noise values.

To investigate the effect of fan speed on sound pressure level, the 630/150/10/1440 and 630/150/10/960 fans were used. Using equation (6.1) the results were as follows:

$$SPL_1 - SPL_2 = 10\log\left(\frac{F_1}{F_2}\right)$$

$$= 10\log\left(\frac{1440^6 \times \left(0.001 + 0.0074 \times \left(\frac{84882.6 \times \frac{3.597}{\cos 43}}{0.630^2}\right)^{-0.2}\right)}{960^6 \times \left(0.001 + 0.0074 \times \left(\frac{84882.6 \times \frac{2.365}{\cos 43}}{0.630^2}\right)^{-0.2}\right)}\right)$$

$$= 10.447 \text{ dB}$$

The measured effect was:

$$SPL_1 - SPL_2 = 93.738 - 89.792$$

$$= 3.946 \text{ dB}$$

There is a definite difference between the theoretical and measured effect of fan speed on the fan sound pressure level. As mentioned before, it seems as if the effect of fan speed on fan noise is overestimated by the equations. A probable cause might be that the equation was derived for a measuring point in the centre of the test ducting, 1.5 m in front of the fan, as mentioned by Fukano et al. (1977). The data used as a comparison was measured at locations in front of and behind the fan by using the BS 848 Standards part 2 (1985) as a guideline.

6.3. LOW-NOISE FAN

The low-noise fan was designed and tested at a set blade angle and therefore it had a fixed configuration which allowed for a speed variance only. If the different fan performance and noise values are compared at different speeds (see Figures 6.33 to 6.37 and Table 6.19 to 6.21), the results are as follows:

Table 6.9: Summary of fan performance for different fan speeds

Fan Speed [rpm]	p_{sf} max. [Pa]	Q max. [m^3/s]	η_t max. [%]
720	85	2.25	70
960	160	3.1	80
1200	270	3.9	79

Table 6.10: Summary of fan noise for different fan speeds

Fan Speed [rpm]	SPL max. [dB]	SPL min. [dB]
720	75	57
960	78	66
1200	85	73

When the general form of the graphs are compared by using the fan laws, it is obvious that the low-noise fan as well as the general application fan adheres to the fan laws for fan pressure and volume flow. This is illustrated in Figure 6.42 and Figure 6.43. Figure 6.37 shows that the efficiency graphs tend to differ for the different speeds because the 960 rpm and 1200 rpm fans have an efficiency of approximately 80%, while the 720 rpm fan has a total efficiency of approximately 70%.

The noise graphs of the low noise fan (see Table 6.19 to 6.21 and Figure 6.33 to 6.35) at the three different speeds also indicate the same general form, although the noise values themselves increase

with fan speed (see Section 6.2.4). Some differences exist between the noise graphs for the different speeds. The low-noise fan is the noisiest at the 63 Hz, 125 Hz and 8000 Hz frequencies, while it is the least noisy at 2000 Hz. The noise at 125 Hz tends to become relatively higher as the fan speed increases, while the noise in the mid-frequencies tends to flatten out as the speed increases. The noise curves all indicate very little turbulent broad band noise, while high laminar broad band noise occurs. The curves' form can be attributed to the overall smooth finish of the blade surface, a smaller relative angle of attack, a very definite leading and trailing edge radius, the small number of blades and the fan's forward sweep design. Another way of evaluating the low-noise fan performance is by comparing it with other fans, for example the general application fan and a comparative fan of known performance (see Section 4.1.1). The seven-bladed low-noise fan is compared to fourteen-bladed fans with narrower blades and with the same hub diameter because of the length of its blade chords.

When the low-noise fan performance at 1200 rpm, scaled to 1440 rpm, is compared to the 630/250/14/1440 general application fan's performance at a blade setting angle of 25°, the results are as follows (see Figures 6.40, 6.41, 6.15 and 6.16):

Table 6.11: Summary of fan performance for different fan types

Fan Type	p_{sf} max. [Pa]	Q max. [m^3/s]	η_t max. [%]
Low-noise/1440(scaled)	385	4.7	79
630/250/14/1440	350	4.6	75

In general, the low-noise fan's performance curves are much smoother than those of the general application fan curves. The smoother curves of the low-noise fan are due the larger blade chord values and stagger angles at the hub, which makes the fan performance less sensitive to a change in volume flow by delaying the onset of stall. The low-noise fan's stall limit as well as its total efficiency are also higher than the general application fan's, which can be attributed to a smaller design lift coefficient, leading to larger stagger angles, at the hub. The higher efficiency can also be attributed to the smoother finish of the low-noise fan surface as well as its better defined leading and trailing edge radii. When comparing the low-noise fan noise to the general application fan and

comparative fan, a new set of test results was used (see Table 6.19 to 6.21 and Figure 6.33 to 6.35) to minimise the time span between test data. The comparison is summarised in Table 6.12.

Table 6.12: Summary of fan noise for different fan types

	SPL (720 rpm) [dB]		SPL (960 rpm) [dB]		SPL (1200 rpm) [dB]	
	max.	min.	max.	min.	max.	min.
Low-noise	75	57	78	66	85	73
Comparative	78	65	80	71	85	77
General	72	61	77	70	85	76

The low-noise fan is the least noisy of the three fans, followed by the general application fan and the comparative fan. Comparing the noise curves of the low-noise fan with those of the other two fans shows that the low-noise fan creates much less turbulent noise than the general application fan. The less turbulent noise of the low-noise fan is due to its better stall resistance, better blade finish, smaller number of blades and forward sweep, as discussed previously. Another point of interest is the low noise level of the general application fan compared to the comparative fan. The general application fan has a much better surface finish than the comparative fan, while the leading and trailing edge radii are well defined. The general application fan, due to its large variation of blade properties along its blade length, adapts better to a change in blade setting angle than the comparative fan which has a more constant blade property distribution along its length. The comparative fan will have a narrower range of optimum blade angles where the noise levels are low, compared to the general application fan.

It is important to note that the reduction in fan noise for the low-noise fan was achieved together with an increase in fan stall limit and total efficiency. This supports the concept that a more efficient fan will generate less noise.

7. CONCLUSIONS AND RECOMMENDATIONS

In order to evaluate the merit of the project, a list of conclusions and recommendations with regard to fan performance, fan noise, test procedures and the design process are given. Due to the extent of the project, only the main points are mentioned in this chapter. The main influences on the project were as follows:

1. The thesis formed part of an external project for Howden Air Industries.
2. The use of the optimised velocity distribution as proposed by Von Backström et. al (1996) was an improvement on previous design processes where the authors mainly used the free vortex velocity distribution.
3. The work done by Bruneau (1994) in his thesis on the design of a single-rotor axial flow fan was a local project and served as a basis for this thesis. He also initiated the use of an optimised velocity profile, although the one he used was optimised for a specific type of equation.
4. The book by Wallis (1983) on the design and use of axial flow fans and systems is a complete collection of notes and data necessary for designing a fan but lacks information on the design of low-noise fans.
5. The article by Wright (1989), used to design the forward swept fan blade, was one of the few that gave exact values for forward swept blade design.
6. The use of the BS 848 Standards parts 1 (1980) and 2 (1985) as a guideline to test the fans, required a considerable amount of preparation of the test set-up.

7.1. TEST PROCEDURE

The fan tests were done using the BS 848 Standards part 1 (1980) and 2 (1985) as a guideline. Some aspects of the procedure need refining as explained earlier. The main aspects are as follows:

1. The use of a flow straightener behind the fan will remove the fluctuating pressure readings experienced during the tests.
2. The throttle must be altered to enable the closing of the air ducting closer to the occurrence of zero volume flow. This will enable the establishing of fan behaviour at very small volume flows.

3. Increasing the opening capability of the throttle will decrease the minimum possible system resistance obtainable for high volume flows.

4. If a proper microphone extension cable for the Bruël and Kjaer sound level meter can be obtained, the calibration of the cable itself will no longer be necessary.

5. Compiling a proper data logging system, as described in Section 6.1, will increase the efficiency of the data collecting process by increasing its accuracy as well as its sampling speed.

6. An auxiliary fan is needed to overcome the resistance of the test facility when testing large daimeter fans.

7.2. DESIGN PROCEDURE

The design procedure was similar to the one followed by Bruneau (1994). An overview of the design process is as follows:

1. The design process was time-efficient, simple and effective judged by the results obtained for both the general application fan and the low-noise fan.

2. The number of blades, as well as the blade chord lengths were chosen after calculating the hub diameters and comparing them and the design solidity with those of the comparative fan series. The optimised velocity profile, led to a high design lift coefficient and camber angle at the hub.

3. The maximum blade number per hub, ten and fourteen, limited the number of possible fan configurations (the fourteen-bladed hub can either have fourteen or seven fan blades). Numbers of eight and twelve might have been better, creating a wider variety of possible fan configurations. Eight and twelve blade numbers would also have led to a larger blade chord length to obtain a similar solidity for the twelve-bladed as for the fourteen-bladed fan. Following the design process, a smaller design lift coefficient and camber angle at the hub would have resulted.

4. The deviation angle value diverged when calculated for a low solidity blade. The equation for the deviation angle was derived for high solidity blades and therefore an alternative must be found to use with low solidity blades. A possible solution might be to calculate the deviation angle up to where it starts diverging and then assume that it is constant as the blade length increases.

5. The low-noise fan design was very empirical because the concept of blade sweep was entirely based on the results of Wright et al. (1989). An equation must be derived whereby the effect of blade sweep on, for instance blade lift coefficient can be quantified.

6. The strength calculations assumed the blade root to be the critical part of the blade. The assumption was proved valid after destructive tests performed by Howden Air Industries on the fan blades.

7.3. GENERAL APPLICATION FAN

The overall performance of the general application fan was very good. The characteristics of the fan can be summerized as follows:

1. The large amount of twist in the blade creates problems regarding negative incidence angles at the blade tip of the small blade setting angles for the large diameter fans.

2. The small stagger angles at the blade hub lead to a high angle of attack at the hub, which means that stall occurs readily for the large blade setting angles once the system resistance starts increasing.

3. The small stagger angles at the hub create a larger space for the air to move through at high solidities and small blade setting angles, which prevents the closing of the air passage found with a flatter blade design.

4. The large variation of properties along the blade length makes the blade design less sensitive to a change in blade setting angle, than for a flatter blade design.

5. The general application fan met the requirements set forth by Howden Air Industries mentioned in Chapter 1. The direct comparison of the maximum static pressures and volume flows obtainable from the results included in this thesis and the requirements for these values set forth by Howden Air Industries is not possible. A comparison was however made between the design point and the data for the 1000 mm fan in Figure 7.1. The design point was specified in Table 4.2 for the 1000 mm fan. As mentioned in Chapter 5 the 1000 mm fan was tested on a type A test facility, which means that the static pressure measured for the fan did not take any pressure recovery into account. The value for static pressure for the design point was calculated by working backwards from the value for static efficiency in Table 4.2. The static efficiency calculated in the table took all the kinetic losses into account and therefore the value obtained for static pressure in such a way can be compared directly to the

measured value. The design point is situated in the centre of the fan's range of performance with regard to both fan static pressure and volume flow. The position of the design point is an indication that the design process was successful because the values used in Section 4.1.1 to determine the design point was taken from the centre area of the comparative fan's range of performance.

6. The performance of the general application fan was also evaluated by comparing it with the corresponding values for a specific configuration of the comparative fan (see Figure 7.2 and 7.3). The comparative fan was used by Howden Air Industries to compile the list of requirements for the general application fan that was to be designed. The static pressure values for the two different fans are very similar, although the comparative fan seems to have a higher static pressure rise for certain blade angles than the general application fan. The general application fan has a wider range of operation regarding its minimum and maximum volume flow values. The general application fan performed as expected. When the total efficiency of the designed blade is compared to the comparative blade, the efficiency of the designed blade is definitely higher. The reason for the higher efficiency of the designed blade is the lower power consumption of the fan rotor. The lower power consumption is due to the optimised velocity profile that is calculated to minimise the losses in the fan.

7.4. LOW-NOISE FAN

The desig of a low-noise fan was a pioneering fan research programme at the University of Stellenbosch. Very little local information on the design of a low-noise fan was available. Information was gathered from articles written by various authors. Considerable time was spent on perfecting the manufacturing of the fan blades because they had such an intricate form. The aspects of the low-noise fan design that has to be emphasised are as follows:

1. The smaller design lift coefficient at the hub gives the low-noise fan a better stall resistance. The smaller lift coefficient at the hub is the result of the larger design solidity used for the fan. The solidity of the seven-bladed low-noise fan was based on the solidity of a fourteen-bladed general application fan.

2. The small number of blades, combined with the large chords prevented the closing of the air passage at the hub.

3. The forward sweep prevents the blade setting angle from being changed. Apart from interfering with the fan casing, another effect, namely fan dihedral, will occur. Dihedral means a blade angle in the axial direction of the fan.

4. The low comparative noise level of both the low noise and the general application fan can partially be ascribed to the use of the optimised velocity profile in both fans' design procedures because fan noise is also considered as a loss of energy in a fan. The fact that the low noise fan noise was lower than the general application fan noise was due to the unique design features of the low noise fan.

5. The forward sweep of the blade shortens the length of the boundary layer on the blade, reducing the source of turbulent noise.

6. The definite leading radius of the blade guides the air smoothly around the blade nose and prevents unnecessary early stall and turbulent noise.

7. The low-noise fan was a definite success because a higher fan total efficiency and static pressure rise were obtained for a lower noise value. The ideal would be to decrease the fan speed untill the same static pressure duty is obtained as for a comparative fan. A decrease in fan speed would reduce the noise even more because fan speed is the factor that has the biggest influence on fan noise. Unfortunately, very few fan motors are supplied with variable speed control and therefore fan speed can either be 2880, 1440, 960, or 720 rpm, depending on the type of motor. The forward sweep designed into the fan blade according to Wright (1989) definitely improves the noise characteristics op the fan, compared to the fourteen-bladed general application fan. The complexity of manufacturing the low-noise fan due to the forward sweep, makes it very expensive compared to the fourteen-bladed general application fan. The general application fan delivers a high static pressure rise for a relative low noise level. It would definitely be suggested that a method must be derived to find a way to numerically optimise the amount of sweep needed in a blade for an optimum noise level.

8. FIGURES

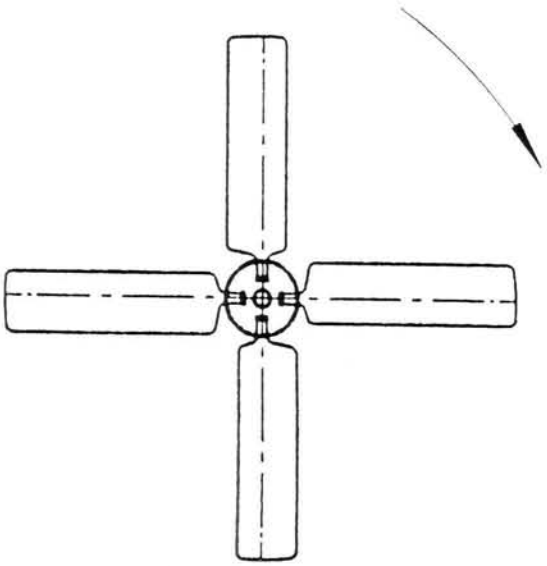

Figure 1.1: Classic axial flow fan (Van der Spek, 1994)

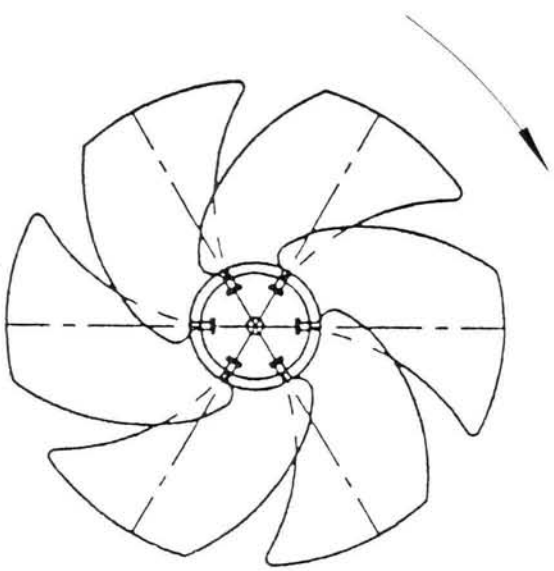

Figure 1.2: Super low-noise axial flow fan (Van der Spek, 1994)

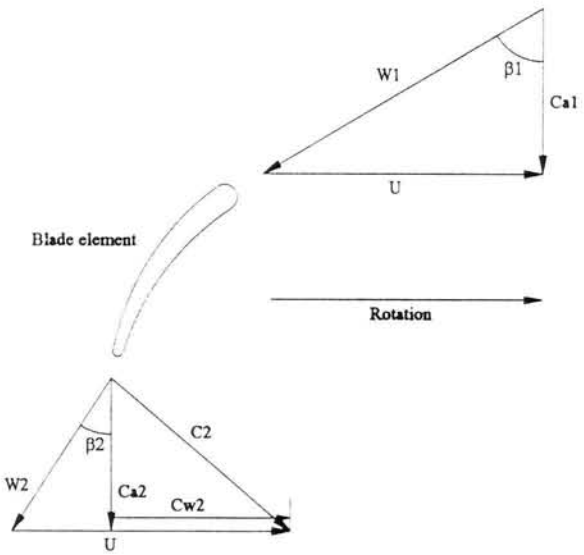

Figure 2.1: Velocity diagrams

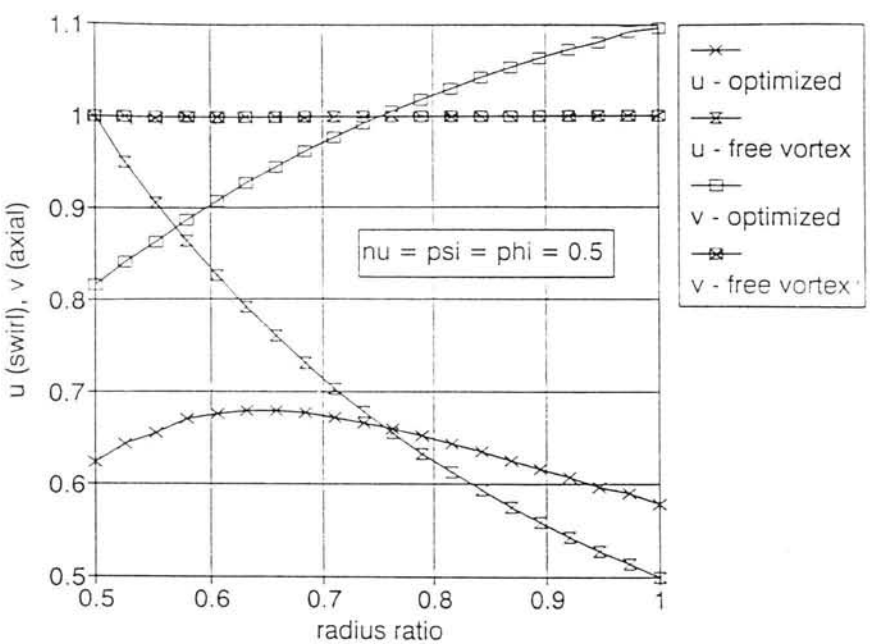

Figure 3.1: Example of optimised and free vortex velocity profiles for $\nu = \phi = \psi = 0.5$ (Von Backström et al. 1996)

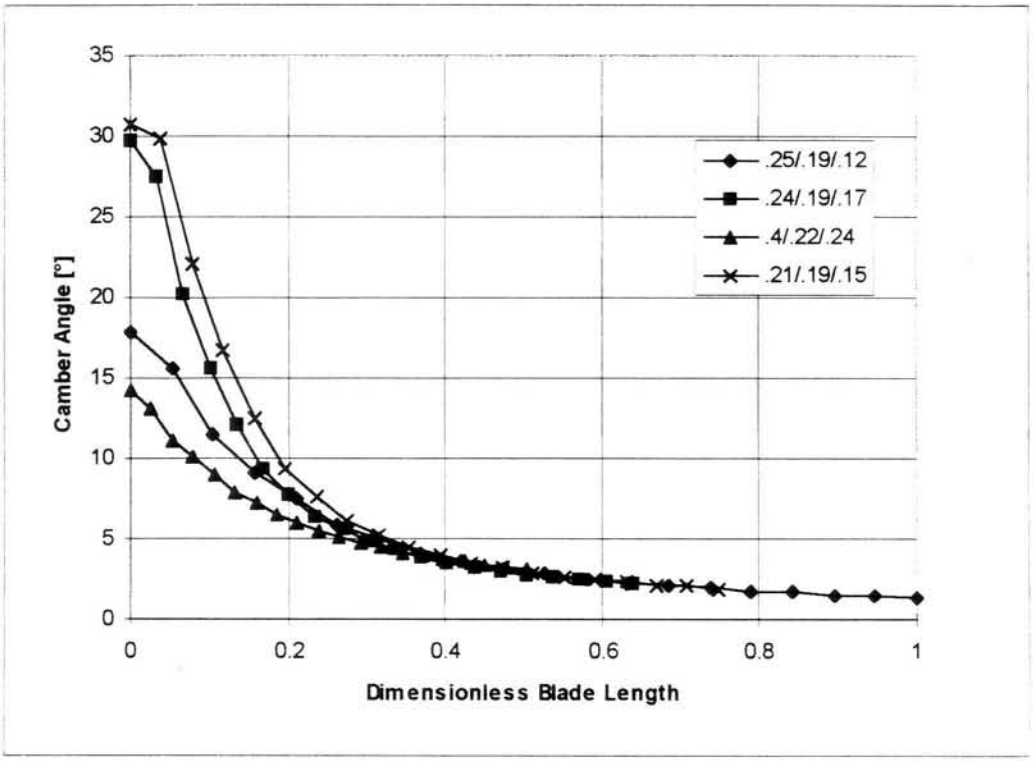

Figure 4.1a: Approximate blade camber for different configurations

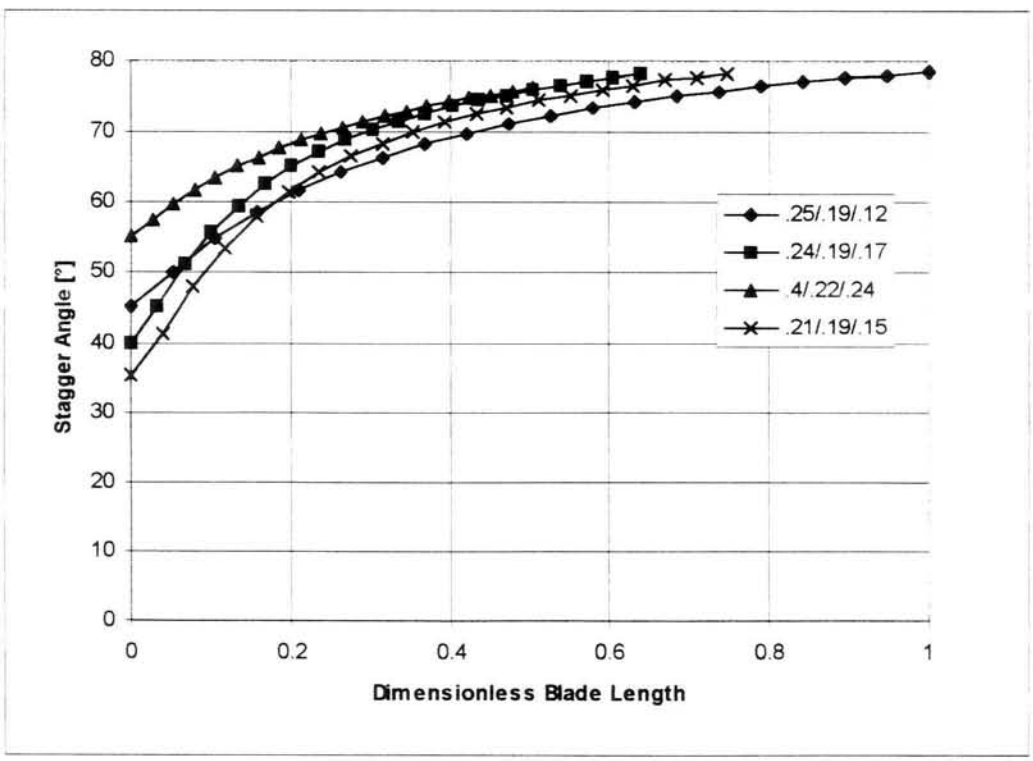

Figure 4.1b: Approximate blade stagger for different configurations

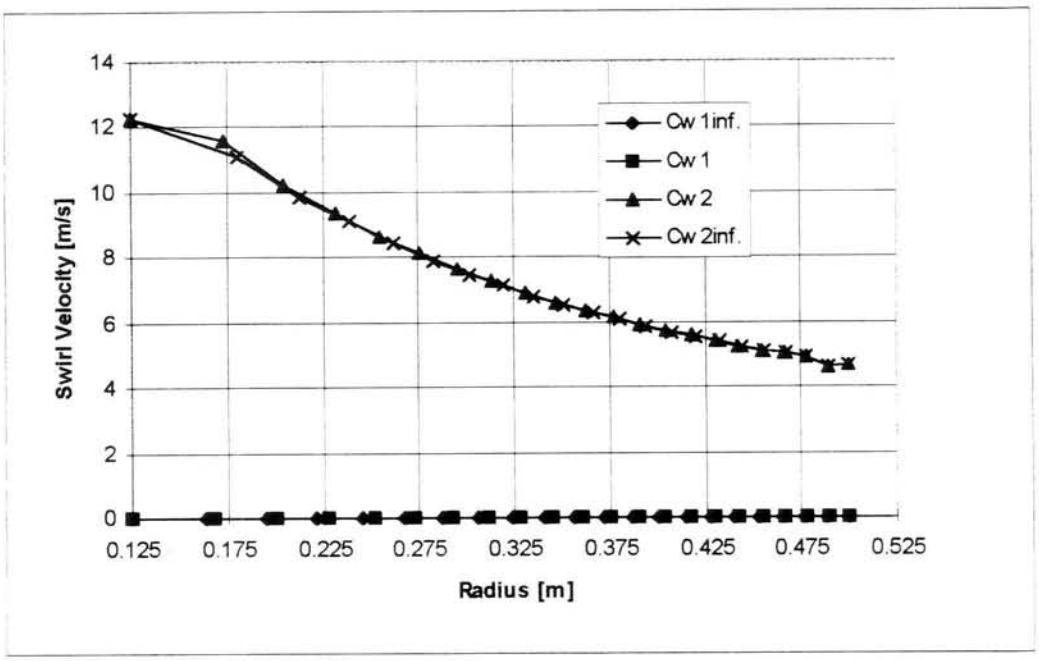

Figure 4.2a: Swirl velocity profiles for general application fan design

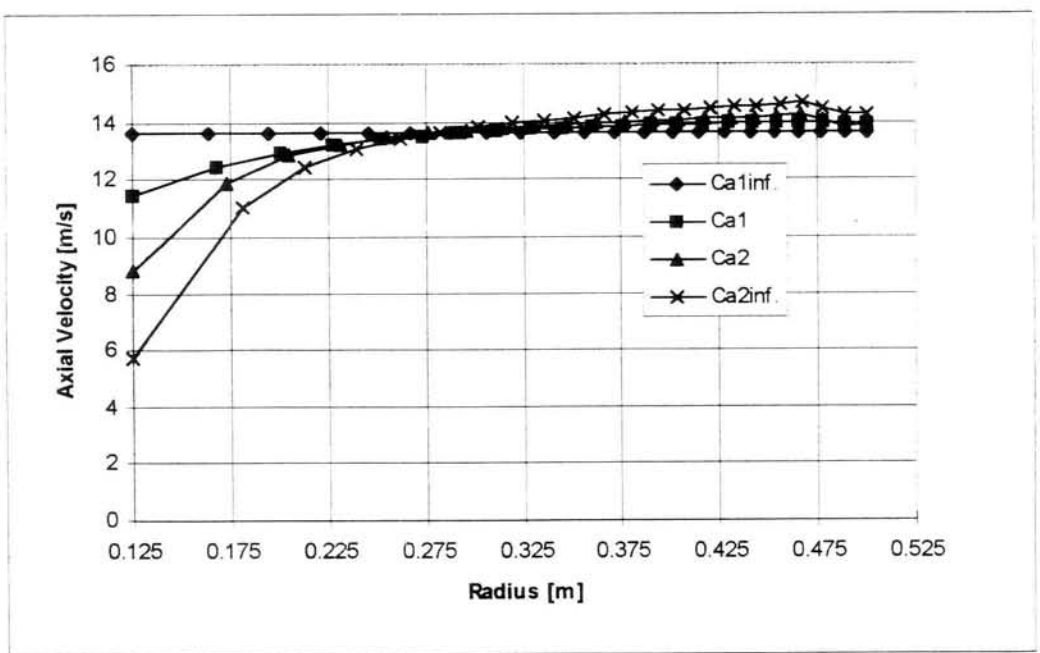

Figure 4.2b: Axial velocity profiles for general application fan design

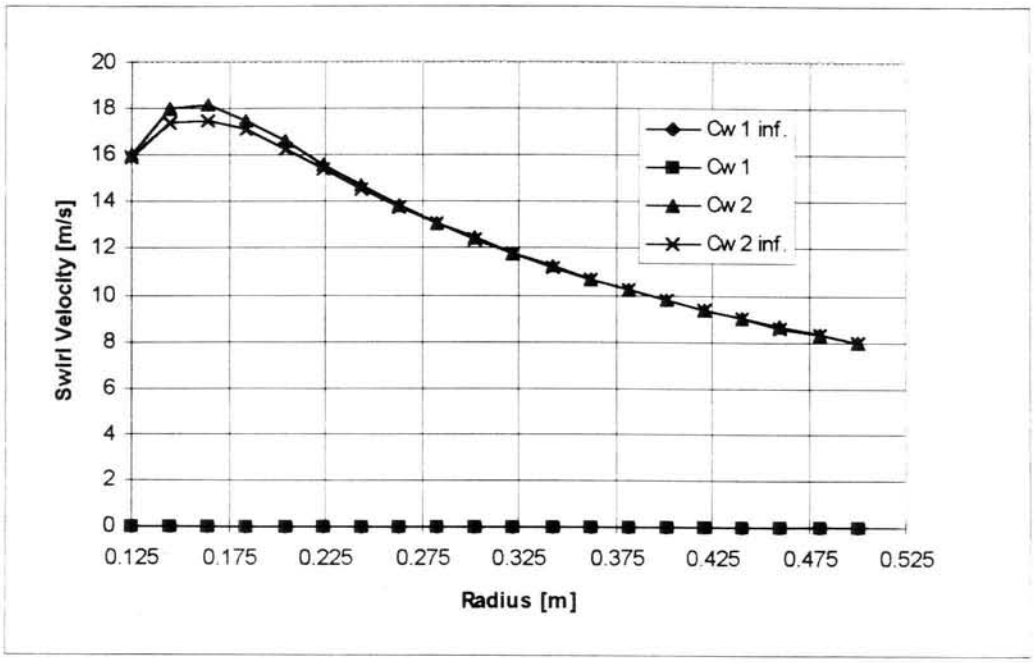

Figure 4.3a: Swirl velocity profiles for low-noise fan design

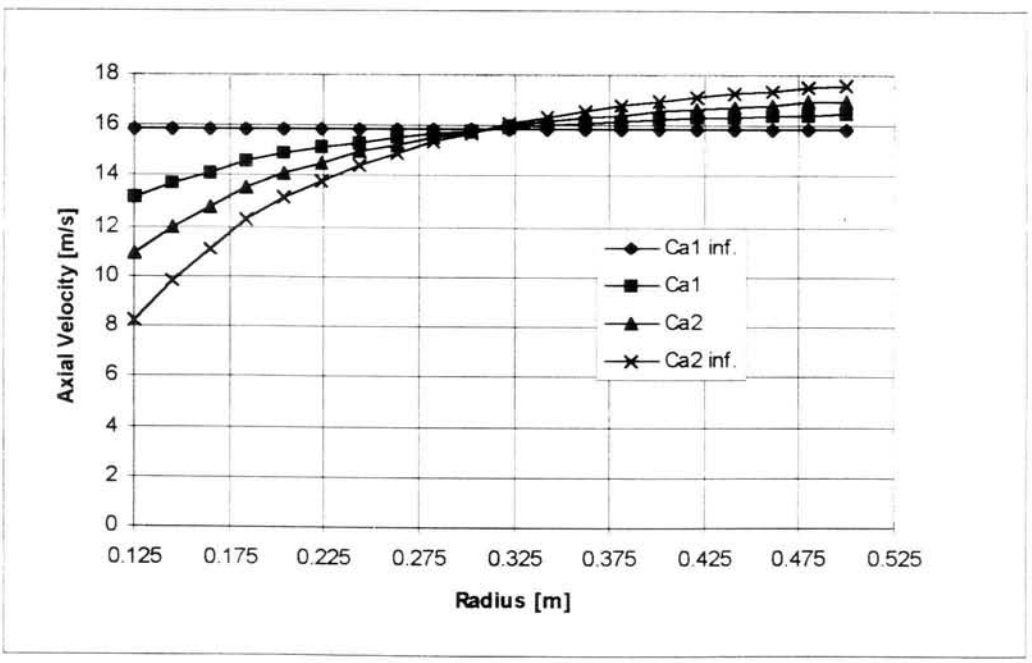

Figure 4.3b: Axial velocity profiles for low-noise fan design

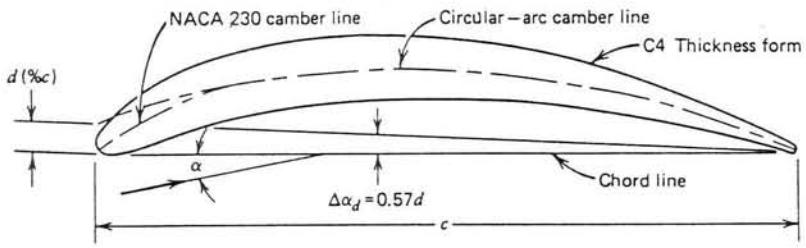

Figure 4.4: F-series airfoil geometry (Wallis, 1983)

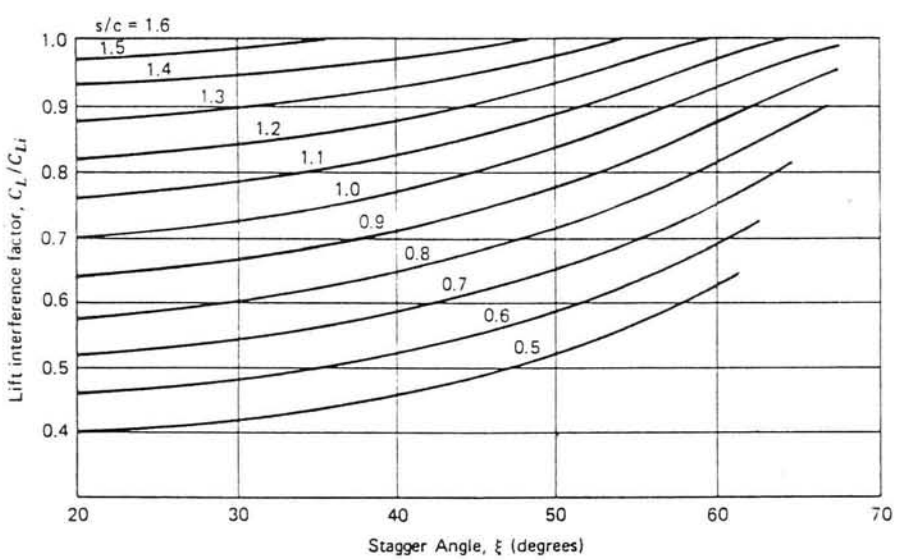

Figure 4.5: Graph for lift interference factors used in design process (Wallis, 1983)

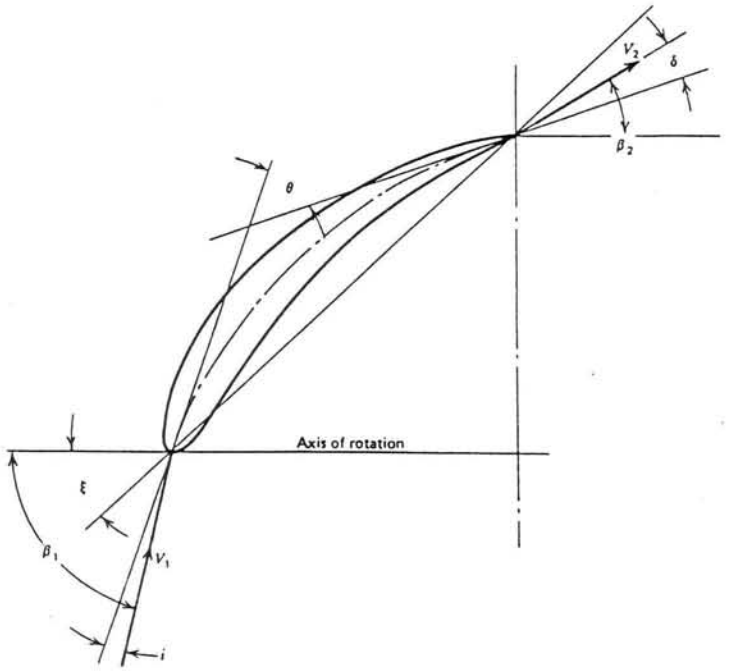

Figure 4.6: Definition of camber and stagger angles (Wallis, 1983)

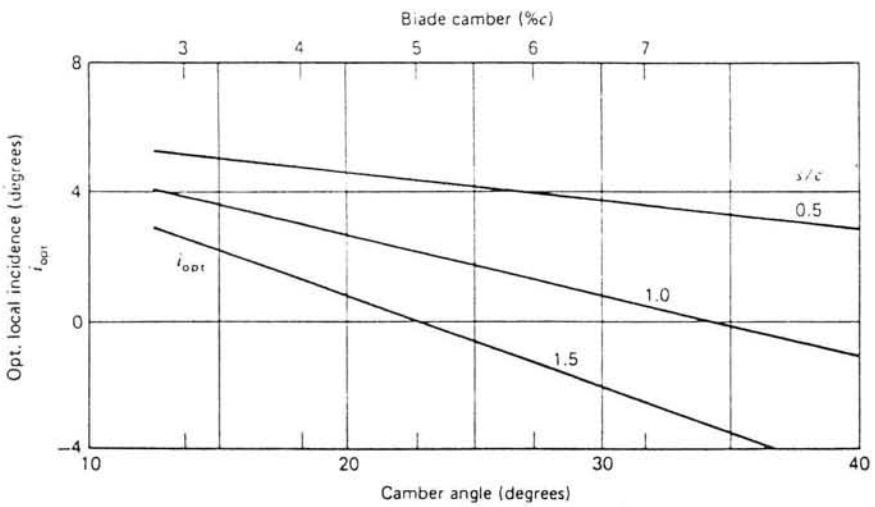

Figure 4.7: Graph for incidence angles used in design process (Wallis, 1983)

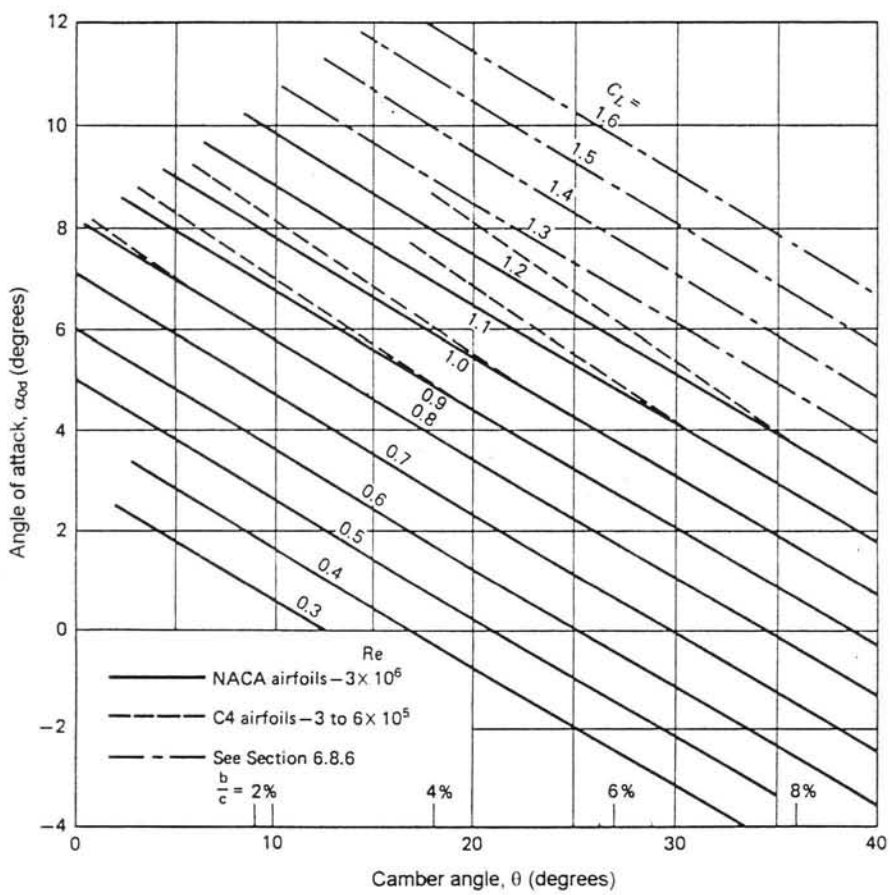

Figure 4.8: Graph of angles of attack used in design process (Wallis, 1983)

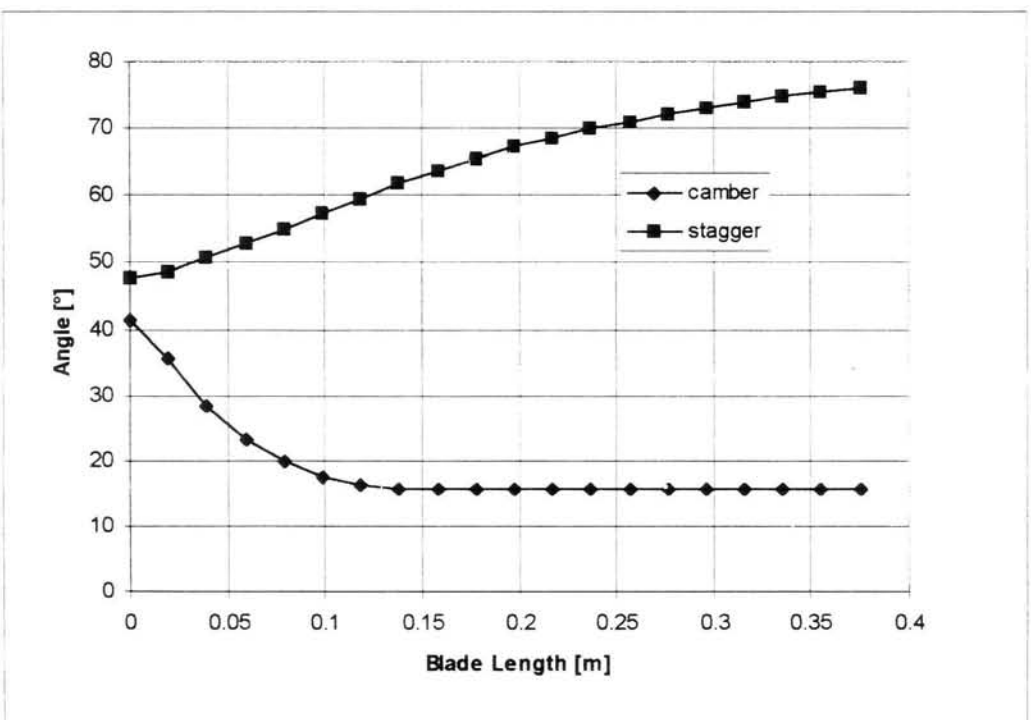

Figure 4.9: Stagger and camber angle distribution for general application fan

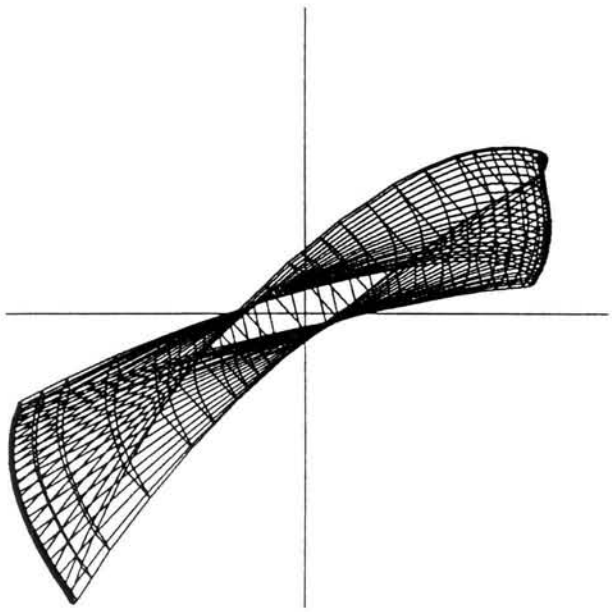

Figure 4.10: Blade profile distribution for general application fan design (Scale 1:1)

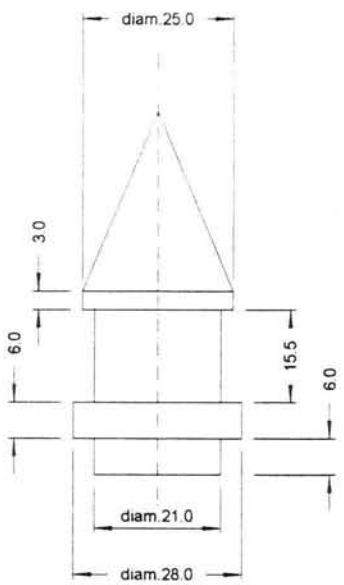

Figure 4.11: Blade root diagram

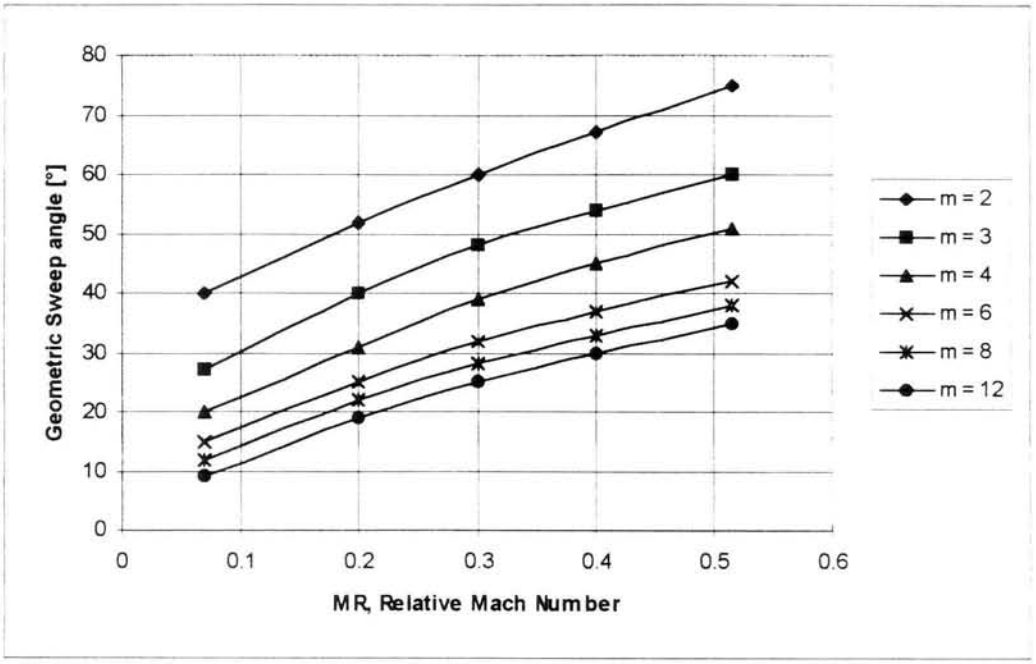

Figure 4.12: Estimated sweep angle required for a 10 dB reduction of a given mode (m) (Wright, 1989)

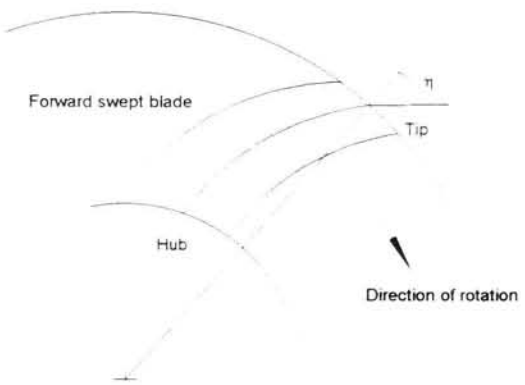

Figure 4.13: Geometric sweep angle definition (rotor viewed in plane of rotation)

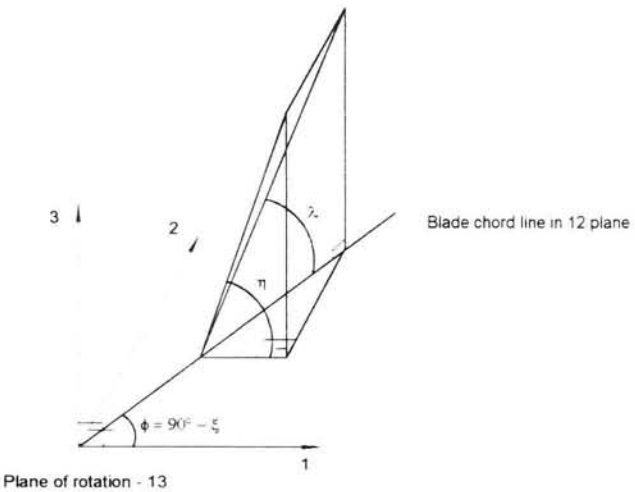

Figure 4.14: Transformation triangle between geometric and aerodynamic sweep

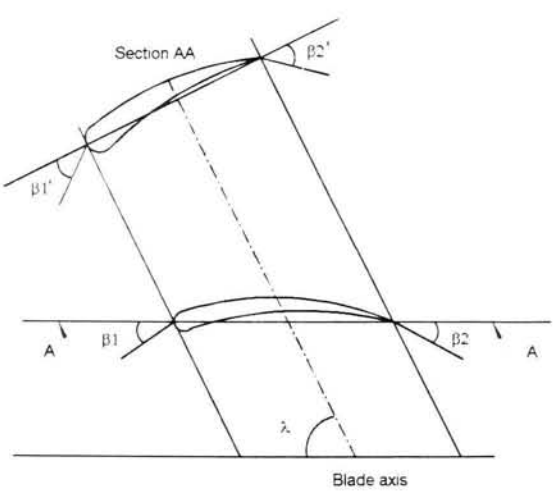

Figure 4.15: Transformation of variables due to blade sweep

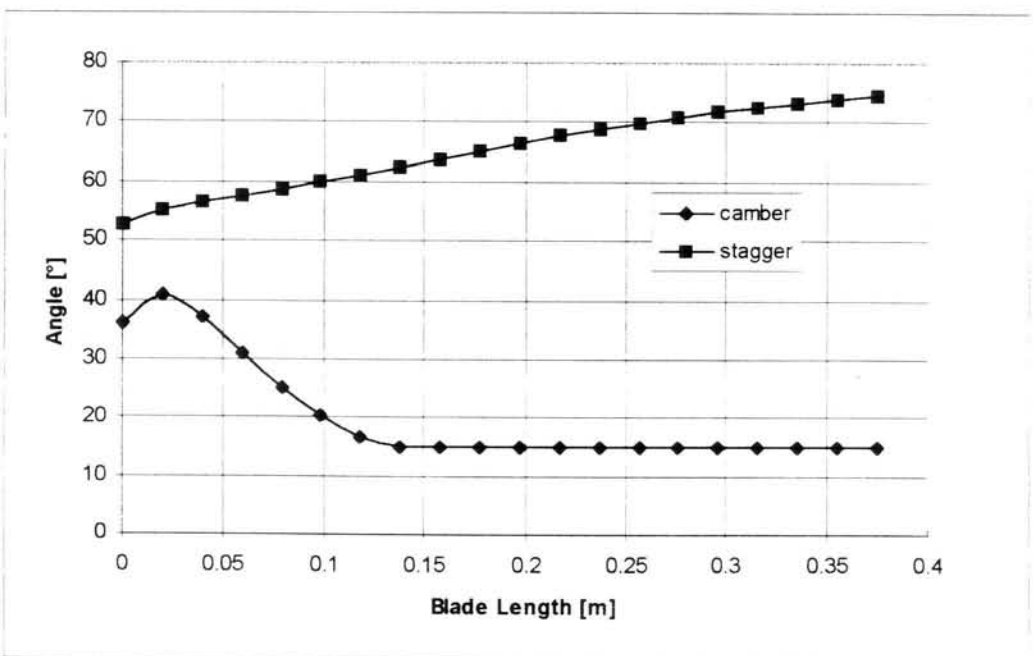

Figure 4.16: Stagger and camber angle distribution for low-noise fan

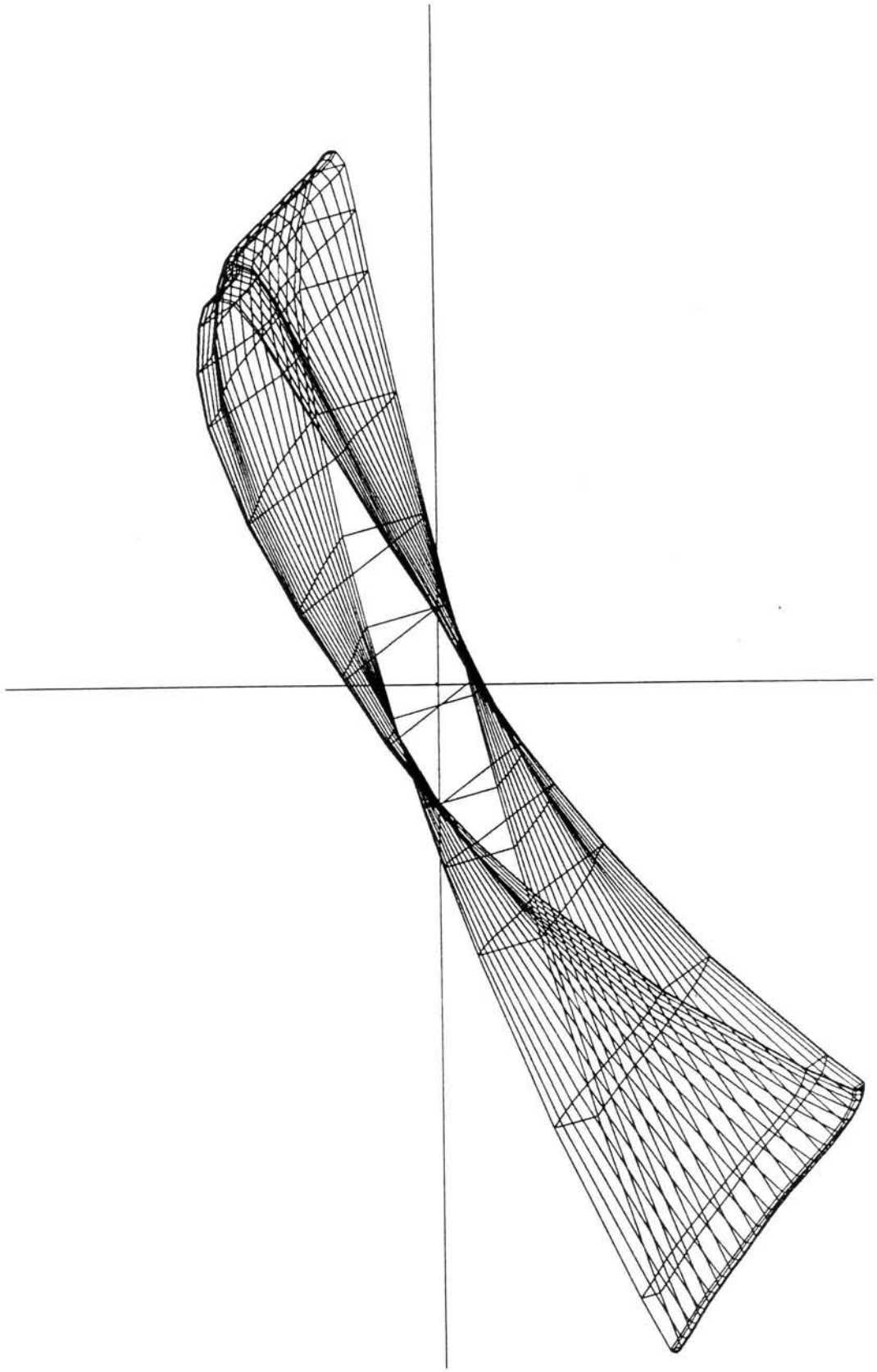

Figure 4.17: Blade profile distribution for low-noise fan (Scale 1:1)

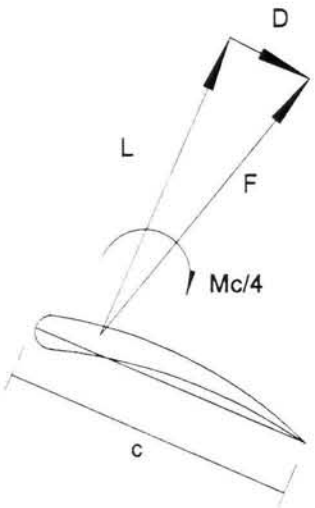

Figure 4.18: Diagram of aerodynamic blade forces

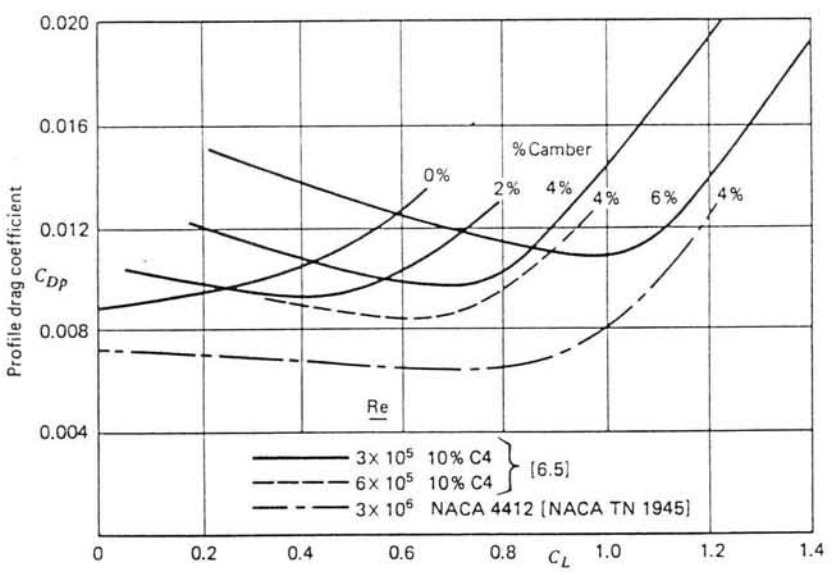

Figure 4.19: Drag coefficients used for F-series airfoil (Wallis, 1983)

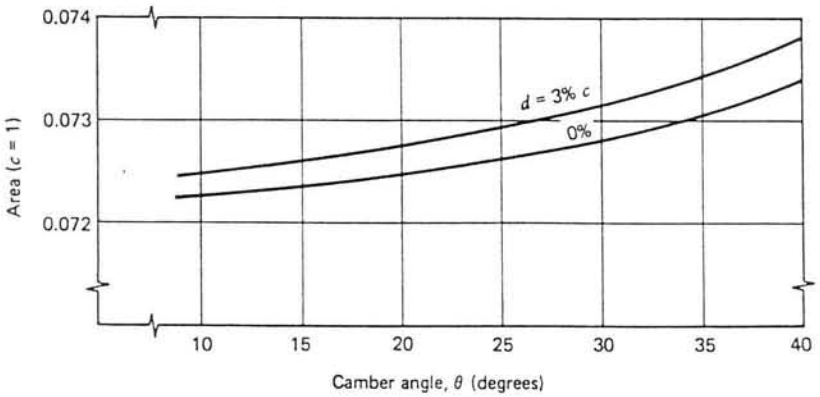

Figure 4.20: Graph for area of 10% thick F-series profile vs. camber angle (Wallis, 1983)

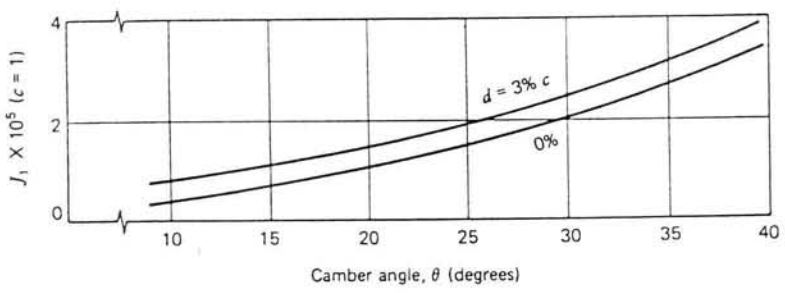

Figure 4.21: Graph of J_1 for 10% thick F-series profile vs. camber angle (Wallis, 1983)

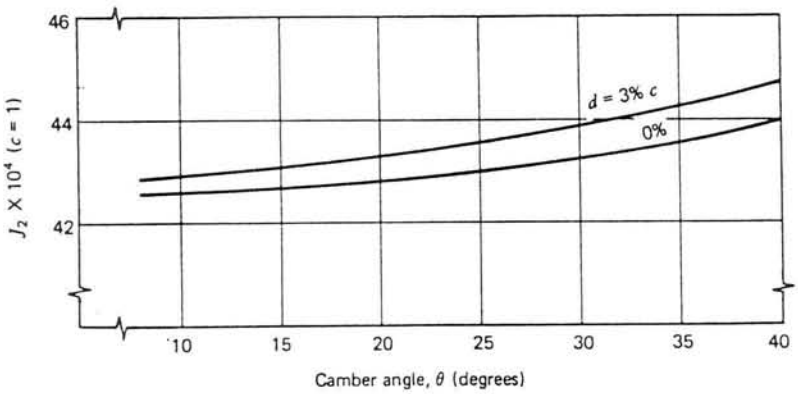

Figure 4.22: Graph of J_2 for 10% thick F-series profile vs. camber angle (Wallis, 1983)

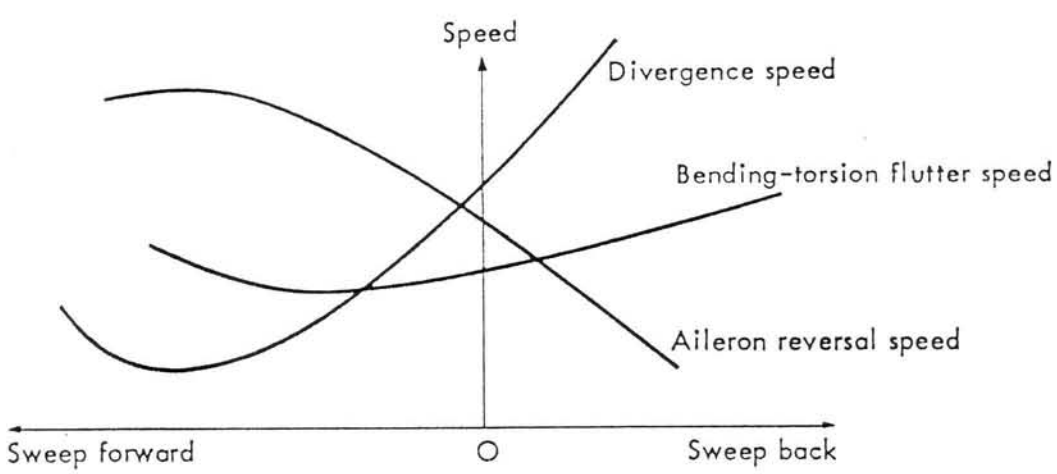

Figure 4.23: Comparison of wing critical speeds (Bisplinghoff et al., 1955)

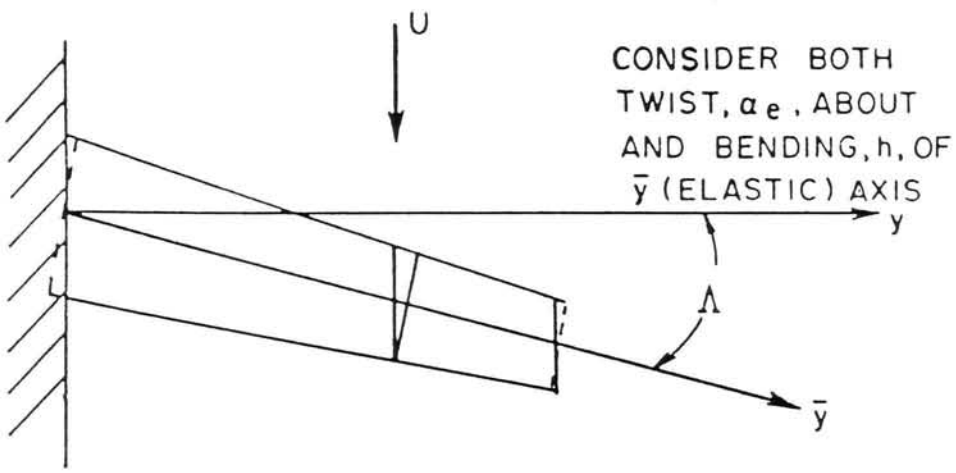

Figure 4.24: Sweptwing geometry (Dowell et al., 1995)

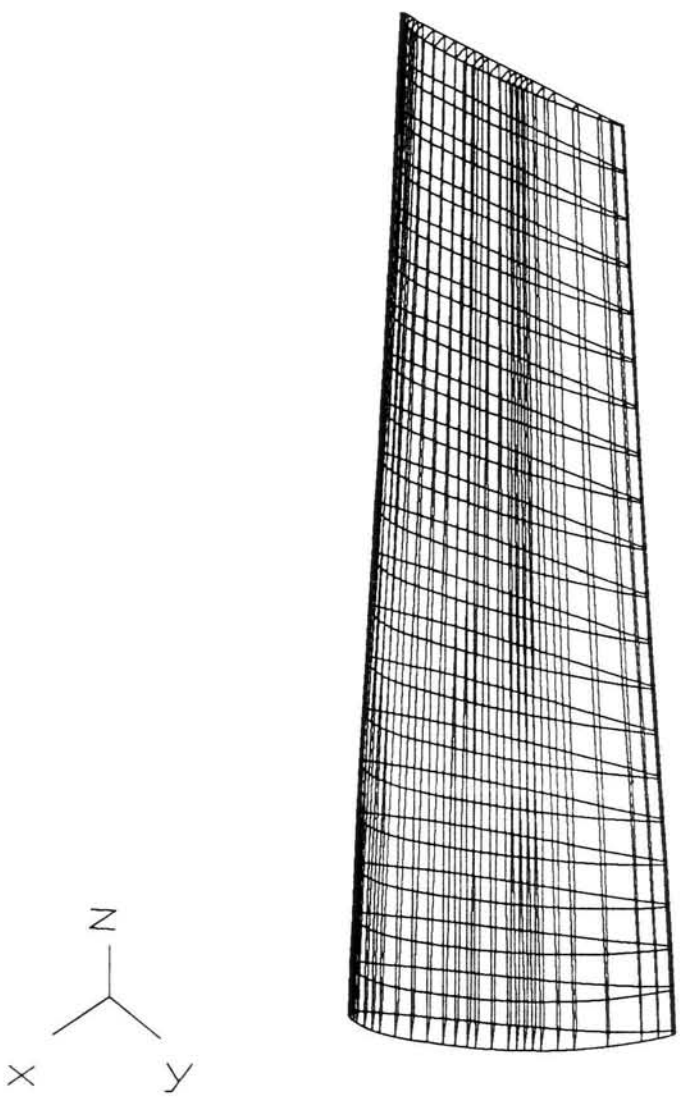

Figure 4.25: General application fan blade design in AutoCad

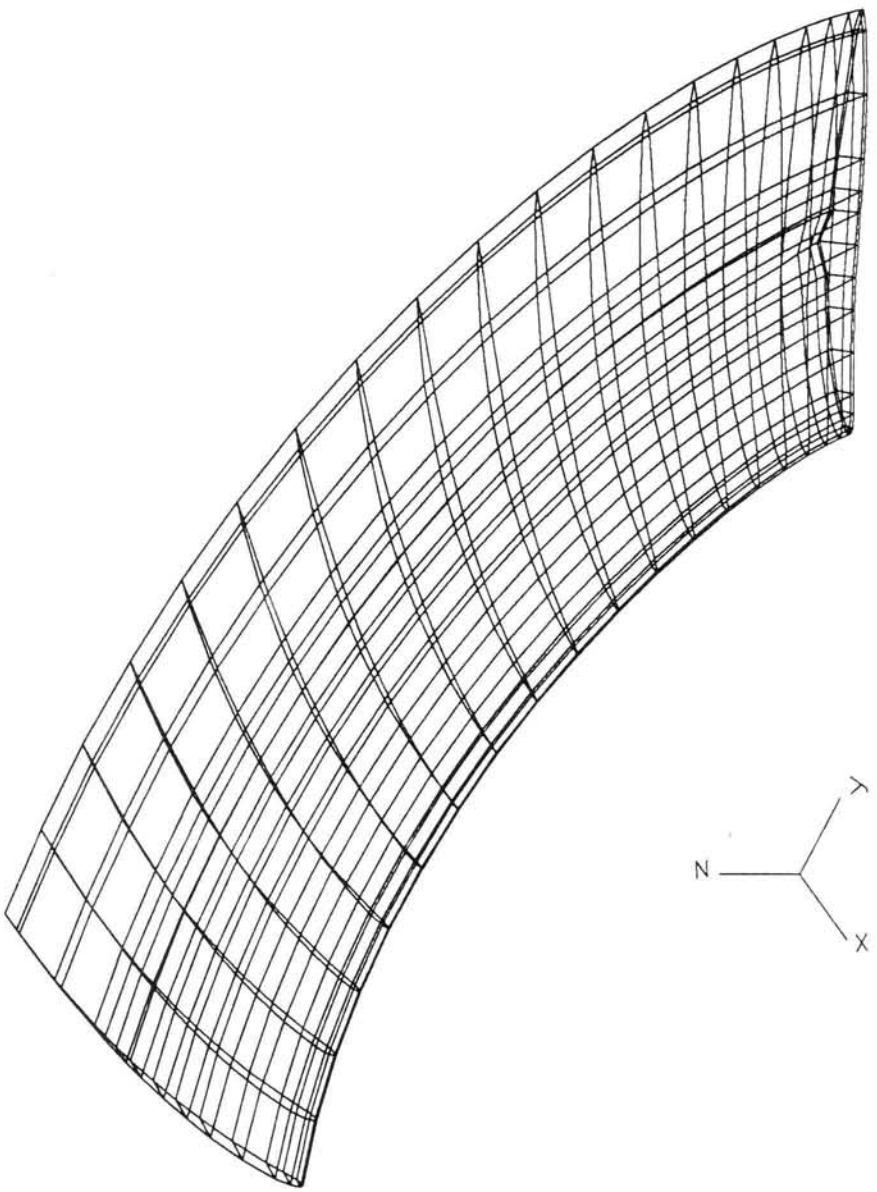

Figure 4.26: Low-noise fan blade design in AutoCad

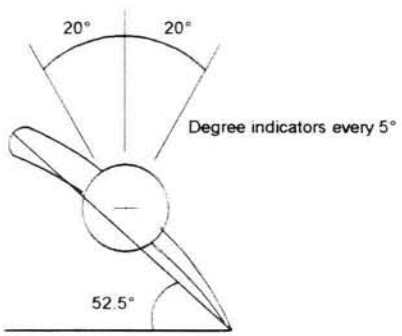

Figure 4.27: Blade setting angle definition for general application fan

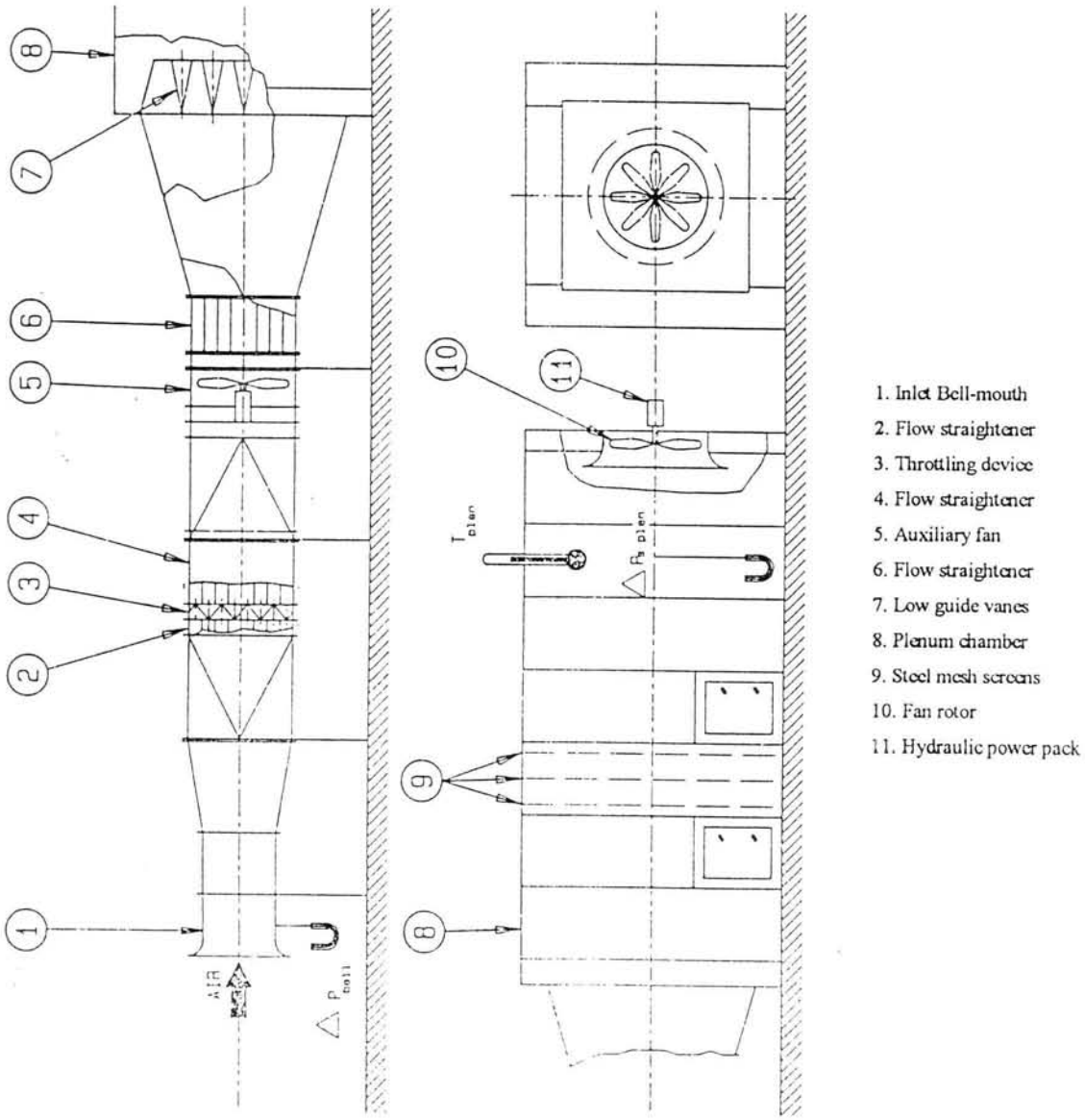

Figure 5.1: Schematic lay-out of Type A test facility for 1000 mm diameter general application fan (Venter, 1990)

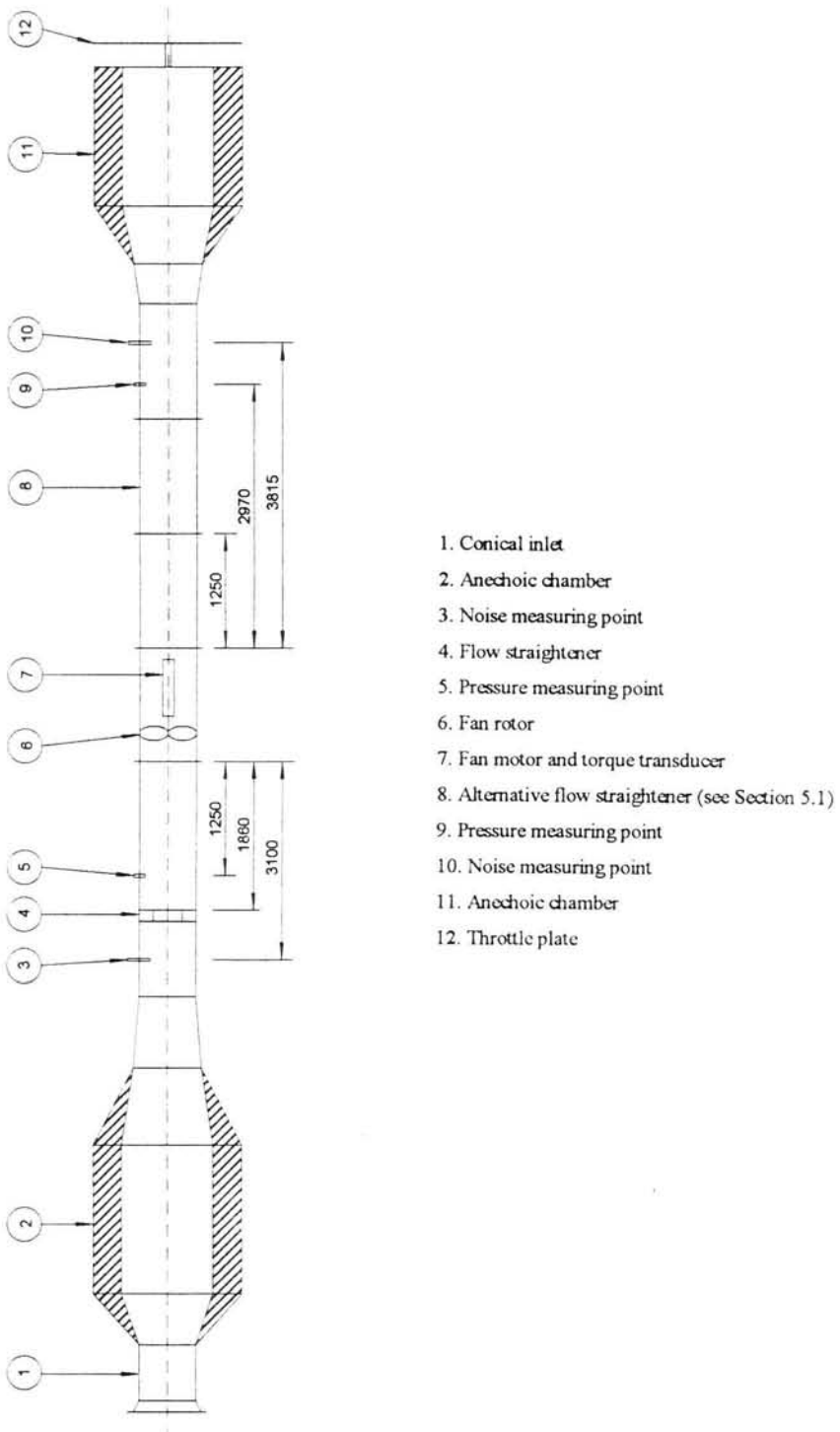

Figure 5.2: Schematic lay-out of Type D test facility for 630 mm diameter fan

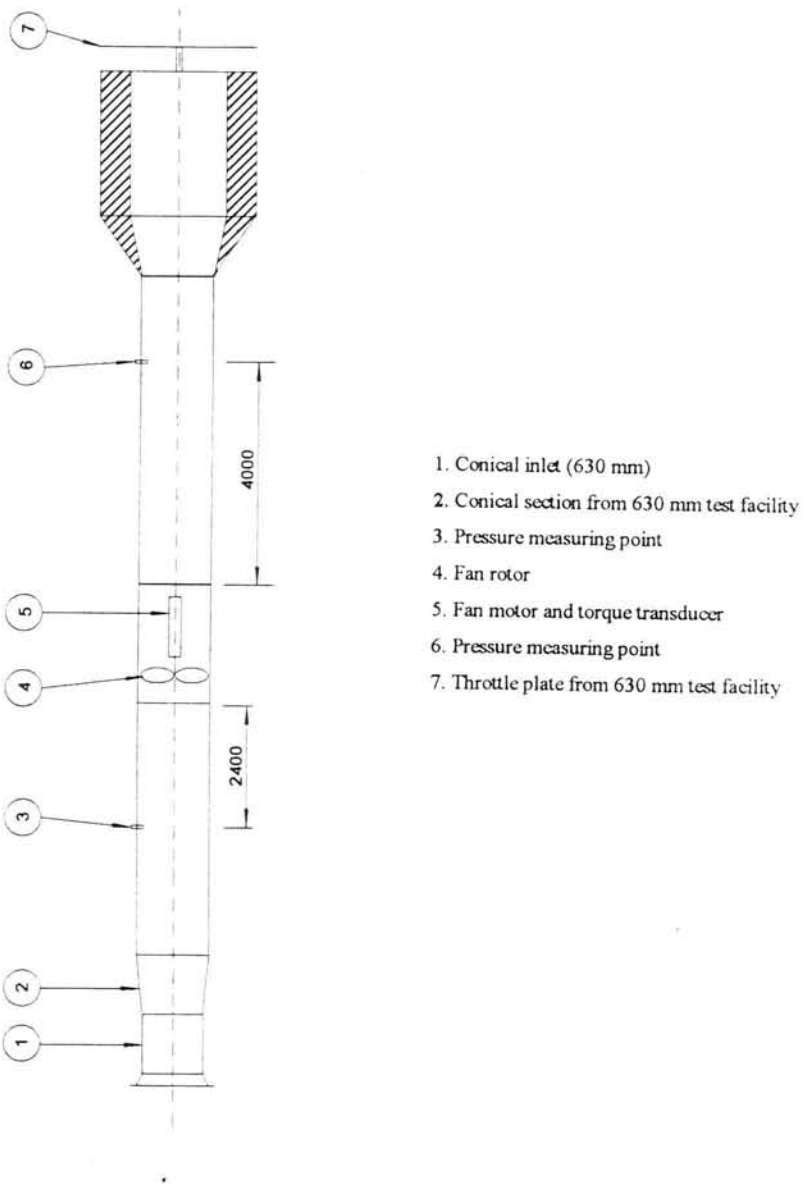

Figure 5.3: Schematic lay-out of Type D test facility for 800 mm diameter fan

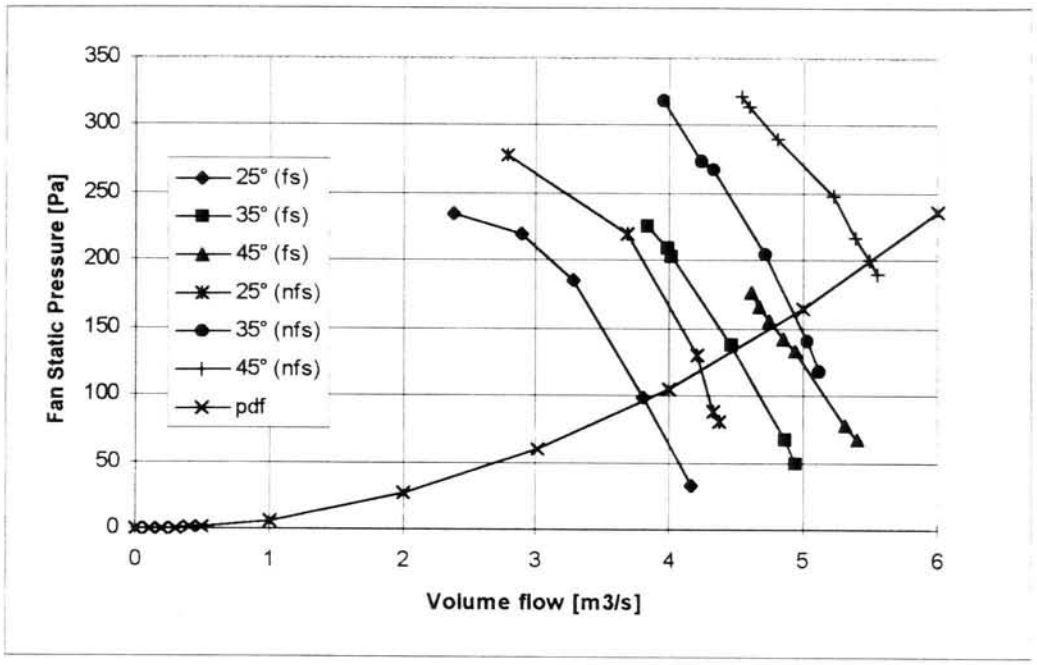

Figure 5.4: Fan static pressure vs. volume flow for different blade angles for 630/250/14/1440 fan (fs - flow straightener, nfs - no flow straightener).

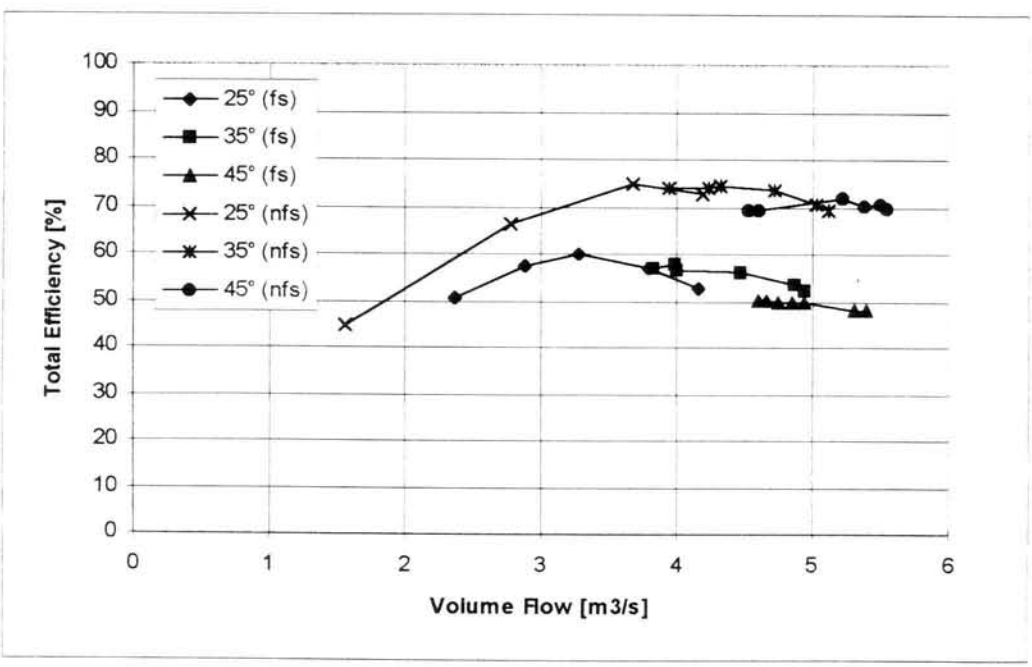

Figure 5.5: Fan total efficiency vs. volume flow for 630/250/14/1440 fan.

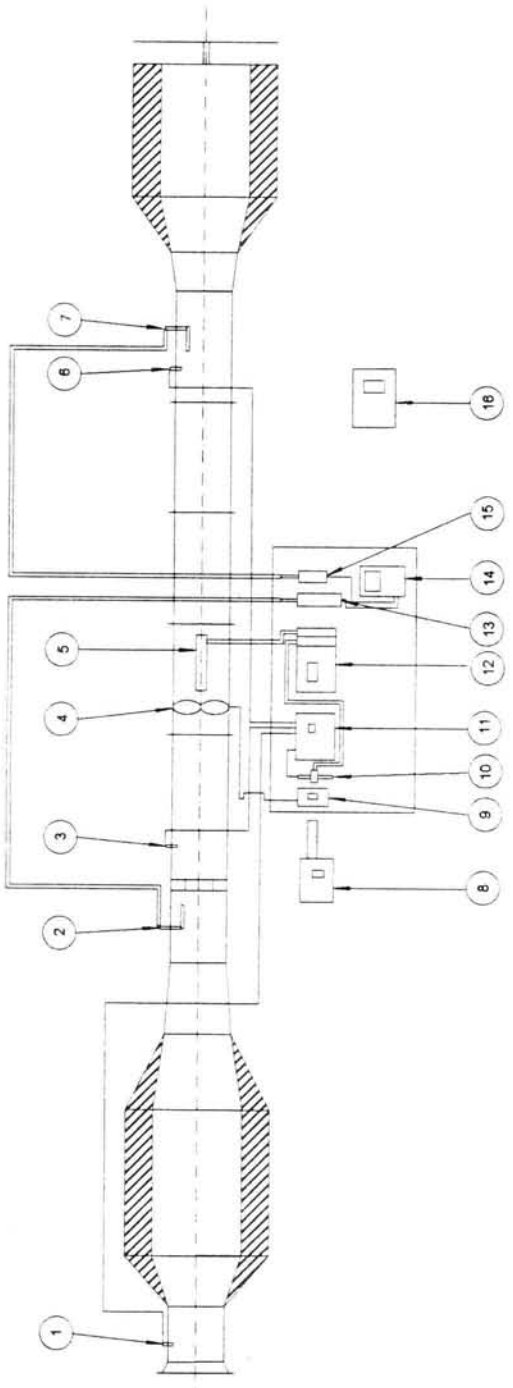

1. Pressure tappiugs for determining volume flow
2. Noise measuring tube and microphone
3. Pressure measuring point in front of fan
4. Fan rotor
5. Fan motor and HBM torque transducer
6. Pressure measuring point behind fan
7. Noise measuring tube and microphone
8. Betz manometer for calibrating pressure readings
9. Frequency read-out coupled to proximity switch
10. HBM pressure transducer
11. FC selection box
12. HBM bridge amplifier
13. B + K sound level meter
14. FFT analyzer
15. Rion sound level meter
16. Frequency inverter

Figure 5.6: Schematic lay-out of measuring equipment.

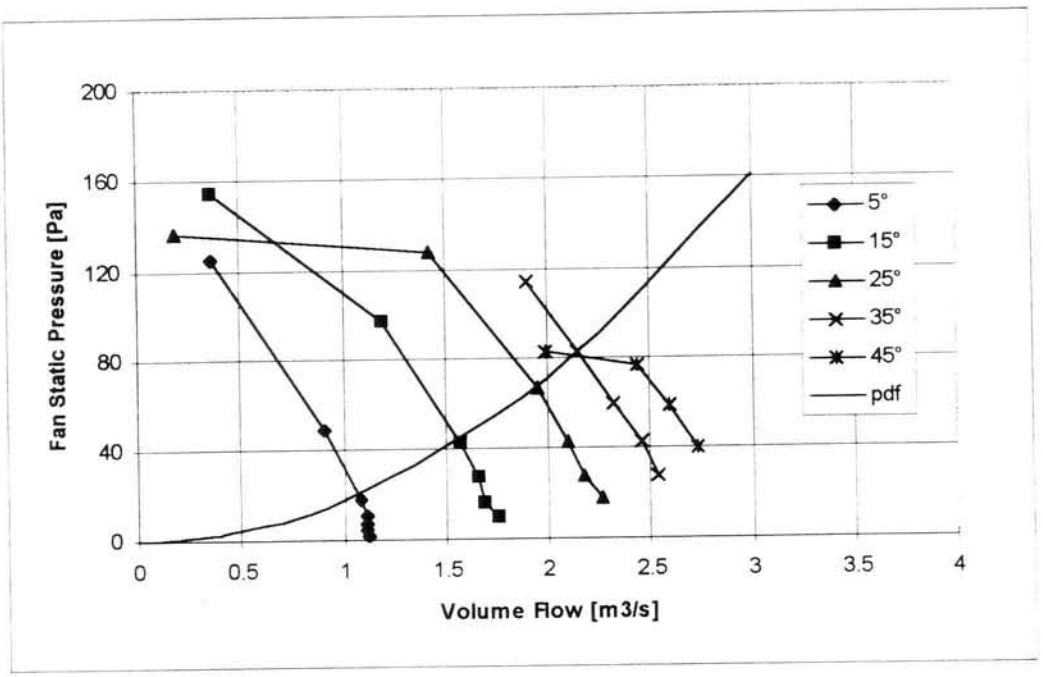

Figure 6.1: Static pressure vs. volume flow for 483/150/5/1440 fan

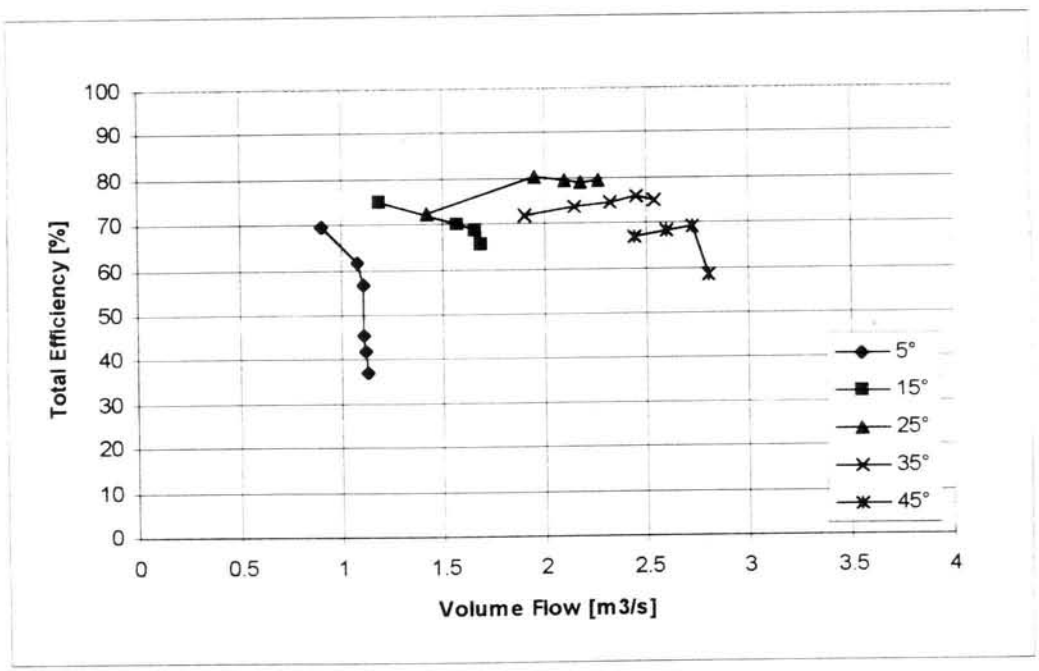

Figure 6.2: Total efficiency vs. volume flow for 483/150/5/1440 fan

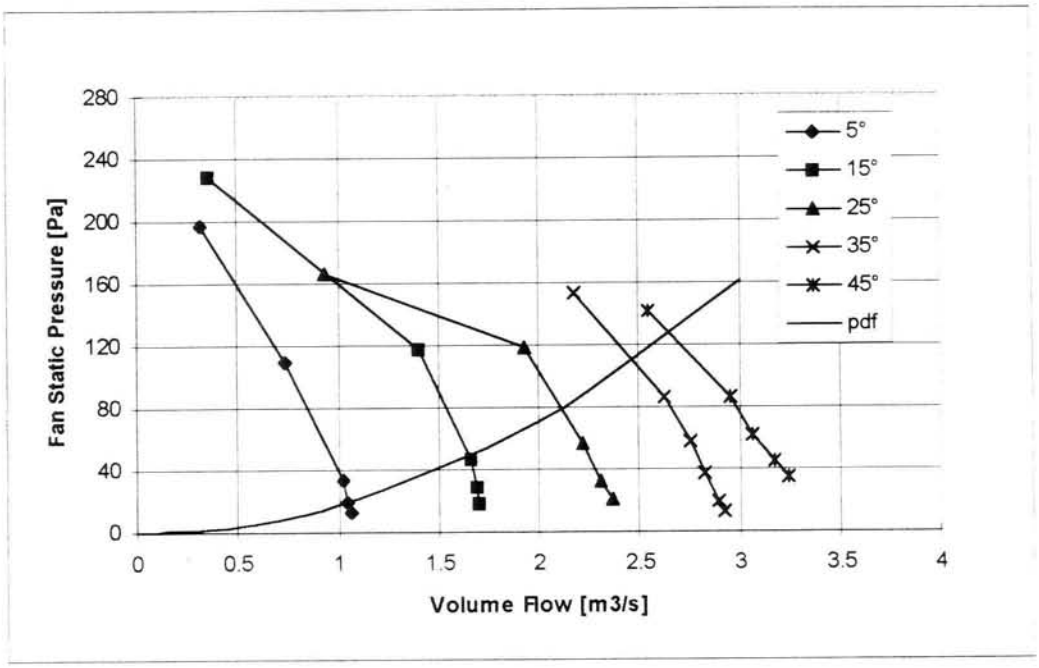

Figure 6.3: Static pressure vs. volume flow for 483/150/10/1440 fan

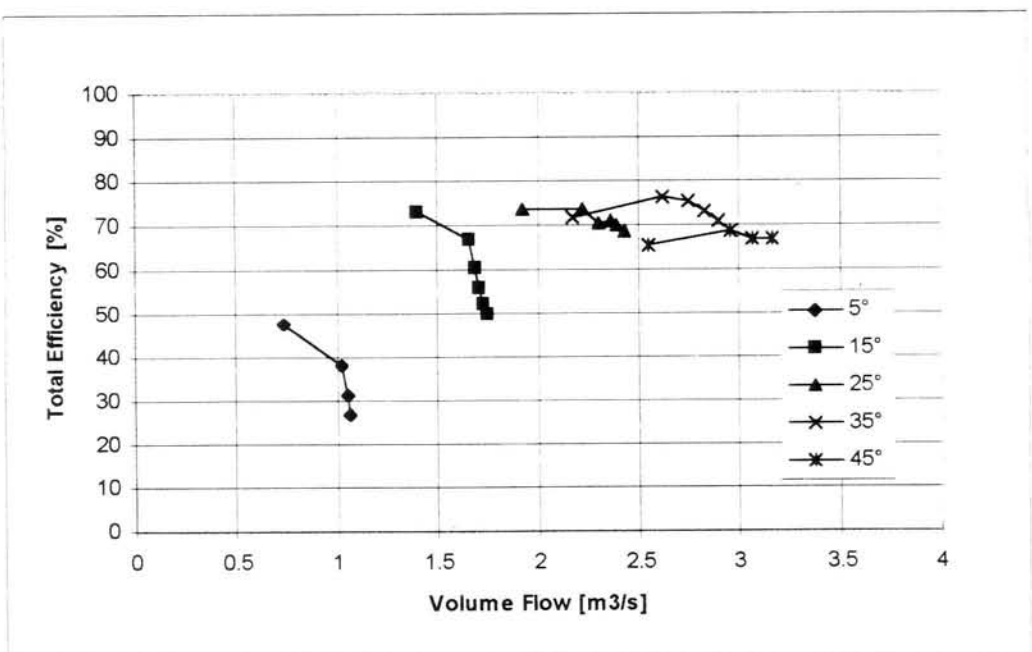

Figure 6.4: Total efficiency vs. volume flow for 483/150/10/1440 fan

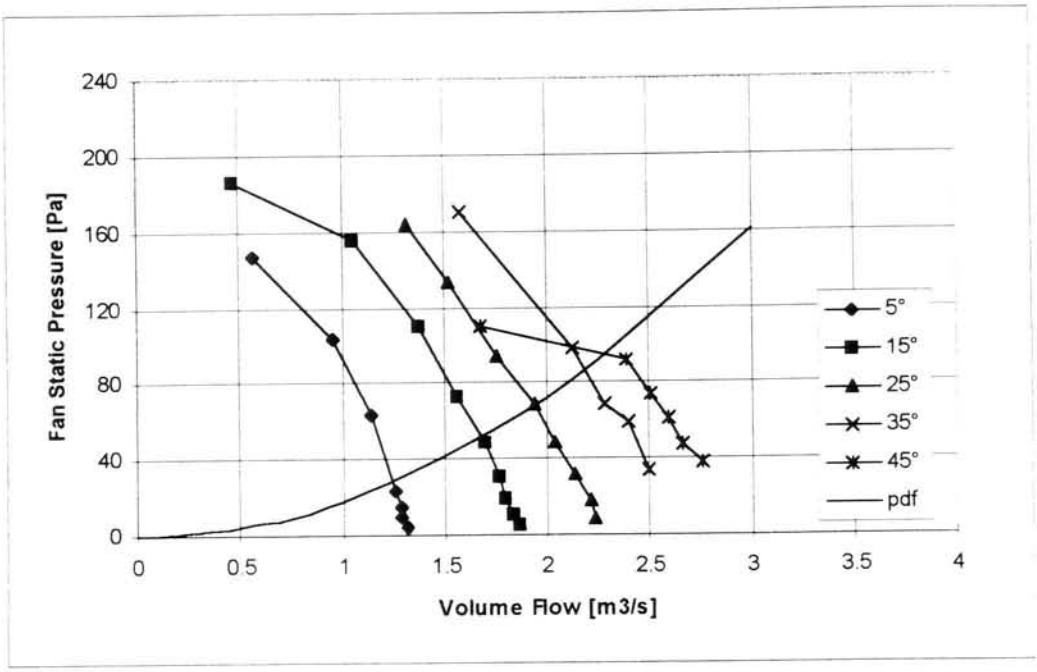

Figure 6.5: Static pressure vs. volume flow for 483/250/7/1440 fan

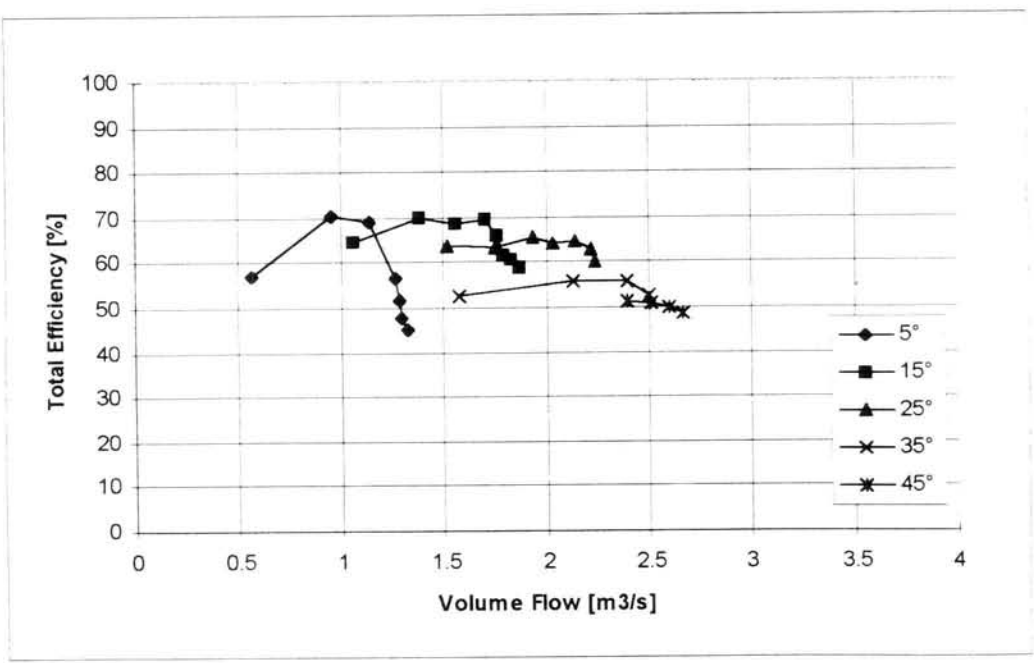

Figure 6.6: Total efficiency vs. volume flow for 483/250/7/1440 fan

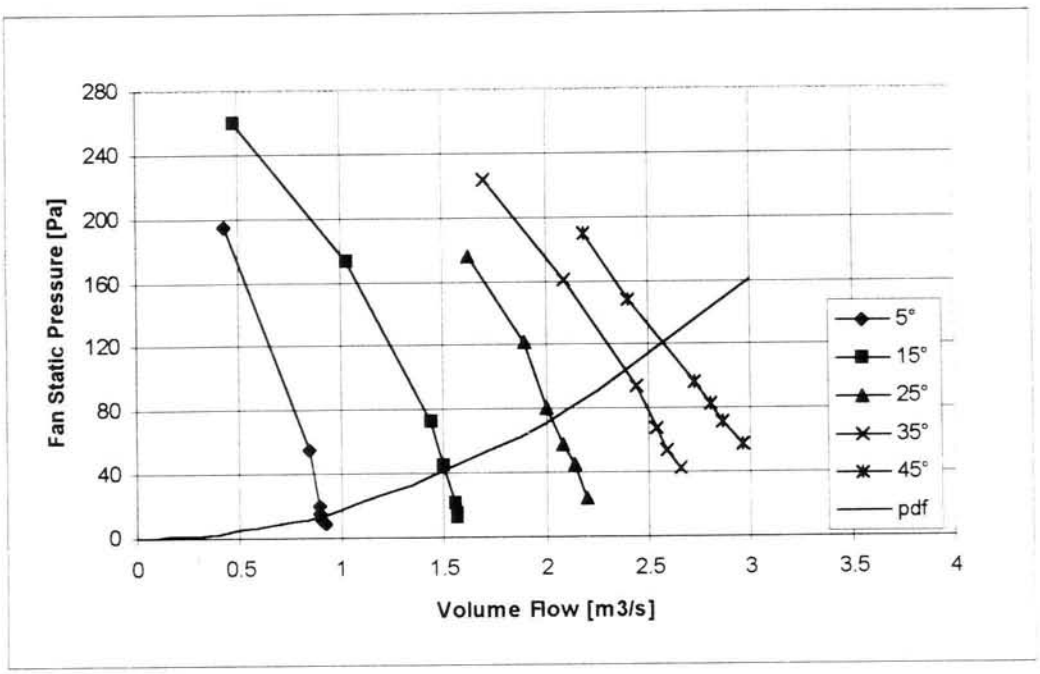

Figure 6.7: Static pressure vs. volume flow for 483/250/14/1440 fan

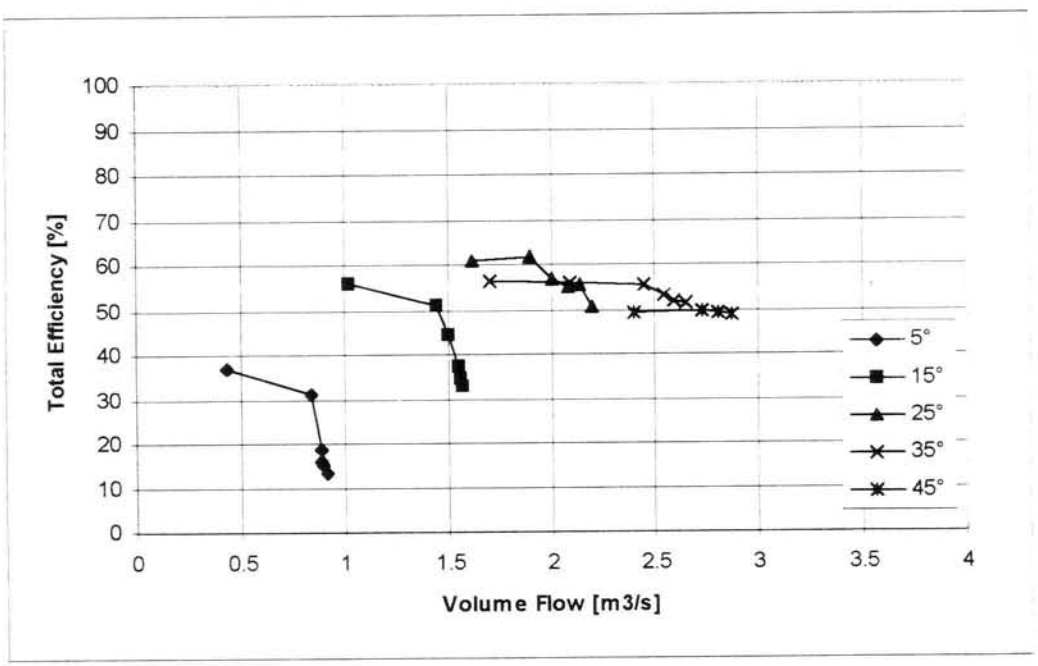

Figure 6.8: Total efficiency vs. volume flow for 483/250/14/1440 fan

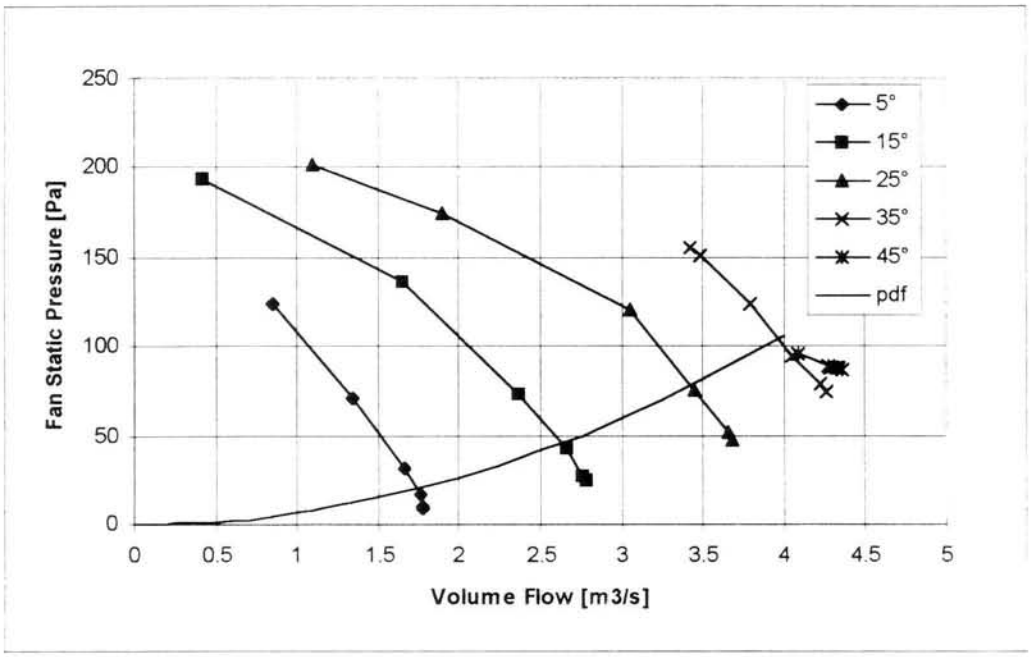

Figure 6.9: Static pressure vs. volume flow for 630/150/5/1440 fan

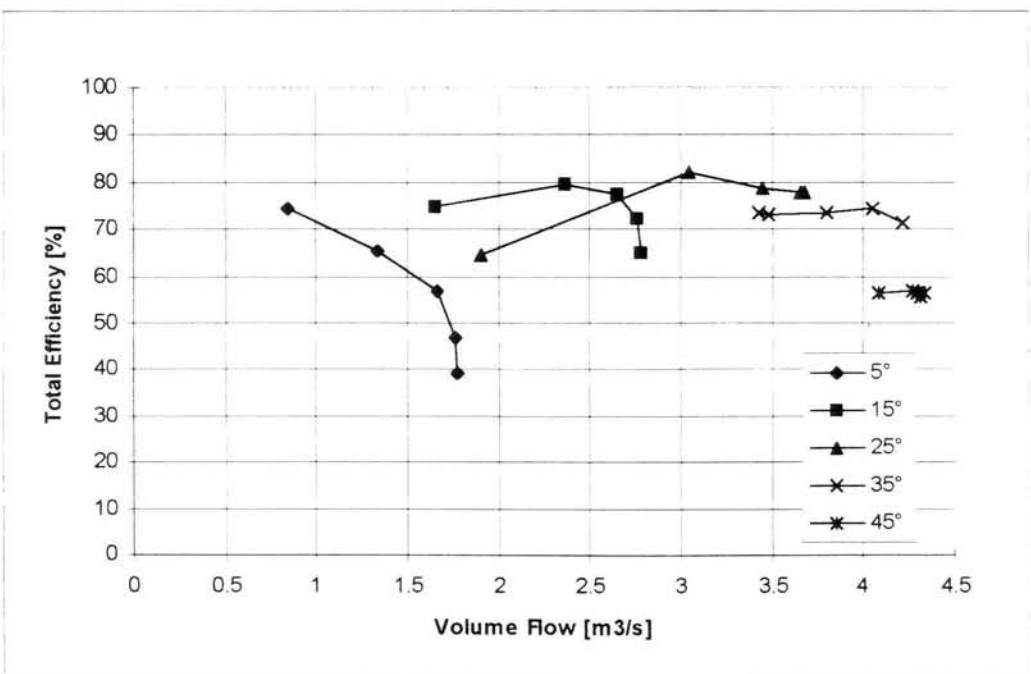

Figure 6.10: Total efficiency vs. volume flow for 630/150/5/1440 fan

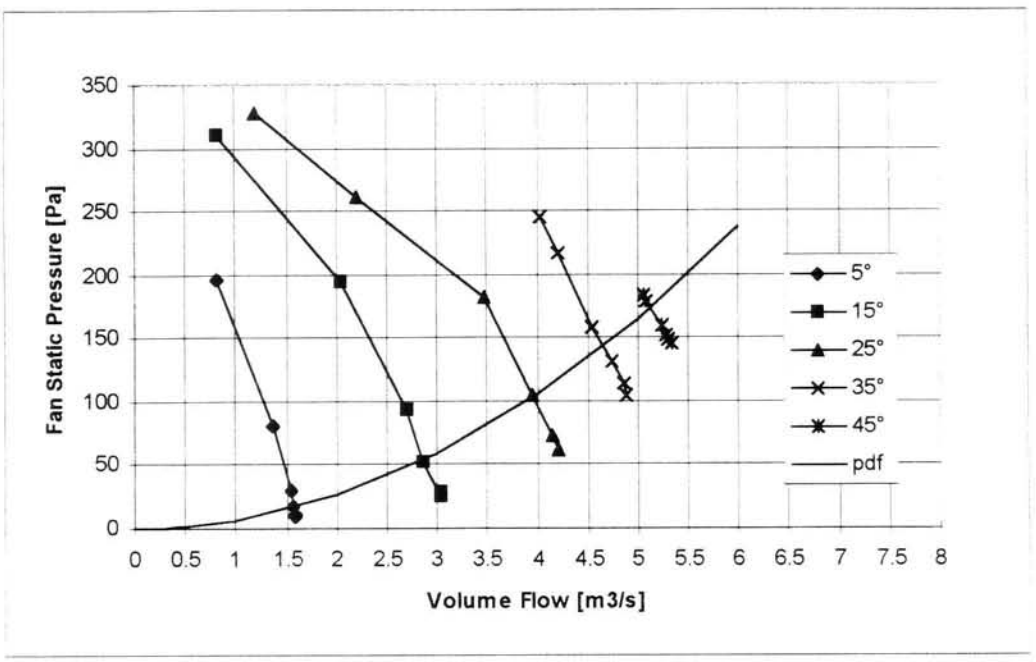

Figure 6.11: Static pressure vs. volume flow for 630/150/10/1440 fan

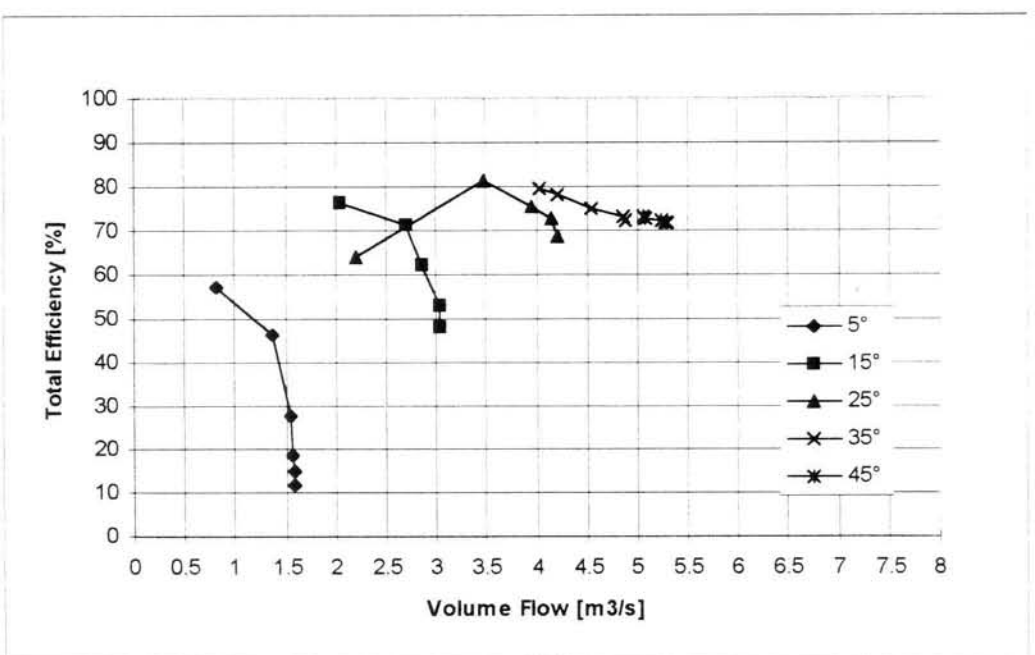

Figure 6.12: Total efficiency vs. volume flow for 630/150/10/1440 fan

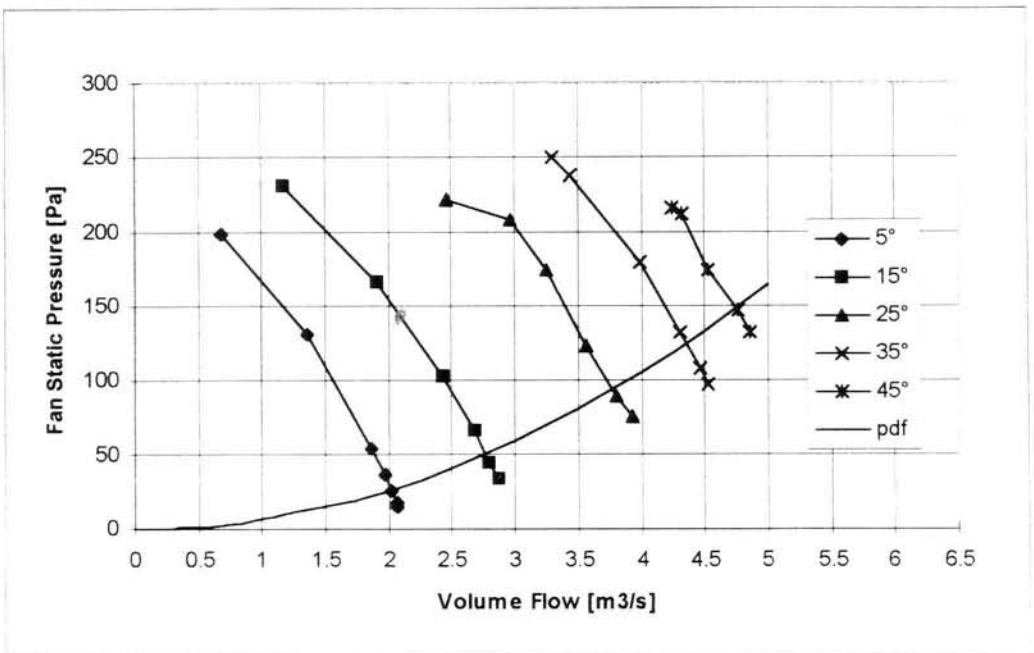

Figure 6.13: Static pressure vs. volume flow for 630/250/7/1440 fan

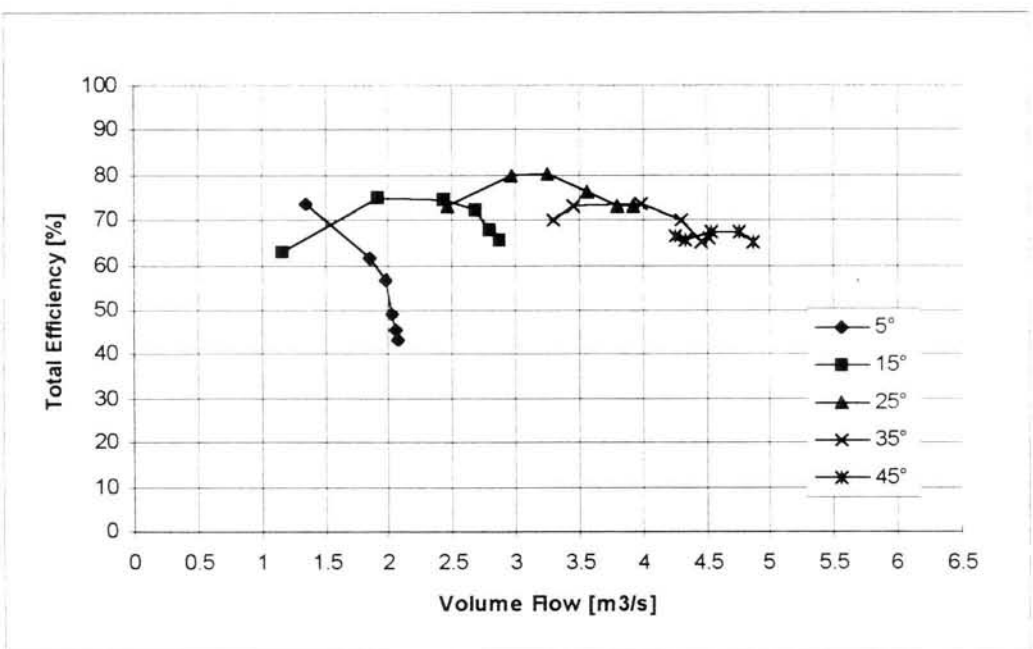

Figure 6.14: Total efficiency vs. volume flow for 630/250/7/1440 fan

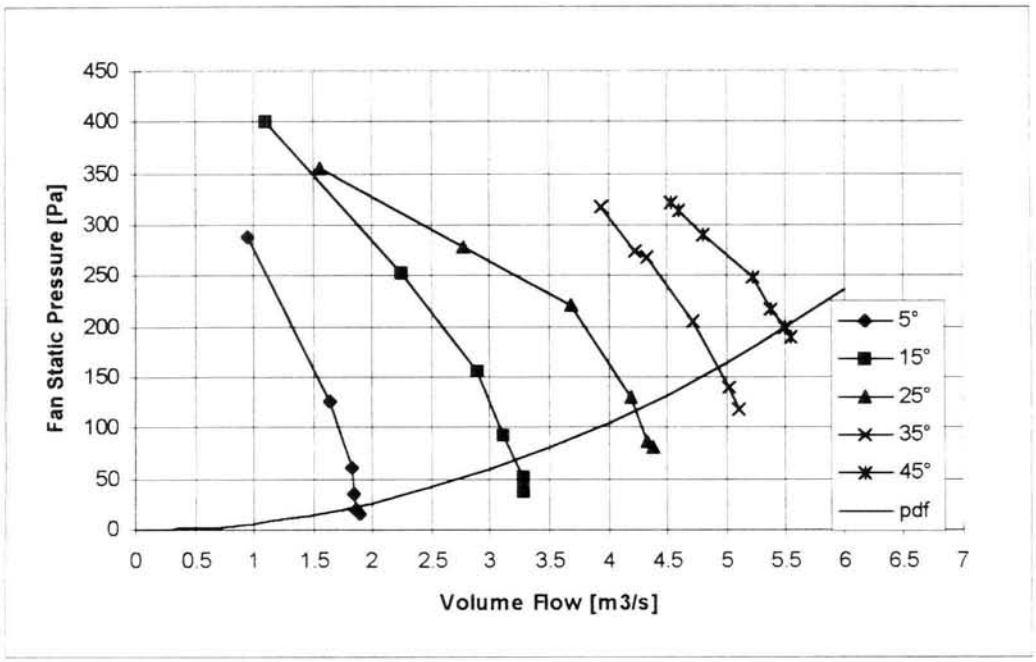

Figure 6.15: Static pressure vs. volume flow for 630/250/14/1440 fan

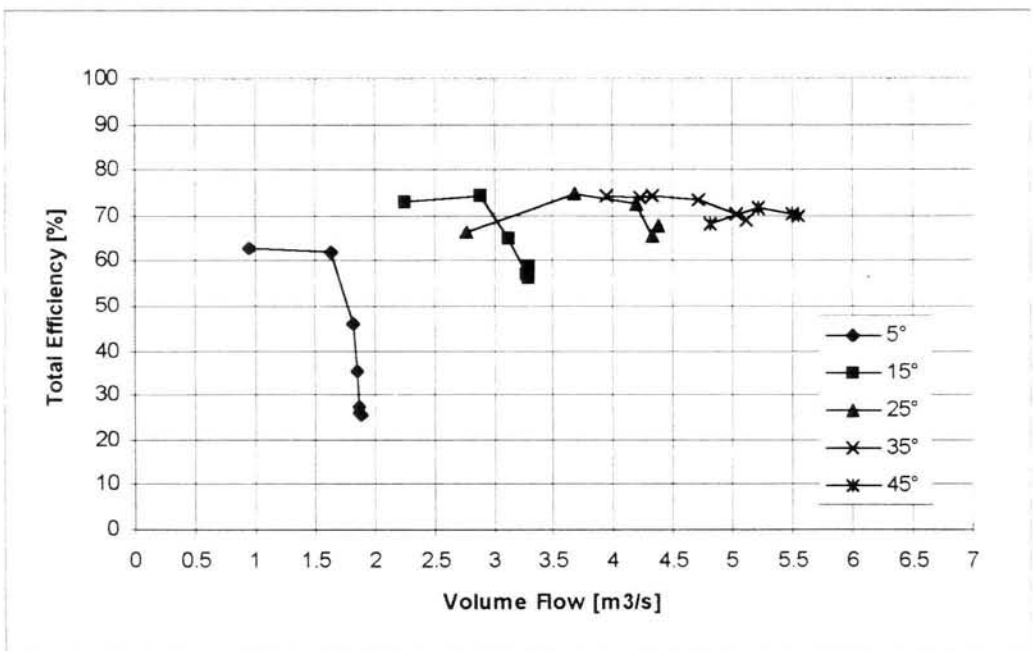

Figure 6.16: Total efficiency vs. volume flow for 630/250/14/1440 fan

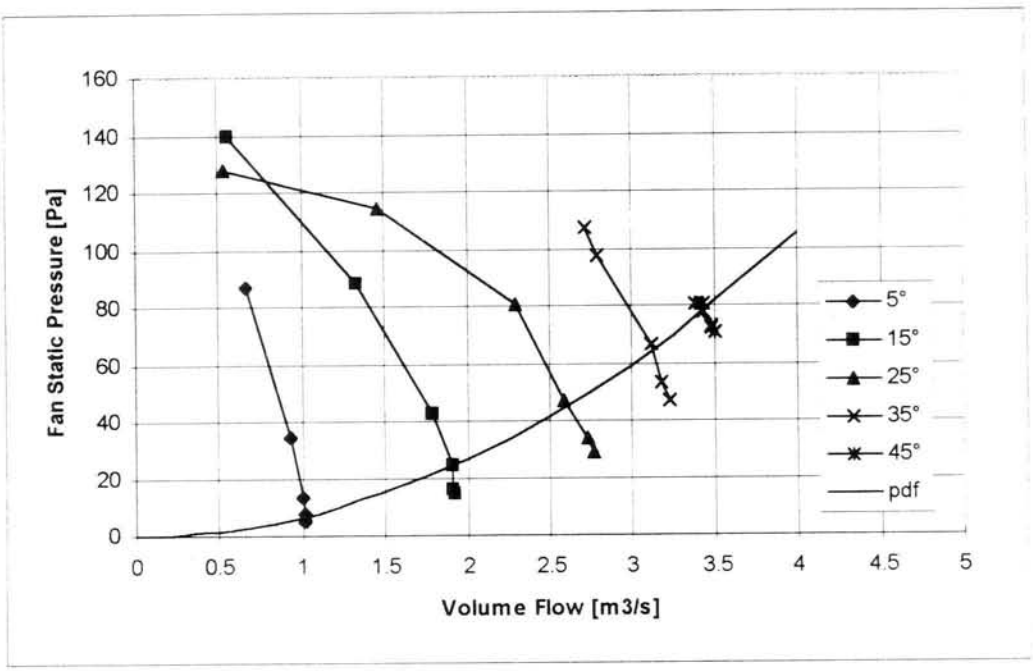

Figure 6.17: Static pressure vs. volume flow for 630/150/10/960 fan

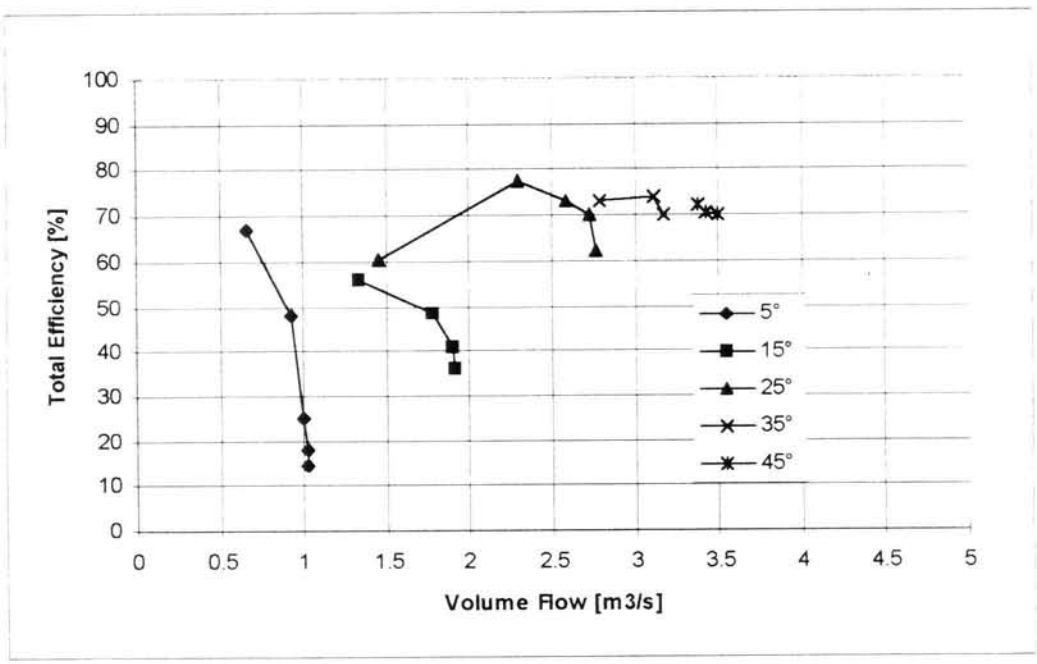

Figure 6.18: Total efficiency vs. volume flow for 630/150/10/960 fan

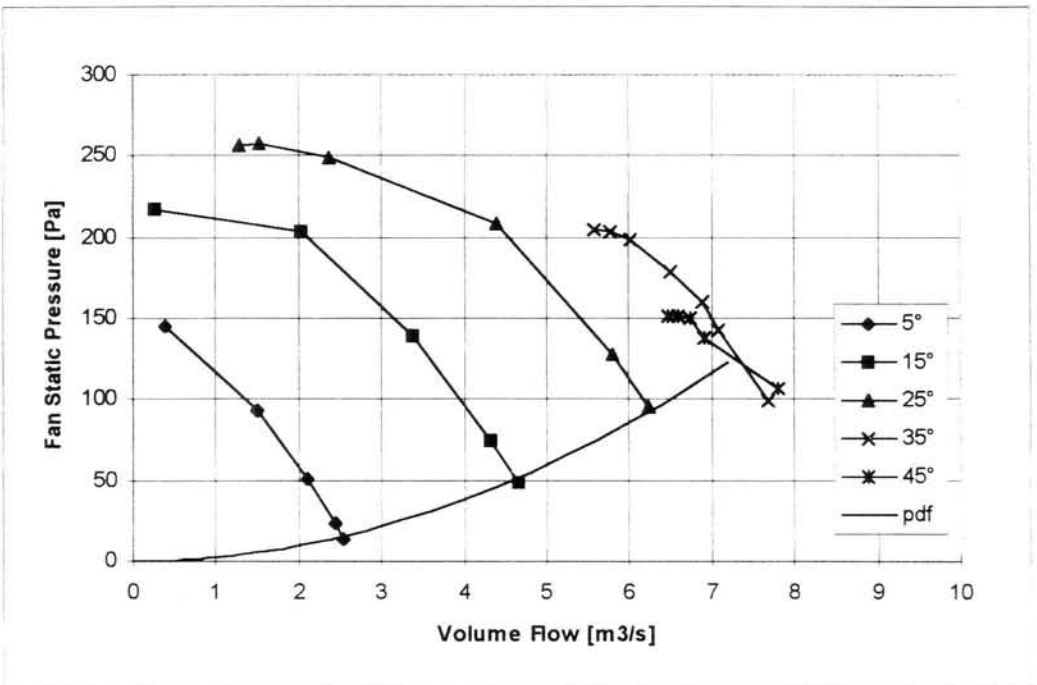

Figure 6.19: Static pressure vs. volume flow for 800/150/5/1440 fan

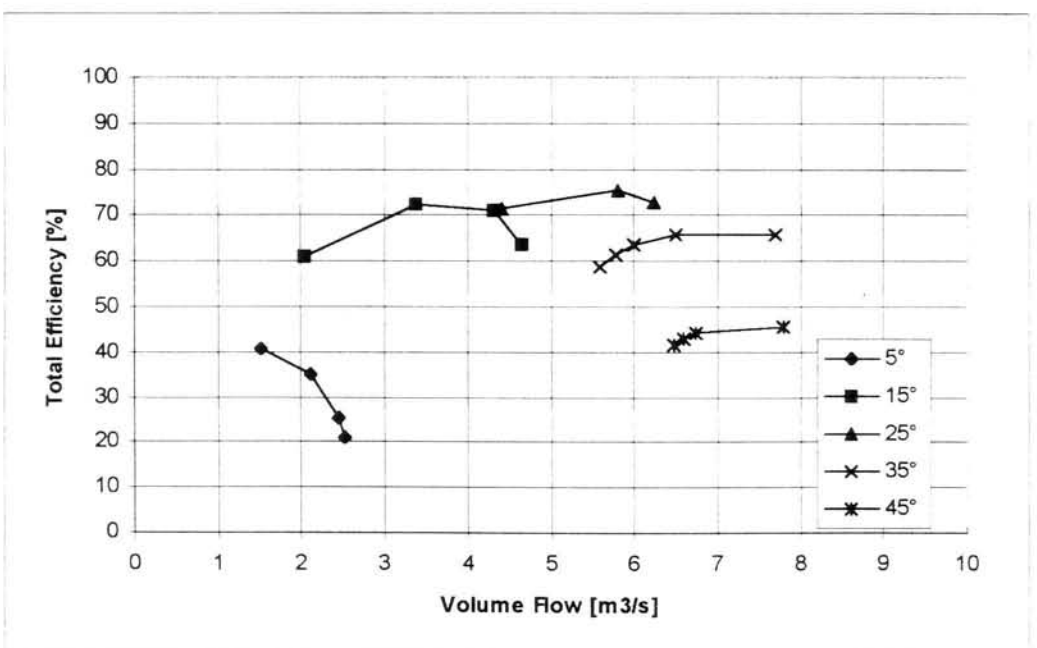

Figure 6.20: Total efficiency vs. volume flow for 800/150/5/1440 fan

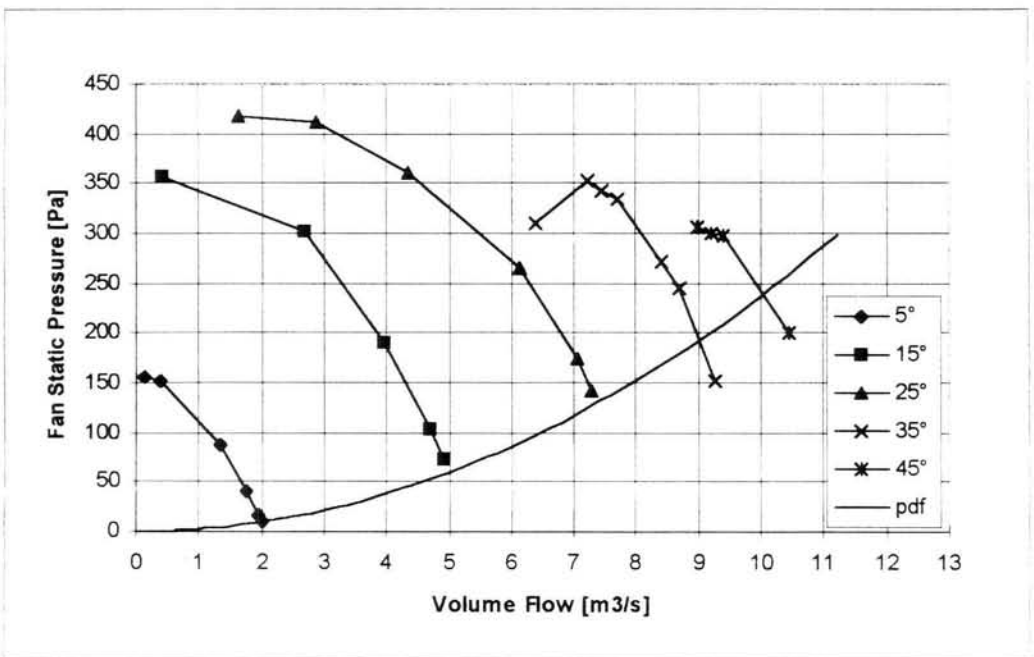

Figure 6.21: Static pressure vs. volume flow for 800/150/10/1440 fan

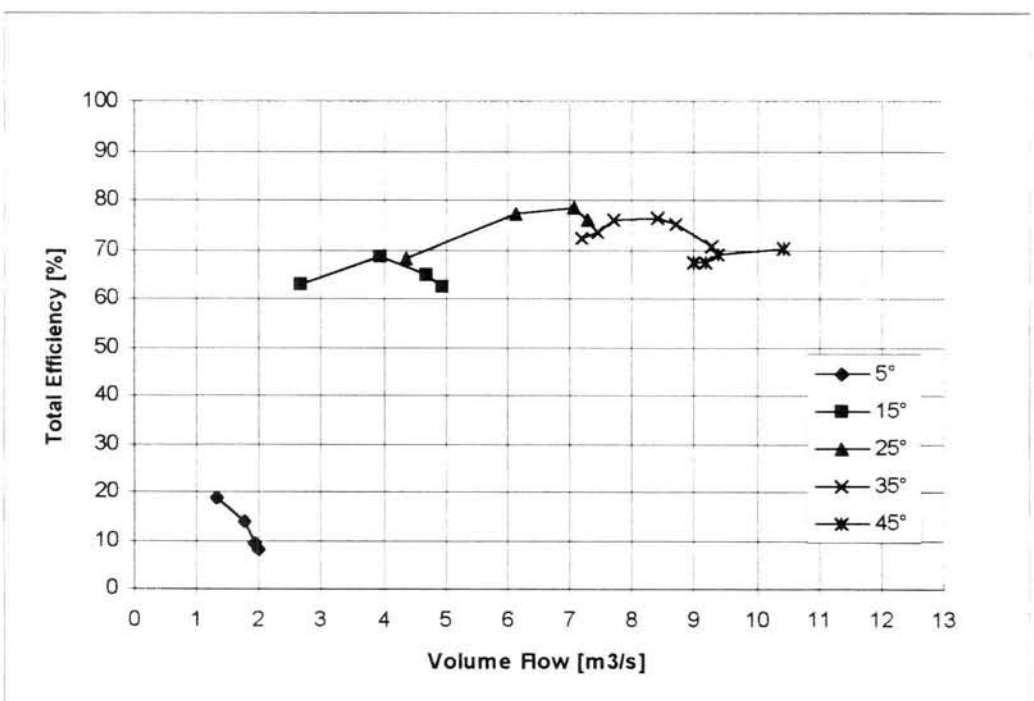

Figure 6.22: Total efficiency vs. volume flow for 800/150/10/1440 fan

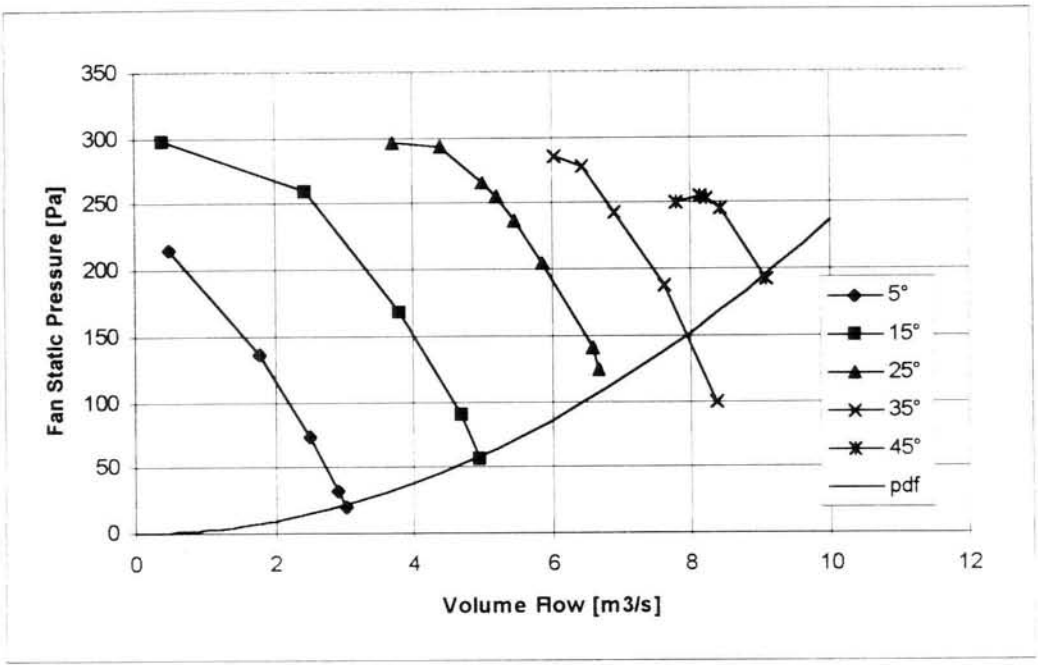

Figure 6.23: Static pressure vs. volume flow for 800/250/7/1440 fan

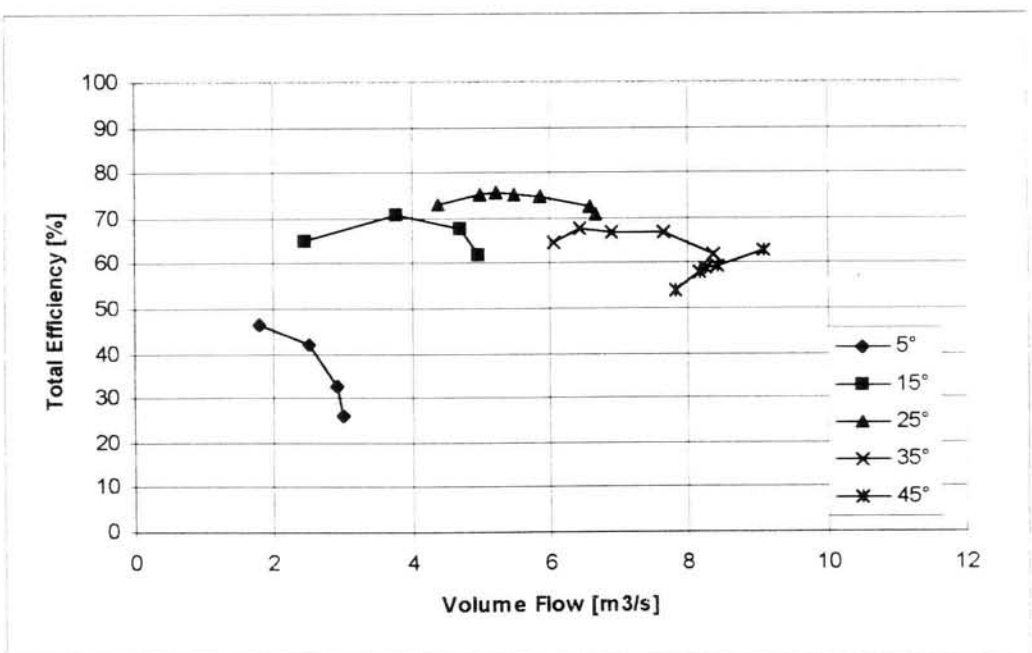

Figure 6.24: Total efficiency vs. volume flow for 800/250/7/1440 fan

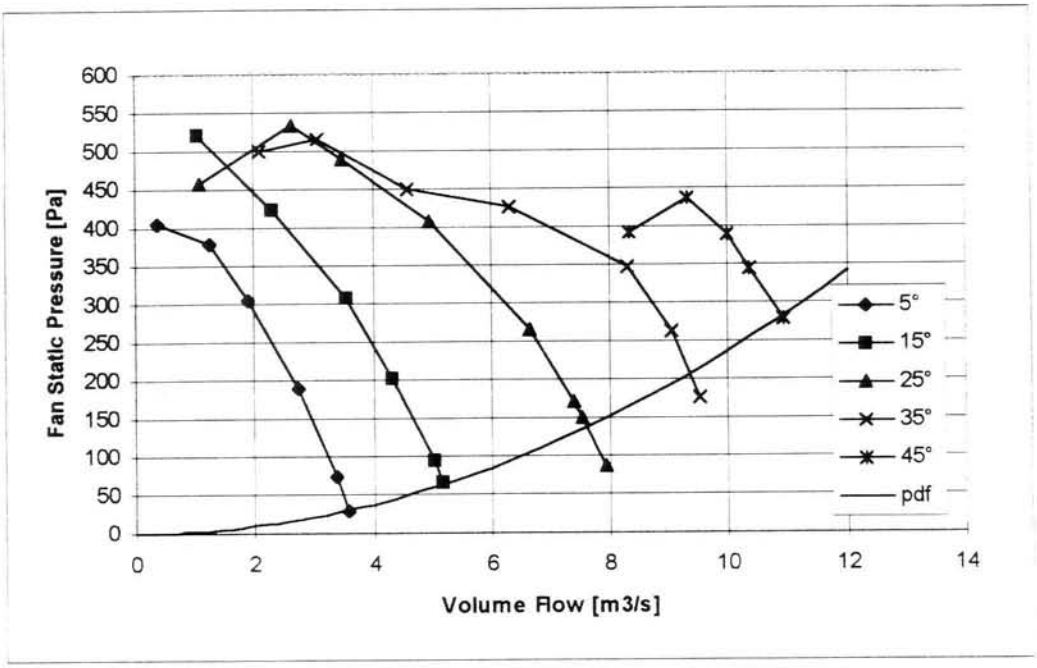

Figure 6.25: Static pressure vs. volume flow for 800/250/14/1440 fan

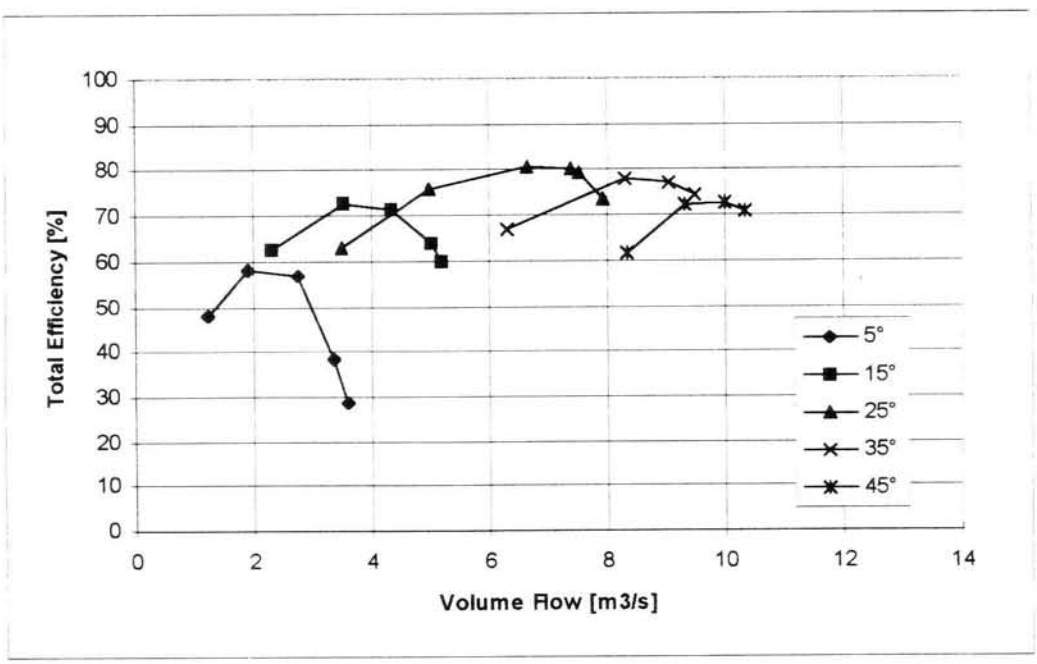

Figure 6.26: Total efficiency vs. volume flow for 800/250/14/1440 fan

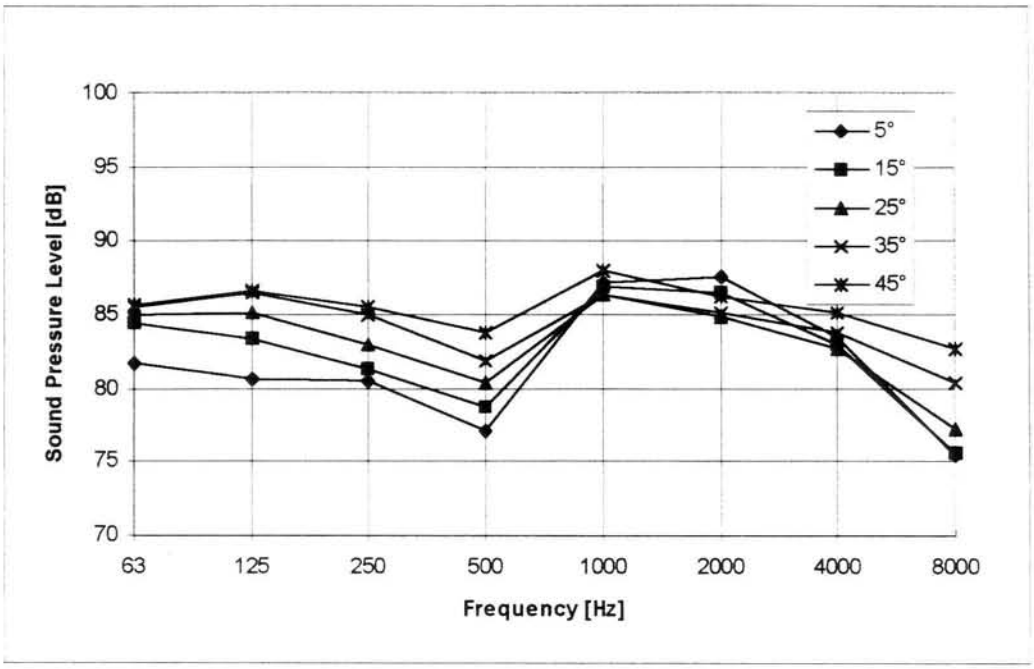

Figure 6.27: Sound pressure levels for 483/150/10/1440 fan

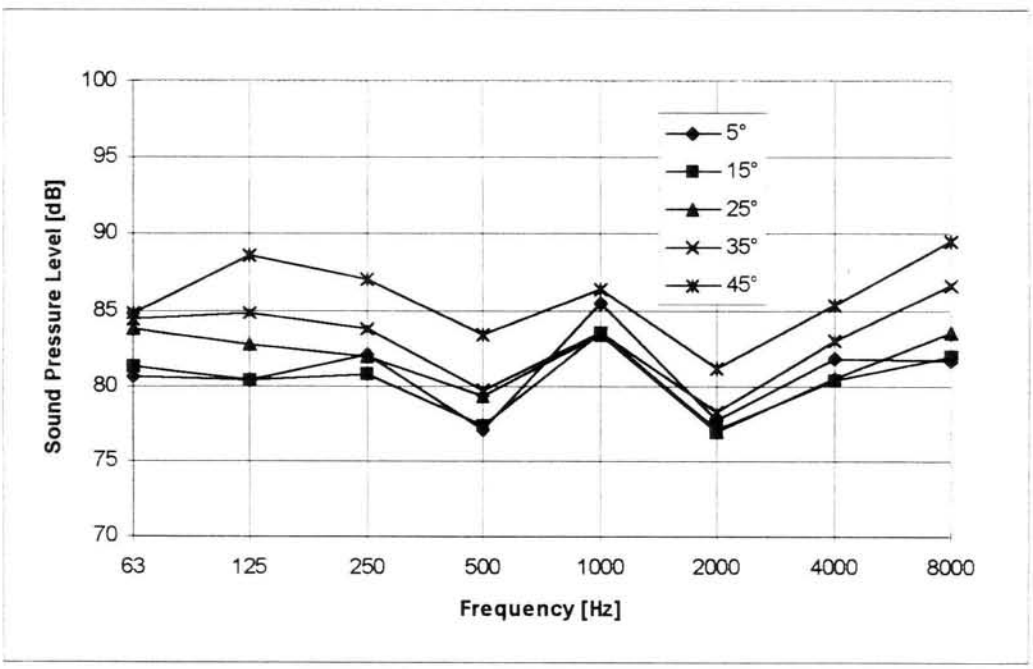

Figure 6.28: Sound pressure levels for 630/150/5/1440 fan

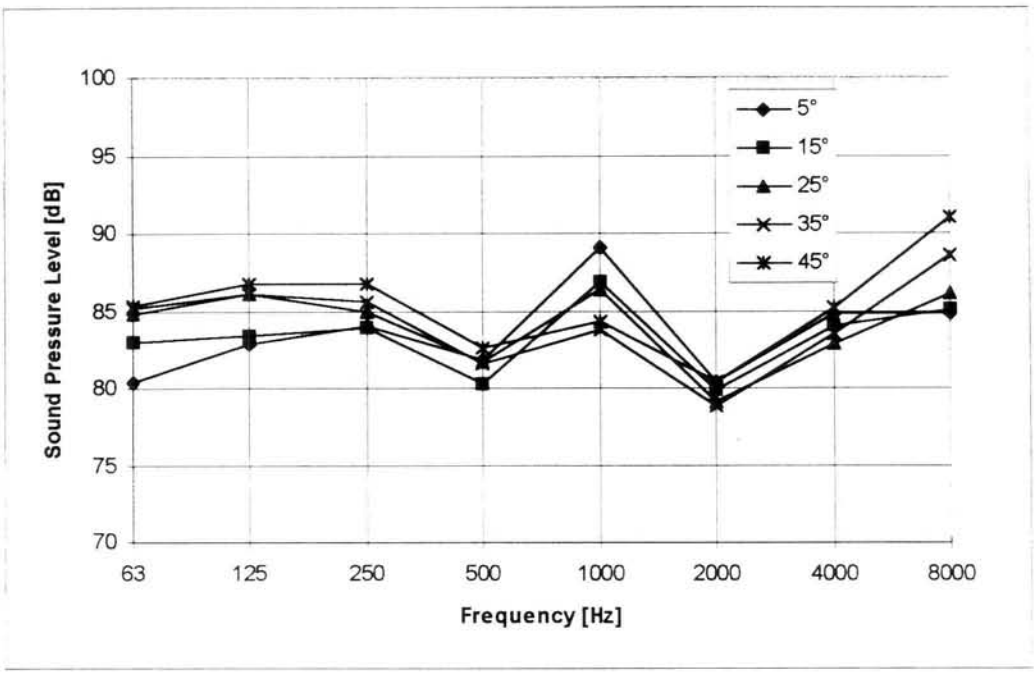

Figure 6.29: Sound pressure levels for 630/150/10/1440 fan

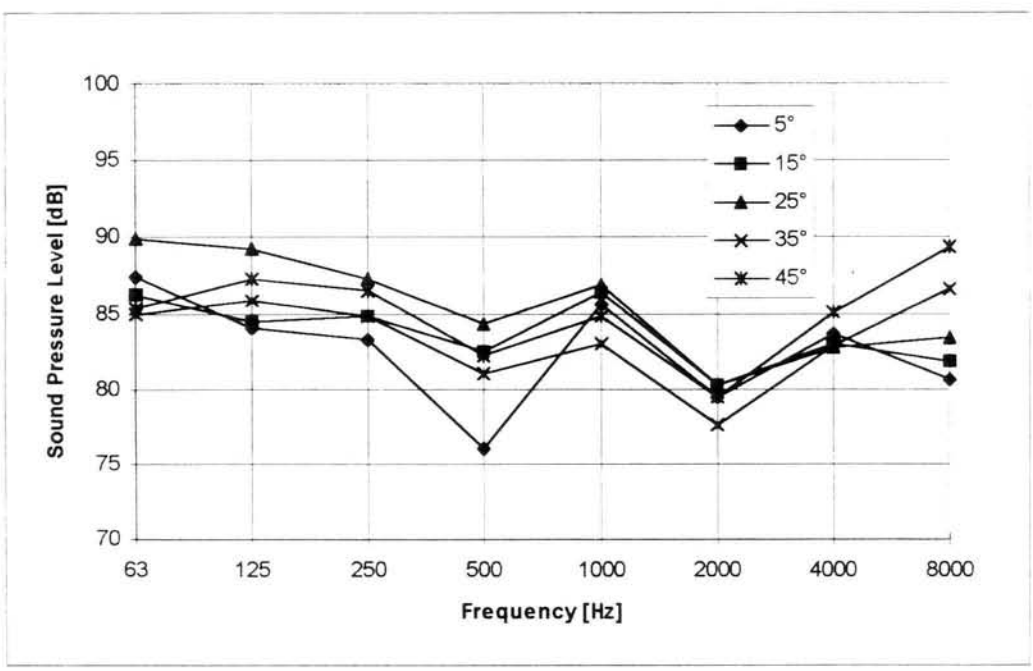

Figure 6.30: Sound pressure levels for 630/250/7/1440 fan

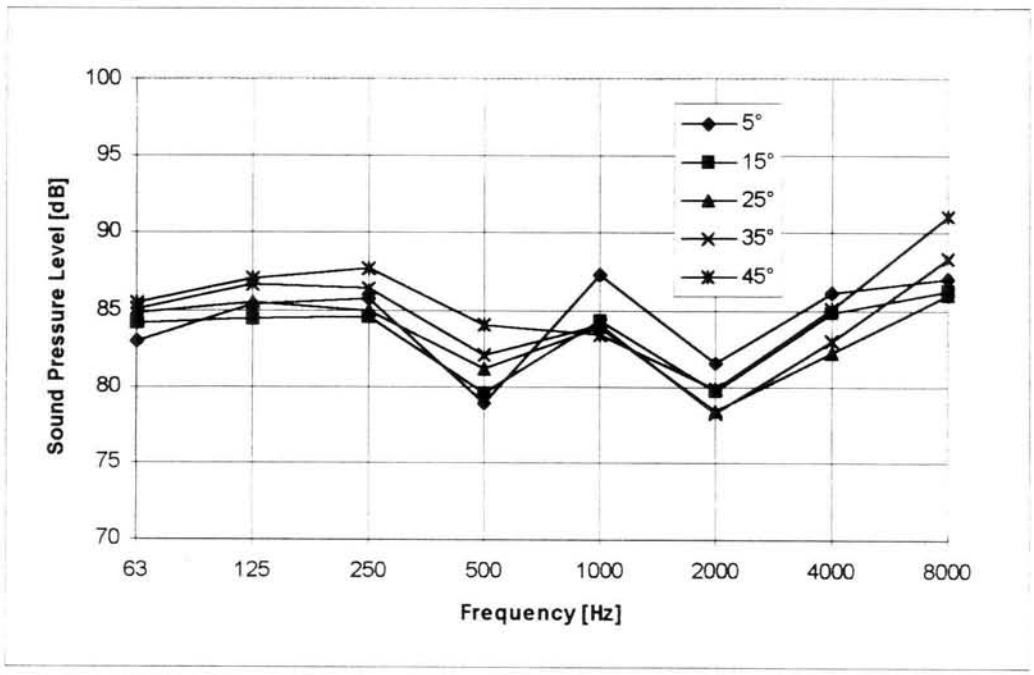

Figure 6.31: Sound pressure levels for 630/250/14/1440 fan

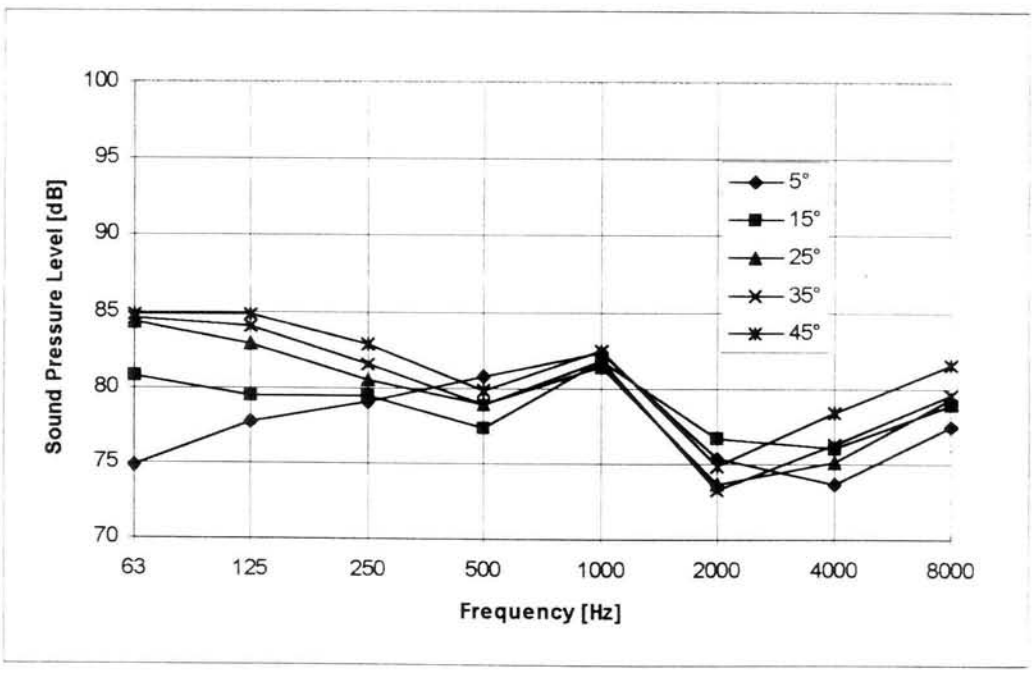

Figure 6.32: Sound pressure levels for 630/150/10/960 fan

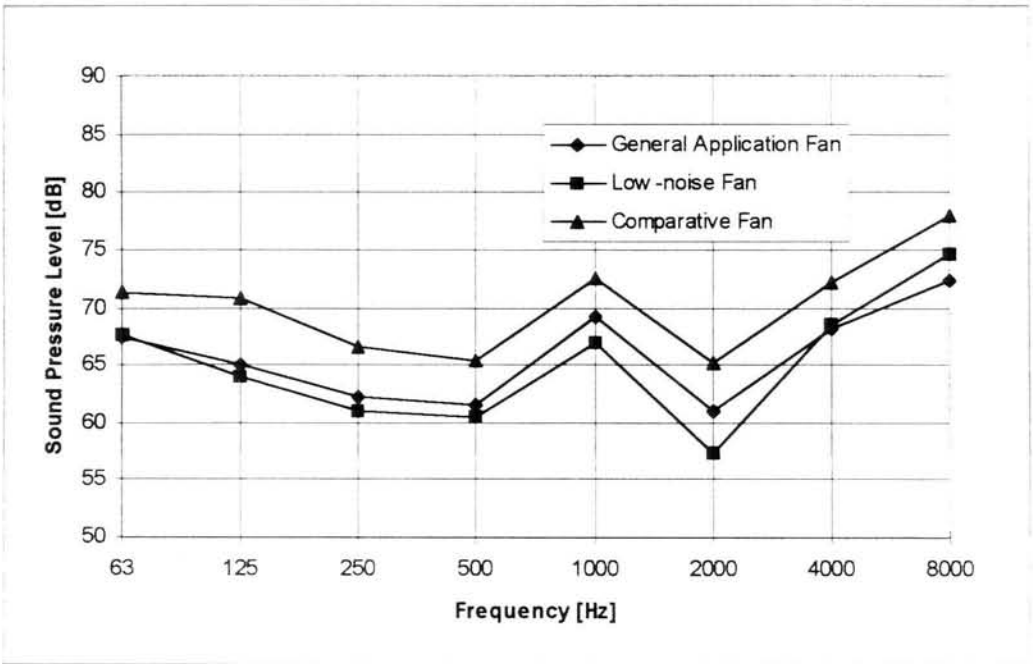

Figure 6.33: Comparison of sound pressure levels of three different fans at 720 rpm

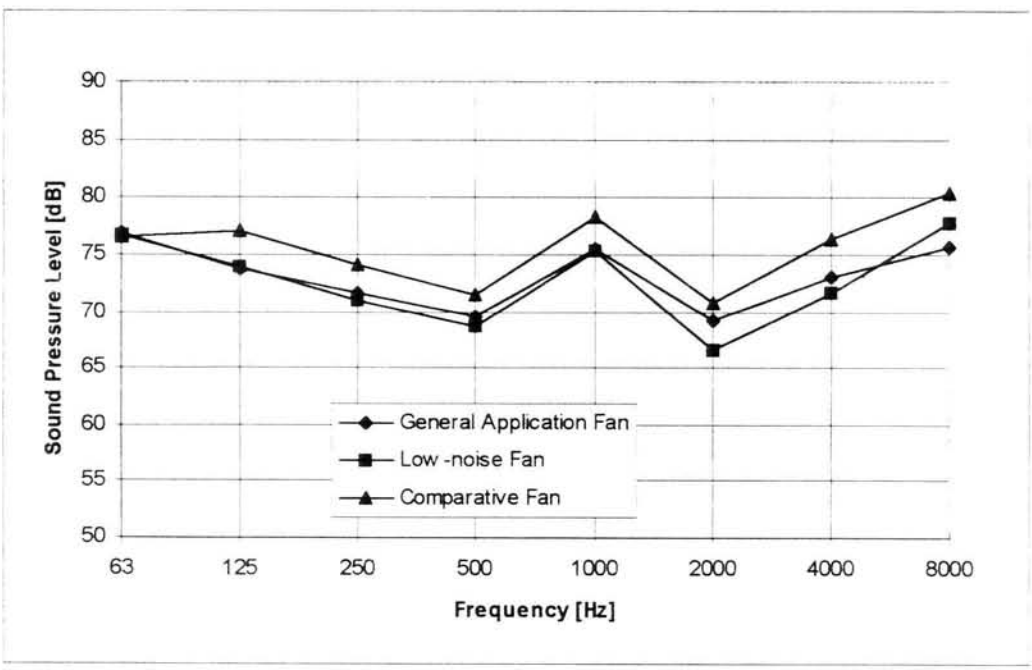

Figure 6.34: Comparison of sound pressure levels of three different fans at 960 rpm.

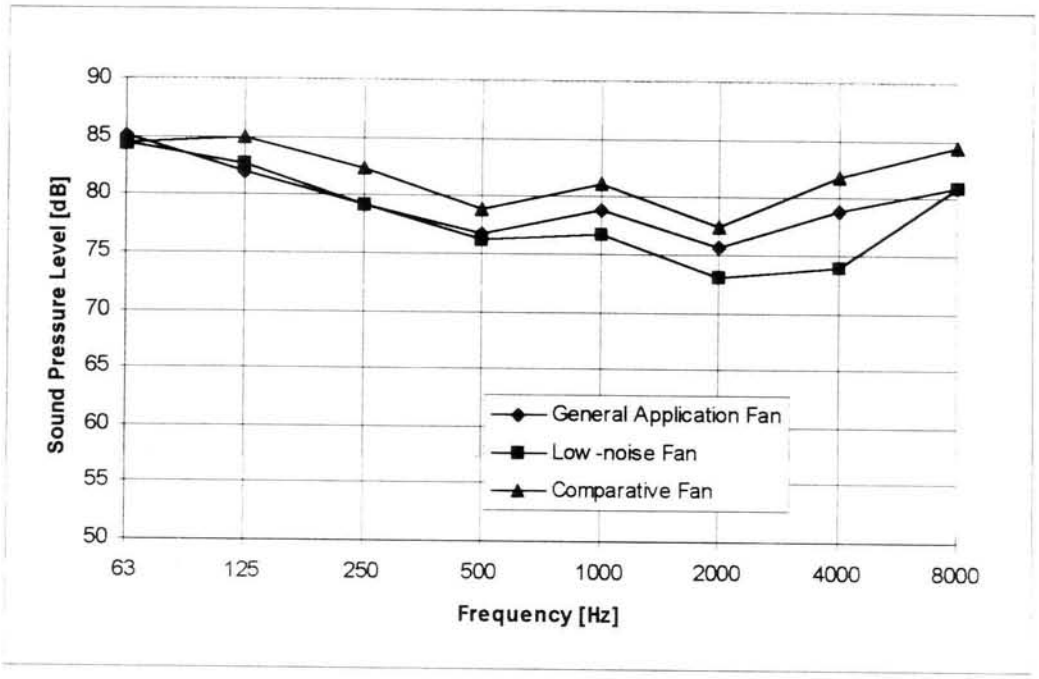

Figure 6.35: Comparison of sound pressure levels of three different fans at 1200 rpm

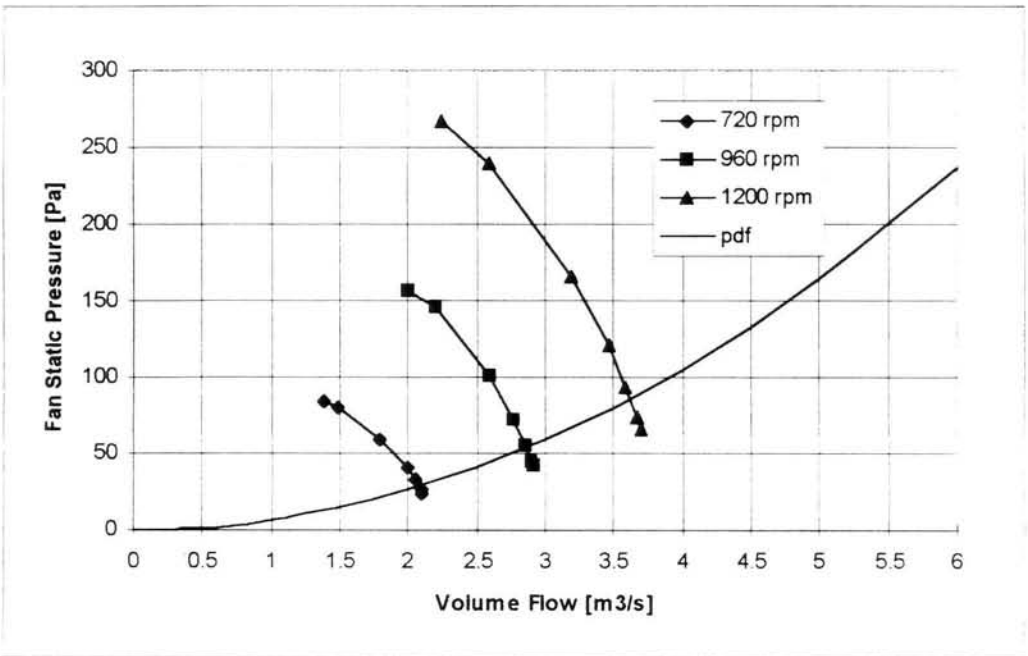

Figure 6.36: Static pressure vs. volume flow for low-noise fan

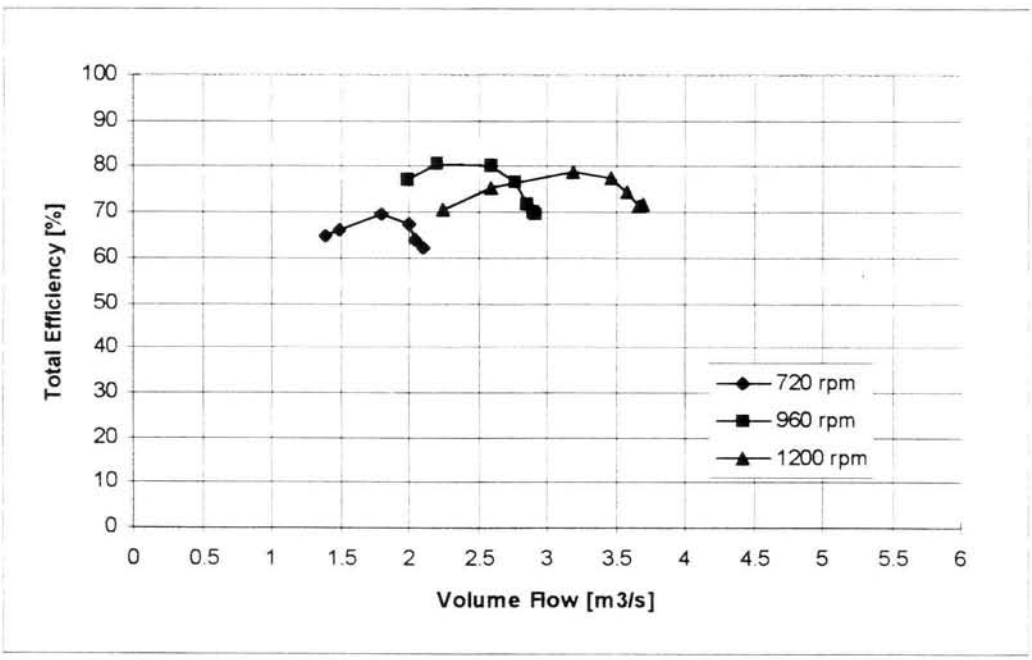

Figure 6.37: Total efficiency vs. volume flow for low-noise fan

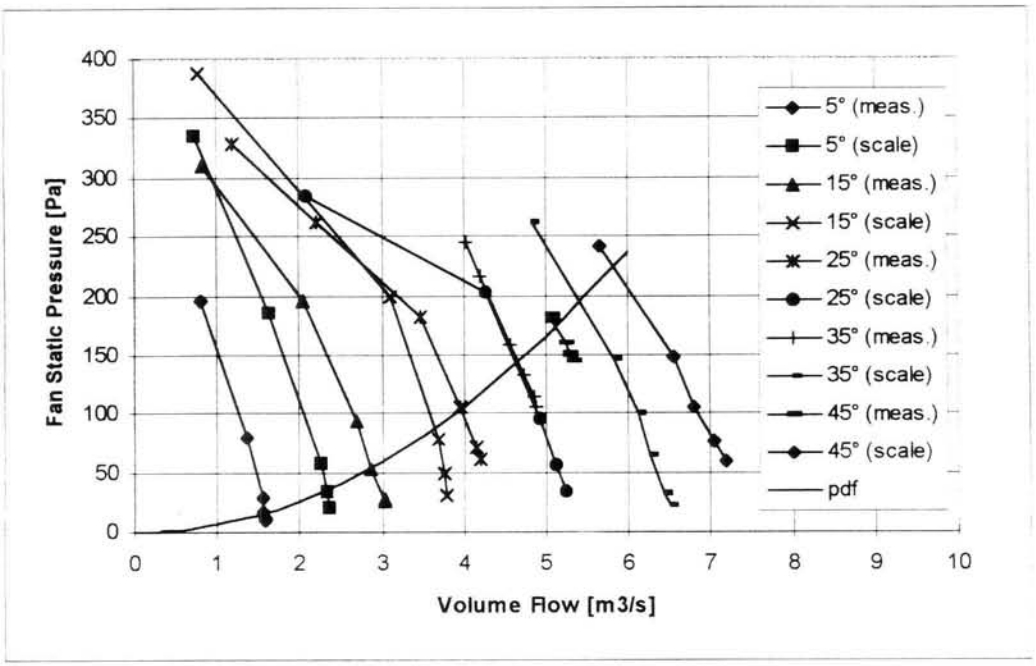

Figure 6.38: Static pressure measured and scaled for diameter for 630/150/10/1440 fan

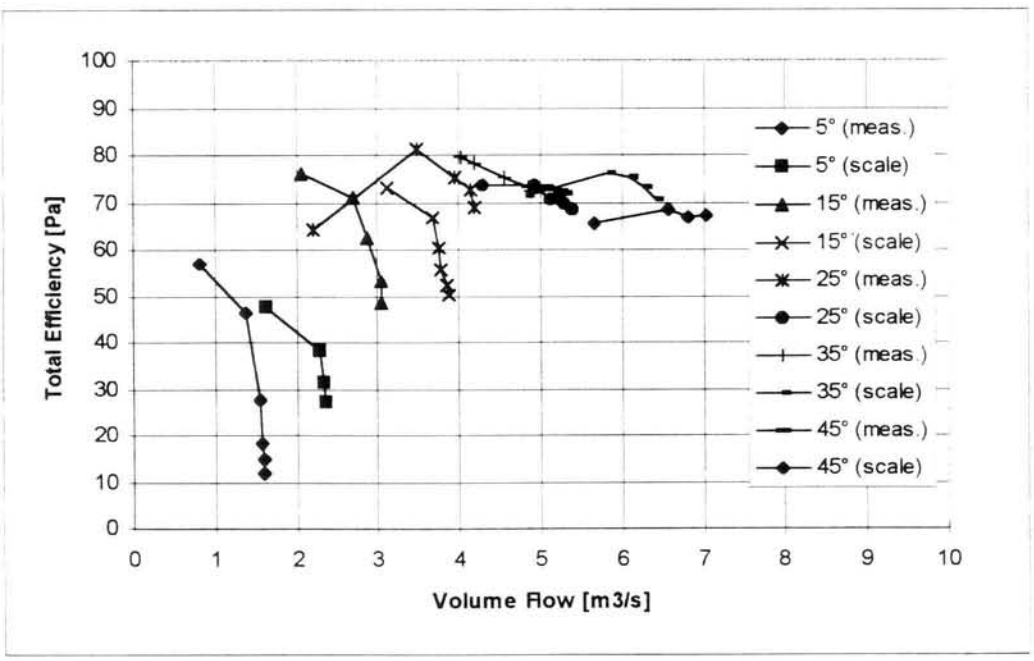

Figure 6.39: Total efficiency measured and scaled for diameter for 630/150/10/1440 fan

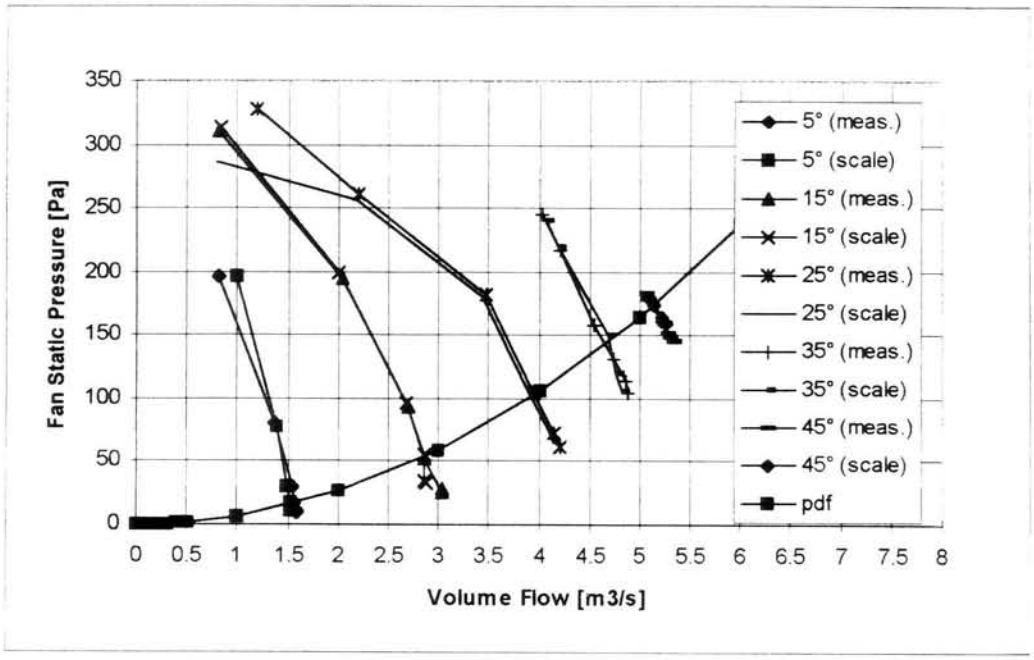

Figure 6.40: Static pressure measured and scaled for fan speed for 630/150/10/1440 fan

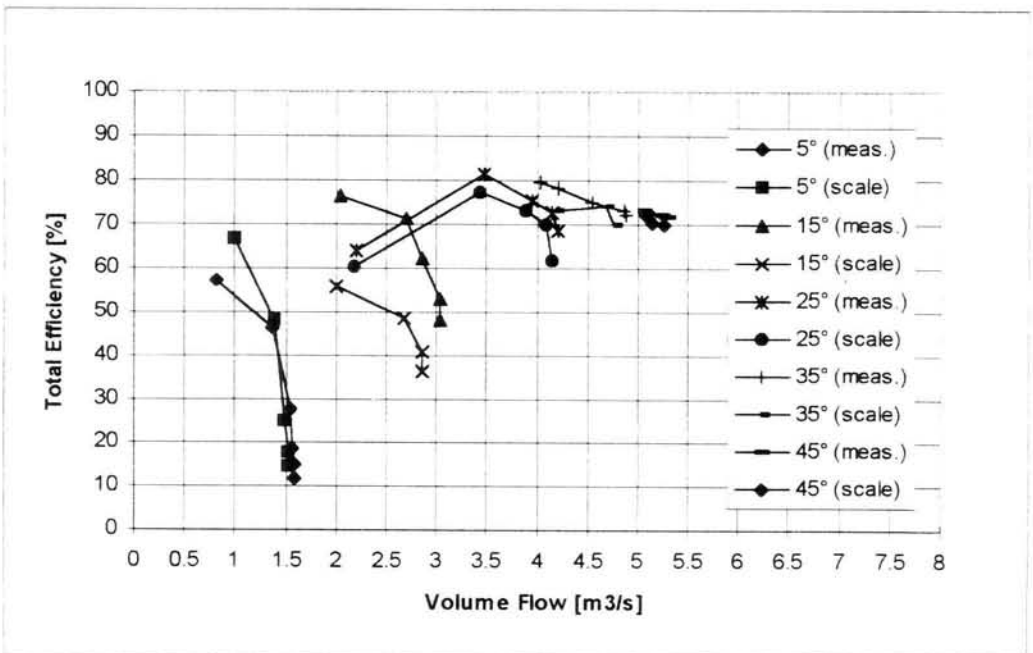

Figure 6.41: Total efficiency measured and scaled for fan speed for 630/150/10/1440 fan

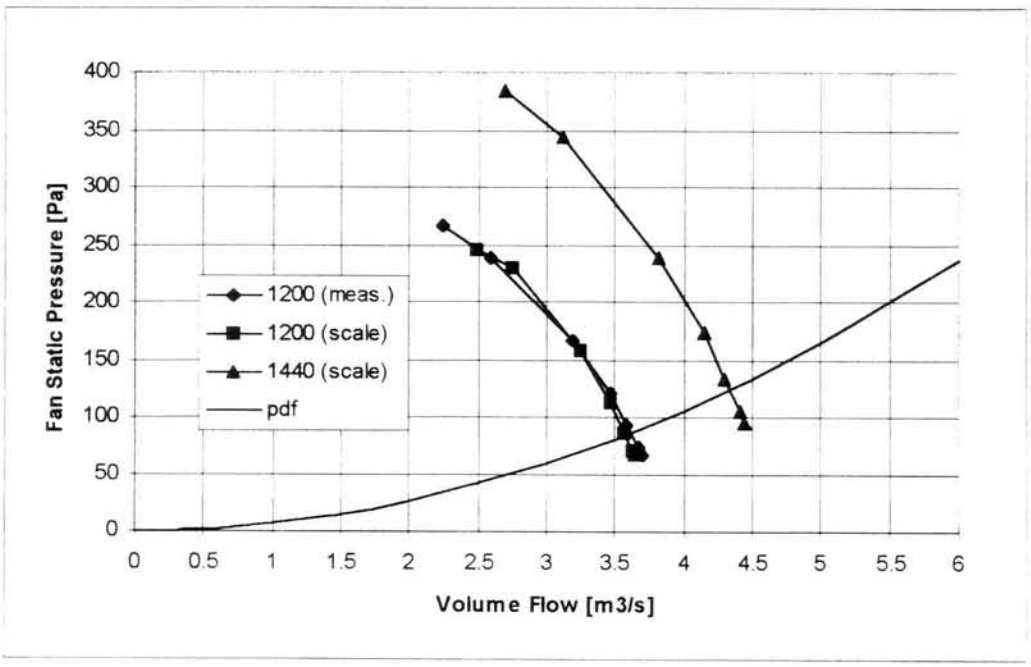

Figure 6.42: Static pressure measured and scaled for fan speed for low-noise fan

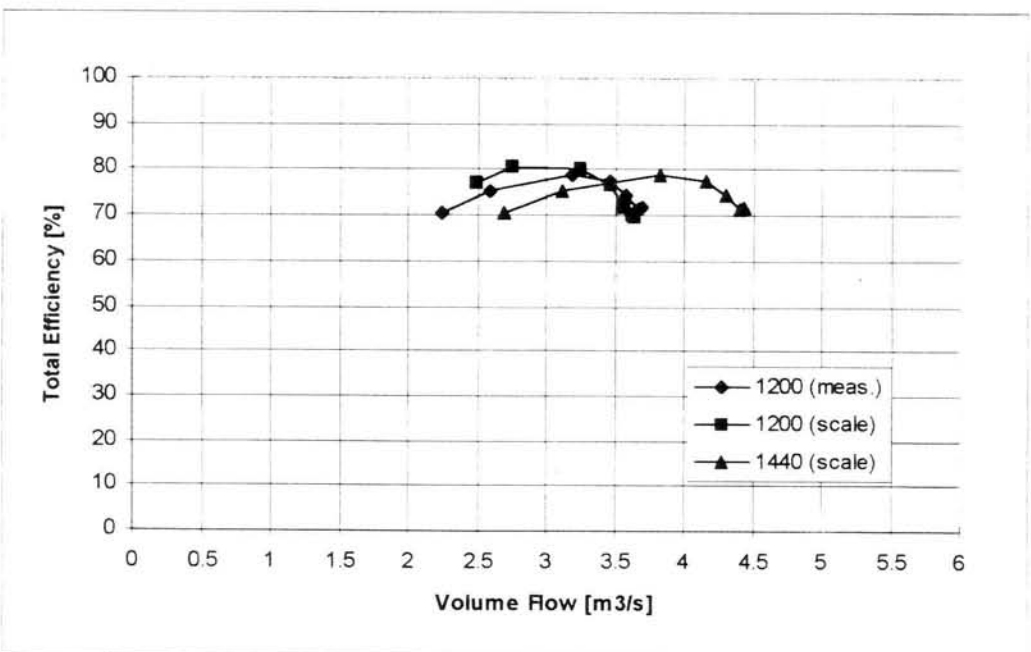

Figure 6.43: Total efficiency measured and scaled for fan speed for low-noise fan

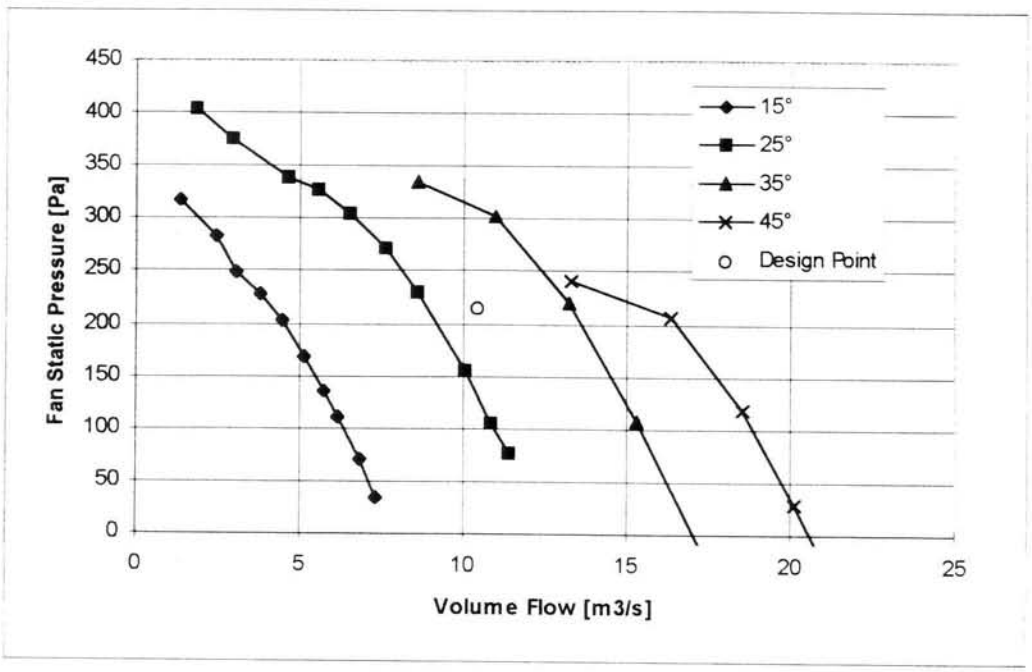

Figure 7.1: Test data for 1000/250/7/720 fan, scaled to 1440 rpm and compared with design point

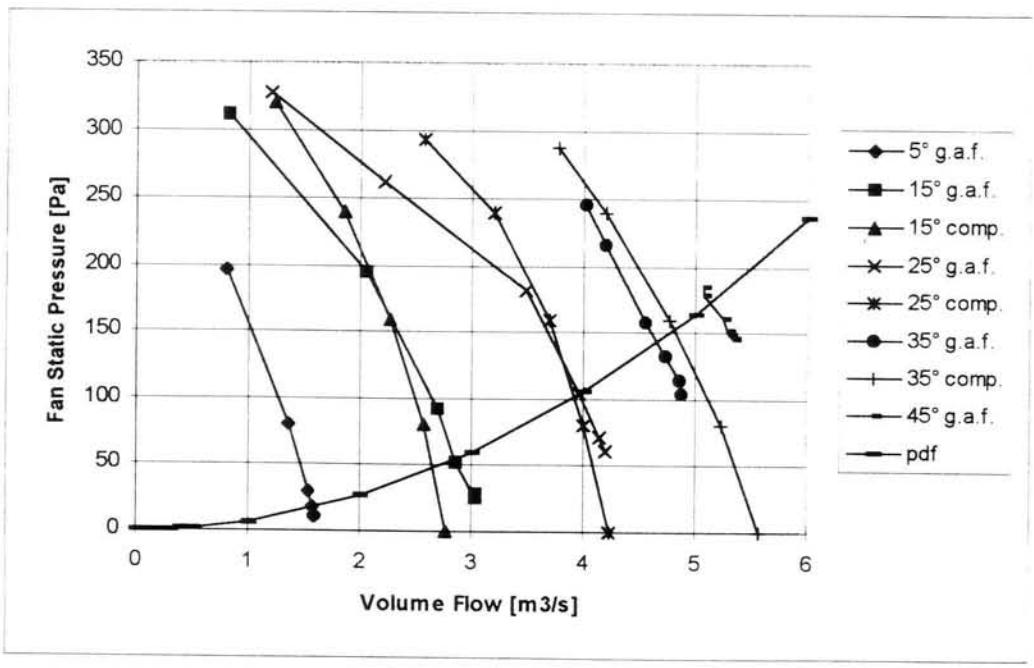

Figure 7.2: Comparison of fan static pressure vs. volume flow for general application fan and comparative fan for 630/150/10/1440 configuration

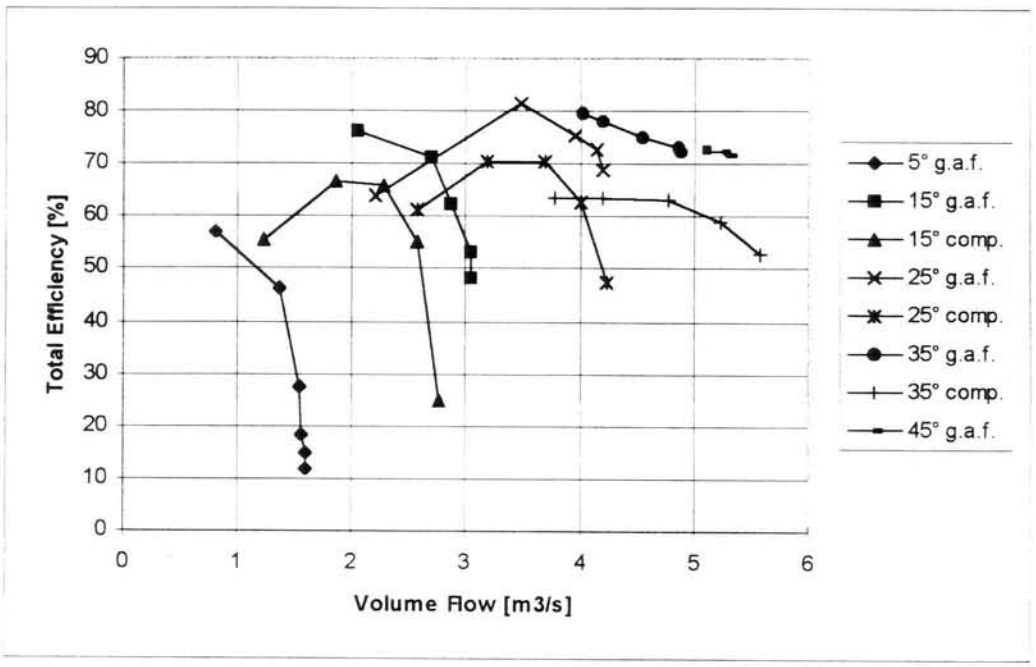

Figure 7.3: Comparison of fan total efficiency vs. volume flow for general application fan and comparative fan for 630/150/10/1440 configuration

9. TABLES

Table 6.13: Sound data for 483/150/10/1440 fan

Volume Flow	Sound Pressure Level per Octave Band [dB]							
[m3/s]	63 HZ	125 Hz	250 Hz	500 Hz	1000 Hz	2000 Hz	4000 Hz	8000 Hz
5° Blade Angle								
1.131	80.1	80.5	81.2	75.7	86.4	87.8	83.5	75.3
1.094	80.7	80.4	80.6	76.1	86.2	88.0	83.3	75.2
1.065	80.7	80.0	80.9	76.4	86.9	87.9	83.5	75.2
1.049	82.4	80.6	80.6	75.5	86.5	87.9	83.9	76.0
1.022	82.8	80.3	79.9	75.6	87.7	87.5	83.8	76.2
0.732	83.6	82.0	80.0	83.0	89.4	86.4	83.0	75.2
15° Blade Angle								
1.743	83.8	82.4	80.8	79.2	87.2	87.2	83.6	76.7
1.729	84.2	83.0	81.3	78.4	86.7	87.1	83.4	76.3
1.703	84.8	83.0	81.3	78.5	87.2	87.0	83.2	76.1
1.691	84.6	82.7	80.8	78.7	87.2	86.5	82.9	75.5
1.658	85.0	83.5	81.1	78.4	86.5	85.7	82.7	75.1
1.399	84.6	85.5	82.9	79.2	86.8	85.2	81.8	74.2
25° Blade Angle								
2.428	85.1	84.7	82.5	80.8	87.9	86.1	83.9	79.0
2.390	84.5	84.9	82.6	80.6	87.3	85.5	83.4	78.3
2.367	84.7	84.6	82.6	80.1	87.0	85.4	83.0	77.8
2.307	85.0	84.7	82.8	80.8	86.3	84.9	82.6	77.3
2.223	85.9	85.9	83.2	79.5	84.7	83.5	81.5	75.7
1.930	84.9	86.0	83.8	80.8	84.8	83.7	81.6	75.1
35° Blade Angle								
2.927	84.3	85.7	84.7	82.1	87.0	86.1	84.7	81.7
2.894	85.7	86.5	84.9	82.1	87.4	85.4	84.1	81.0
2.824	85.4	86.6	84.4	81.7	87.2	85.7	84.1	80.9
2.754	85.4	86.9	85.0	81.6	85.7	84.9	83.5	80.0
2.623	86.2	85.6	84.4	81.2	85.9	84.4	83.1	79.5
2.178	86.3	87.5	86.2	82.6	85.0	84.4	83.0	79.1
45° Blade Angle								
3.239	86.4	87.5	85.5	84.3	87.8	86.0	85.2	83.6
3.170	86.1	86.1	85.2	83.9	87.5	86.1	85.4	83.6
3.068	85.5	86.1	85.4	84.6	88.1	86.4	85.6	83.7
2.955	85.2	86.1	85.7	84.7	87.6	86.1	85.3	83.3
2.547	85.7	86.7	85.8	82.9	86.6	85.3	84.7	81.8
1.810	84.9	87.6	86.2	82.2	90.7	87.4	84.3	80.1

Table 6.14: Sound data for 630/150/5/1440 fan

Volume Flow	Sound Pressure Level per Octave Band [dB]							
[m3/s]	63 HZ	125 Hz	250 Hz	500 Hz	1000 Hz	2000 Hz	4000 Hz	8000 Hz
5° Blade Angle								
1.777	79.3	81.6	83.0	76.9	85.1	79.3	83.7	83.8
1.771	80.1	81.2	82.4	75.7	85.3	78.5	83.1	82.8
1.764	80.8	80.5	81.9	75.6	86.0	78.0	82.2	81.9
1.666	81.0	79.6	81.3	77.3	86.7	77.4	81.2	80.7
1.339	81.6	79.0	81.9	79.7	84.2	75.4	78.9	78.9
15° Blade Angle								
2.786	80.2	78.9	79.6	76.3	82.1	75.9	79.5	81.6
2.754	82.1	79.7	79.5	75.0	82.5	74.6	78.6	79.9
2.654	79.9	80.6	81.1	78.3	83.6	77.8	80.9	82.3
2.369	82.6	82.5	82.9	79.6	85.9	79.9	82.5	83.8
25° Blade Angle								
3.681	83.0	82.4	81.7	79.7	83.1	76.6	79.9	83.3
3.654	82.5	81.6	80.9	78.2	82.6	76.2	79.3	83.0
3.450	84.8	83.2	82.3	79.5	83.5	77.1	80.4	83.4
3.048	84.5	83.9	82.8	79.8	84.0	78.1	82.0	84.6
35° Blade Angle								
4.260	84.3	85.0	84.0	80.2	83.7	78.5	83.1	87.2
4.221	84.2	84.2	83.2	79.5	83.4	78.0	82.6	86.8
4.054	84.2	84.4	83.7	79.4	83.2	78.1	82.8	86.3
3.797	85.0	85.5	84.4	79.9	83.5	78.3	83.2	86.5
45° Blade Angle								
5.154	85.0	88.6	87.1	83.7	86.8	81.1	85.3	89.7
5.137	84.6	88.4	87.0	83.5	86.0	81.1	85.4	89.5
5.110	84.8	88.8	87.1	82.6	86.6	81.4	85.4	89.7
5.077	85.0	88.5	87.1	83.8	86.2	81.1	85.3	89.3

Table 6.15: Sound data for 630/150/10/1440 fan

Volume Flow	Sound Pressure Level per Octave Band [dB]							
[m3/s]	63 HZ	125 Hz	250 Hz	500 Hz	1000 Hz	2000 Hz	4000 Hz	8000 Hz
5° Blade Angle								
1.586	79.9	82.6	83.5	78.6	88.3	79.6	84.7	83.4
1.586	81.0	83.6	84.8	81.2	89.3	81.2	85.9	86.3
1.564	80.7	83.3	84.2	81.5	89.3	80.8	85.3	85.5
1.543	80.3	82.9	83.8	82.0	90.1	80.1	84.7	84.8
1.365	79.8	82.1	83.5	85.6	88.6	79.9	83.5	83.9
15° Blade Angle								
3.036	81.8	82.7	83.6	79.3	85.5	79.7	84.5	85.9
3.036	81.8	82.7	83.4	78.8	85.7	79.7	84.6	85.6
2.860	83.3	82.9	83.3	78.3	85.9	79.5	83.8	84.8
2.698	83.3	84.2	84.6	77.5	87.6	80.6	84.6	84.8
2.047	84.5	84.2	84.6	87.2	89.4	80.0	82.9	84.3
25° Blade Angle								
4.200	85.3	85.2	83.8	80.8	84.9	78.7	82.2	87.1
4.149	84.6	84.9	83.8	80.9	84.6	78.4	82.0	86.4
3.956	84.6	84.3	83.8	79.2	85.2	78.2	82.3	86.1
3.476	85.1	86.0	86.0	83.7	88.9	81.0	84.0	86.5
2.206	84.4	90.2	87.5	83.6	88.2	79.1	83.4	84.6
35° Blade Angle								
4.878	85.1	85.8	85.5	81.7	83.6	78.9	83.4	89.2
4.860	84.9	85.7	85.3	81.1	83.5	78.9	83.3	88.9
4.739	85.1	86.1	85.7	81.4	83.6	79.0	83.5	89.1
4.553	85.5	86.2	85.5	81.8	83.8	78.8	83.3	87.9
4.203	85.5	86.6	85.8	82.0	84.3	78.6	83.8	88.0
45° Blade Angle								
6.294	85.5	86.3	86.9	82.5	84.3	80.4	85.4	91.8
6.242	85.4	87.1	86.7	83.0	84.5	80.5	85.3	91.4
6.225	85.2	86.8	86.7	82.2	84.2	80.3	85.3	90.7
6.178	85.3	86.9	86.8	82.4	84.3	80.2	84.9	90.5

Table 6.16: Sound data for 630/250/7/1440 fan

Volume Flow	Sound Pressure Level per Octave Band [dB]							
[m3/s]	63 HZ	125 Hz	250 Hz	500 Hz	1000 Hz	2000 Hz	4000 Hz	8000 Hz
5° Blade Angle								
2.073	87.0	84.0	83.6	76.3	85.0	79.1	84.3	81.5
2.060	87.6	84.2	83.5	75.8	84.6	79.2	84.0	80.9
2.021	87.7	84.4	83.2	75.7	85.4	79.2	83.7	80.7
1.971	87.8	84.1	83.0	75.6	85.3	79.5	83.2	80.3
1.859	86.9	83.3	82.8	76.7	87.3	80.4	82.6	79.7
15° Blade Angle								
2.868	85.5	82.9	83.3	79.0	84.5	78.4	82.0	81.2
2.800	85.3	83.4	84.4	80.0	84.8	78.9	82.1	80.6
2.677	86.4	84.1	83.9	80.4	84.9	78.8	81.9	80.0
2.436	87.0	85.8	86.2	81.3	86.9	81.8	84.0	83.0
1.914	87.1	85.9	86.1	91.3	90.6	82.9	84.6	84.2
25° Blade Angle								
3.921	88.6	87.2	85.9	83.6	88.1	79.9	82.1	83.2
3.798	89.9	89.1	86.8	84.1	87.1	79.9	82.2	83.3
3.567	89.6	88.8	87.2	84.0	86.9	79.8	82.1	82.6
3.247	90.8	90.6	87.9	83.8	85.2	79.9	82.8	83.0
2.962	90.5	90.6	88.6	86.0	87.0	81.8	84.6	84.7
35° Blade Angle								
4.522	84.2	85.4	84.2	80.8	82.3	77.8	82.3	86.8
4.459	84.9	85.5	84.5	80.9	82.6	77.8	82.5	86.9
4.309	84.6	85.7	84.8	80.9	82.6	77.6	82.7	86.8
3.988	84.7	85.8	84.9	80.7	83.0	77.1	82.6	85.9
3.446	85.9	86.7	85.6	81.4	84.1	77.5	83.9	86.7
45° Blade Angle								
5.655	85.3	86.8	86.1	81.5	83.6	79.1	84.8	90.5
5.540	85.4	87.0	86.0	81.6	84.2	79.1	85.3	89.9
5.269	85.3	86.7	86.5	82.1	84.5	79.0	84.6	88.8
5.030	85.5	88.8	87.4	83.5	86.8	80.7	85.4	88.5

Table 6.17: Sound data for 630/250/14/1440 fan

Volume Flow	Sound Pressure Level per Octave Band [dB]							
[m3/s]	63 HZ	125 Hz	250 Hz	500 Hz	1000 Hz	2000 Hz	4000 Hz	8000 Hz
5° Blade Angle								
1.886	82.8	85.2	86.4	78.4	86.5	81.2	86.8	87.3
1.874	82.3	84.7	85.8	77.9	86.1	80.6	86.6	86.6
1.868	83.3	85.5	86.5	79.0	86.6	81.8	87.2	87.8
1.849	83.3	85.3	86.2	78.8	86.9	82.0	86.8	87.6
1.819	83.1	85.4	85.5	77.7	87.5	82.4	85.8	87.1
1.642	83.0	85.9	84.1	81.5	89.8	81.6	83.9	85.7
15° Blade Angle								
3.288	84.4	84.8	84.9	79.8	84.6	80.1	85.1	86.8
3.288	84.3	84.3	84.4	79.6	84.5	79.6	84.8	86.1
3.275	83.9	84.1	84.5	79.1	83.5	79.5	84.4	85.9
25° Blade Angle								
4.372	84.5	85.1	84.4	80.4	83.8	78.3	82.1	86.3
4.328	84.7	85.1	84.6	80.8	83.7	78.1	82.0	86.1
4.198	84.8	85.4	85.0	81.6	83.7	78.2	82.1	86.1
3.683	85.3	86.5	85.9	81.6	84.4	79.1	82.5	85.4
35° Blade Angle								
5.111	84.8	86.5	86.2	82.2	83.0	78.6	83.0	89.0
5.024	84.7	86.3	86.3	82.0	83.0	78.7	83.0	89.0
4.714	85.7	86.9	86.3	81.7	87.2	77.9	82.6	87.9
4.328	85.3	86.9	86.8	82.4	82.8	77.7	83.0	87.3
45° Blade Angle								
6.642	85.4	87.0	87.9	84.0	83.4	80.1	84.9	91.4
6.586	85.4	87.1	87.6	84.4	83.7	80.1	85.4	91.9
6.451	85.5	87.1	87.6	83.8	83.1	79.7	84.9	91.1
6.252	85.6	87.0	87.5	83.9	83.5	79.7	84.9	90.5
5.759	85.4	86.8	87.8	84.1	83.3	79.3	85.1	90.3

Table 6.18: Sound data for 630/150/10/960 fan

Volume Flow	Sound Pressure Level per Octave Band [dB]							
[m3/s]	63 HZ	125 Hz	250 Hz	500 Hz	1000 Hz	2000 Hz	4000 Hz	8000 Hz
5° Blade Angle								
1.019	74.2	77.6	79.5	79.2	83.3	78.0	75.3	77.9
1.019	78.0	78.9	79.6	87.1	81.9	70.6	70.3	77.6
1.019	74.9	77.7	79.5	79.9	82.9	77.8	75.4	77.7
0.997	71.6	74.4	76.7	77.2	81.3	74.7	72.8	75.8
0.928	75.5	80.1	79.6	80.6	82.2	75.7	74.4	78.4
15° Blade Angle								
1.921	79.7	79.2	79.6	76.5	81.7	77.7	76.7	80.9
1.909	79.5	79.1	79.3	76.8	82.0	77.7	74.7	80.7
1.903	80.4	79.1	79.1	76.5	82.1	77.1	77.0	79.5
1.783	81.3	79.7	78.9	75.7	82.1	76.7	77.0	77.1
1.333	82.7	80.3	80.7	81.2	80.9	74.1	74.4	76.7
25° Blade Angle								
2.761	84.9	82.0	80.0	79.2	81.1	73.6	75.1	79.8
2.725	84.2	81.5	79.7	79.9	81.3	73.2	74.9	79.7
2.589	84.1	81.5	79.5	77.7	81.4	73.2	75.0	80.0
2.292	84.5	82.4	81.3	78.5	81.8	74.2	75.9	79.0
1.457	83.6	87.0	81.9	79.0	81.1	73.9	74.9	77.7
35° Blade Angle								
3.221	84.4	83.8	81.4	79.5	81.5	73.5	76.0	79.8
3.176	84.4	83.9	81.3	79.1	82.1	73.0	76.3	79.9
3.117	84.4	84.2	81.6	79.2	81.5	73.3	76.4	79.7
2.794	85.0	84.4	81.8	78.0	81.9	73.2	76.6	79.0
45° Blade Angle								
4.141	85.0	85.0	82.8	79.6	82.8	74.8	78.5	82.0
4.115	85.1	85.1	82.9	80.6	81.9	75.0	78.3	81.2
4.000	85.1	84.9	82.9	79.5	82.7	74.9	78.4	81.6
4.049	84.2	84.4	82.5	79.3	82.3	74.6	78.1	81.1

Table 6.19: Sound data for three different fans at 720 rpm

Volume Flow	Sound Pressure Level per Octave Band [dB]							
[m3/s]	63 HZ	125 Hz	250 Hz	500 Hz	1000 Hz	2000 Hz	4000 Hz	8000 Hz
General Application Fan								
2.154	67.3	65.2	62.5	62.1	69.7	61.7	68.0	72.6
2.138	66.9	64.8	62.3	60.9	70.0	60.4	68.0	71.7
2.102	67.3	64.6	62.0	62.1	69.0	61.1	68.3	72.3
2.012	67.0	64.9	61.6	61.2	68.7	61.1	68.4	72.7
1.847	68.5	65.8	63.1	61.5	69.0	60.7	68.3	72.2
Low-noise Fan								
2.100	67.8	64.0	61.2	60.9	67.3	57.5	68.5	76.2
2.100	67.5	64.1	61.2	60.2	66.9	57.4	68.9	74.2
2.049	67.5	63.8	61.0	60.7	66.8	57.3	68.1	73.8
1.996	67.6	63.7	61.0	60.3	66.7	57.2	68.5	74.0
Comparative Fan								
2.110	71.6	70.7	66.3	65.9	73.1	65.6	72.3	77.9
2.100	71.4	70.5	66.1	64.8	72.8	65.3	72.4	78.3
2.020	71.1	71.1	66.6	65.3	72.6	65.0	72.5	77.8
1.950	71.4	71.2	67.2	65.3	72.0	64.6	71.8	78.1

Table 6.20: Sound data for three different fans at 960 rpm

Volume Flow	Sound Pressure Level per Octave Band [dB]							
[m3/s]	63 HZ	125 Hz	250 Hz	500 Hz	1000 Hz	2000 Hz	4000 Hz	8000 Hz
General Application Fan								
2.879	76.4	73.5	71.4	70.0	75.4	70.4	73.4	76.3
2.864	76.1	73.0	71.0	69.7	75.7	69.5	73.2	75.7
2.807	76.8	73.3	71.0	69.6	75.2	69.3	73.1	75.3
2.689	77.0	73.8	71.7	68.9	75.7	68.5	73.1	75.6
2.462	78.4	75.2	72.7	70.0	75.7	68.3	72.8	75.4
Low-noise Fan								
2.923	77.1	74.4	71.3	69.3	76.3	67.5	71.5	79.2
2.919	76.4	74.3	71.2	68.8	75.5	67.0	71.8	78.6
2.867	76.1	73.8	70.6	68.6	75.6	66.8	71.7	78.3
2.782	76.2	72.9	70.0	68.4	75.2	66.9	71.7	77.5
2.609	77.6	74.3	71.6	68.0	74.0	65.1	71.4	75.0
Comparative Fan								
2.900	77.0	77.1	73.7	70.8	77.9	71.2	76.4	80.6
2.800	76.3	76.7	73.4	71.2	78.5	70.7	76.5	80.1
2.750	76.0	77.2	73.9	71.4	78.5	70.6	76.2	80.4
2.610	77.2	77.6	75.1	72.8	78.5	70.6	76.3	80.6

Table 6.21: Sound data for three different fans at 1200 rpm

Volume Flow	Sound Pressure Level per Octave Band [dB]							
[m3/s]	63 HZ	125 Hz	250 Hz	500 Hz	1000 Hz	2000 Hz	4000 Hz	8000 Hz
General Application Fan								
4.347	84.3	81.3	79.0	77.4	79.1	76.9	79.1	81.9
4.315	83.9	81.1	78.7	76.6	78.7	76.5	78.7	81.3
4.213	85.2	81.4	78.7	76.0	78.9	75.5	78.4	80.7
4.067	85.6	81.7	78.9	76.1	78.2	75.0	78.6	79.1
3.742	86.4	84.0	80.5	77.4	79.5	74.7	78.8	81.2
Low-noise Fan								
3.713	82.2	83.0	79.1	76.1	76.7	73.6	74.1	81.0
3.660	84.2	82.1	78.7	76.2	76.2	73.5	74.3	80.8
3.563	84.7	82.1	78.6	75.7	77.2	73.4	73.9	82.2
3.409	85.1	82.3	79.1	75.8	76.8	72.7	73.2	80.7
3.146	86.1	83.9	80.5	77.6	76.7	72.4	73.7	80.2
Comparative Fan								
2.923	84.7	85.1	82.6	78.5	81.7	77.4	81.8	84.6
2.919	84.2	84.7	82.1	79.0	80.5	77.5	81.6	84.1

10. REFERENCES

Abott, J. H., von Doenhoff, A. E., "Theory of Wing Sections", Dover Publications Inc., New York, 1959.

Akaike, S., Kikuyama, K., Kitada, M., Kuwayama, K., "Rotational Noise Analysis and Prediction for an Axial Fan with Unequal Blade Pitches", ASME (Paper), GT-376, 1994.

Bard, H., Böös, E., "Aerodynamic Fan Design - Computer Techniques", Industrial Fans - Aerodynamic Design, Instn. of Mech. Engrs., April 1987.

Bass., R. M., "Factors Influencing the Aerodynamic Design of Low Pressure Axial Fans", Industrial Fans - Aerodynamic Design, Instn. of Mech. Engrs., April 1987.

Bisplinghoff, R. L., Ashley, H., Halfman, R. L., "Aeroelasticity", Addison-Wesley Publishing Company, Inc., 1955.

British Standards Institution, "Fans for General Purpose, Part 1, Methods of Testing Performance", BS 848, 1980.

British Standards Institution, "Fans for General Purpose, Part 2, Methods of Noise Testing", BS 848, 1985.

Bruneau, P. R. P., "The Design of a Single Rotor Axial Flow Fan for a Cooling Tower Application", M. Eng. thesis, University of Stellenbosch, 1994.

Carter, A. D. S., "The Low Speed Performance of Related Aerofoils in Cascades", Gt. Britain Aer. Research Council, ARC CP 29, 1950.

Dixon, S. L., "Fluid Mechanics-Thermodynamics of Turbomachinery", Third Edition, William Clowes Ltd., Great Britian, 1978.

Dowell, E. H., et al., "A Modern Course in Elasticity", Third Edition, Kluwer Academic Publishers, Netherlands, 1995.

Downie, R. J., Thompson, M. C., Wallis, R. A., "An Engineering Approach to Blade Designs for Low to Medium Pressure Rise Rotor-Only Axial Fans", Experimental Thermal and Fluid Science, Vol. 6, Part 4, 1993.

Eck, B., "Fans", Pergamon Press, Oxford, 1973.

Falk, K. H., "Aircraft Propellor Handbook", The Ronald Press Company, NewYork, 1937.

Fukano, T., Kodama, Y., Senoo, Y., "Noise Generated by Low Pressure Axial Flow Fans, i: Modelling of Turbulent Noise", Journal of Sound and Vibration, Vol. 50, Part 1, 1977.

Fukano, T., Kodama, Y., Takamatsu, Y., "Noise Generated by Low Pressure Axial Flow Fans, ii: Effects of Number of Blades, Chord Length and Camber of Blade", Journal of Sound and Vibration, Vol. 50, Part 1, 1977.

Fukano, T., Kodama, Y., Takamatsu, Y., "Noise Generated by Low Pressure Axial Flow Fans, iii: Effects of Rotational Frequency, Blade Thickness and Outer Blade Profile", Journal of Sound and Vibration, Vol. 56, Part 2, 1978.

Fukano, T., Takamatsu, Y., Kodama, Y., "The Effects of Tip Clearance on the Noise of Low Pressure Axial and Mix Flow Fans", Journal of Sound and Vibration, Vol. 105, Part 2, 1986.

Gordon, C. G., "Fan Noise and its Prediction", Conference on Fan Technology and Practice, Institution of Mechanical Engineers, April 1972.

Graham, J. B., "Noise of Fans and Blowers", Proceedings of Short Course: Reduction of Machinery Noise, Purdue University, West Lafayette, December 1975.

Hawthorne, W. R., Horlock, J. H., "Actuator Disc Theory of the Incompressible Flow in Axial Compressors", Proc. Instn. Mech. Engrs., London, 1962.

Hay, N., Metcalfe, R., Reizes, J. A., "A Simple Method for the Selection of Axial Flow Fan Blade Profiles", Proc. Instn. Mech. Engrs., Vol. 192, No.25, 1978.

Hay, N., Mather, J. S. B., Metcalfe, R., "Fan blade Selection for Low Noise", Industrial fans - Aerodynamic Design, Instn. of Mech. Engrs., April 1987.

Jackson, D. G., Wright, T., "An Intellingent/Learning Axial Fan Design System", ASME, GT-27, June 1991.

Japikse, D., "Advanced Topics in Turbomachinery Technology", Concepts ETI, Inc., Vermont, 1986.

Kawaguchi, K., Kadota, S., Suzuki, M., Matsui, K., Kikuyama, K., "Study on Low-Noise Fan: Noise Reduction of Pusher-Type Condensor Cooling Fan", Transactions of the Japan Society of Mechanical Engineers, Part B, Vol. 59, No. 558, February 1993.

Keller, C., "The Theory and Performance of Axial Flow Fans", McGraw-Hill Book Company, Inc., 1937.

Lee, C., Chung, M. K., Kim, Y.-H.., "A Prediction Model for the Vortex Shedding Noise from the Wake of an Airfoil or Axial Flow Fan Blades", Journal of Sound and Vibration, Vol. 164, Part 2, 1993.

Longhouse, R. E., "Noise Mechanism Separation and Design Considerations for Low Tip Speed, Axial Flow Fans", Journal of Sound and Vibration, Vol. 48, Part 4, 1976.

Mckenzie, A. B., "The Selection of Fan Blade Geometry for Optimum Efficiency", Proc. Instn. Mech. Engrs., Vol. 192, No. 25, 1978.

Meyers, J. G., Wright, T., "An Inviscid Low-solidity Cascade Design Routine", American Society of Mechanical Engineers (Paper), GT-162, 1993.

Patterson, G. N., "Ducted Fans: Design for High Efficiency", Report ACA-7, Australian Council for Aeronautics, July 1944.

Powell, M. J. D., "A Fast Algorithm for Non-linearly Constrained Optimisation Calculations", Lecture Notes in Mathematics 630, Springer Verlag, Berlin, 1978.

Sharland, I. J., "Sources of Noise in Axial Flow Fans", Journal of Sound and Vibration, Vol. 1, Part 3, 1964.

Shigley, J. E., "Mechanical Engineering Design", First Metric Edition, McGraw-Hill, Inc., 1986.

Smith, L. H., Hsuan, Y., "Sweep and Dihedral Effects in Axial Flow Turbomachinery", Transactions of the ASME, Journal of Basic Engineering, Vol. 85, 1963.

Smith, T. W., "A Practical Approach to the Design of Axial and Mixed Flow Fans", Industrial Fans - Aerodynamic Design, Instn. of Mech. Engrs., April 1987.

Thwaites, B., "A Note on the Design of Ducted fans", The Aeronautical Quarterly, Vol. 3, November 1951.

Tyler, J. M., Sofrin, T. G., "Axial Flow Compressor Noise Studies", Society of Automotive Engineers Transactions, Vol. 70, 1962.

Van der Spek, H. F., "Advanced Low Noise Cooling Fans", 9th Cooling Tower and Spraying Pond Symposium IAHR, Von Karmen Institute for Fluid Dynamics, Brussels, September 1994.

Van der Spuy, S. J., "Die Ontwerp van 'n Waaiertoetstonnel vir Klank- en Werkverrigtingmeting", Final Year Project, University of Stellenbosch, 1994.

Van Niekerk, C. G., "Ontwerp van Waaiers met Hoë Rendement en Lae Lawaai-intensiteit", D. Sc. thesis, University of Pretoria, 1964.

Venter, S. J., "The Effectiveness of Axial Flow Fans in A-Frame Plenums", Ph.D. thesis, University of Stellenbosch, 1990.

Von Backström, T. W., Buys, J. D. and Stinnes, W. H., "Minimisation of the Exit Loss of a Rotor-Only Axial Fan", Eng. Opt., Vol. 26, 1996.

Wallis, R. A., "Axial Flow Fans and Ducts", John Wiley & Sons, Inc., (1983 & 1961).

Wallis, R. A., "The Development of Blade Sections for Axial Flow Fans", Instn. Engrs. Aus., Mechanical and Chemical Engineering Transactions, Nov. 1972.

Wallis, R. A., "The F-series Airfoils for Fan Blade Sections", Instn. Engrs. Aus., Mechanical Engineering Transactions, 1977.

Wright, S. E., "The Acoustic Spectrum of Axial Flow Machines", Journal of Sound and Vibration, Vol. 45, Part 2, 1976.

Wright, T., Ralston, S. A., "Computer-Aided Design of Axial Fans Using Small Computers", ASHRAE Transactions, Vol. 93, Part 2, 1987.

Wright, T., Simmons, W. E., "Blade Sweep for Low-Speed Axial Fans", American Society of Mechanical Engineers (Paper), GT-53, 1989.

APPENDIX A: FAN LAY-OUT DESIGN

A.1 EXIT VELOCITY PROFILE

The theory comprising the article of Von Backström et al. (1996) is described in this section. The method determines the optimum exit velocity profile by minimising the kinetic flux losses in varying the flow and pressure coefficient. As mentioned in Chapter 3, the model incorporated the following assumptions:

1. A uniform total pressure distribution across the fan inlet.
2. The Euler turbo-machinery equation is applicable.
3. Simple radial equilibrium applies in front of and behind the fan.
4. The flow is assumed to be incompressible and inviscid.

The simplifications associated with the free vortex velocity distribution as well as its applications in practise was used as reference case in the article.

The following dimensionless coefficients were used in the analysis:

1. Hub - tip ratio

$$\nu = \frac{r_i}{r_o} \tag{A.1}$$

2. Pressure Coefficient

$$\psi = \frac{p_{tf}}{\frac{1}{2}\rho U_o^2} = \frac{\rho U_o C_{wo}}{\frac{1}{2}\rho U_o^2} = \frac{2C_{wo}}{U_o} \tag{A.2}$$

3. Flow Coefficient

$$\phi = \frac{C_a}{U_o} \tag{A.3}$$

A.1.1 DESIGN LIMITATIONS

The traditional fan design limitations were summarized as follows:

1. Backflow will occur at the hub if the swirl velocity at the hub is too high in relation to the throughflow velocity. Backflow is prevented by limiting the hub absolute exit flow angle to about 50°, which gives the limitation:

$$\psi < 2.2 \times \nu \times \phi \qquad \text{(A.4)}$$

2. The maximum flow deflection in cascades limits the stagnation pressure rise obtainable from a certain number of fan blades, resulting in a maximum hub absolute exit flow angle of 45°. The maximum exit flow angle gives a more stringent limitation than in equation (A.4):

$$\psi < 2.0 \times \nu \times \phi \qquad \text{(A.5)}$$

3. The last limitation reflects the basic operation of a fan where the rotor should not turn the flow beyond the axial direction. If this happens, that section of the fan will create a static pressure drop instead of a static pressure rise. The rotor hub is limited to a relative exit flow angle of 0°. The limitation is given as:

$$\psi < 2.0 \times \nu^2 \qquad \text{(A.6)}$$

The hub-tip ratio cannot exceed unity and therefore equation (A.6) puts an absolute limit of 2 on the value of the pressure coefficient. Combining this limitation, the fact that the hub-tip ratio must be less than unity and equation (A.5), another constraint is formed namely:

$$\phi < 1 \qquad \text{(A.7)}$$

A.1.2 MINIMISATION FORMULATION

The velocity profiles were obtained by minimising the integral for kinetic energy flux at the fan outlet. The kinetic energy flux is given by:

$$L = \pi \times \rho \times \int_{ri}^{ro} r.C_a.\left(C_a^{\,2} + C_w^{\,2}\right)dr \qquad (A.8)$$

By non-dimensionalising as follows:

$$t = r / r_i \qquad (A.9)$$

$$a = r_o / r_i \qquad (A.10)$$

$$u(t) = C_w\left(r_i \times t\right)/\left(r_i \times \Omega\right) \qquad (A.11)$$

$$v(t) = C_a\left(r_i \times t\right)/\left(r_i \times \Omega\right) \qquad (A.12)$$

equation (A.8) is simplified to:

$$F = L/\left(\pi \times \rho \times r^5 \times \Omega^3\right)$$

$$= \int_{ri}^{ro} v.\left(v^2 + u^2\right).t.\,dt \qquad (A.13)$$

The following constraints applied to this functional (equation (A.13)):

1) Radial Equilibrium:

$$\Omega \times \left[\frac{d\left(C_w.r\right)}{dr}\right] = \frac{C_w}{r} \times \left[\frac{d\left(C_w.r\right)}{dr}\right] + C_a \times \frac{dC_a}{dr}$$

$$\Rightarrow t \times \frac{du}{dt} + u = \frac{u^2}{t} + u \times \frac{du}{dt} + v \times \frac{dv}{dt} \qquad (A.14)$$

2) Dimensionless Work Rate:

$$A = \frac{1}{\Omega^2 \times r_i^5} \int_{ri}^{ro} r^2 . C_a . C_w . dr$$

$$= \int_1^a t^2 . u . v . dt$$

$$= Wo / \left(2 \times \pi \times \rho \times r_i^5 \times \Omega^3\right) \qquad (A.15)$$

where

$$Wo = 2 \times \pi \times \rho \times \Omega \times \int_{ri}^{ro} r^2 . C_a . C_w . dr$$

3) Dimensionless Flow Rate:

$$B = \frac{1}{\Omega \times r_i^3} \int_{ri}^{ro} r . C_a . dr$$

$$= \int_1^a t . v . dt$$

$$= \dot{m} / \left(2 \times \pi \times \rho \times r_i^3 \times \Omega\right) \qquad (A.16)$$

where

$$\dot{m} = 2 \times \pi \times \rho \times \int_{ri}^{ro} r . C_a . dr$$

The values for A, B and a were obtained from the free vortex theory as follows:

$$a = 1/v \qquad (A.17)$$

$$A = \psi \times \phi \times \left(1 - v^2\right) / \left(4 \times v^5\right) \qquad (A.18)$$

$$B = \phi \times \left(1 - v^2\right) / \left(2 \times v^3\right) \qquad (A.19)$$

The above values ensured that the work rate and flow rate of the optimised velocity profile corresponded to that of the free vortex velocity profile.

A.1.3 MINIMISATION SOLUTION

The equations described in section 1.1.2 were evaluated numerically, discretising the fan blade radius into n equal intervals of length h. The integrals were evaluated using the trapezoidal rule:

$$\int_1^a f(t).\,dt \approx \frac{h}{2} \times f(t_0) + h \times \sum_{i=1}^{n-1} f(t_i) + \frac{h}{2} \times f(t_n) \qquad (A.20)$$

A higher order approximation was used for the derivatives in equation (A.17):

$$i = 0: f'(t_i) \approx \left[-25f(t_0) + 48f(t_1) - 36f(t_2) + 16f(t_3) - 3f(t_4)\right]/(12h)$$

$$i = 1: f'(t_i) \approx \left[-3f(t_0) - 10f(t_1) + 18f(t_2) - 6f(t_3) + f(t_4)\right]/(12h)$$

$$i < i < n - 1: f'(t_i) \approx \left[f(t_{i-2}) - 8f(t_{i-1}) + 8f(t_{i-1}) - f(t_{i-2})\right]/(12h)$$

$$i = n - 1: f'(t_i) \approx \left[-f(t_{n-4}) + 6f(t_{n-3}) - 18f(t_{n-2}) + 10f(t_{n-1}) + 3f(t_n)\right]/(12h)$$

$$i = n: f'(t_i) \approx \left[3f(t_{n-4}) - 16f(t_{n-3}) + 36f(t_{n-2}) - 48f(t_{n-1}) + 25f(t_n)\right]/(12h)$$

(A.21)

where:

$$t_i = 1 + i \times h$$

$$i = 0, 1, 2, \ldots, n$$

The minimisation problem was discretised into a numerical problem with (2n + 2) variables and (n + 3) non-linear constraints and was solved for given values of a, A and B using the sequential programming method of Powell and Han, as described by Powell (1978).

A.2 DETERMINING THE OPTIMUM HUB-TIP RATIO

The hub-tip ratio was optimised for maximum static efficiency, using the restraints mentioned in the article by Von Backström et al. (1996). The definitions of the different power terms are as follows:

1. The effective power is the power associated with the static pressure rise over the fan.

$$P_e = Q \times p_{sf} \qquad (A.22)$$

2. The power associated with the kinetic energy of the exit velocity profile is derived from the value for kinetic energy:

$$Ke = \frac{1}{2} \times m \times V^2 \qquad (A.23)$$

This gives the kinetic power loss:

$$P_k = \frac{1}{2} \times \dot{m} \times V^2 \qquad (A.24)$$

$$P_k = \left(\int_{ri}^{ro} \frac{1}{2} C_a^2 . \rho C_a \, 2\pi r \, dr\right) + \left(\int_{ri}^{ro} \frac{1}{2} C_w^2 . \rho C_a \, 2\pi r \, dr\right) \qquad (A.25)$$

As mentioned previously in Section 3.2.1, the simplifications associated with the free vortex velocity profile were used where the form of the optimised velocity profile was not yet known. C_a is uniform because of the free vortex assumption and therefore its value can be calculated as follows:

$$C_a = \frac{Q}{\pi\left(r_o^2 - r_i^2\right)} \qquad (A.26)$$

3. The shaft power is the power that is transferred from the fan motor to the fan rotor through the fan shaft. It is given by:

$$P_s = T \times \Omega \qquad (A.27)$$

If no mechanical losses are assumed, the shaft power is equal to the Euler power. The shaft power can therefore be given by:

$$P_s = \dot{m} \times U \times C_w \qquad (A.28)$$

where

$$U = \Omega \times r \qquad (A.29)$$

This gives:

$$P_s = 2 \times \pi \times \rho \times \Omega \times \int_{ri}^{ro} r^2 . C_a . C_w . dr \qquad (A.30)$$

4. The main sources of power loss in the fan blades are blade drag, blade tip leakage and annulus losses. The power leaving the fan rotor is given by:

$$P_{bo} = \eta_r \times P_s \qquad (A.31)$$

If a reasonable assumption is made and it is assumed that the blades are 85% effective, then the rotor efficiency is given by:

$$\eta_r = 0.85$$

The fan static efficiency is given by:

$$\eta_s = \frac{P_e}{P_s} \qquad (A.32)$$

but

$$P_e = P_{bo} - P_k \qquad (A.33)$$

$$P_s = \frac{P_{bo}}{\eta_r} \qquad (A.34)$$

This gives:

$$\eta_s = \left(\frac{P_{bo} - P_k}{P_s} \right)$$

$$= \left(\eta_r - \frac{P_k}{P_s} \right) \qquad (A.35)$$

The values for kinetic power (equation (A.25)) and shaft power (equation (A.30)) are known and therefore it can be calculated as follows:

$$\frac{P_k}{P_s} = \frac{(\int_{ri}^{ro} \frac{1}{2} C_a^2 . \rho C_a \, 2 \pi \, r \, dr) + (\int_{ri}^{ro} \frac{1}{2} C_w^2 . \rho C_a \, 2 \pi \, r \, dr)}{2 \times \pi \times \rho \times \Omega \times \int_{ri}^{ro} r^2 . C_a . C_w . dr}$$

This gives:

$$\frac{P_k}{P_s} = \frac{\frac{1}{2} \times C_a^{\,2} \times \int_{ri}^{ro} r.\,dr}{\Omega \times \int_{ri}^{ro} r^2.\,C_w.\,dr} + \frac{\frac{1}{2} \times \int_{ri}^{ro} C_w^{\,2}.\,r.\,dr}{\Omega \times \int_{ri}^{ro} r^2.\,C_w.\,dr} \qquad (A.36)$$

The simplifications associated with using the free vortex velocity profile is given by:

C_a = constant

C_w = k/r, where k is a constant

This simplified equation (A.36) as follows:

$$\frac{P_k}{P_s} = \frac{\frac{1}{2} \times C_a^{\,2} \times \left.\frac{r^2}{2}\right|_{ri}^{ro}}{\Omega \times k \times \left.\frac{r^2}{2}\right|_{ri}^{ro}} + \frac{\frac{1}{2} \times \int_{ri}^{ro} \frac{k^2}{r}.\,dr}{\Omega \times \int_{ri}^{ro} k.\,r.\,dr}$$

$$= \frac{1}{2} \times \frac{C_a^{\,2} \times r_o}{r_o \times \Omega \times k} + \frac{1}{2} \times \frac{k^2 \times \ln r\big|_{ri}^{ro}}{\Omega \times k \times \left.\frac{r^2}{2}\right|_{ri}^{ro}}$$

$$= \frac{1}{2} \times \frac{C_a}{U_o} \times \frac{C_a}{C_{wo}} + \frac{k}{2 \times \Omega} \times \frac{\ln r_o - \ln r_i}{\frac{r_o^2}{2} - \frac{r_i^2}{2}}$$

$$= \frac{1}{2} \times \frac{C_a}{U_o} \times \frac{C_a}{C_{wo}} + \frac{k}{2 \times \Omega} \times \frac{\ln\left(\frac{r_o}{r_i}\right)}{\frac{r_o^2}{2} \times \left(1 - \frac{r_i^2}{r_o^2}\right)}$$

$$= \frac{1}{2} \times \frac{C_a}{U_o} \times \frac{C_a}{C_{wo}} + \frac{k}{r_o} \times \frac{1}{\Omega \times r_o} \times \frac{1}{\left(1 - \frac{r_i^2}{r_o^2}\right)} \times \ln\left(\frac{r_o}{r_i}\right)$$

$$= \frac{1}{2} \times \frac{C_a}{U_o} \times \frac{C_a}{C_{wo}} + \frac{C_{wo}}{U_o} \times \frac{1}{\left(1 - \frac{r_i^2}{r_o^2}\right)} \times \ln\left(\frac{r_o}{r_i}\right) \qquad (A.37)$$

Using the equations for ϕ, ψ and ν (equations (A.1) to (A.3)) equation (A.37) simplifies to:

$$\frac{P_k}{P_s} = \frac{1}{2} \times \frac{C_a}{U_o} \times \frac{C_a}{U_o} \times \frac{U_o}{C_{wo}} + \frac{C_{wo}}{U_o} \times \frac{1}{(1-\nu^2)} \times \ln\left(\frac{1}{\nu}\right)$$

$$= \frac{\phi^2}{\psi} + \frac{\psi}{2} \times \frac{1}{(1-\nu^2)} \times \ln\left(\frac{1}{\nu}\right) \qquad \text{(A.38)}$$

Equation (A.35) was simplified in a similar way:

$$\eta_s = \left(\eta_r - \frac{\phi^2}{\psi} + \frac{\psi}{2} \times \frac{1}{(1-\nu^2)} \times \ln(\nu)\right) \qquad \text{(A.39)}$$

Using the maximum allowable value for the pressure coefficient according to equation (A.5), equation (A.39) was simplified to:

$$\eta_s = \left(\eta_r - \frac{\phi}{2 \times \nu} + \frac{\nu \times \phi}{(1-\nu^2)} \times \ln(\nu)\right) \qquad \text{(A.40)}$$

The relation between flow coefficient and hub-tip ratio is as follows:

$$\phi = \frac{Q}{U_o \times \pi \times r_o^2 \times (1-\nu^2)}$$

$$= \frac{K_1}{(1-\nu^2)} \qquad \text{(A.41)}$$

where

$$K_1 = \frac{Q}{U_o \times \pi \times r_o^2} \qquad \text{(A.42)}$$

Inserting equation (A.41) into equation (A.40):

$$\eta_s = \left(\eta_r - \frac{K_1}{2 \times \nu \times (1-\nu^2)} + \frac{\nu \times K_1}{(1-\nu^2)^2} \times \ln(\nu)\right) \qquad \text{(A.43)}$$

In order to obtain the hub-tip ratio for maximum static efficiency, the derivative of equation (A.43) with respect to ν must be calculated:

$$\frac{d\eta_s}{d\nu} = \frac{-K_1 \times \left(1 - 3\nu^2\right)}{2 \times \left(\nu - \nu^3\right)^2} + K_1 \times \left(\frac{2 \times \left(1 - \nu^2\right) + 8 \times \nu^2}{4 \times \left(1 - \nu^2\right)^3}\right) \ln\left(\frac{1}{\nu}\right) - \frac{K_1}{\left(1 - \nu^2\right)^2} \qquad (A.44)$$

Setting equation (A.44) equal to zero and solving ν, a hub-tip ratio was obtained that maximises the static efficiency. The value for K_1 cancels out when one sets equation (A.44) equal to zero.

APPENDIX B: FAN BLADE DESIGN CALCULATIONS

With the advantage of hindsight, the data used in the calculations will be for the 1000/250/7/1440 fan configuration. This corresponds to the design configuration used to design the general application fan. The 1000/250/14/1440 fan configuration data will be used for the swept blade design calculations.

B.1 CALCULATION OF FAN EXIT VELOCITY PROFILE

The equations from the article described in Appendix A, Section A.1 were used for the calculations in this section.

B.1.1 CHOOSING THE VALUES FOR a, A AND B

The values for ν, ϕ and ψ were calculated (see equations (A.1) to (A.3)) using the values obtained from the data sheets of a comparative fan series from HAI (see Section 4.1.1). The value for ϕ was calculated from the data for the 1000/250/7/1440 fan as follows:

$$Q = \frac{Q_{max}}{2} \qquad (B.1)$$

$$= \frac{20.8}{2}$$

$$= 10.4 \text{ m}^3/\text{s}$$

$$\Omega = 2 \times \pi \times \text{rpm}/60 \qquad (B.2)$$

$$= 2 \times \pi \times 1440/60$$

$$= 150.796 \text{ m/s}$$

This gave:

$$\phi = \frac{C_a}{U_o}$$

$$= \frac{Q\left(\pi \times \left(r_o^2 - r_i^2\right)\right)}{\Omega \times r_o} \qquad \text{(B.3)}$$

$$= \frac{10.4\left(\pi \times \left(0.5^2 - 0.125^2\right)\right)}{150.796 \times 0.5}$$

$$= 0.19$$

where

Q_{max} = 20.8 m^3/s

r_o = 0.5 m

r_i = 0.125 m

rpm = 1440 rpm

The value for ψ was calculated from the value for fan shaft power from the data sheets. A rotor efficiency of 85 % and a mechanical efficiency of 90 % were assumed. This gave a total efficiency of 76.5 %. The fan shaft power was calculated as follows:

$$p_{tf} = \frac{P_s \times \eta_t}{Q} \qquad \text{(B.4)}$$

$$= \frac{5700 \times 0.765}{10.4}$$

$$= 419.28 \text{ Pa}$$

This gave:

$$\psi = \frac{2p_{tf}}{\rho \times U_o^2} \qquad \text{(B.5)}$$

$$= \frac{2 \times 419.28}{1.2 \times 75.398^2}$$

$$= 0.12$$

where

ρ = 1.2 kg/m^3

P_s = 5700 W

The value for hub-tip ratio was calculated as:

$$\nu = \frac{r_i}{r_o} \qquad (B.6)$$

$$= \frac{0.125}{0.5}$$

$$= 0.25$$

The values for ϕ, ψ and ν were used to calculate a, A and B, according to the free vortex theory, as follows:

$$a = \frac{1}{\nu} \qquad (B.7)$$

$$= \frac{1}{0.25}$$

$$= 4$$

$$A = \frac{\psi \times \phi \times \left(1 - \nu^2\right)}{4 \times \nu^5} \qquad (B.8)$$

$$= \frac{0.12 \times 0.19 \times \left(1 - 0.25^2\right)}{4 \times 0.25^5}$$

$$= 5.472$$

$$B = \frac{\phi \times \left(1 - \nu^2\right)}{2 \times \nu^3} \qquad (B.9)$$

$$= \frac{0.19 \times \left(1 - 0.25^2\right)}{2 \times 0.25^3}$$

$$= 5.7$$

The velocity profile with the minimum exit kinetic for these values of a, A and B were calculated using the minimisation solution for 20 radial segments, as described in Section A.1.3. As described in Section 4.1.2, the configuration of 1000/250/7/1440 was chosen since it had a velocity profile which gave an average camber and twist over the blade length. The velocity profile in terms of t, u(t) and v(t) is given in Table B1.

Table B1: Optimised exit velocity profile

t	u(t)	v(t)
1.000	0.651	0.500
1.158	0.656	0.577
1.316	0.617	0.619
1.474	0.582	0.657
1.632	0.546	0.692
1.789	0.507	0.706
1.947	0.476	0.728
2.105	0.446	0.739
2.263	0.420	0.753
2.421	0.396	0.760
2.579	0.375	0.770
2.737	0.355	0.776
2.895	0.338	0.783
3.052	0.322	0.787
3.211	0.307	0.792
3.368	0.294	0.796
3.526	0.282	0.800
3.684	0.270	0.802
3.842	0.260	0.807
4.000	0.250	0.807

B.1.2 APPLYING ACTUATOR DISK THEORY TO THE VELOCITY PROFILES

The velocity profiles calculated previously were for positions far downstream from the fan rotor. Far upstream from the fan rotor it can be assumed that the axial velocity in the ducting is uniform and that there is zero swirl velocity. The actuator disk theory was used to calculate the velocity profiles at the leading and trailing edges of the fan blade.

For the sample calculation the values at the second radial point from the fan hub were used:

$t = 1.158$

$u(t) = 0.656$

$v(t) = 0.577$

Transferring these values to their actual dimensional values the following resulted:

$$r = t \times r_i \qquad \text{(B.10)}$$

$$= 1.158 \times 0.125$$

$$= 0.145 \text{ m}$$

$$C_{w_{s2}} = u(t) \times r_i \times \Omega \qquad \text{(B.11)}$$

$$= 0.656 \times 0.125 \times 150.796$$

$$= 12.358 \text{ m/s}$$

$$C_{a_{s2}} = v(t) \times r_i \times \Omega \qquad \text{(B.12)}$$

$$= 0.577 \times 0.125 \times 150.796$$

$$= 10.871 \text{ m/s}$$

Using the assumptions for flow far upstream of the fan, the following were obtained:

$$C_{w_{x1}} = 0$$

$$C_{a_{x1}} = \phi \times U_o$$

$$= 0.19 \times 75.398$$

$$= 14.326 \text{ m/s}$$

The above results enabled the calculation of the mean axial velocity at the actuator disk (Dixon, 1978):

$$C_{am} = \frac{1}{2} \times \left(C_{a_{x1}} + C_{a_{x2}}\right) \qquad \text{(B.13)}$$

$$= \frac{1}{2} \times (14.326 + 10.871)$$

$$= 12.599 \text{ m/s}$$

In the positions up - and downstream from the fan, a difference in axial velocity at a certain point and the far up - and downstream positions is seen as a velocity perturbation. The axial velocity perturbation at the actuator disk is given by Δ_0 and that at a specific point by Δ. The calculation of the perturbation velocities used the following approximations:

$$\beta_1 = \tan^{-1}\left(\frac{U}{C_{a_{x1}}}\right)$$

$$= \tan^{-1}\left(\frac{150.796 \times 0.145}{14.326}\right)$$

$$= 56.768^\circ$$

$$\beta_2 = \tan^{-1}\left(\frac{U - C_{w2}}{C_{a2}}\right)$$

$$= \tan^{-1}\left(\frac{21.865 - 12.358}{10.871}\right)$$

$$= 41.172^\circ$$

$$\xi = \tan^{-1}\left[\frac{1}{2} \times \left(\tan\beta_1 + \tan\beta_2\right)\right]$$

$$= \tan^{-1}\left[\frac{1}{2} \times \left(\tan 56.768^\circ + \tan 41.172^\circ\right)\right]$$

$$= 50.206^\circ$$

$c = 0.08$ m (see Section 4.1.3)

The validity of these approximations was checked by using the final values calculated with the corrected velocity profiles in the above equations and then repeating the calculations. The difference calculated in this way was so small that the answers obtained using the approximations were accepted as final values. Using the values calculated up to this point, the following calculations were done:

$$\Delta_0 = \frac{1}{2} \times \left(C_{a\alpha 1} - C_{a\alpha 2}\right) \qquad \text{(B.14)}$$

$$= \frac{1}{2} \times \left(14.326 - 10.871\right)$$

$$= 1.7275 \text{ m/s}$$

In front of the fan:

$$x = 0.43 \times c \times \cos(\xi) \qquad \text{(B.15)}$$

$$= 0.43 \times 0.08 \times \cos(50.206^\circ)$$

$$= 0.022 \text{ m}$$

Behind the fan:

$$x = 0.57 \times c \times \cos(\xi) \qquad \text{(B.16)}$$

$$= 0.57 \times 0.08 \times \cos(50.206^\circ)$$

$$= 0.029 \text{ m}$$

The values calculated in equations (B.14), (B.15) and (B.16) were used to calculate the velocity perturbations in front of and behind the fan as follows:

In front of the fan:

$$\Delta = \Delta_0 \times \left[1 - \exp\left(-\frac{\pi \times x}{r_o - r_i}\right)\right] \qquad \text{(B.17)}$$

$$= 1.7275 \times \left[1 - \exp\left(-\frac{\pi \times 0.022}{0.375}\right)\right]$$

$$= 0.291 \text{ m/s}$$

Behind the fan:

$$\Delta = \Delta_0 \times \left[1 - \exp\left(+\frac{\pi \times x}{r_o - r_i}\right)\right] \qquad \text{(B.18)}$$

$$= 1.7275 \times \left[1 - \exp\left(+\frac{\pi \times -0.029}{0.375}\right)\right]$$

$$= 0.373 \text{ m/s}$$

The axial velocities in front of and behind the fan rotor were calculated for the sample point, using the velocity perturbations:

$$C_{a1} = C_{am} + \Delta \qquad \text{(B.19)}$$

$$= 12.599 + 0.291$$

$$= 12.890 \text{ m/s}$$

$$C_{a2} = C_{am} - \Delta \qquad \text{(B.20)}$$

$$= 12.599 - 0.373$$

$$= 12.226 \text{ m/s}$$

To determine the swirl velocity distribution behind the fan the streamline shift had to be calculated because the value $r \times C_w$ is constant along a streamline. It was assumed that the velocities at each radius were applicable to the control volume formed by the area that was bordered by the

streamlines. The streamlines were situated halfway between each radial point, except at the blade hub and tip where the streamlines were assumed to coincide with the inner and outer radii respectively. The calculations were started by calculating the location of the streamlines far behind the fan:

$$r_{stl_{\infty i}} = \frac{r_i + r_{i-1}}{2}$$

$$= \frac{0.145 + 0.164}{2}$$

$$= 0.155 \text{ m for } i = 2$$

The above values were valid for all the streamlines except:

$$r_{stl_{\infty 0}} = r_1$$

$$= 0.125 \text{ m}$$

$$r_{stl_{\infty 20}} = r_{20}$$

$$= 0.5 \text{ m}$$

The areas between the streamlines were calculated as:

$$A_{stl\,j} = \pi \times \left(r_{stl_{\infty j}}^{\ 2} - r_{stl_{\infty j-1}}^{\ 2} \right) \qquad \text{(B.21)}$$

$$= \pi \times \left(0.155^2 - 0.135^2 \right)$$

$$= 0.01795 \text{ m}^2 \text{ for } j = 2$$

The volume flows between the streamlines were calculated using the areas between the streamlines:

$$Q_{\infty 2} = C_{a_{\infty 2}} \times A_{stl} \qquad \text{(B.22)}$$

$$= 10.871 \times 0.01795$$

$$= 0.19513 \text{ m}^3/\text{s}$$

where the velocity at the first radial point was used in conjunction with the first streamline area. Incompressible flow was assumed and therefore the volume flow through the fan is constant and no

density changes were taken into account. The volume flow directly behind the fan rotor was calculated as before and based on the same area distribution. The calculations were as follows:

$$Q_2 = C_{a\,2} \times A_{stl\,2}$$

$$= 12.226 \times 0.01795$$

$$= 0.21946\ m^3/s$$

Determining a curve-fit between these volume flows and the radial streamline locations corresponding to the areas used, the following equation was obtained:

$$r_{stl_x} = -.00004 \times Q_2^4 + 0.001 \times Q_2^3 - 0.0107 \times Q_2^2 + 0.0789 \times Q_2 + 0.1311 \qquad (B.23)$$

The radial values directly behind the fan between which the same flow exists as far behind the fan, were calculated using equation (B.23) and replacing Q_2 with $Q_{x\,2}$ while solving r. These radial values represented the streamline locations directly behind the fan. Using the flow conditions at the second point from the hub as an example the following calculations resulted:

$$r_{stl_2} = -.00004 \times Q_{x\,2}^4 + 0.001 \times Q_{x\,2}^3 - 0.0107 \times Q_{x\,2}^2 + 0.0789 \times Q_{x\,2} + 0.1311$$

$$= -.00004 \times 0.195^4 + 0.001 \times 0.195^3 - 0.0107 \times 0.195^2$$
$$+0.0789 \times 0.195 + 0.1311$$

$$= 0.152\ m$$

The next step was to calculate the values of $C_{w\,x}$ at the streamlines. A curve-fit was determined for the values of $C_{w\,x}$ at the radial points. This gave:

$$C_{w_x} = -48235 \times r^6 + 98072 \times r^5 - 81077 \times r^4 + 34724 \times r^3 - 8034.4 \times r^2$$
$$+ 912.18 \times r - 26.993 \qquad (B.24)$$

From equation (B.24) the values for C_{w_x} at the streamlines were calculated. For the sample point the calculations were as follows:

$$C_{w_x} = -48235 \times r_{stl_x}^{\ 6} + 98072 \times r_{stl_x}^{\ 5} - 81077 \times r_{stl_x}^{\ 4} + 34724 \times r_{stl_x}^{\ 3} - 8034.4 \times r_{stl_x}^{\ 2} + 912.18 \times r_{stl_x} - 26.993$$

$$= -48235 \times 0.155^6 + 98072 \times 0.155^5 - 81077 \times 0.155^4 + 34724 \times 0.155^3 - 8034.4 \times 0.155^2 + 912.18 \times 0.155 - 26.993$$

$$= 11.994 \text{ m/s}$$

Using these values the swirl velocity at the streamlines just after the fan rotor was calculated:

$$C_{w2} = \frac{C_{w_{x2}} \times r_{stl_x}}{r_{stl_2}} \qquad \text{(B.25)}$$

$$= \frac{11.994 \times 0.155}{0.152}$$

$$= 12.235 \text{ m/s}$$

A curve-fit was done between C_{w2} and $r_{stl\,2}$ to obtain the function for swirl velocity distribution after the fan:

$$C_{w2} = -57859 \times r^6 + 117031 \times r^5 - 96172 \times r^4 + 40912 \times r^3 - 9401.9 \times r^2 + 1064.8 \times r - 33.541 \qquad \text{(B.26)}$$

The values for C_{w2} at the different radii were determined by substituting the radial point values into equation (B.26). For the sample point the calculation was as follows:

$$C_{w2} = -57859 \times 0.145^6 + 117031 \times 0.145^5 - 96172 \times 0.145^4 + 40912 \times 0.145^3 - 9401.9 \times 0.145^2 + 1064.8 \times 0.145 - 33.541$$

$$= 12.361 \text{ m/s}$$

B.2 GENERAL APPLICATION FAN BLADE DESIGN

The following section describes the calculations, using the velocity profiles obtained previously, to design the general application fan blades. As mentioned before, the design corresponded to the 1000/250/7/1440 fan configuration. Following the calculations of Section B.1, the sample calculations in this section will be done for the second radial point from the fan hub. The following values are valid for the calculations in this section:

C_{a1} = 12.890 m/s

C_{a2} = 12.226 m/s

C_{w1} = 0 m/s

C_{w2} = 12.361 m/s

r = 0.145 m

r_i = 0.125 m

r_o = 0.500 m

n_b = 7

rpm = 1440 rpm

Ω = 150.796 rad/s

U_o = 75.398 m/s

B.2.1 CALCULATING THE CHORD LENGTHS AND LIFT COEFFICIENTS

These calculations were based on the procedures described by Wallis (1983). No allowance was made for cascade effects in the calculations due to the low solidity of the fan rotor. The first step in the design was to calculate the flow angles for the velocity profiles that were adjusted by means of the actuator disk theory:

$$\alpha_1 = \tan^{-1}\left(\frac{C_{w1}}{C_{a1}}\right) \qquad \text{(B.27)}$$

$$= \tan^{-1}\left(\frac{0}{12.890}\right)$$

$$= 0$$

$$\beta_1 = \tan^{-1}\left(\frac{U}{C_{a1}}\right) \qquad \text{(B.28)}$$

$$= \tan^{-1}\left(\frac{0.145 \times 150.796}{12.890}\right)$$

$$= 59.480^{\circ}$$

$$\alpha_2 = \tan^{-1}\left(\frac{C_{w2}}{C_{a2}}\right) \qquad \text{(B.29)}$$

$$= \tan^{-1}\left(\frac{12.361}{12.226}\right)$$

$$= 45.315^{\circ}$$

$$\beta_2 = \tan^{-1}\left(\frac{U - C_{w2}}{C_{a2}}\right) \qquad \text{(B.30)}$$

$$= \tan^{-1}\left(\frac{21.865 - 12.361}{12.226}\right)$$

$$= 37.861^{\circ}$$

$$\beta_m = \tan^{-1}\frac{1}{2}\left(\tan\beta_1 + \tan\beta_2\right) \qquad \text{(B.31)}$$

$$= \tan^{-1}\frac{1}{2}\left(\tan 59.480^{\circ} + \tan 37.861^{\circ}\right)$$

$$= 51.044^{\circ}$$

The average axial velocity over the blade chord was calculated as follows:

$$C_{am} = \frac{1}{2} \times \left(C_{a1} + C_{a2}\right) \qquad \text{(B.32)}$$

$$= \frac{1}{2} \times \left(12.890 + 12.226\right)$$

$$= 12.558 \text{ m/s}$$

All of the above values were combined to calculate the blade loading factor:

$$C_L\sigma = 2 \times \left(\frac{C_{w2}}{C_{am}}\right) \times \cos\beta_m \qquad \text{(B.33)}$$

$$= 2 \times \left(\frac{12.361}{12.558}\right) \times \cos 51.044^\circ$$

$$= 1.238$$

where the solidity ratio is given by:

$$\sigma = \frac{c}{s} \qquad \text{(B.34)}$$

The next value that was calculated was the blade pitch (s):

$$s = \frac{2 \times \pi \times r}{n_b} \qquad \text{(B.35)}$$

$$= \frac{2 \times \pi \times 0.145}{7}$$

$$= 0.130$$

(The number of blades used in the design was seven, as explained in Section 4.2.2.)

The chord lengths at the hub and tip could now be calculated by choosing an appropriate value for C_L and using equation (B.36):

$$c = \frac{2 \times \pi \times r \times C_L\sigma}{n_b \times C_L} \qquad \text{(B.36)}$$

The value for C_L was 1.85 at the hub and 0.8 at the tip. This gave:

$$c_o = \frac{2 \times \pi \times r_o \times C_L\sigma_o}{n_b \times C_{Lo}}$$

$$= \frac{2 \times \pi \times 0.5 \times 0.126}{7 \times 0.8}$$

$$= 0.071\,\text{m}$$

$$c_i = \frac{2 \times \pi \times r_i \times C_L \sigma_i}{n_b \times C_{Li}}$$

$$= \frac{2 \times \pi \times 0.125 \times 1.430}{7 \times 1.85}$$

$$= 0.087 \text{ m}$$

The chord length distribution along the blade length was calculated by linearly interpolating between the hub and tip blade chord lengths (the calculation is done for the sample point):

$$c = c_i - (c_i - c_o) \times \left(\frac{r - r_i}{r_o - r_i} \right) \qquad \text{(B.37)}$$

$$= 0.087 - (0.016) \times \left(\frac{0.145 - 0.125}{0.375} \right)$$

$$= 0.086 \text{ m}$$

The lift coefficient was calculated using:

$$C_L = 2 \times \frac{s}{c} \times \left(\frac{C_{w2}}{C_{am}} \right) \times \cos \beta_m \qquad \text{(B.38)}$$

$$= 2 \times \frac{0.130}{0.086} \times \left(\frac{12.361}{12.558} \right) \times \cos 51.044^\circ$$

$$= 1.872$$

The effect of the lift interference factor on the lift coefficient was ignored due to the low solidity of the general application fan design configuration. According to Wallis (1983) the lift interference factor could be estimated using Figure 4.5, which gave the final lift coefficient value as follows:

$$C_{Li} = C_L / \text{LIF} \qquad \text{(B.39)}$$

The lift interference factor was taken into consideration for the low-noise fan due to its higher solidity ratio.

B.2.2 CALCULATING THE CAMBER AND STAGGER ANGLES

As mentioned before, all the calculations are done for the same sample point. The values for camber angle were obtained using the following equation:

$$\theta = \beta_1 - \beta_2 + \delta - i \qquad \text{(B.40)}$$

The values for incidence angle were taken from a graph in Wallis (1983) (see Figure 4.7). The camber angle had to be known and was obtained provisionally as:

$$\theta = \beta_1 - \beta_2$$

$$= 59.480 - 37.860$$

$$= 21.620\ ^\circ$$

This gave:

$$i = 0.82\ ^\circ$$

Since the value for camber angle was only provisional, the process was iterative and had to be repeated, depending on the variation in camber angle that occurred after each calculation.

The values for δ were calculated using equation (B.41) (Carter 1950):

$$\delta = \left(m \times (\beta_1 - \beta_2) \times \sqrt{\frac{s}{c}} \right) \Big/ \left(1 - m \times \sqrt{\frac{s}{c}} \right) \qquad \text{(B.41)}$$

According to Bruneau (1994) the value for m could be approximated by equation (4.29):

$$m = 0.209253 + \frac{0.2322389}{10^2} \times \xi - \frac{0.3736909}{10^4} \times \xi^2 + \frac{0.8668135}{10^6} \times \xi^3 \qquad \text{(B.42)}$$

The function gave deviation angle values that decreased with a decrease in solidity, up to a certain value from where it started increasing and eventually diverged. The values for deviation at these radii were kept constant with the lowest deviation angle value calculated. The value for stagger angle in equation (B.40) was approximated as:

$$\xi = \beta_m$$

$$= 51.044\ ^\circ$$

This gave:

$$m = 0.209253 + \frac{0.2322389}{10^2} \times 51.044^\circ - \frac{0.3736909}{10^4} \times \left(51.044^\circ\right)^2 + \frac{0.8668135}{10^6} \times \left(51.044^\circ\right)^3$$

$$= 0.346$$

The value for deviation angle could be calculated using equation (B.41):

$$\delta = \left(0.346 \times \left(59.48 - 37.86\right) \times \sqrt{1.513}\right) \Big/ \left(1 - 0.346 \times \sqrt{1.513}\right)$$

$$= 14.630^\circ$$

The values for deviation and incidence angles enabled the calculation of the camber angle using equation (B.40):

$$\theta = 59.480 - 37.86 + 14.630 - 0.82$$

$$= 35.43^\circ$$

The angles of attack for the blade profiles were obtained from the graph in Wallis (1983) (see Figure 4.8). The angle had to be adjusted for the blade nose droop:

$$\alpha = \alpha_{0d} - 0.57 \times d \qquad \text{(B.43)}$$

where d is in percentage chord. The blade was designed for a maximum nose droop of 3% along the blade length. This gave:

$$\alpha = 12.022^\circ - 0.57 \times 3$$

$$= 10.312^\circ$$

The value for α was used to calculate the stagger angle:

$$\xi = \beta_1 - \alpha \qquad \text{(B.44)}$$

$$= 59.480^\circ - 10.312^\circ$$

$$= 49.168^\circ$$

The angle of attack is dependent on the camber angle of the blade profile. The angle of attack was determined using the camber angle, which in turn affected the value for stagger angle. The stagger angle affected the camber angle via equation (B.42), while the camber angle affected itself via the value for incidence angle in Figure 4.7. The values for both camber and stagger angles were obtained by iteration.

B.3 LOW-NOISE FAN BLADE DESIGN

The calculations shown for the low-noise fan design are those which differed from the general application fan design. The information regarding the detail of the design for the low-noise fan is given in Section 4.3. The velocity profile was calculated in the same way as for the general application fan and is illustrated in Figure 4.3. The same type of airfoil as the one used for the general application fan, namely the F-series, was used for the low-noise fan. The second radial point from the hub is used for the low-noise fan sample calculations. The same point was used for the general application fan calculations. The known variables for the sample point were as follows:

C_{a1} = 13.683 m/s

C_{a2} = 11.971 m/s

C_{w1} = 0 m/s

C_{w2} = 18.031 m/s

β_1 = 57.915 °

β_2 = 17.589 °

r = 0.145 m

r_i = 0.125 m

r_o = 0.500 m

n_b = 7

rpm = 1440 rpm

Ω = 150.796 rad/s

U_o = 75.398 m/s

B.3.1 CALCULATING THE LOW-NOISE DESIGN VARIABLES

As described in Section 4.3.1, the design variables were the same as for the general application fan design, with the only difference being the use of blade sweep in the design procedure. The first value that was calculated was the geometric sweep angle. The geometric sweep angle is the angle of blade sweep as viewed from the front of the axial flow fan. The curve for geometric sweep angle was represented as follows (Wright et. al (1989)):

$$\eta = 37.9261 + 79.1634 \times M_R - 0.3152/M_R - 23.0131 \times M_R^3 \qquad (B.45)$$

where M_R is given by equation (B.46):

$$M_R = \frac{\Omega \times r}{\sqrt{RT}} \qquad (B.46)$$

$$= \frac{150.796 \times 0.145}{\sqrt{287 \times 293.16}}$$

$$= 0.075$$

where

$R = 287$ J/kgK

$T = 293.16$ K (20 °C)

Using this value in equation (B.45) the value for geometric sweep was calculated:

$$\eta = 37.9261 + 79.1634 \times 0.075 - 0.3152/0.075 - 23.0131 \times 0.075^3$$

$$= 37.987^\circ$$

Integrating equation (B.45) gave the equation for θ_s (see Figure 4.13). Equation (B.45) was important in defining the form of the blade axis for design purposes:

$$\theta_s = 37.9261 \times \ln(r) + 79.1634 \times G \times r + \frac{0.3152}{G \times r} - \frac{23.0131 \times G^3 \times r^3}{3} + K \qquad \text{(B.47)}$$

$$= 37.9261 \times \ln(0.145) + 79.1634 \times 0.4395 \times 0.145 + \frac{0.3152}{0.4395 \times 0.145} - \frac{23.0131 \times 0.4395^3 \times 0.145^3}{3} + 68.778$$

$$= 5.443^\circ$$

where

$G = 0.4395$

$K = 68.778$

Smith et al. (1963) defined another angle, namely the aerodynamic sweep angle, λ, which represents the amount of blade sweep along the blade surface itself, taking the blade stagger angle into account. Using Figure 4.14 to transform η into λ, equation (B.48) was derived:

$$\tan\lambda = \tan\eta \times \cos\phi \qquad \text{(B.48)}$$

where

$$\phi = 90 - \xi$$

where

$$\beta_m = \tan^{-1}\frac{1}{2}(\tan\beta_1 + \tan\beta_2)$$

$$= \tan^{-1}\frac{1}{2}(\tan 57.915^\circ + \tan 17.589^\circ)$$

$$= 43.712^\circ$$

This gave:

$$\phi = 90 - \xi$$

$$= 90 - 43.712$$

$$= 46.288^\circ$$

$$\lambda = \tan^{-1}(\tan\eta \times \cos\phi)$$

$$= \tan^{-1}(\tan 37.987^{\circ} \times \cos 46.288^{\circ})$$

$$= 31.169^{\circ}$$

All the blade variables had to be transformed by the angle λ at the different radii (see Figure 4.15). The next step was to calculate the "swept" values for the flow angles (see Figure 4.15):

$$\beta_{s1} = \tan^{-1}(\tan\beta_1 \times \cos\lambda) \qquad \text{(B.49)}$$

$$= \tan^{-1}(\tan 57.915^{\circ} \times \cos 31.169^{\circ})$$

$$= 53.770^{\circ}$$

$$\beta_{s2} = \tan^{-1}(\tan\beta_2 \times \cos\lambda) \qquad \text{(B.50)}$$

$$= \tan^{-1}(\tan 17.589^{\circ} \times \cos 31.169^{\circ})$$

$$= 15.176^{\circ}$$

$$\beta_{sm} = \tan^{-1}\frac{1}{2}(\tan\beta_{s1} + \tan\beta_{s2}) \qquad \text{(B.51)}$$

$$= \tan^{-1}\frac{1}{2}(\tan 53.770^{\circ} + \tan 15.176^{\circ})$$

$$= 39.284^{\circ}$$

The above values were used to calculate the blade loading factor:

$$C_L\sigma = 2 \times \left(\frac{C_{w2}}{C_{am}}\right) \times \cos\beta_{sm} \qquad \text{(B.52)}$$

$$= 2 \times \left(\frac{18.031}{12.827}\right) \times \cos 39.284^{\circ}$$

$$= 2.176$$

The values for lift coefficient were 1.4 at the hub and 0.7 at the tip. The solidity ratios at the hub and tip of the blade could be calculated from the blade loading factors calculated along the blade length.

$\sigma_i = 1.645$

$\sigma_o = 0.478$

Once the values for solidity ratio at the blade hub and tip were calculated, the values for "swept" blade spacing were calculated at the hub and tip (Smith et. al. (1963)):

$$s_s = s \Big/ \sqrt{1 + (\tan \eta)^2} \qquad \text{(B.53)}$$

$$s_{si} = 0.112 \Big/ \sqrt{1 + (\tan 36.555\,^\circ)^2}$$

$$= 0.090$$

$$s_{so} = 0.449 \Big/ \sqrt{1 + (\tan 53.629\,^\circ)^2}$$

$$= 0.266$$

where (see equation (B.35))

$s_i = 0.112$

$s_o = 0.449$

$\eta_i = 36.555\,^\circ$

$\eta_o = 53.629\,^\circ$

Using the values for "swept" spacing, the "swept" chord at the blade hub and tip were determined using equation (B.54):

$$c_s = \sigma \times s_s \qquad \text{(B.54)}$$

$$c_{si} = 1.645 \times 0.090$$

$$= 0.148 \text{ m}$$

$$c_{si} = 0.478 \times 0.266$$

$$= 0.127 \text{ m}$$

Interpolating linearly between the "swept" chord values at the hub and tip gave the "swept" chord distribution over the blade length.

$$c_s = c_{si} - \left(c_{si} - c_{so}\right) \times \left(\frac{r - r_i}{r_o - r_i}\right) \qquad \text{(B.55)}$$

$$= 0.148 - (0.021) \times \left(\frac{0.145 - 0.125}{0.375}\right)$$

$$= 0.147 \text{ m}$$

From these the solidity distribution over the blade were calculated using:

$$\sigma = c_s / s_s$$

$$= 0.147/0.102$$

$$= 1.438$$

From this value for solidity the lift coefficient was calculated using equation (B.52):

$$C_L = \frac{2}{\sigma} \times \left(\frac{C_{w2}}{C_{am}}\right) \times \cos\beta_{sm}$$

$$= \frac{2}{1.438} \times \left(\frac{18.031}{12.827}\right) \times \cos 39.284^\circ$$

$$= 1.513$$

The "swept" camber angle distribution was calculated using equation (B.56):

$$\theta_s = \beta_{s1} - \beta_{s2} + \delta - i + \Delta^0 \qquad \text{(B.56)}$$

The values for δ were calculated using equations (B.41) and (B.42). The "swept" variables were used in the equations. A preliminary value for the stagger angle was assumed:

$$\xi = \beta_{sm}$$

$$= 39.284\ ^\circ$$

$$m = 0.209253 + \frac{0.2322389}{10^2} \times 39.284\ ^\circ - \frac{0.3736909}{10^4} \times \left(39.284\ ^\circ\right)^2 + \frac{0.8668135}{10^6} \times \left(39.284\ ^\circ\right)^3$$

$$= 0.295$$

$$\delta = \left(m \times \left(\beta_{s1} - \beta_{s2}\right) \times \sqrt{s\ c}\right) \Big/ \left(1 - m \times \sqrt{s\ c}\right)$$

$$= \left(0.295 \times \left(53.770 - 15.176\right) \times \sqrt{0.695}\right) \Big/ \left(1 - 0.295 \times \sqrt{0.695}\right)$$

$$= 12.587\ ^\circ$$

The value for incidence angle was obtained from the same graph used previously (see Figure 4.7). Since the value of i is dependent on the value of θ, a preliminary value was calculated:

$$\theta_s = \beta_{s1} - \beta_{s2}$$

$$= 53.770\ ^\circ - 15.176\ ^\circ$$

$$= 38.594\ ^\circ$$

This gave a value for i of:

$$i = 1.65\ ^\circ$$

The value for downwash deviation angle, Δ^0, was calculated at the fan hub using the method proposed by Smith et al. (1963). The effect of the downwash deviation angle on the camber angle was very small and therefore the method used is discussed very briefly. The method started off by calculating the value for downwash at the wall, Dw_w. The next step was to calculate the locations, a perpendicular distance, h, from the wall, for 50% and 10% of Dw_w, as a fraction of the chord length, c. A curve was then fitted through these values to obtain the downwash distribution:

$$Dw = -\left[\left((2.448 - 0.5975 \times h\ c)/(1 + 79.785 \times h\ c)\right)^{\frac{1}{1.782}}\right]$$

where (for the sample point)

h/c = 0.161 [The value for c in this equation is the swept chord value]

This gave:

Dw = - 0.369

The downwash deviation angles at the different radii were calculated as follows:

$$\Delta^0 = \frac{180}{\pi} \times \frac{\Gamma}{c \times W_m} \times Dw \qquad \text{(B.56)}$$

where

$$c = c_s/\cos\lambda \qquad \text{(B.57)}$$

$$= 0.147/\cos 31.169^\circ$$

$$= 0.172 \text{ m}$$

$$W_m = C_{am}/\cos\beta_m \qquad \text{(B.58)}$$

$$= 12.827/\cos 43.712^\circ$$

$$= 17.746 \text{ m/s}$$

$$\Gamma = \frac{2\pi}{n_b} \times \left|r \times C_{w2}\right| \qquad \text{(B.59)}$$

$$= \frac{2\pi}{7} \times \left|0.145 \times 18.031\right|$$

$$= 2.347 \text{ rad. m}^2/\text{s}$$

This gave:

$$\Delta^0 = \frac{180}{\pi} \times \frac{2.347}{0.172 \times 17.746} \times -0.369$$

$$= -16.265\ ^\circ$$

The value for downwash angle was very large and therefore it was decided to limit the value for downwash angle to be smaller than or equal to half the value for deviation angle at that specific radius. The original value for downwash angle was very large close to the wall and therefore the deviation angle was cancelled out by the wall effects. The above limiting values were used to prevent the downwash angle from cancelling out the deviation angle. This gave (for the sample point):

$$\Delta^0 = -6.294\ ^\circ$$

Using equation (B.56), the swept camber angle was calculated:

$$\theta_s = 53.770 - 15.176 + 12.587 - 1.65 - 6.294$$

$$= 43.237\ ^\circ$$

The "swept" stagger angle distribution was calculated using equation (B.60):

$$\xi_s = \beta_{s1} - \alpha \qquad \text{(B.60)}$$

The values for angle of attack, α, were obtained from the graph in Wallis (1983) (see Figure 4.8):

$$\alpha = \alpha_{0d} - 0.57 \times d$$

where

$\alpha_{0d} = 5.5\ ^\circ$

$d = 2$ (The droop was designed to be less for a lower noise level)

This gave:

$$\alpha = 4.360\ ^\circ$$

From the above value for angle of attack, a swept stagger angle was calculated:

$$\xi_s = 53.770 - 4.360$$

$$= 49.410\ ^\circ$$

The calculations were repeated with the new stagger angle values because the stagger angles were approximated at the start of the calculations. Finally, after convergence has been reached, the "unswept" values for stagger and camber angle at the different radii were calculated:

$$\xi = \tan^{-1}\left(\tan \xi_s / \cos \lambda\right) \qquad \text{(B.61)}$$

$$= \tan^{-1}\left(\tan 50.747^\circ / \cos 31.169^\circ\right)$$

$$= 55.040^\circ$$

$$\theta = \tan^{-1}\left(\tan \theta_s / \cos \lambda\right) \qquad \text{(B.62)}$$

$$= \tan^{-1}\left(\tan 36.588^\circ / \cos 31.169^\circ\right)$$

$$= 40.944^\circ$$

APPENDIX C: SAMPLE CALCULATIONS FOR STRENGTH ANALYSIS

The calculations for the general application fan and the low-noise fan were exactly the same, except for the aeroelastic calculations which were only done for the low-noise swept blade. The calculations used the material data and force coefficients presented in Figures 4.5 and 4.6 respectively. Where applicable, all the sample calculations were done for the second radial point from the hub (r = 0.145 m). The general application fan was used to illustrate the sample calculations for the aerodynamic and centrifugal loads, while the low-noise fan was used to illustrate the sample calculations for the aeroelastic load.

C.1 AERODYNAMIC LOADS

These loads are listed as follows:

1) Twisting moment
2) Bending loads
3) Shear loads

The first step was to calculate the lift and drag forces over each of the segments. These segments were formed by the areas around the radial divisions along which the blade was designed.

$$L = C_L \times \frac{1}{2} \times \rho \times C_{am}^{\ 2} \times A \qquad (C.1)$$

$$D = C_D \times \frac{1}{2} \times \rho \times C_{am}^{\ 2} \times A \qquad (C.2)$$

with

$\rho = 1.2\ kg/m^3$

$A = c \times \Delta r$

$= 0.0859 \times 0.0197$

$= 0.001692\ m^2$

$C_L = 1.877$

$C_D = 0.0128$

$C_{am} = 12.558\ m/s$

This gave:

$$L = C_L \times \frac{1}{2} \times \rho \times C_{am}^{\ 2} \times A$$

$$= 1.877 \times \frac{1}{2} \times 1.2 \times 12.558^2 \times 0.001692$$

$$= 0.301\ \text{N}$$

$$D = C_D \times \frac{1}{2} \times \rho \times C_{am}^{\ 2} \times A$$

$$= 0.0128 \times \frac{1}{2} \times 1.2 \times 12.558^2 \times 0.001692$$

$$= 0.002\ \text{N}$$

The value for resultant force was calculated:

$$F = \sqrt{L^2 + D^2}$$

$$= \sqrt{0.301^2 + 0.002^2}$$

$$= 0.3005\ \text{N}$$

and the angle between F and L:

$$\text{delta} = \tan^{-1} \frac{D}{L}$$

$$= \tan^{-1} \frac{0.002}{0.301}$$

$$= 0.381^\circ$$

Following the calculation method described in Section 4.1.1, the direction in which the components of the resultant forces over the different segments gave the maximum bending moment, as well as the direction which gave the maximum shear force were calculated. The values for maximum bending moment and shear force were calculated as follows:

$$M_{bend} = \sum_{j=1}^{n} F_j \times \left(\cos\left(\phi_j - \phi_{ref}\right)\right) \times l_{mom} \qquad \text{(C.3)}$$

This gave:

$$M_{bend} = \sum_{j=2}^{n-1} F_j \times \left(\cos\left(\phi_j - \phi_{ref}\right)\right) \times \left(r_j - r_1\right)$$

$$+ F_1 \times \left(\cos\left(\phi_1 - \phi_{ref}\right)\right) \times \frac{\left(r_2 - r_1\right)}{4}$$

$$+ F_{20} \times \left(\cos\left(\phi_{20} - \phi_{ref}\right)\right) \times \left(r_{20} - r_1 - \left(\frac{r_{20} - r_{19}}{4}\right)\right)$$

$$F_{shear} = \sum_{j=1}^{n} F_j \times \left(\cos\left(\phi_j - \phi_{ref}\right)\right)$$

where

$$\phi_j = delta_j + \left(90° - \xi_j\right)$$

$$n = 20$$

This gave:

$$M_{bend} = 0.68723 \text{ Nm}$$

$$F_{shear} = 4.19585 \text{ N}$$

The aerodynamic twisting moment was calculated as follows:

$$M_{c\,4} = C_{Mc\,4} \times \frac{1}{2} \times \rho \times C_m^{\,2} \times A \times c \qquad \text{(C.4)}$$

$$= -0.075 \times \frac{1}{2} \times 1.2 \times 12.558^2 \times 0.001692 \times 0.0859$$

$$= -0.001 \text{ Nm}$$

This gave numerically:

$$M_{c\,4\,total} = \sum_{j=1}^{n} M_{c\,4\,i}$$

This gave:

$$M_{c\,4\,total} = -0.00592 \text{ Nm}$$

The next moment that was calculated is the one due to distance offset between the quarter chord point and the segment centroid. According to Wallis (1983) the distance the centroid is located from the leading edge is almost constant at 43.45% of the chord length. This gave:

$$\Delta x = (0.4345 - 0.25) \times c$$

$$= 0.1845 \times 0.0859$$

$$= 0.016 \text{ m}$$

This gave:

$$M_{add} = 0.1845 \times c \times L \qquad (C.5)$$

$$= 0.016 \times 0.301$$

$$= 0.005 \text{ Nm}$$

These values for the different blade sections gave:

$$M_{add\ total} = \sum_{j=1}^{n} M_{add\ i}$$

$$= 0.062568 \text{ Nm}$$

C.2 CENTRIFUGAL LOADS

The centrifugal loads were listed as:

1) Twisting moment

2) Centrifugal load

These forces occur due to the revolution of the fan blades around a fixed axis. The axial force due to the centrifugal loads is given by:

$$F_{axial} = \rho \times \Omega^2 \times \int_{ri}^{ro} (A \times r).\, dr \qquad (C.6)$$

Where

ρ = material density [kg/m^3]

Ω = fan revolution speed

= 303.687 rad/s

A = cross-section area [m^2]

The value for the cross-sectional area was obtained from a curve-fit on a graph given by Wallis (1983) (see Figure 4.20):

$$A = \left(\frac{t}{10}\right) \times \left(1 \times 10^{-6} \times \theta^2 - 7 \times 10^{-6} \times \theta + 0.0725\right) \times c^2 \qquad (C.7)$$

where

θ = 35.677 °

t = thickness-to-chord ratio

= 10.789 %

c = 0.086 m

Implemented in equation (C.7) the above gave:

$$A = \left(\frac{10.789}{10}\right) \times \left(1 \times 10^{-6} \times \left(35.677\ ^\circ\right)^2 - 7 \times 10^{-6} \times \left(35.677\ ^\circ\right) + 0.0725\right) \times 0.086^2$$

$$= 0.000587\ m^2$$

Numerically, the integral in equation (C.6) was represented as follows:

$$F_{axial} = \rho \times \Omega^2 \times \sum_{j=2}^{9} A_i \times r_i \times \left(r_i - r_{i-1}\right)$$

$$+ \rho \times \Omega^2 \times A_1 \times \left(r_1 + \frac{r_2 - r_1}{4}\right) \times \frac{\left(r_2 - r_1\right)}{2}$$

$$+ \rho \times \Omega^2 \times A_{10} \times \left(r_{10} + \frac{r_{10} - r_9}{4}\right) \times \frac{\left(r_{10} - r_9\right)}{2}$$

$$= \rho \times 303.687^2 \times 1.63 \times 10^{-5}$$

$$= \rho \times 1.5033\ N$$

The centrifugal twisting moment is given by (Wallis, 1983):

$$M_{cent} = \rho \times \frac{\Omega^2}{2} \times \int_{ri}^{ro} \left(\sin(2 \times \gamma) \times \left(J_2 - J_1\right)\right).\, dr \qquad (C.8)$$

where

$$\gamma = 90° - \xi$$

$$= 90 - 48.734$$

$$= 41.266\ °$$

J_2 and J_1 were obtained from curve-fits from graphs in Wallis (1983) (see Figures 4.21 and 4.22):

$$J_2 = \left(\frac{t}{10}\right) \times \left(0.0014 \times \theta^2 - 0.0068 \times \theta + 42.868\right) \times 10^{-4} \times c^4 \quad \text{(C.9)}$$

$$= \left(\frac{10.789}{10}\right) \times \left(0.0014 \times \left(35.677\ °\right)^2 - 0.0068 \times \left(35.677\ °\right) + 42.868\right) \times 10^{-4} \times 0.086^4$$

$$= 262.10^{-9}\ m^4$$

$$J_1 = \left(\frac{t}{10}\right) \times \left(0.0022 \times \theta^2 - 0.0031 \times \theta + 0.6648\right) \times 10^{-5} \times c^4 \quad \text{(C.10)}$$

$$= \left(\frac{10.789}{10}\right) \times \left(0.0022 \times \left(35.677\ °\right)^2 - 0.0031 \times \left(35.677\ °\right) + 0.6648\right) \times 10^{-5} \times 0.086^4$$

$$= 1.980.10^{-9}\ m^4$$

Equation (C.8) simplifies numerically to:

$$M_{cent} = \rho \times \frac{\Omega^2}{2} \times \sum_{j=2}^{9} \sin(2 \times \gamma_j) \times (J_{2j} - J_{1j}) \times (r_j - r_{j-1})$$

$$+ \rho \times \frac{\Omega^2}{2} \times \sin(2 \times \gamma_1) \times (J_{21} - J_{11}) \times \frac{(r_2 - r_1)}{2}$$

$$+ \rho \times \frac{\Omega^2}{2} \times \sin(2 \times \gamma_{10}) \times (J_{210} - J_{19}) \times \frac{(r_{10} - r_9)}{2}$$

$$= \rho \times \frac{303.687^2}{2} \times 3.16 \times 10^{-8}$$

$$= \rho \times 0.0014572 \text{ Nm}$$

C.3 BLADE STRESSES

The critical part of the blade was identified as the blade root, as mentioned in Section 4.3.3. For the general application fan this gave:

$r_{outer} = 0.0105$ m

$r_{inner} = 0.004$ m

All the sample calculations in this section are for the general application fan. The characteristic values for the cross-section were calculated:

$$A_{root} = \pi \times (r_{outer}^2 - r_{inner}^2)$$
$$= \pi \times (0.0105^2 - 0.004^2)$$
$$= 296.095 \times 10^{-6} \text{ m}^2$$

$$I_{root} = \frac{\pi \times (d_{outer}^4 - d_{inner}^4)}{64}$$
$$= \frac{\pi \times (0.021^4 - 0.008^4)}{64}$$
$$= 9.346 \times 10^{-9} \text{ m}^4$$

$$J_{root} = \frac{\pi \times (d_{outer}^4 - d_{inner}^4)}{32}$$
$$= \frac{\pi \times (0.021^4 - 0.008^4)}{32}$$
$$= 18.691 \times 10^{-9} \text{ m}^4$$

The calculations for the different materials gave:

1) Nylon

$$\tau_{shear} = \frac{F_{shear}}{A_{root}}$$
$$= \frac{4.19585}{296.095 \times 10^{-6}}$$
$$= 14.17 \text{ kPa}$$

$$\sigma_{axial} = \frac{F_{axial}}{A_{root}}$$
$$= \frac{1140 \times 1.5033}{296.095 \times 10^{-6}}$$
$$= 5.787879 \text{ MPa}$$

$$\sigma_{bend} = \frac{M_{bend} \times y_{max}}{I_{root}}$$
$$= \frac{0.68723 \times 0.0105}{9.346 \times 10^{-9}}$$
$$= 772.08 \text{ kPa}$$

$$T_{root} = -\left(M_{c\ 4\ total} + M_{add\ total}\right) + M_{cent}$$
$$= -(0.00592 + 0.062568) + 1.661208$$
$$= 1.59272 \text{ Nm}$$

$$\tau_{torsion} = \frac{T_{root} \times r_{outer}}{J_{root}}$$
$$= \frac{1.59272 \times 0.0105}{18.691 \times 10^{-9}}$$
$$= 0.89700819 \text{ MPa}$$

This gave the total stresses:

$$\tau_{total} = 0.89701 + 0.01417$$
$$= 0.9112 \text{ MPa}$$

$$\sigma_{total} = 0.77208 + 5.787879$$
$$= 6.55996 \text{ MPa}$$

The safety factors were based on the yield strength and maximum shear strength:

$$sf_{sigma} = \frac{\sigma_{yield}}{\sigma_{total}}$$

$$= \frac{75}{6.6}$$

$$= 11.4$$

$$sf_{tau} = \frac{\tau_{max}}{\tau_{total}}$$

$$= \frac{37.5}{0.9}$$

$$= 41.2$$

2) Aluminium

$$\tau_{shear} = \frac{F_{shear}}{A_{root}}$$

$$= \frac{4.19585}{296.095 \times 10^{-6}}$$

$$= 14.17 \text{ kPa}$$

$$\sigma_{axial} = \frac{F_{axial}}{A_{root}}$$

$$= \frac{2710 \times 1.5033}{296.095 \times 10^{-6}}$$

$$= 13.758905 \text{ MPa}$$

$$\sigma_{bend} = \frac{M_{bend} \times y_{max}}{I_{root}}$$

$$= \frac{0.68723 \times 0.0105}{9.346 \times 10^{-9}}$$

$$= 772.08 \text{ kPa}$$

$$T_{root} := -\left(M_{c\ 4\ total} + M_{add\ total}\right) + M_{cent}$$
$$= -(0.00592 + 0.062568) + 3.949012$$
$$= 3.880524 \text{ Nm}$$

$$\tau_{torsion} = \frac{T_{root} \times r_{outer}}{J_{root}}$$
$$= \frac{3.880524 \times 0.0105}{18.691 \times 10^{-9}}$$
$$= 2.179953 \text{ MPa}$$

This gave the total stresses:

$$\tau_{total} = 2.179953 + 0.01417$$
$$= 2.1941 \text{ MPa}$$

$$\sigma_{total} = 0.77208 + 13.7589$$
$$= 14.53099 \text{ MPa}$$

This gave:

$$sf_{sigma} = \frac{\sigma_{yield}}{\sigma_{total}}$$
$$= \frac{180}{14.53}$$
$$= 12.4$$

$$sf_{tau} = \frac{\tau_{max}}{\tau_{total}}$$
$$= \frac{90}{2.1941}$$
$$= 41.02$$

C.4 AEROELASTIC CALCULATIONS FOR FORWARD-SWEPT FAN BLADES

Dowel et al. (1995) derived a set of equations constituting an Eigenvalue problem for a beam of constant spanwise properties:

$$\lambda_D = \frac{\partial \bar{C}_L}{\partial \alpha} \frac{\sin \Lambda \times \cos \Lambda \times \bar{c} \times \bar{l}^3 \times q}{E \times I} \qquad (C.11)$$

$$= -6.33$$

The variables for equation (C.11) are illustrated in Figure 4.24. A straight beam with constant spanwise properties was used for the low-noise fan blade. To determine the critical blade properties the beam properties were assumed equal to the blade hub properties in the one instance and equal to the blade tip properties in the other. As a sample calculation only the calculation at the hub is illustrated.

At the hub the following properties exist:

$t = 11\,\%\,c$

$I = 3.130.10^{-8}\ m^4$

$E = 207.10^9$ Pa (This value is due to the steel insert used for the blade shaft)

$$\frac{\partial \bar{C}_L}{\partial \alpha} = 6.875$$

The values for I and $\frac{\partial \bar{C}_L}{\partial \alpha}$ were obtained from graphs in Wallis (see Figure 4.8 and 4.21). The value for $\bar{l}$ was calculated, assuming Λ to be equal to - 45 °, as follows:

$$\bar{l} = (r_o - r_i)/\cos(\Lambda)$$

$$= 0.530\ m$$

The sweep angle, Λ, was calculated from $\theta_{s\,ave}$, along the fan radius as follows:

$$\Lambda = -\theta_{s\,ave} - \sin^{-1}\left(r_i \times \frac{\sin(\theta_{s\,ave})}{\bar{l}}\right) \qquad \text{(C.12)}$$

$$= -35.317\,^{\circ} - \sin^{-1}\left(0.125 \times \frac{\sin(35.317\,^{\circ})}{0.530}\right)$$

$$= -43.153\,^{\circ}$$

Iterating between the value of Λ and $\bar{l}$ the following values were obtained:

$$\Lambda = 43.366\,^{\circ}$$

$$\bar{l} = 0.516$$

From the above values the following value was calculated:

$$\bar{c} = c \times \cos\Lambda$$

$$= 0.170 \times \cos 43.366\,^{\circ}$$

$$= 0.124 \text{ m}$$

The air velocity was taken as the average blade velocity along the blade radius at 1440 rpm. The value for velocity was calculated as:

$$U = 47.124 \text{ m/s}$$

and

$$q = \frac{1}{2} \times \rho \times U^2$$

$$= \frac{1}{2} \times 1.2 \times 47.124^2$$

$$= 1332.403 \text{ Pa}$$

The value for λ_D was obtained using equation (C.11) as follows:

$$\lambda_D = 6.875 \times \frac{\sin(-43.366\,^{\circ}) \times \cos(-43.366\,^{\circ}) \times 0.124 \times 0.516^3 \times 1332.403}{207.10^9 \times 3.130.10^{-8}}$$

$$= -0.012$$

APPENDIX D: PHOTOS OF FAN BLADES AND TEST FACILITY COMPONENTS

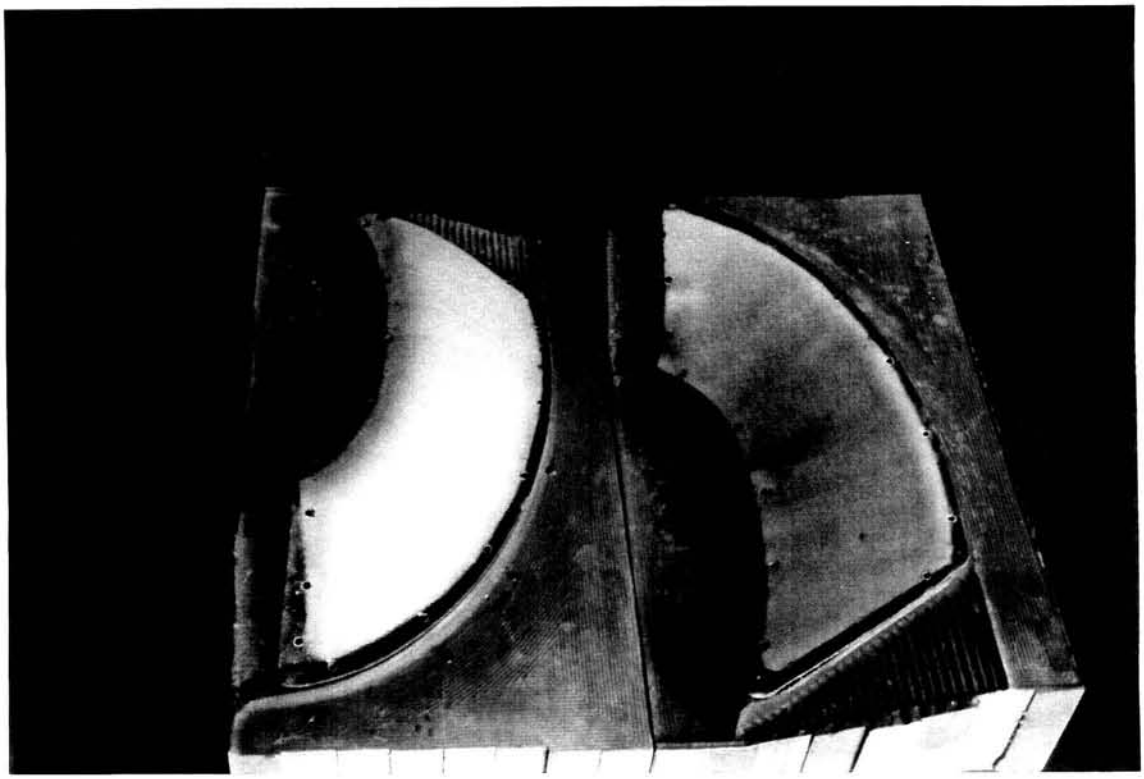

Figure D1: Photo of Jeluton wood blocks with mould halves on top of them

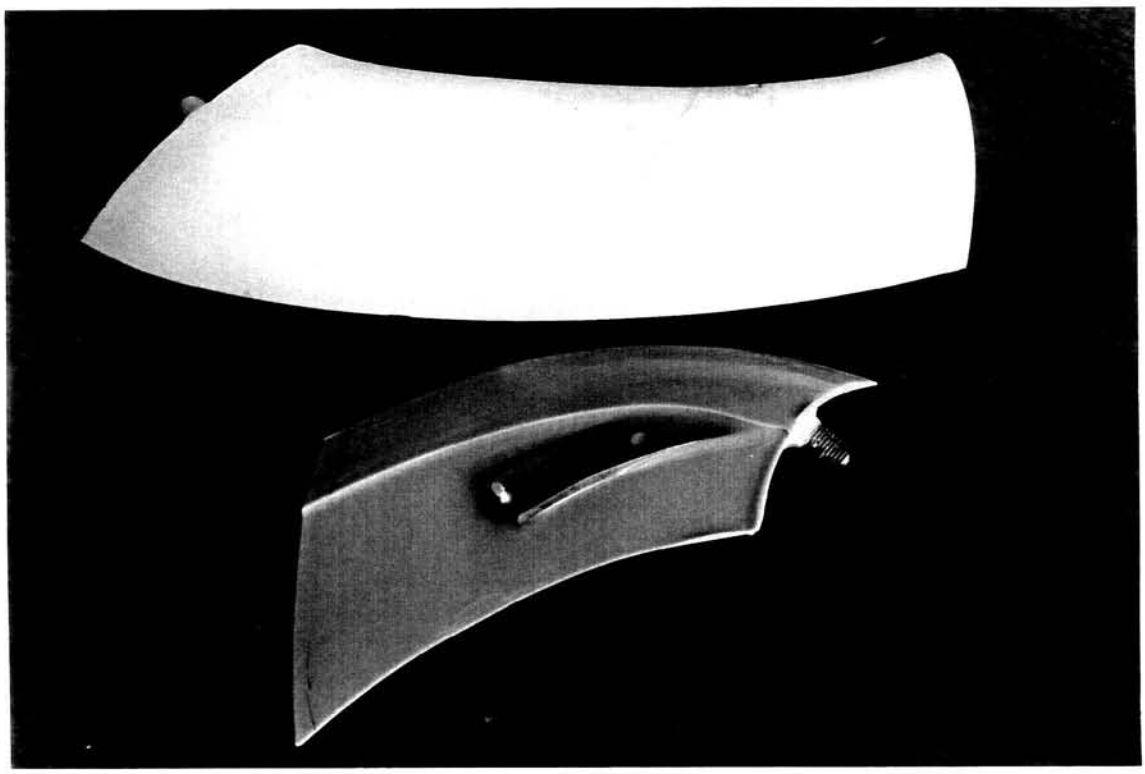

Figure D2: Photo of blade section showing steel insert and full length swept blade

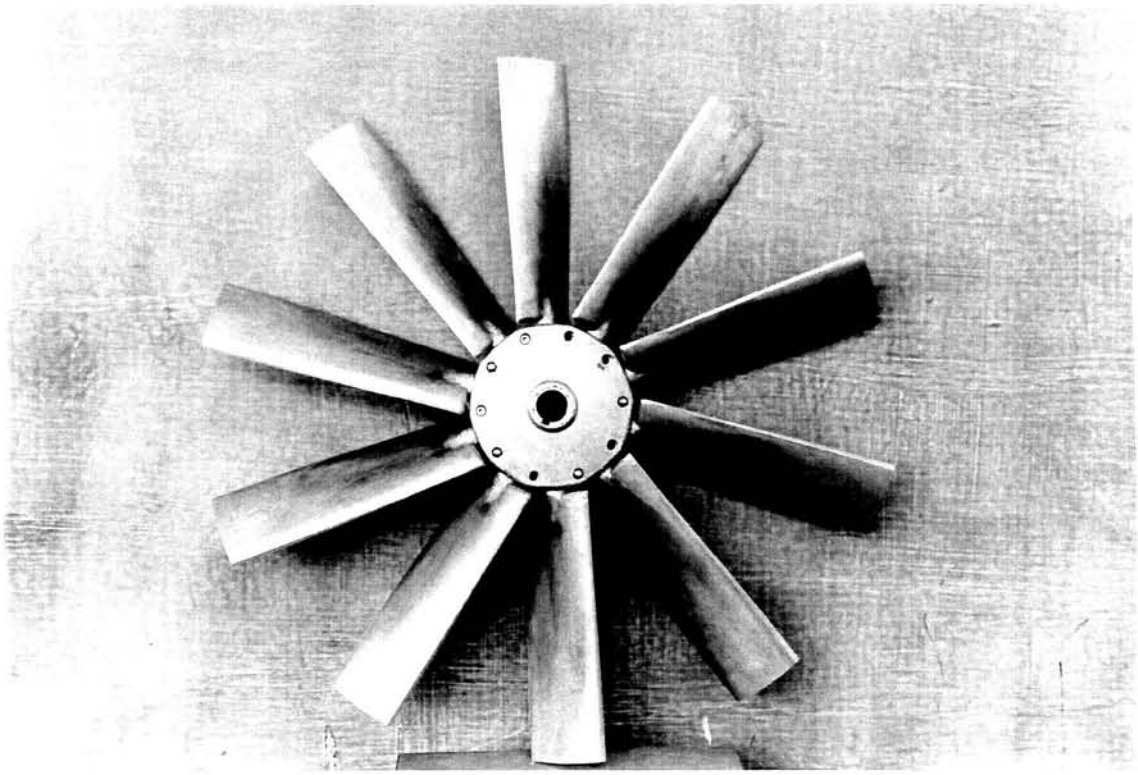

Figure D3: Photo of 630 mm diameter general application fan with 150 mm hub diameter

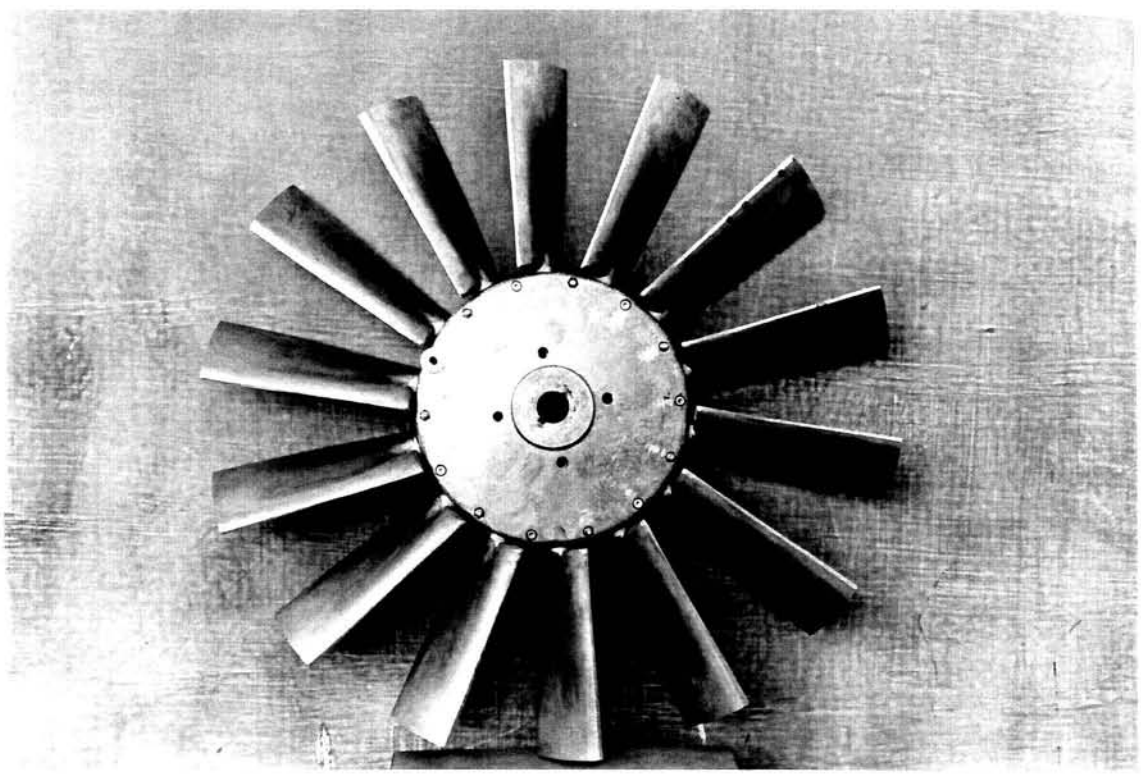

Figure D4: Photo of 630 mm diameter general application fan with 250 mm hub diameter

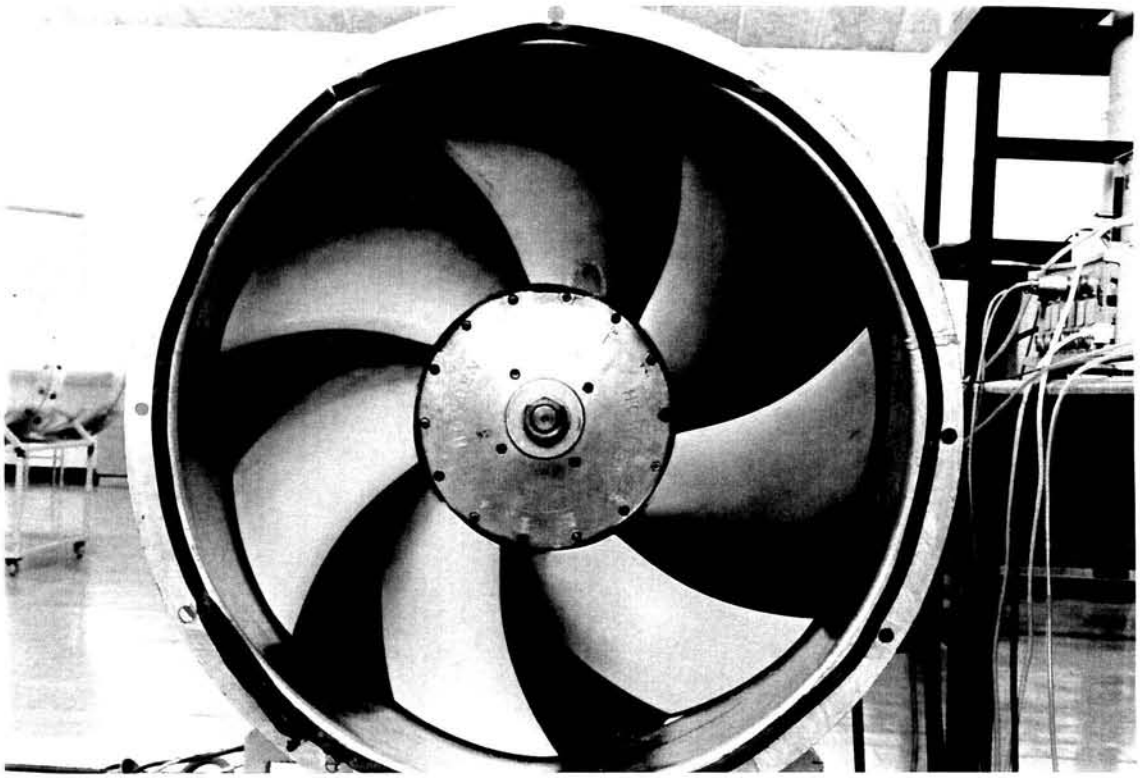

Figure D5: Photo of 630 mm diameter low-noise fan

Figure D6: Photo of test facility for 630 mm diameter fan

Figure D7: Photo of flow straightener used for 630 mm diameter fans

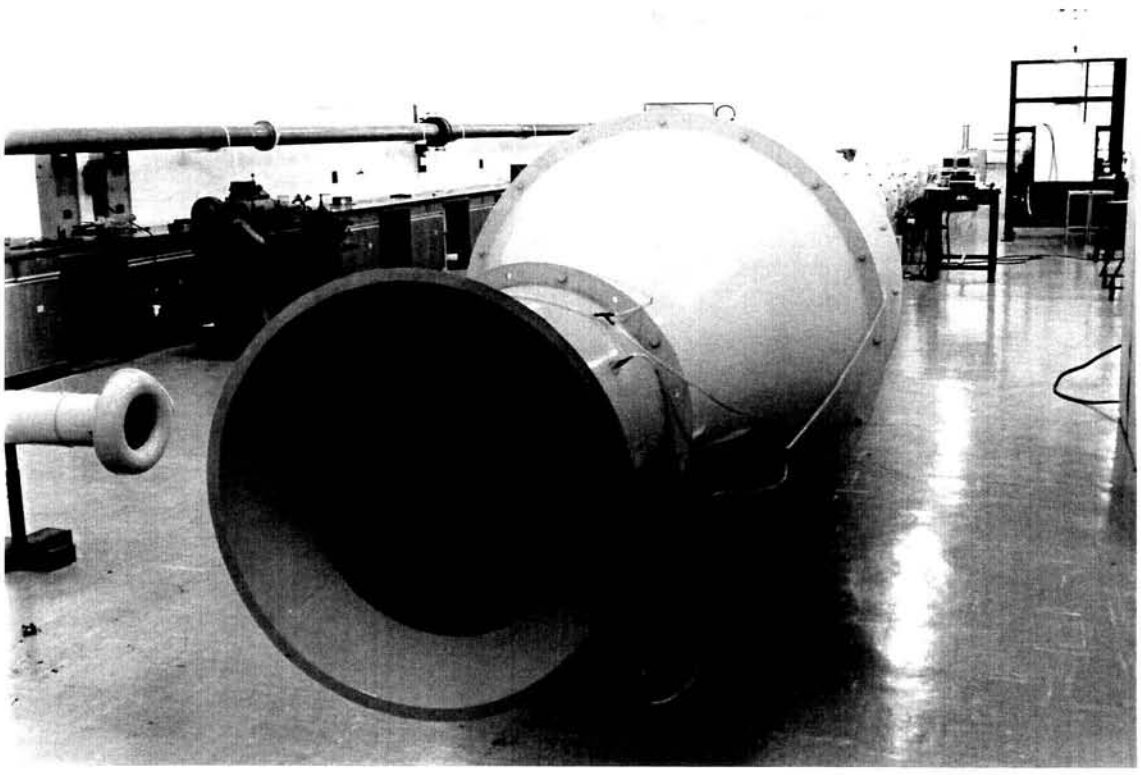

Figure D8: Photo of conical inlet of test facility

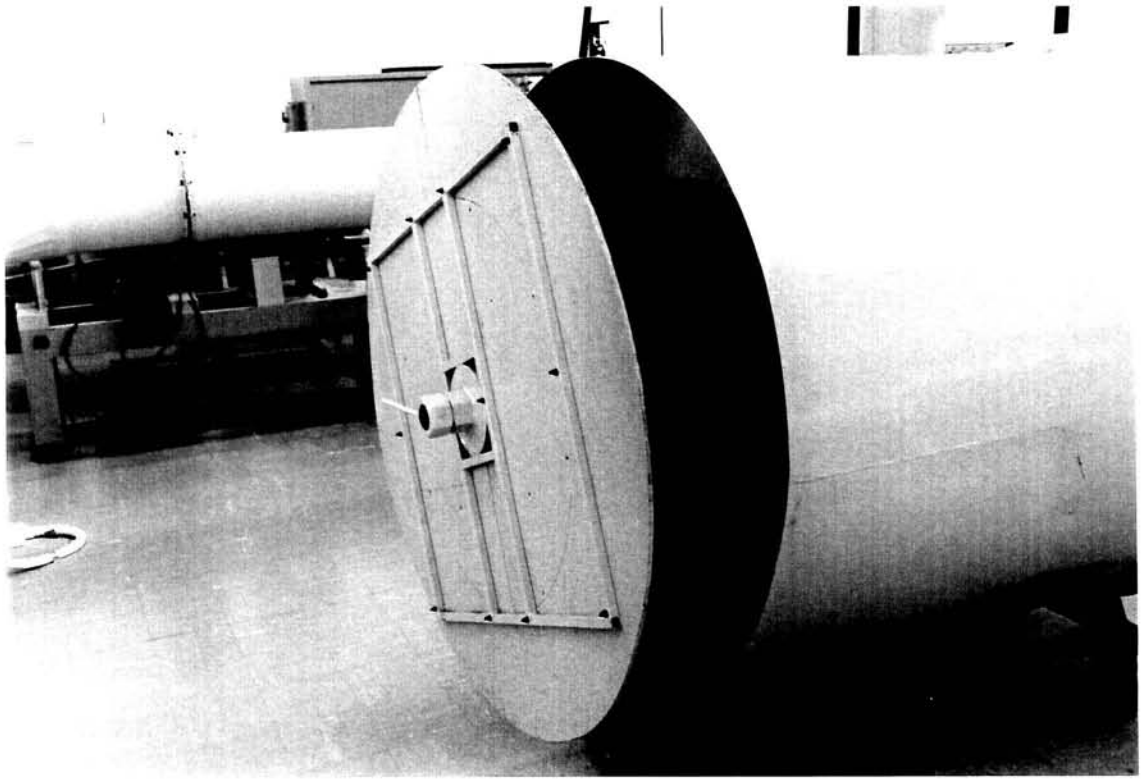

Figure D9: Photo of throttled outlet of test facility

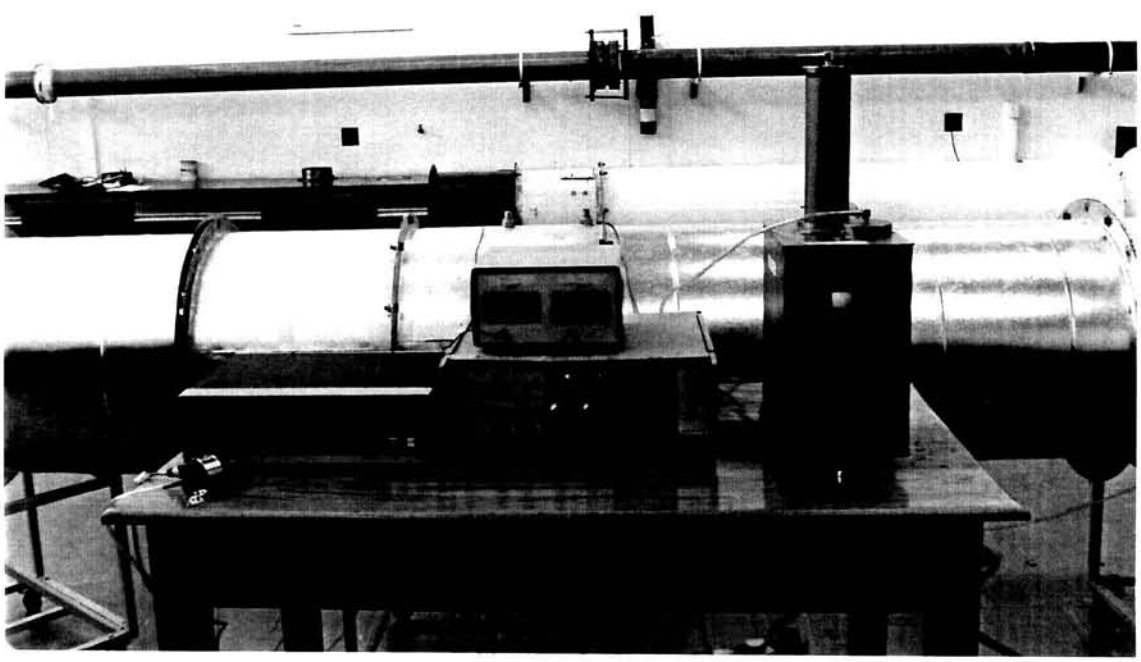

Figure D10: Photo of performance measuring apparatus used in fan tests

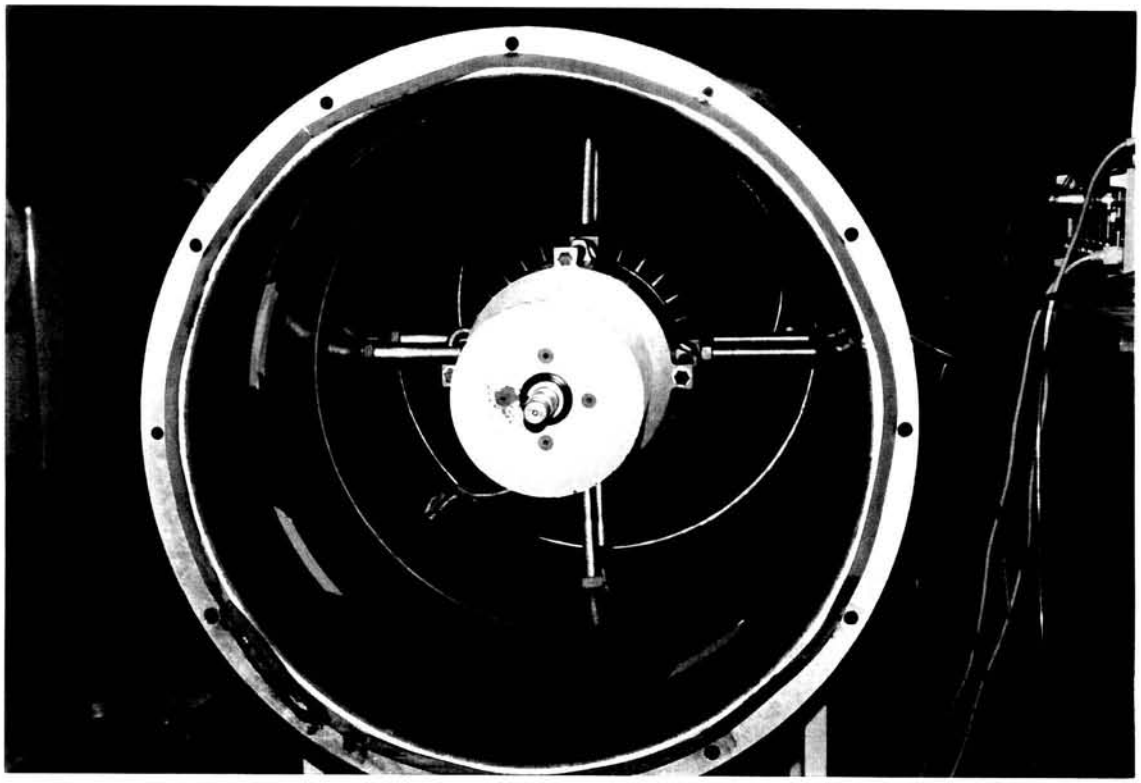

Figure D11: Photo of torque transducer installed in 630 mm diameter fan casing

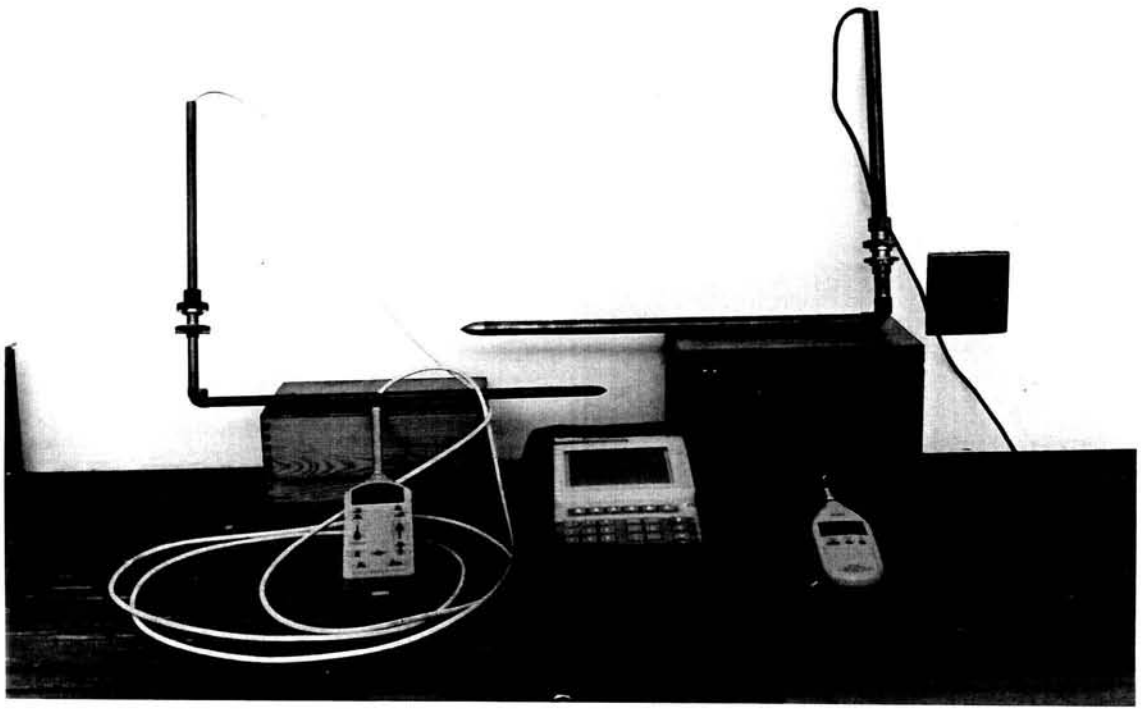

Figure D12: Photo of noise measuring apparatus used in fan tests

E. CALIBRATION OF TEST FACILITY

This chapter includes the calibration of the following items:

1. Torque transducer.
2. Pressure transducer.
3. Proximity switch.
4. Sound level meters.
5. Extension cable of Bruël and Kjaer sound level meter.

E.1 TORQUE TRANSDUCER

The torque transducer was calibrated with a wooden arm (length = 0.5 m) that was fitted onto the front of the shaft leaving the torque transducer. The other end of the shaft was prevented from turning by removing an inspection plate at the back end of the motor and anchoring the rotor inside the motor. The specific method of anchoring was used because there was no other way of reaching the shaft between the motor and the torque transducer due to the casing surrounding it. Different weights were then suspended from the tip of the arm to enable different torque readings to be read. The readings were read from the bridge amplifier and is given in Table E.1.

Table E.1: Calibration readings for torque transducer

Weight [kg]	Reading [mV]
0	0
0.909	219
1.815	450
2.724	688
3.631	925

A curve-fit through these values resulted in a linear relationship for mass vs. milliVolt, given as:

$$m_a = 0.003961 \times mV_T \qquad (E.1)$$

Using the values:

$g = 9.7962\ m/s^2$

$l_a = 0.500\ m$

the relationship for torque vs. milliVolt resulted:

$$T = 0.0194 \times mV_T \qquad (E.2)$$

E.2 PRESSURE TRANSDUCER

A Betz manometer was used to calibrate the pressure transducer. A pressure tube was connected in parallel to the positive pressure sides of both the Betz manometer and the pressure transducer. By blowing into the open end of the tube, a pressure was registered on the Betz manometer, in millimetre water, as well as on the bridge amplifier, in milliVolt. The relationship between these two values is linear and therefore only two readings were taken, namely a zero pressure reading and one at approximately 35 mm water pressure. The pressure calibration was repeated before each set of readings for a specific blade angle. The readings for the 630/250/14/1440 fan at a five degree blade angle are used as an example (see Table E.2).

Table E.2: Calibration readings for pressure transducer

Pressure [m H_2O]	Reading [mV]
0.000	96
0.036	2341

A curve-fit through the above set of values gave a relationship between meter water pressure and milliVolt amplifier reading. This was given as:

$$h = 1.6.10^{-5} \times mV_p - 0.00154 \qquad (E.3)$$

Using the following values:

$g = 9.7962\ m/s^2$

$\rho_{water} = 998\ kg/m^3$

The equation for pressure in terms of the milliVolt reading was obtained:

$$p = 0.156 \times mV_p - 15.056 \qquad (E.4)$$

E.3 PROXIMITY SWITCH

The proximity switch was activated by a six-legged ring that was installed on the shaft between the torque transducer and the motor. The reading on the frequency read-out was compared to the reading on a hand-held tachometer. The reading on the tachometer was in revolutions per minute and the reading on the frequency read-out in frequency divided by six. Since:

$$rpm = \frac{f}{60}$$

the values on the tachometer was a factor of ten larger than the readings on the frequency read-out. This gave the equation for fan speed as:

$$rpm = f_{ro} \times 10 \qquad (E.5)$$

E.4 SOUND LEVEL METERS

The FFT-analyzer gave a voltage reading and therefore this reading had to be calibrated with respect to the reading on the sound level meter. The calibration process was repeated for both types of sound level meters used in the testing procedure. It involved using a standard, 1000 Hz noise source of 94 dB that was installed over the microphone of the sound level meter. The voltage output of the meter was varied by changing the full-scale value of the meter. The 94 dB of the noise source corresponded to a full-scale setting of 100 dB on the sound level meter and therefore the rest of the readings were adjusted according to the different full-scale values. The voltage readings on the FFT-analyzer were used to compile two tables with the decibel values converted back to sound pressure readings. The tables are given as Table E.3 and E.4.

Table E.3: Bruël and Kjaer sound level meter calibration readings

Pressure [Pa]	Reading [mV]
1.002374	453.074
0.316979	143.559
0.100239	44.984
0.000000	0.000

Table E.4: Rion sound level meter calibration readings

Pressure [Pa]	Reading [mV]
1.002374	504.374
0.316979	158.788
0.100239	50.325
0.000000	0.000

A curve-fit through the above sets of values gave two different linear relations for the two sound level meters. The equations gave the sound pressure levels in terms of the milliVolt readings. The equations are as follows:

1) Bruël and Kjaer

$$p_{slm\,3} = 0.0024 \times mV_{slm} \qquad (E.6)$$

2) Rion

$$p_{slm\,4} = 0.002 \times mV_{slm} \qquad (E.7)$$

E.5 EXTENSION CABLE

Once the sound level meters were calibrated for the FFT-analyzer, the extension cable was fitted to the Bruël and Kjaer sound level meter. The voltage losses due to the cable impedance at the different frequencies had to be determined. A white-noise source was used to generate a set of noise values at the different frequencies. These values were read with the Rion sound level meter and compared to the Bruël and Kjaer readings with its extension cable. The voltage values for the Rion sound level meter were converted to decibels using the equation for that sound level meter. The decibel values were then converted back to voltage readings using the equation for the Bruël and Kjaer sound level meter and the deviations due to the losses in the extension cable were determined by subtracting the original Bruël and Kjaer voltage readings from the converted Rion voltage readings.

An assumption was made that the losses in the cable would change linearly with the voltage read on the Bruël and Kjaer sound level meter. The assumption was based on the following:

1. The input sound disturbance observed by both sound level meters is the same and therefore the input voltage into both systems would be the same.
2. The signal received by the Rion sound level meter will pass through the capacitor of the microphone and through a resistive load which changes the current signal to a voltage signal to be read by the meter.
3. The signal observed by the Bruël and Kjaer sound level meter will pass through the capacitor microphone and through the cable, which serves as an inductive load. The current then passes through the resistive load and changes into a voltage signal which is read by the meter.
4. The voltage difference between the two meter's signals will change according to the strength of the original input due to the extra inductive load which changes with frequency. The input for both meters is the same and therefore the relation between the two voltage outputs of the two meters depends on the constant values of the circuit, namely the resistive load, capacitance of the microphone and the inductance of the extension cable. The relations between the voltage readings by the Bruël and Kjaer meter and the Rion meter, as well as the voltage difference, will all be linear functions.

5. The voltage difference will be zero when both the meters read a zero reading, in other words there is no input signal and therefore the linear relation between the Bruël and Kjaer reading and the voltage difference will pass through zero.

There is some uncertainty about whether the extension cable induces an inductive load that is in series with the capacitor microphone or a capacitive load in parallel with the capacitor microphone. The uncertainty is of no importance in this instance because in both cases the load changes with frequency and leads to linear relations between the mentioned values. The values that were observed in the readings, as well as the calculated gradient for the linear relation between the reading with the extension cable and the voltage difference, are given in Table E.5.

Table E.5: Deviation values for Bruël and Kjaer extension cable

Frequency [Hz]	B + K [mV]	Deviation [mV]	Gradient
63	10.456	284.408	27.200
125	10.312	276.670	26.831
250	15.056	221.660	14.722
500	38.536	248.535	6.449
1000	61.231	332.493	5.430
2000	21.961	179.833	8.189
4000	34.163	164.930	4.828
8000	7.449	84.384	11.328

The voltage difference for the extension cable was determined as:

$$mV_{ext} = \text{Gradient} \times mV_{slm\,3} \qquad \text{(E.8)}$$

APPENDIX F: SAMPLE CALCULATIONS FOR PROCESSING OF FAN TEST DATA

All the calculations were done according to the BS 848 Standards part 1 (1980) and 2 (1985). The sample calculations were done for the 630/250/14/1440 fan at a 5 ° blade angle at its sixth throttle setting point. The noise calculations were done for the same point at 2000 Hz. For these settings the readings were as follows:

$f_{ro} = 143.5$ Hz

$mV_i = -18$ mV

$mV_1 = -75$ mV

$mV_2 = 770$ mV

$mV_{delta} = 5$ mV

$T_{atm} = 299.3$ K

$P_{atm} = 99157.53$ Pa

$mV_T = 131$ mV

$mV_{slm3} = 22.89$ mV

$mV_{slm4} = 197.7$ mV

The first calculation was done to obtain the ambient air density from:

$$\rho_{atm} = \frac{P_{atm}}{R \times T_{atm}} \qquad (F.1)$$

Where

$R = 287$ J/kgK

This gave:

$$\rho_{atm} = \frac{99157.53}{287 \times 299.3}$$

$$= 1.155\ kg/m^3$$

The fan speed was obtained using equation (E.5) as follows:

$$rpm = f_{ro} \times 10 \qquad (F.2)$$

$$= 143.5 \times 10$$

$$= 1435\ rpm$$

This gave:

$$\Omega = \frac{2 \times \pi \times \text{rpm}}{60} \qquad \text{(F.3)}$$

$$= \frac{2 \times \pi \times 1435}{60}$$

$$= 150.796 \text{ rad/s}$$

All the pressure readings, measured in milliVolt, were adjusted by a zero pressure reading deviation determined at the start, before taking each set of pressure readings. The pressure drop that was measured across the conical inlet was determined as follows:

$$\rho_{water} = 998 \text{ kg/m}^3$$

$$g = 9.796 \text{ m/s}^2$$

$$mV_{pvf} = mV_i - mV_{delta}$$

$$= -18 - 5$$

$$= -23 \text{ mV}$$

$$h_{vf} = 1.6.10^{-5} \times mV_{pvf} - 0.00154 \qquad \text{(F.4)}$$

$$= 1.6.10^{-5} \times -23 - 0.00154$$

$$= -0.001908 \text{ m}$$

$$\Delta p = \rho_{water} \times g \times |h_{vf}| \qquad \text{(F.5)}$$

$$= 998 \times 9.796 \times 0.001908$$

$$= 18.65 \text{ Pa}$$

The mass flow rate was calculated from the pressure drop measured across the conical inlet as follows:

$$q_m = \alpha\varepsilon \times \left[\frac{\pi \times d_i^{\,2}}{4}\right] \times \sqrt{2 \times \rho_{atm} \times \Delta p} \qquad \text{(F.6)}$$

where

$$\alpha\varepsilon = 1 - 0.5 \times Re_{di}^{-0.2} \qquad \text{(see Section 5.3)}$$

As a first approximation, $\alpha\varepsilon$ was set equal to 0.96.

$$d_i = 0.620 \text{ m}$$

This gave:

$$q_m = 0.96 \times \left[\frac{\pi \times 0.620^2}{4}\right] \times \sqrt{2 \times 1.155 \times 18.65}$$

$$= 1.902 \text{ kg/s}$$

From the mass flow rate the volume flow rate was calculated:

$$Q = \frac{q_m}{\rho_{atm}} \qquad \text{(F.7)}$$

$$= \frac{1.902}{1.155}$$

$$= 1.645 \text{ m}^3/\text{s}$$

The density inside the conical inlet was assumed to be equal to the atmospheric density. The volume flow rate that was calculated was used to calculate the Reynolds number inside the conical inlet as follows:

$$V = \frac{Q}{A_i}$$

$$= \frac{1.645}{\pi \times 0.310^2}$$

$$= 5.449 \text{ m/s}$$

$$\mu = 1.8 \times 10^{-5} \text{ Ns/m}^2$$

$$Re_{di} = \frac{\rho_{atm} \times V \times d_i}{\mu}$$

$$= \frac{1.155 \times 5.449 \times 0.620}{1.8 \times 10^{-5}}$$

$$= 216\,767$$

The Reynolds number was used to calculate the value for $\alpha\varepsilon$:

$$\alpha\varepsilon = 1 - 0.5 \times Re_d^{-0.2}$$

$$= 1 - 0.5 \times 216767^{-0.2}$$

$$= 0.957$$

The new value for $\alpha\varepsilon$ changed the value for volume flow rate as follows:

$$Q = 1.640\ m^3/s$$

F.1 PROCESSING OF FAN PERFORMANCE DATA

The same subscripts that were mentioned in Section 5.3.1 were used for these calculations. The first values that were calculated were the static pressures at the measuring points in front of and behind the fan. The static pressures, measured in meter water, were calculated for these two points using the zero pressure reading deviation as well as equation (E.3):

$$mV_{p3} = mV_1 - mV_{delta}$$

$$= -75 - 5$$

$$= -80\ mV$$

$$mV_{p4} = mV_2 - mV_{delta}$$

$$= 770 - 5$$

$$= 765\ mV$$

$$h_{p3} = 1.6.10^{-5} \times mV_{p3} - 0.00154$$

$$= 1.6.10^{-5} \times -80 - 0.00154$$

$$= -0.00282\ m$$

$$h_{p4} = 1.6.10^{-5} \times mV_{p4} - 0.00154$$

$$= 1.6.10^{-5} \times 765 - 0.00154$$

$$= 0.0107\ m$$

Using similar equations to equation (F.5) the static pressures were calculated in Pascal:

$$p_{s3} = \rho_{water} \times g \times h_{p3}$$

$$= 998 \times 9.796 \times -0.00282$$

$$= -27.57 \text{ Pa}$$

$$p_{s4} = \rho_{water} \times g \times h_{p4}$$

$$= 998 \times 9.796 \times 0.0107$$

$$= 104.61 \text{ Pa}$$

To calculate the total pressures, the following values were needed:

1) Ducting cross-sectional area

$$r_3 = 0.315 \text{ m}$$

$$A_3 = \pi \times r_3^2 \qquad \text{(F.8)}$$

$$= \pi \times 0.315^2$$

$$= 0.312 \text{ m}^2$$

$$= A_1$$

$$= A_4$$

2) Air densities in ducting

$$\rho_3 = \rho_{atm} \times \left(\frac{p_{atm} + p_{s3}}{p_{atm}} \right) \qquad \text{(F.9)}$$

$$= 1.155 \times \left(\frac{99157.53 - 27.57}{99157.53} \right)$$

$$= 1.154 \text{ kg/m}^3$$

$$\rho_4 = \rho_{atm} \times \left(\frac{p_{atm} + p_{s4}}{p_{atm}} \right)$$

$$= 1.155 \times \left(\frac{99157.53 + 104.610}{99157.53} \right)$$

$$= 1.156 \text{ kg/m}^3$$

3) Air velocities in ducting

$$V_3 = \frac{q_m}{\rho_3 \times A_3} \qquad \text{(F.10)}$$

$$= \frac{1.902}{1.154 \times 0.312}$$

$$= 5.283 \text{ m/s}$$

$$= V_1$$

$$V_4 = \frac{q_m}{\rho_4 \times A_4}$$

$$= \frac{1.902}{1.156 \times 0.312}$$

$$= 5.273 \text{ m/s}$$

4) Air viscosity

$$\mu = 1.8 \times 10^{-5} \text{ Ns/m}^2$$

5) Reynolds numbers

$$Re_{d1} = \frac{\rho_3 \times V_1 \times d_1}{\mu} \qquad \text{(F.11)}$$

$$= \frac{1.154 \times 5.283 \times 0.630}{1.8 \times 10^{-5}}$$

$$= 213308$$

$$Re_{d4} = \frac{\rho_4 \times V_4 \times d_4}{\mu}$$

$$= \frac{1.156 \times 5.273 \times 0.630}{1.8 \times 10^{-5}}$$

$$= 213308$$

The static pressure at point three was used to calculate the total pressure in front of the fan (upstream):

$$p_{t1} = p_{s3} + \left[1 - \left(A_3/A_1\right)^2 + \xi_{31}\right] + \left(\frac{1}{2} \times \rho_3 \times V_3^{\,2}\right) \qquad \text{(F.12)}$$

where

$$\xi_{31} = 0.015 + 1.26 \times \left(Re_{d1}\right)^{-0.3} \qquad \text{(F.13)}$$

$$= 0.015 + 1.26 \times \left(213308\right)^{-0.3}$$

$$= 0.046744$$

This gave:

$$p_{t1} = -27.57 + \left[1 - \left(0.312/0.312\right)^2 + 0.046744\right] + \left(\frac{1}{2} \times 1.154 \times 5.283^2\right)$$

$$= -11.419 \text{ Pa}$$

As in the case of point three the static pressure at point four was used to calculate the total pressure behind the fan (downstream):

$$p_{t2} = p_{s4} + \left[1 + \xi_{24}\right] + \left(\frac{1}{2} \times \rho_4 \times V_4^{\,2}\right) \qquad \text{(F.14)}$$

where

$$\xi_{31} = 0.015 + 1.26 \times \left(Re_{d4}\right)^{-0.3} + 0.95 \times \left(Re_{d4}\right)^{-0.12} \qquad \text{(F.15)}$$

$$= 0.015 + 1.26 \times \left(213308\right)^{-0.3} + 0.95 \times \left(213308\right)^{-0.12}$$

$$= 0.264637$$

This gave:

$$p_{t2} = 104.61 + [1 + 0.264637] + \left(\frac{1}{2} \times 1.156 \times 5.273^2\right)$$

$$= 121.946 \text{ Pa}$$

The two values for total pressure were used to calculate the fan total, dynamic and static pressures as follows:

$$p_{tf} = p_{t2} - p_{t1} \qquad \text{(F.16)}$$

$$= 121.946 + 11.419$$

$$= 133.365 \text{ Pa}$$

$$p_{df} = \frac{1}{2} \times \rho_4 \times V_4^2 \qquad \text{(F.17)}$$

$$= \frac{1}{2} \times 1.156 \times 5.273^2$$

$$= 16.071 \text{ Pa}$$

$$p_{sf} = p_{tf} - p_{df}$$

$$= 133.365 - 16.071$$

$$= 117.294 \text{ Pa}$$

The shaft power was calculated as follows:

$$P_s = T \times \Omega \qquad \text{(F.18)}$$

where

$$T = 0.0194 \times mV_T \qquad \text{(F.19)}$$

$$= 0.0194 \times 131$$

$$= 2.541 \text{ Nm}$$

This gave:

$$P_s = 2.541 \times 150.796$$

$$= 383.173 \text{ W}$$

The fan data was corrected for a standard density of 1.2 kg/m^3 and fan speed of 1440 rpm by using the fan scaling laws:

$$Q_2 = Q_1 \times \left(\frac{rpm_2}{rpm_1}\right) \qquad \text{(F.20)}$$

$$= 1.645 \times \left(\frac{1440}{1435}\right)$$

$$= 1.651\ m^3/s$$

$$p_{sf2} = p_{sf1} \times \left(\frac{rpm_2}{rpm_1}\right)^2 \times \left(\frac{\rho_{atm\,2}}{\rho_{atm\,1}}\right) \qquad \text{(F.21)}$$

$$= 117.294 \times \left(\frac{1440}{1435}\right)^2 \times \left(\frac{1.200}{1.155}\right)$$

$$= 122.715\ Pa$$

$$p_{tf2} = p_{tf1} \times \left(\frac{rpm_2}{rpm_1}\right)^2 \times \left(\frac{\rho_{atm\,2}}{\rho_{atm\,1}}\right)$$

$$= 133.365 \times \left(\frac{1440}{1435}\right)^2 \times \left(\frac{1.200}{1.155}\right)$$

$$= 139.528\ Pa$$

$$P_{s2} = P_{s1} \times \left(\frac{rpm_2}{rpm_1}\right)^3 \times \left(\frac{\rho_{atm\,2}}{\rho_{atm\,1}}\right) \qquad \text{(F.22)}$$

$$= 383.173 \times \left(\frac{1440}{1435}\right)^3 \times \left(\frac{1.200}{1.155}\right)$$

$$= 402.278\ W$$

Using the corrected values, the fan static and total efficiencies were calculated:

$$\eta_s = \frac{Q \times p_{sf}}{P_s} \qquad \text{(F.23)}$$

$$= \frac{1.651 \times 122.715}{402.278}$$

$$= 50.4\ \%$$

$$\eta_t = \frac{Q \times p_{tf}}{P_s} \qquad (F.24)$$

$$= \frac{1.651 \times 139.528}{402.278}$$

$$= 57.3\,\%$$

F.2 PROCESSING OF FAN NOISE DATA

The fan noise was measured in front of and behind the fan, using the Bruël and Kjaer and the Rion sound level meters respectively. The values measured for the 2000 Hz octave band of the 630/250/14/1440 fan configuration were used for the sample calculations. For the Rion sound level meter the calculation was as follows:

$$Lp_{f4} = 20 \times \log \frac{p_{sound}}{p_{ref}} \qquad (F.25)$$

where

$$p_{ref} = 0.00002 \text{ Pa}$$

$$p_{slm\,4} = 0.002 \times mV_{slm4} \qquad (F.26)$$

$$= 0.002 \times 197.7$$

$$= 0.3954 \text{ Pa}$$

This gave:

$$Lp_{f4} = 20 \times \log \frac{0.3954}{0.00002}$$

$$= 85.920 \text{ dB}$$

For the Bruël and Kjaer sound level meter the calculation was as follows:

$$Lp_{f3} = 20 \times \log \frac{p_{sound}}{p_{ref}} \qquad (F.27)$$

where

$$mV_{ext} = \text{Gradient} \times mV_{slm\,3} \qquad \text{(F.28)}$$

$$= 8.189 \times 22.890$$

$$= 187.446\ mV$$

$$p_{slm\,3} = 0.0024 \times \left(mV_{slm3} + mV_{ext}\right) \qquad \text{(F.29)}$$

$$= 0.0024 \times (22.89 + 187.446)$$

$$= 0.5048\ Pa$$

This gave:

$$Lp_{f3} = 20 \times \log \frac{0.5048}{0.00002}$$

$$= 88.042\ dB$$

The sound pressure values were corrected using the corrections prescribed by the BS 848 Standards part 2 (1985):

C_1 = correction for frequency response

C_2 = acoustic calibration of windshield

C_3 = correction for turbulent noise suppression

C_4 = modal correction for in-duct test

C_5 = wind-generated false noise over sampling tube

The correction values for C_1, C_3 and C_4 were all obtained from the tables given in the BS 848 Standards part 2 (1985). The values for C_2 and C_5 were obtained by using the methods prescribed in the BS 848 Standards part 2 (1985). The values for C_2 were obtained by measuring an octave distribution of white-noise with the Rion sound level meter with and without the sampling tube (also called the measuring tube) to determine the difference in noise measured in decibles. The method is in accordance with the BS 848 Standards part 2 (1985). The results are given in Table F.1. The sampling tubes for the two different sound level meters are basically identical and therefore the one set of data was used for both sampling tubes.

Table F.1: C_2 correction values for sound pressure levels

Frequency [Hz]	C_2 [dB]
63	-0.174
125	-0.330
250	0.000
500	-0.230
1000	-7.053
2000	-9.338
4000	-4.882
8000	2.452

The values for C_5 corresponded to the wind generated noise of the sampling tube. The noise measured by the sound level meter, due to air flowing over the sampling tube, was determined. The BS 848 Standards part 2 (1985) prescribed the values for C_5 according to the difference between the fan noise being measured and the wind generated noise of the sampling tube. Since the velocity used to determine the wind generated noise corresponded to a volume flow of 20 m^3/s and these values were more than 10 dB less than the lowest noise values measured for the fan tests, the values for C_5 were assumed to be zero.

The correction values given in the BS 848 Standards part 2 (1985), namely C_1, C_3 and C_4, were all in one-third octave bands and therefore they were converted to octave band values using the following equation:

$$C_{63} = 10 \times \log\left[\frac{1}{3} \times \left(10^{C_{50}/10} + 10^{C_{63}/10} + 10^{C_{80}/10}\right)\right] \qquad \text{(F.30)}$$

where the frequency values are used as an example.

The correctional values identified for the two different sound readings were:

1) Bruël and Kjaer

$C_1 = -0.233$ dB

$C_2 = -9.338$ dB

$C_3 = 0$ dB

$C_4 = 3.019$ dB

$C_5 = 0$ dB

1) Rion

$C_1 = -0.233$ dB

$C_2 = -9.338$ dB

$C_3 = 0$ dB

$C_4 = 2.377$ dB

$C_5 = 0$ dB

The corrected sound pressure levels were calculated using the following equation:

$$Lp_c = Lp_f + C_1 + C_2 + C_3 + C_4 + C_5 \qquad (F.31)$$

Using equation (F.30) to calculate the sound pressure level in front of the fan gave:

$$Lp_{c3} = 87.722 - 0.233 - 9.338 + 0 + 3.019 + 0$$

$$= 81.490 \text{ dB}$$

Using equation (F.30) to calculate the sound pressure level behind the fan gave:

$$Lp_{c4} = 85.920 - 0.233 - 9.338 + 0 + 2.377 + 0$$

$$= 78.726 \text{ dB}$$

To obtain a single sound pressure level for the fan in a specific octave band, the values were combined using:

$$Lp = 10 \times \log\left[\frac{1}{2} \times \left(10^{Lp_{c3}\,10} + 10^{Lp_{c4}\,10}\right)\right]$$

$$= 10 \times \log\left[\frac{1}{2} \times \left(10^{81.490\,10} + 10^{78.726\,10}\right)\right]$$

$$= 80.324 \text{ dB}$$

The equations shown for the calculation of the sound pressure levels in this appendix are the ones used to obtain the data shown in the tables and the figures of the fan noise data. The noise data can also be converted to sound power values as well as dBA values, using the methods described in the BS 848 Standards part 2 (1985).